



**HAL**  
open science

# Efficient thermomechanical modeling of large parts fabricated by Directed Energy Deposition Additive Manufacturing processes.

Vaibhav Nain

► **To cite this version:**

Vaibhav Nain. Efficient thermomechanical modeling of large parts fabricated by Directed Energy Deposition Additive Manufacturing processes.. Mechanics of materials [physics.class-ph]. Université de Bretagne Sud, 2022. English. NNT : 2022LORIS630 . tel-03962675

**HAL Id: tel-03962675**

**<https://theses.hal.science/tel-03962675>**

Submitted on 30 Jan 2023

**HAL** is a multi-disciplinary open access archive for the deposit and dissemination of scientific research documents, whether they are published or not. The documents may come from teaching and research institutions in France or abroad, or from public or private research centers.

L'archive ouverte pluridisciplinaire **HAL**, est destinée au dépôt et à la diffusion de documents scientifiques de niveau recherche, publiés ou non, émanant des établissements d'enseignement et de recherche français ou étrangers, des laboratoires publics ou privés.

# THESE DE DOCTORAT DE

L'UNIVERSITE BRETAGNE SUD

ECOLE DOCTORALE N° 602

*Sciences pour l'Ingénieur*

Spécialité : « Energétique, thermique et combustion »

Par

**Vaibhav NAIN**

## **Efficient thermomechanical modeling of large parts fabricated by Directed Energy Deposition Additive Manufacturing processes**

Soutenance prévue à Illkirch-Graffenstaden, le 15 Juin 2022

Unité de recherche : Institut de Recherche Dupuy De Lôme (IRDL) UMR CNRS 6027

Thèse N° : 630

### **Rapporteurs avant soutenance :**

Michel BELLET  
Pierre JOYOT

Professeur des Universités – MINES Paris - PSL  
Maître de conférences – HDR – ESTIA

### **Composition du Jury :**

|                    |   |  |
|--------------------|---|--|
| Président :        | Anne Marie HABRAKEN   | Directrice de recherche FNRS – Liège Université  |
| Examineurs :       | Michel BELLET<br>Pierre JOYOT<br>Patrice PEYRE<br>Iryna TOMASHCHUK<br>Didier BOISSELIER | Professeur des Universités – MINES Paris - PSL<br>Maître de conférences - HDR – ESTIA<br>Directeur de recherche CNRS – Arts et Métiers – CNAM<br>Maître de conférences - HDR – Université Bourgogne Franche-Comté<br>Ingénieur – IREPA LASER |
| Dir. de thèse :    | Muriel CARIN  | Professeur des Universités – Université Bretagne Sud   |
| Co-dir. de thèse : | Thierry ENGEL   | Maître de conférences – Université de Strasbourg   |

# Acknowledgments

I warmly thank Muriel Carin, my thesis director, and Thierry Engel, my thesis co-director for encouraging me to successfully pursue my Ph.D. I would like to express my gratitude to them for providing excellent guidance and valuable suggestions. It has been a real pleasure to work with you.

I would like to thank Anne Marie Habraken for the honour she gave me by presiding over the jury. I would like to thank Michel Bellet and Pierre Joyot for agreeing to review my thesis, and Patrice Peyre, and Iryna Tomashchuk for accepting to be jury members. The jury's critical questions concerning the thesis work especially the macro-scale model helped me to dwell more on this topic and deepen my understanding.

I would like to thank Jean-Paul Gaufillet for providing me the opportunity to work at Irepa Laser. Thanks to Didier Boisselier for guiding me and providing industry insight throughout the thesis that made it possible to successful completion of the thesis.

I would like to acknowledge my colleagues and friends at Irepa Laser. Thanks to Lucas Seguy, Nathan Mayer, Haris Dzanic, and Alexis Fritsch for all the help to perform the experiments at Irepa Laser. Without their help, it would have been difficult to obtain quality experimental data that is necessary for the numerical model validation.

I would like to thank Tom Van Eekelen from SIEMENS Digital Industries Software with whom I had numerous discussions concerning the simulation methodology required for industrial software.

Also, I would like to acknowledge Christophe Cordier from INSA Strasbourg who introduced me to COMSOL and helped me to take the initial steps in understanding the software.

Special thanks to Paul Bourot, Guillaume Savirama, and Jerome Wursthorn with whom I enjoyed numerous coffee breaks, lunches, and time spent beyond working hours where we shared pleasant moments.

Lastly, I would like to thank my Maa and Papa for the love and support they have bestowed upon me throughout my life.

# Table of contents

## Contents

|  |           |
|--|-----------|
| Acknowledgments.....   | i         |
| Table of contents .....  | ii        |
| Nomenclature.....  | v         |
| General introduction.....  | viii      |
| <b>Chapter 1: Literature review .....</b>                          | <b>1</b>  |
| 1.1 Introduction.....  | 2         |
| 1.2 Types of Additive Manufacturing processes.....                 | 2         |
| 1.3 Prior work in welding.....                                     | 10        |
| 1.4 Prior Work in LDED modeling .....                              | 12        |
| 1.5 Identification of needs or Research Gap .....                  | 32        |
| <b>Chapter 2: Metal deposition modeling .....</b>                  | <b>33</b> |
| 2.1 Introduction.....  | 34        |
| 2.2 Experiment Set-Up (PIMM) .....                                 | 34        |
| 2.3 Meso-scale conduction-based pure thermal model for LDED.....   | 35        |
| 2.4 Numerical implementation.....                                  | 40        |
| 2.5 Material Modeling .....  | 42        |
| 2.6 Conclusions.....   | 56        |
| <b>Chapter 3: Thermal Model for LDED.....</b>                      | <b>58</b> |
| 3.1 Introduction.....  | 59        |
| 3.2 Modeling approach.....   | 59        |
| 3.3 Experiment Set-Up.....   | 62        |
| 3.4 Numerical implementation.....                                  | 68        |
| 3.5 Modeling results and discussion.....                           | 69        |
| 3.6 Conclusions.....   | 84        |
| <b>Chapter 4: Mechanical Model for LDED .....</b>                  | <b>85</b> |
| 4.1 Introduction.....  | 86        |
| 4.2 Modeling approach.....   | 87        |
| 4.3 Experiment Set-Up of a SS 316L wall build by LDED process..... | 100       |
| 4.4 Numerical implementation.....                                  | 102       |
| 4.5 Results and discussion .....                                   | 103       |
| 4.6 Simulation Speed-up.....                                       | 115       |

---

|   |  |            |
|---|--|------------|
| 4.7   | Conclusions.....   | 120        |
| <b>Chapter 5: Efficient thermo-mechanical model for large parts by LDED .....</b> |  | <b>122</b> |
| 5.1   | Introduction.....  | 123        |
| 5.2   | Modeling approach.....   | 123        |
| 5.3   | Experiment Set-Up of a SS 316L large wall build by LDED process..... | 125        |
| 5.4   | Numerical implementation.....  | 127        |
| 5.5   | Results and discussion .....   | 128        |
| 5.6   | Conclusions.....   | 134        |
| <b>Chapter 6: Multi-scale model for LDED.....</b>                                 |  | <b>136</b> |
| 6.1   | Introduction.....  | 137        |
| 6.2   | Experiment results.....  | 137        |
| 6.3   | Multi-scale method (Layer-by-Layer approach) .....                   | 138        |
| 6.4   | Work in progress .....   | 152        |
| <b>General Conclusions and Future Work .....</b>                                  |  | <b>161</b> |
| <b>Résumé étendu de la thèse .....</b>  |  | <b>164</b> |
| <b>Appendix .....</b>   |  | <b>xii</b> |
| <b>References.....</b>  |  | <b>xv</b>  |



---

# Nomenclature

## Acronyms

|       |  |
|-------|--|
| ISO   | International Organisation for Standardisation |
| ASTM  | American Society for testing and materials     |
| AM    | Additive Manufacturing                         |
| LPBF  | Laser Powder Bed Fusion                        |
| EPBF  | Electron Beam Powder Bed Fusion                |
| DED   | Directed Energy Deposition                     |
| LDED  | Laser Directed Energy Deposition               |
| PADED | Plasma Arc Directed Energy Deposition          |
| WAAM  | Wire + Arc Additive Manufacturing              |
| HAZ   | Heat Affected Zone                             |
| CAD   | Computer Aided Design                          |
| RS    | Residual Stress                                |
| FEM   | Finite Element Method                          |
| CMM   | Coordinate Measuring Machine                   |
| LDS   | Laser Displacement Sensor                      |
| DIC   | Digital Image Correlation                      |
| CFD   | Computational Fluid Dynamics                   |
| ALE   | Arbitrary Lagrangian Eulerian                  |
| IS    | Inherent Strain                                |
| MIS   | Modified Inherent Strain                       |
| DE    | Double Ellipsoid                               |
| EE    | Elongated Ellipsoid                            |
| G-3D  | Gaussian Volumetric                            |
| TH-2D | Top Hat Surface                                |
| TC    | Thermocouple                                   |

|     |                      |
|-----|----------------------|
| SE  | Single Ellipsoid     |
| CF  | Correction Factor    |
| EP  | Elasto-Plastic       |
| EVP | Elasto-Visco-Plastic |
| SR  | Stress relaxation    |
| EXP | Experiment           |
| SIM | Simulation           |
| DOE | Design of experiment |

### Symbols

|                    |   |
|--------------------|---|
| $\rho$             | Density   |
| $C_p$              | Specific Heat Capacity                          |
| $k$                | Thermal Conductivity                            |
| $A$                | Laser Absorptivity                              |
| $f_{f,r}$          | Weighting fraction for front and rear ellipsoid |
| $a_{f,r}$          | Front and rear ellipsoid longitudinal length    |
| $b$                | Transversal width of ellipsoid                  |
| $c$                | Ellipsoid depth                                 |
| $h_{free}$         | Heat transfer coefficient of natural convection |
| $h_{forced}$       | Heat transfer coefficient of forced convection  |
| $\varepsilon$      | Emissivity                                      |
| $\sigma$           | Stefan-Boltzmann constant                       |
| $T_s$              | Surface temperature                             |
| $T_{amb}$          | Ambient temperature                             |
| $\sigma$           | Stress  |
| $\varepsilon_{to}$ | Total strain                                    |
| $\varepsilon_{el}$ | Elastic strain                                  |
| $\varepsilon_{pl}$ | Plastic strain                                  |

---

|                    |  |
|--------------------|--|
| $\varepsilon_{th}$ | Thermal strain                                     |
| $\varepsilon_{tr}$ | Transformation stress                              |
| $F$                | Yield function                                     |
| $\sigma_m$         | Von Mises stress                                   |
| $\sigma_y$         | Yield stress                                       |
| $\varepsilon_{eq}$ | Equivalent plastic strain                          |
| $E$                | Young's modulus                                    |
| $\nu$              | Poisson's ratio                                    |
| $k_{quiet}$        | Thermal conductivity of quiet/dummy material       |
| $C_{P_{quiet}}$    | Specific heat capacity of quiet/dummy material     |
| $E_{quiet}$        | Young's modulus of quiet/dummy material            |
| $L_f$              | Latent heat of fusion                              |
| $V_s$              | Laser scanning speed                               |
| $\alpha$           | Coefficient of thermal expansion                   |
| $\sigma_{sat}$     | Saturation flow stress                             |
| $\beta$            | Saturation exponent                                |
| $T_{relax}$        | Stress relaxation temperature                      |
| $T_{anneal}$       | Annealing temperature                              |
| $\hat{a}$          | Elongated Ellipsoid length                         |
| $K_E$              | Dimensionless parameter (Elongation factor)        |
| $K_Q$              | Dimensionless parameter (Source correction factor) |
| $t_{DW}$           | Dwell time   |
| $N_B$              | Number of beads/tracks                             |
| $N_L$              | Number of layers                                   |
| $t_f$              | Flash/exposure time                                |

# General introduction

Today, Additive Manufacturing (AM) needs to go towards large, even very large parts, which can reach several meters in length (for example structural elements) or in diameter (for example aircraft engine casings).

IREPA LASER has been a forerunner in terms of additive manufacturing, having conducted research for more than 20 years, and jointly with INSA Strasbourg, several theses have led to the CLAD™ process (Construction Laser Additive Direct) (Sankaré, 2007). The MAGIC machine was developed on this basis, making it possible to build parts with a volume of up to 800x800x1000 mm<sup>3</sup> today as presented in **Fig 1.1**. Such dimensions inevitably result in significant deformations and mechanical stresses, related both to the process (localized melting and rapid cooling), the material, the clamping conditions, and also to the part manufacturing strategy.

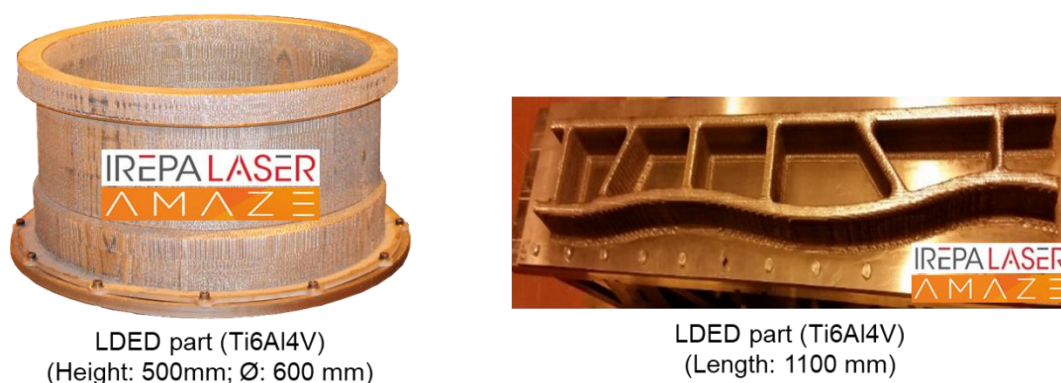


Figure 1. 1: Large scale part fabrication by LDED (Laser Directed Energy Deposition)

These large parts require very long manufacturing times, which can reach several hundred hours, involving the use of large quantities of materials representing high costs, particularly in the case of materials with high added value such as titanium alloys. The deformations and induced mechanical stresses lead to defects, which can result in part rejection. These catastrophic situations have serious consequences in financial terms, but also for machine time and lost materials. The main approach still applied today is by trial and error until a geometrically-accurate part is produced. In the case of large parts, however, this approach is difficult to apply, and it becomes essential to be able to simulate deformations before manufacturing. Simulation becomes essential as it allows to make corrections and contributes to achieving the objective of “part first time right”. To achieve this goal, a better knowledge of the distribution and accumulation of residual stresses is however necessary (Dunbar et al., 2016). Numerical modeling of the AM process is thus the ideal solution for predicting thermal and mechanical behaviour, making it possible to optimize operating conditions and manufacturing strategies.

Thus, in the present work, the focus is to develop an efficient thermo-mechanical model capable to simulate large parts manufactured by Laser Directed Energy Deposition (LDED) Additive Manufacturing (AM) processes. The present thesis work comes under a work package of an industrial project named PAMPROD. It is a FRENCH national project. It is part of a 3-year PSpC project coordinated by the company APERAM, bringing together French actors and industrialists in additive manufacturing. The main objective of the PAMPROD project is to develop a large industrial robotic machine, combining wire and powder deposition that is capable of manufacturing large parts.

## Consortium

As part of this thesis, close collaboration is carried out between IREPA-LASER, University of Bretagne-Sud, and INSA Strasbourg.

- IREPA LASER is a research institute of laser application processes, specialised in laser processing and materials. It develops innovative and sustainable manufacturing solutions and assists their operational implementation in the industry. It has a technological platform with different laser processes (welding, AM, surface functionalisation). All the experimental works of this Ph.D. thesis were carried out at IREPA LASER using Laser Directed Energy Deposition (LDED) technology. Furthermore, IREPA LASER has become the solution partner of SIEMENS in 2020. It is envisioned that the results obtained from the Ph.D. thesis work developed with COMSOL Multiphysics® will be tested, evaluated, and integrated on SIEMENS NX software within the framework of the PAMPROD project.
- The Université Bretagne Sud (UBS) through its IRDL laboratory (Dupuy de Lôme Research Institute) is specialized for more than 20 years in numerical modeling of welding processes and for ten years in AM. Moreover, a dozen Ph.D. thesis were conducted using COMSOL Multiphysics®, the software selected for this Ph.D.
- INSA Strasbourg has been collaborating with IREPA LASER for more than 20 years, developing laser processes and associated characterization means, as well as modeling the laser-material interaction, only in the thermal regime for powder deposition, welding, and more recently, the simulation of large parts in AM with powder i.e., LDED.

## Objectives

Compared to other conventional manufacturing technologies, DED offers a unique opportunity of fabricating large-scale complex-shaped parts directly from a digital CAD file within a short time. Parts can be fabricated in a continuous layer-by-layer fashion by melting powder or wire employing a laser, electron beam, or electric arc. But the large thermal gradients originating from process physics result in the accumulation of distortion and residual stresses. Especially for big parts, this often results in fabricated parts going out of tolerance which leads to part rejection. To reduce the distortion, traditionally in the industry, this is resolved by an expensive experimental trial-and-error iterations approach. Furthermore, this approach does not contribute to understanding the process-physics as well. Therefore, to successfully reduce distortion in metallic DED big parts, an experimentally validated efficient numerical model is needed.

*The objective of the present work is to develop and experimentally validate thermo-mechanical Finite Element (FE) models for metallic parts fabricated by Laser Directed Energy Deposition (LDED).*

In this work, multiple FE models for Laser DED (LDED) process are developed and validated with experimental results. In-situ temperature and distortion measurements are done during the fabrication of different Stainless Steel 316L walls. In addition to in-situ distortion data, post-process distortion measurements are also taken to validate the thermo-mechanical model. Different walls with varying process parameters were fabricated to confirm the versatility of the proposed model.

The conventional meso-scale Thermo-elastoplastic model showed that stress relaxation plays a crucial role in determining the distortion magnitude and is validated with experimental results. The conventional model is validated against in-situ temperature and distortion measurement as well as post-process distortion measurement for all experiment cases. But the conventional model was found to be infeasible to simulate big parts. Hence, an efficient model is developed that drastically reduces the computation time up to a factor of

15-20 by maintaining acceptable levels of computation accuracy above 90%. Finally, other part-scale models are also developed to investigate these models in terms of computation speed and accuracy.

The objectives of the present thesis work can be summarised as follows:

- Develop and identify suitable metal deposition model for LDED
- Develop and experimentally validate thermal model for LDED
- Develop and experimentally validate mechanical model for LDED
- Develop and experimentally validate Efficient thermo-mechanical model for large LDED parts
- Develop and investigate the feasibility of Multi-scale model for LDED
- Transfer and integrate thesis work to commercial software (SIEMENS)

## Thesis outline

An outline of the work done to develop and experimentally validate the thermo-mechanical models for the LDED process is presented here. Contributions of the work done in the thesis are organized into six chapters. The **chapter 1** presents a literature review of numerical modelling of AM processes especially LDED. The different strategies proposed for thermomechanical simulations of AM processes are discussed, in order to identify the best practices to calculate distortions, especially for large parts.

The **chapter 2** is dedicated to the metal deposition strategy. Different numerical methods to model metal deposition are analysed, such as Quiet/active, hybrid activation and ALE method. These methods are implemented in combination with a thermal model using different surface and volumetric heat sources to model input laser energy. From that study, a Goldak's Double Ellipsoid (DE) Heat source is chosen by comparing successfully the calculated temperatures with experimental data given in literature for Ti-6Al-4V material for single bead wall structures.

In **chapter 3**, the focus is placed on the development of the thermal model with special attention to the reduction of computation time. First, a series of experiments is performed at Irepa Laser to record the thermal response of Stainless Steel 316L via thermocouples and Infra-Red camera during deposition of single bead wall structures for different laser power and dwell time. Second, these experimental data are compared to results calculated by a thermal model using a Goldak's Double Ellipsoid Heat source. Then, a new heat source is proposed based on an Elongated Ellipsoid (EE) formulation. Its effects on the computation time and thermal error are analysed. Solutions are proposed to keep computation thermal error below 10%.

The **chapter 4** is dedicated to the development of thermomechanical model for LDED. First, experiments are performed to record the thermo-mechanical response of Stainless Steel 316L via thermocouples and Laser Displacement Sensor (LDS) respectively during deposition of single and double bead wall structures for different dwell time. Second, a thermomechanical model is implemented using an elasto-plastic behaviour. The need to include stress relaxation in order to obtain consistent mechanical response is shown with a thermal model using DE heat source. Then, a thermo-mechanical model with stress relaxation that employs EE heat source is implemented to demonstrate its effectiveness on the reduction of computation time while keeping computation thermo-mechanical error below 10%.

The **chapter 5** aims at showing the relevance of the previous strategy to simulate efficiently the thermomechanical response of large parts manufactured by LDED. New experiments are performed to record the thermo-mechanical response of Stainless Steel 316L via thermocouples and LDS respectively during deposition of double bead wall structures for different number of layers (50 and 100). Thermo-mechanical

model with stress relaxation and EE heat source is used to demonstrate its effectiveness to reduce the computation time becomes more significant for large parts.

In **chapter 6**, other strategies to reduce computation time are investigated for LDED. Multi-scale method is implemented and its effectiveness to give a global idea of the material response is studied by comparing with experiment results. Inherent Strain-based method for LDED is also investigated.

Finally, the manuscript ends with a conclusion giving a summary of the work done during this Ph.D. and presents some highlighting areas for future work.

# Chapter 1: Literature review

|  |    |
|--|----|
| Chapter 1: Literature review .....                           | 1  |
| 1.1 Introduction.....  | 2  |
| 1.2 Types of Additive Manufacturing processes.....           | 2  |
| 1.2.1 Type of Directed Energy Deposition (DED) .....         | 3  |
| 1.2.2 Laser Beam Directed Energy Deposition (LDED) .....     | 4  |
| 1.2.3 Heat Source and Powder Interaction.....                | 6  |
| 1.2.4 The Melt-Pool .....                                    | 7  |
| 1.2.5 Conduction Heat Transfer.....                          | 7  |
| 1.2.6 Issues related to LDED .....                           | 8  |
| 1.3 Prior work in welding.....                               | 10 |
| 1.4 Prior Work in LDED modeling .....                        | 12 |
| 1.4.1 Meso-scale modeling: conduction-based simulations..... | 13 |
| 1.4.2 Meso-scale modeling: flow-based simulations .....      | 26 |
| 1.4.3 Part-scale models.....                                 | 28 |
| 1.5 Identification of needs or Research Gap .....            | 32 |

## 1.1 Introduction

*The objective of the present chapter is to do a detailed literature review concerning the numerical modeling of the LDED process and to identify research gap from the review. The secondary objective is to identify the best practises employed in the domain of numerical modeling as it contributes in developing a better understanding of the concerned topic.*

Just consider a hypothetical situation that a space shuttle is on its specified mission and one of its parts breaks down in outer space. Practically that would require a cargo space shuttle to deliver this spare part which is unimaginable or it should be repaired at International Space Station. Ideally, it would be great to manufacture this required spare part on board the space shuttle. NASA has been looking and probing this prospect of manufacturing a part by 3-D Print Technology in space itself. Product personalization is a growing trend in world markets and if products can be produced anywhere independent of the location, such as Space Shuttle or any personalized product at home will be a big revolution in the manufacturing and transportation sector. This, considering this trend, Amazon has recently led a patent for Mobile 3-D Printing Delivery Trucks (Apsley et al., 2015). Additive manufacturing (AM) can certainly be a significant contributor to fulfilling the demands for this futuristic trend.

## 1.2 Types of Additive Manufacturing processes

As defined by ISO/ASTM (International Organization for Standardization/American Society for Testing and Materials) F2792-12a, Additive Manufacturing (AM) is a process of joining materials to make objects from 3D model data, usually layer upon layer, as opposed to subtractive manufacturing methodologies. Synonyms may also be mentioned: additive fabrication, additive processes, additive techniques, additive layer manufacturing, layer manufacturing, and freeform fabrication (Milewski, 2017).

As classified by ISO/ASTM 52900, Metal AM methods can be broadly classified in two namely Powder Bed Fusion (PBF) and Directed Energy Deposition (DED) (Milewski, 2017).

Within the present work, we clarify the type of Metal AM process by adding a designation of the heat source used for the specific technology, such as L for Laser Beam (LPBF, LDED) or E for electron beam (EPBF, EDED).

As defined by ISO/ASTM F2792-12a, PBF is an additive manufacturing process in which thermal energy selectively fuses regions of a powder bed. "Thermal Energy" means that an energy source (e.g. LPBF, EPBF) is focused to melt powder being deposited that is lying on a powder bed (Milewski, 2017).

As defined by ISO/ASTM F2792-12a, DED is an additive manufacturing process in which focused thermal energy is used to fuse materials by melting as they are being deposited. "Focused thermal energy" means that an energy source (e.g., laser LDED, electron beam EDED, or plasma arc PADED) is focused to melt the material being deposited (Milewski, 2017).

Laser Directed Energy Deposition (LDED) and Wire + Arc Additive Manufacturing Process (WAAM) are commonly used additive manufacturing (AM) processes. In both of these processes, net and near net shape components are fabricated in a layer-by-layer (digital slicing) manner directly from digital drawing files (.stl). The main feature of AM processes is their flexibility that allows complex and different part geometries on the part scale ranging from mm<sup>3</sup> to m<sup>3</sup>. In LDED and WAAM process, each layer is fabricated by fusing individual passes from a wire (WAAM or DED-PA) or powder feedstock material (LDED), which experiences rapid heating,

melting, solidification, and cooling during the deposition process. As the part is fabricated, the deposited material undergoes multiple repeated heating and cooling cycles as more pass and layers are added. One of the consequences of the thermal gradients induced in the components by the layer-by-layer deposition of material in AM processes is the build-up of undesirable levels of distortion and RS. This unwanted distortion and RS can lead to loss of tolerance and failure. Currently, these issues are tackled using an experimental trial and error approach where several samples are fabricated to iteratively reach the desired outcome. In addition to being time-consuming and expensive, the trial-and-error approach does not help in developing the scientific understanding related to mitigation of distortion and RS, as even small changes to the build plan (Process Parameters, *etc.*) can result in large changes in distortion and stress accumulation. To avoid trial and error approach, an experimentally validated predictive model is needed that can calculate possible distortion and stress accumulation and be helpful to find the best strategies to mitigate these distortions and RS.

### 1.2.1 Type of Directed Energy Deposition (DED)

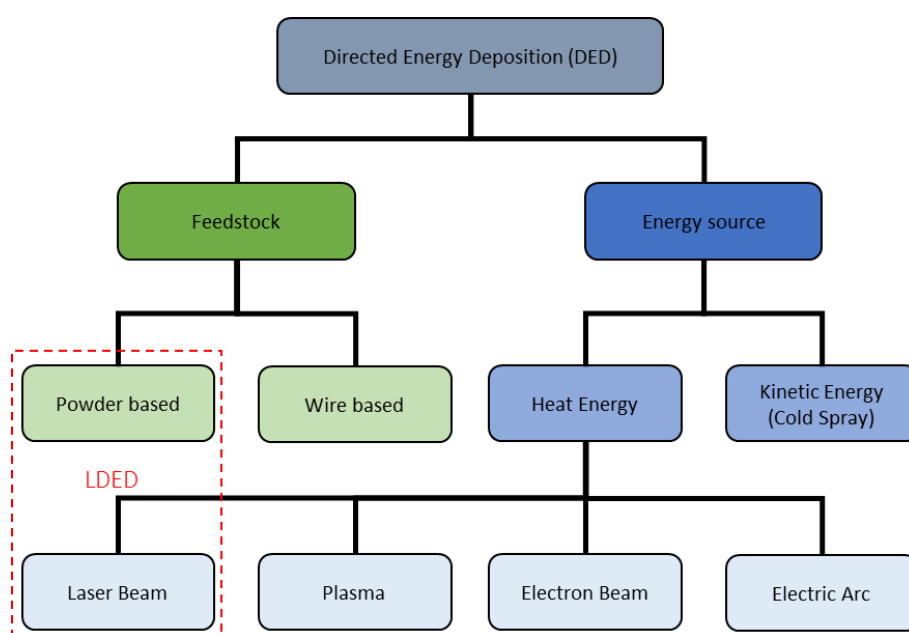


Figure 1. 2: Classification of DED system

Generally, DED systems have a concentrated energy source and a stream of raw material (powder or wire), both intersecting at a common focal point, usually in the presence of inert shield gas. The energy density generated at a common focal point melts the incoming raw material in and around that spot, giving rise to the formation of a melt pool. Currently, there are various types of DED systems, which include (but are not limited to): Powder-feed (LDED) and wire-feed based DED (PADED, WAAM, LDED) based on the type of feedstock, fusion-based DED, and kinetic energy based DED (based on the type of energy source). Fusion-based DED can be further sub-classified depending upon the heat source such as Laser based DED (LDED), electron beam-based DED (EDED), plasma-based DED (PADED) and electric arc-based DED (PADED or WAAM). The powder-based DED system (LDED) is the most commonly used metal DED technique and it has been studied extensively in the literature. **Fig 1.2** summarises the different DED categories explained above in the form of flow chart (Dass and Moridi, 2019).

In the present work, as shown in the red box in **Fig 1.2**, only LDED technology is considered. In the following sections, numerical modeling done by previous researchers in LDED is presented, and also the research gap

between the current industry issues and proposed solutions in the literature is identified. But before that, brief literature on welding is presented because a lot of LDED work is taken from welding technologies.

## 1.2.2 Laser Beam Directed Energy Deposition (LDED)

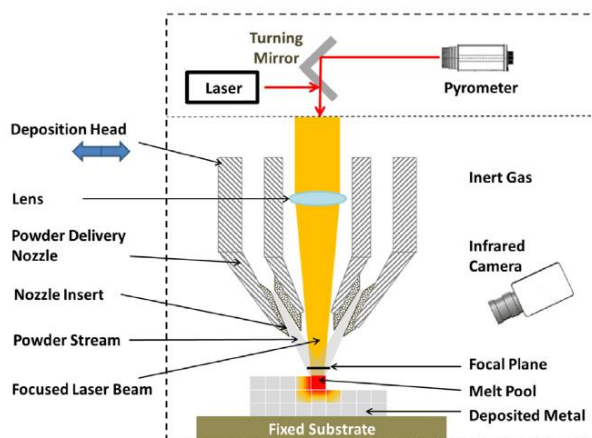


Figure 1. 3: Schematic of LDED process with thermal monitoring (Thompson et al., 2015)

LDED process fully melts the incoming delivered metal powder brought by the co-axial nozzle as shown in Fig 1.3 (Thompson et al., 2015). The laser/powder co-axial nozzle is traversed according to the programmed scan path followed by melt-pool, hence continuously depositing the fabricated part on the substrate or fabricated part. Usually, metal powder is brought by the inert gas that prevents the molten metal from oxidation. The gas acts as a carrier to deliver the powder stream to a common focal point of laser beam i.e., melt-pool usually.

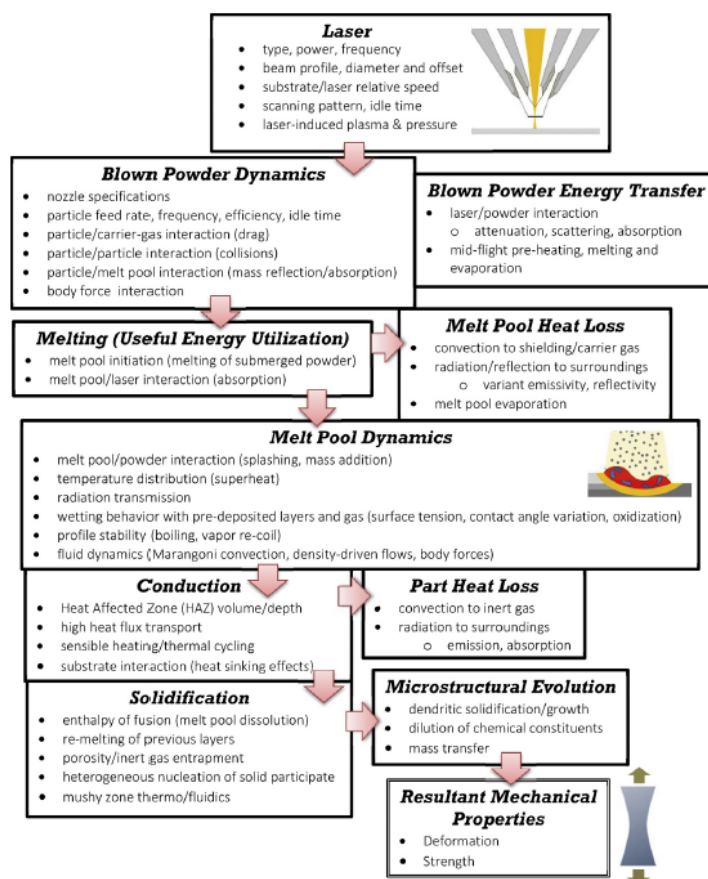


Figure 1. 4: Physical Process of DED occurring at a given instant in time (Thompson et al., 2015)

So, it can be said that LDED depends upon the feeding of powder into the molten metal created by a laser beam on a pre-defined melt-path to deposit metal layer-by-layer approach on a substrate or build-plate.

LDED process consists of many coupled and interconnected physical events and all are occurring at a very small-time scale. At a given instant of time, there are different possible energy transfers that is taking place as shown in **Fig 1.4** (Thompson et al., 2015). Some of these physical events include: laser delivery, particle/powder delivery (energy and dynamics), laser/powder/gas interaction, initialization of melt-pool (melting), melt-pool energy/stability, heat loss to environment via thermal radiation and convection, solidification, intra-fabricated part conduction, thermal cycling and fabricated part to substrate conduction. Some of the detailed physical 'sub-events' for each category are shown in **Fig 1.4**. All the above-stated physical events and sub-events in the LDED process have been studied and investigated for the past few decades either directly in the field of LDED or in the related manufacturing processes, e.g., laser welding/cladding.

In the earlier days, LDED systems usually had single co-axial nozzles in the atmosphere, while current LDED machines can have up-to four nozzles and also utilize the inert atmosphere in the gas chamber or machine chamber to minimize the high oxidation rates that are associated with high-temperature metal processing.

The main parameters of the powder delivery system that influences the consistency of powder focus with laser beam focus are powder feed rate, delivery gas flow rate, nozzle size, shape, location, and powder impingement. Different nozzle configurations for LDED are available and are shown in the **Fig. 1.5** (Milewski, 2017).

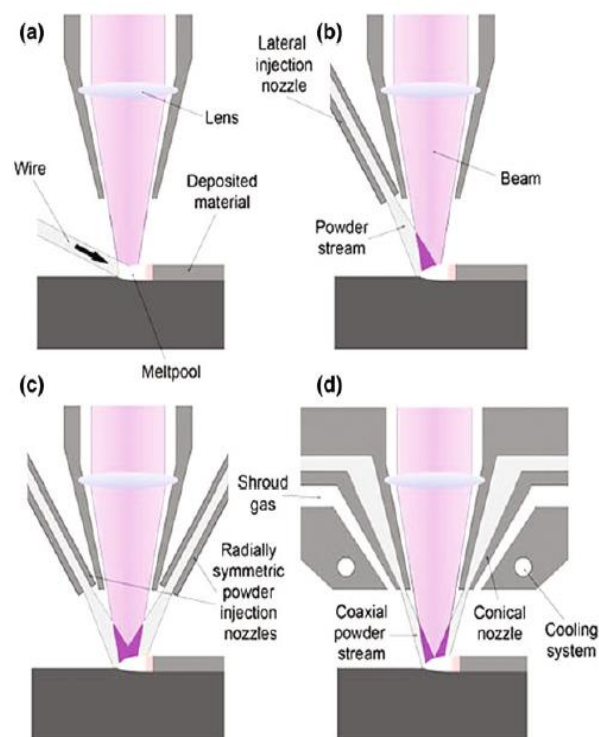


Figure 1. 5: LDED Nozzle Configuration (Milewski, 2017)

The simplest configuration is shown in **Fig 1.5** (a) and (b) with a single wire or powder feeding nozzle with an already defined relationship with the laser beam and melt-pool in terms of positioning of the powder focus, melt-pool/feeder distance, and angle of incidence of powder focus etc. Change of focal position affects the penetration resulting into a change in dilution in the base material due to the deposition of build material (powder).

### 1.2.3 Heat Source and Powder Interaction

Mostly, in industrial applications for LDED, laser is operated in continuous mode rather than pulse mode. The laser energy distribution can be of Gaussian or Top-Hat and depends upon the particular machine settings or operator's choice. During the powder flight, a fraction of the laser energy is absorbed by powder particles and a part of it is absorbed by the substrate leading to the formation of a melt-pool as shown in **Fig 1.6** (Marion, 2016). The remaining laser energy is reflected from powder particles and substrate.

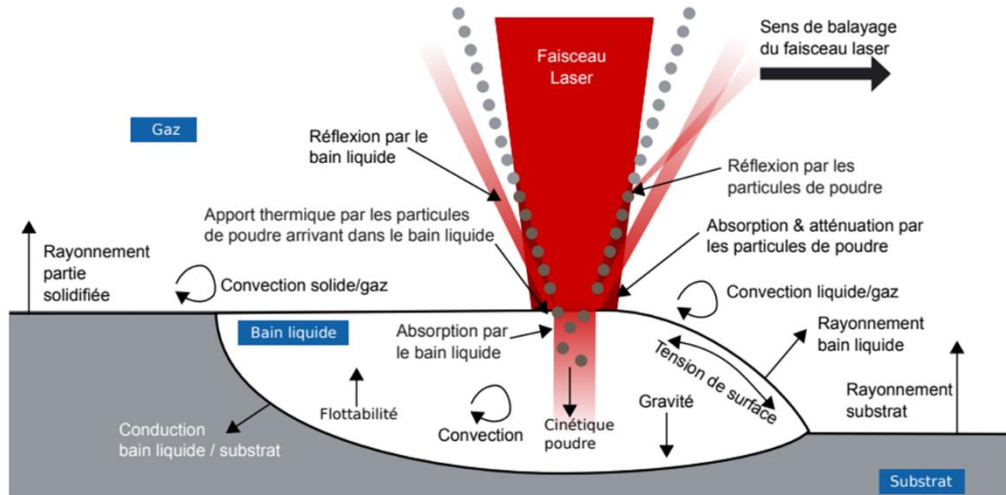


Figure 1. 6: Physical phenomenon during laser material interaction in LDED (Marion, 2016)

The fraction of the total laser energy that is consumed in heating the powder particles (Laser attenuation) as they emerge from the nozzle and travel through the beam during the flight depends upon different process parameters namely, powder density (size and distribution), in-flight duration (nozzle-melt pool), and gas velocity (Manvatkar et al., 2014). as shown in **Fig 1.7**.

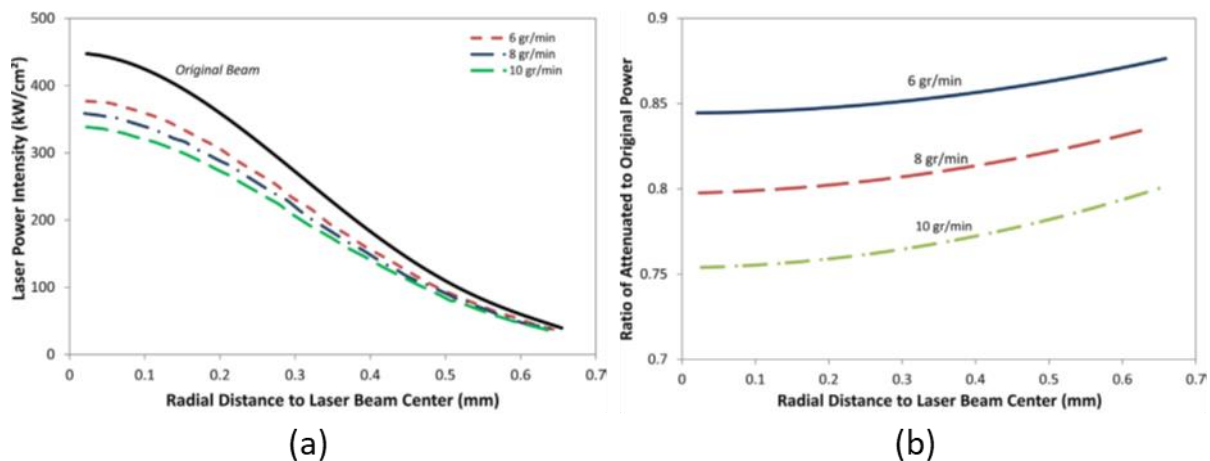


Figure 1. 7: (a) Laser powder intensity vs radial distance for various powder feed rates (He and Mazumder, 2007)  
(b) Ratio of attenuated-to-original power vs radial distance for various powder feed rates (He and Mazumder, 2007)

The powder particles are usually heated to a higher temperature and can sometimes reach their melting temperature (Morville et al., 2012a). The remaining beam energy impinges on the deposit surface resulting in a melt-pool. The amount of energy absorbed by the deposit surface depends on laser beam characteristics, deposit geometry and the shielding gas (He and Mazumder, 2007). The powder stream also plays a big role in

the radial laser power intensity profile because of the intersection of powder particles with a laser beam (He and Mazumder, 2007). The ratio of attenuated to original laser power is also affected due to the powder stream (He and Mazumder, 2007). For fixed laser power, with an increase in powder feed rate, there is a slight decrease in the mean temperature of the powder stream and a higher degree of laser attenuation as shown in **Fig. 1.7** for a Gaussian irradiation profile. It can be seen that laser attenuation can be a significant factor and can result in only 75% of original power reaching the melt pool surface (He and Mazumder, 2007). Toward the centre of the laser beam (with Gaussian profile), the ratio of attenuated-to-original laser power is lowest, indicating that the powder closest to the beam center absorbs more.

## 1.2.4 The Melt-Pool

The melt-pool is the region of superheated molten metal in proximity to the laser/material interface usually in the form of a spherically shaped droplet that travels at the scan speed. The peak temperature in the melt-pool may be hundreds of degrees above the liquidus temperature of the deposited metal or substrate, but usually process parameters are optimized in such a way that the peak temperatures are kept less than boiling temperature (Morville, 2012a). As shown in the **Fig 1.8**, the melt-pool is placed at the top of the Heat Affected Zone (HAZ), melt-pool is thermodynamically unstable leading to the adjustment in shape and in internal energy because of the heat transfer to the surrounding and solid/liquid interaction (Thompson et al., 2015).

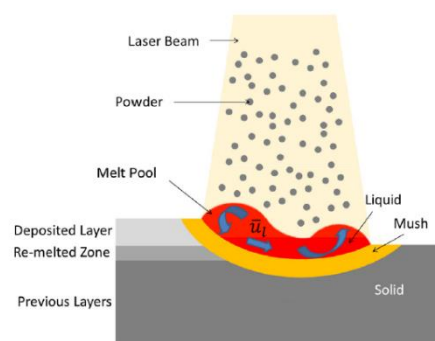


Figure 1. 8: Heat Affected Zone (HAZ) and melt-pool in DED-L (Thompson et al., 2015)

The heat transfer within the melt-pool is latent because of the phase change (melting), the temperature distribution is at or higher than the liquidus temperature of the material. The thermal gradient across the melt-pool can be in the range of 100 to 1000 K/mm (Ye et al., 2006; Yin et al., 2008). Marangoni convection is fluid motion governed or driven by surface tension gradients can increase the heat transfer by convection within the melt-pool. The Marangoni convection also influences/acts on the melt-pool shape and flow (Morville, 2012a). This indicates that melt-pool heat transfer (and temperature distribution) is coupled with its morphology that is also coupled with the wetting behaviour at the part interface.

## 1.2.5 Conduction Heat Transfer

Around the vicinity of the melt pool and mushy zone, there is a domain of higher temperature range and heat transfer relative to the remaining part and environment. This 'heat affected zone (HAZ) comprises considerable temperature gradients due to the laser-initiated melt pool, phase-change heat transfer and surrounding environment. Heat transfer within the HAZ is predominantly sensible (conduction) in pre-deposited layers but, latent heat transfer occurs within the mushy zone and re-melting can occur for very high laser powers. The depth of the HAZ is usually referred as the penetration depth that depends upon part height, laser power, laser travel/scan speed, and temperature. The repeatable passing of the laser over a previously

deposited solid region of the part results in ‘thermal cycling’ effects – that is disturbances in the localized temperature field with sharp increase of temperature, with instantaneously very high heating rates and then leads to low cooling rates. This behaviour of temperature results in solid state transformations, which then leads to evolution of microstructure and thermomechanical interactions such as RS formation and distortion (Michaleris, 2011).

## 1.2.6 Issues related to LDED

Due to the process physics in the LDED process, a number of issues arise in the fabricated part that can lead to part rejection or failure:

Geometrical defects are considered to be the most important or influential defects. These defects are taken as the variation of the produced part geometry in comparison to intended CAD model. This can lead to the rejection of the deposited part due to one of the following reasons:

### 1. Varying layer height

The deposition layer height is not uniform at the start of the deposition process as the process is not stable that leads to lower or higher part than the original intended part. This defect can be due to the non-uniform powder feeding rate, laser scan speed and laser power (Li et al., 2003). This issue can be resolved by using the dynamic values of either the powder feeding rate, laser scan speed, laser power or a combination of these parameters as a function z-height (deposited layers height) (Xiong et al., 2008).

### 2. Material shrinkage/Distortion

Due to the laser-material interaction, deposition of the hot material leads to fusion, solidification and cooling phenomenon. During cooling, shrinkage of the material in the current layer as well as deposited layer takes place. Material shrinkage upon cooling leads to smaller part dimensions in reference to original CAD or intended part (Pinkerton and Li, 2004). Material shrinkage/distortion is not just limited to deposited part, but substrate also experiences this phenomenon as shown in **Fig. 1.9**.



Figure 1. 9: Distortion accumulation in large parts fabricated by LDED

Distortion can be a real problem especially for large part as distortion keeps on accumulating with deposition of each layer. Distortion magnitude (build direction) can exceed the nozzle-workpiece distance leading to damage of the nozzle. Other possibility is distortion magnitude (transversal direction) that can exceed the width of deposition layer and starts to bend making it impossible for further fabrication of new layer as the preceding layer position is not feasible.

### 3. Warping at substrate/deposited part zone

In some cases, excess of stress concentration can happen at the deposited part-substrate junction accumulated due to the excessive heat input or non-optimised deposition strategies/process parameters (Miedzinski, 2017). This can lead to detachment of the deposited part at the bottom layer or deposited part-substrate junction as shown in **Fig 1.10**. This detachment results in part-rejection and scrap.



Figure 1. 10: Warping leading to build-part's detachment from the substrate/base-plate (Irepa Laser: AMAZE Project)

This issue can be resolved by either of the following strategies:

- (a) Pre-heating the substrate to a certain calibrated/optimised temperature.
- (b) Optimisation of deposition strategies.
- (c) Optimisation of dwell/waiting time between successive layers.

### 4. Residual stress (RS)

RS ( $\sigma$ ) are generated due to the unique process physics of LDED characterised by rapid heating and cooling of the current deposited layer followed by re-melting and cooling of previously deposited layers during the deposition of new layer. RS is also a critical defect of the deposited part because this leads to poor material properties and part distortion (Acevedo et al., 2020). Laser-material interaction leads to the heating/fusion state of the deposited material, that leads to material expansion ( $\epsilon$ ). But this phenomenon is constrained due to the surrounding material/substrate that has much lower temperature than the deposited material. This

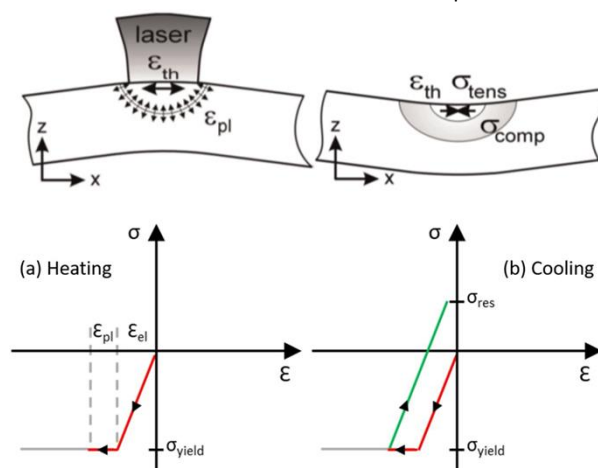


Figure 1. 11: Residual stress formation during (a) heating (b) cooling (Acevedo et al., 2020)

restraining leads to the generation of compressive stress in the deposited/heated zone. On the contrary, during the cooling down period, when heat source is not radiating and is moved, the previously deposited material or heated zone is cooling that leads to thermal shrinkage/contraction in this zone. But the shrinkage/contraction is partially restrained by already present plastic strain accumulated during the heating period. This leads to the formation of tensile stress in the heated/deposited zone and compressive stress in the nearby zone/substrate/already deposited layers. This phenomenon is explained in the schematic shown in Fig 1.11.

Generation of RS can depend upon many factors such as dwell time, deposition strategies or any process parameter that influences the thermal evolution in the workpiece (C. Li et al., 2018). RS issue can be resolved by the following strategies:

(a) In-situ process control

- i. Pre-heating of substrate leads to lesser thermal gradient that results in less RS (Acevedo et al., 2020)
- ii. Optimisation of deposition strategies can also drastically reduce RS (Acevedo et al., 2020).
- iii. Infra-Red Camera can be helpful in identifying the low or excess thermal gradient zone (Acevedo et al., 2020).

(b) Post-process control

Post-process heat treatment techniques such as Annealing can reduce 70% of RS in the build-part (Shiomi et al., 2004). That's why in LDED process, distortion is considered the most important defect because once distortion is accumulated in the build-part, it is non-recoverable. On the contrary, RS in the build-part can be removed using different heat treatment techniques.

Hence, in the industrial research and applications, a lot of efforts are put on to optimise the process parameters that results in minimum level of distortion and not RS. Because, in the usual process, heat treatment of the deposited part is always done. ***Therefore, in the present work of the thesis, the development of the numerical model is done by keeping this point in mind and all calibrations and validations of the numerical model is done with respect to distortion.***

## 1.3 Prior work in welding

The utilisation of Finite Element Method (FEM) in AM to predict the temperature history leading to distortion and RS originates from the prior research performed on multi-pass welding. In Multi-pass welding, a heat source is used to melt material onto a workpiece where it is allowed to cool and then solidify. This process is quite similar to AM, in which heat source is used to melt material onto a substrate where it is allowed to cool and solidify. Both in Multi-pass welding and AM, thermal gradient led to unwanted distortion and RS.

As welding and AM processes share many similarities, their numerical models can also be compared. The pioneer work in numerical modeling of distortion and RS began in 1970's when Hibbitt and Marcal (Hibbitt and Marcal, 1973) demonstrated the capability of an uncoupled 2D thermo-mechanical model to predict the mechanical response of simple bead-on-plate welds. There were also some other models that were developed during 1970's (Andersson, 1978; Friedman, 1975; Ueda and Yamakawa, 1973). Geometric complexity was reduced, they used 2D Lagrangian, plane strain, plane stress, or axisymmetric kinematic models. The material model was taken as Elasto-Plastic with temperature dependent properties. The heating effect of the arc was usually modelled as a prescribed flux. Thermal stresses were not computed above a reference cut-off temperature.

After the development of the above mentioned models in 1970's, further new Finite Element Models for welding were developed by researchers to predict thermal and mechanical response (Argyris et al., 1982; Free and Porter Goff, 1989; Lindgren et al., 1999; Michaleris et al., 1995; Tekriwal and Mazumder, n.d.). Argyris (Argyris et al., 1982) performed a Visco-Plastic stress analysis of a weld. At first, an in-plane thermal analysis is done. Then this analysis is coupled with a cross-sectional thermal analysis and a plane stress-strain analysis. Tekriwal and Mazumder (Tekriwal and Mazumder, n.d.) proposed a method of modeling mechanical response of a weld in which first a 3D transient heat transfer analysis is done. Then these results are used in a transient Thermo-Elasto-Plastic analysis to calculate stress and strain, yielding accurate results when compared with experiment results. This approach is now commonly utilised in thermal and mechanical analyses for both welding and AM. Free et al (Free and Porter Goff, 1989) performed a 2D uncoupled thermo-mechanical analysis for multi-pass welds to predict RS. In the model, thermal and mechanical material properties were taken as temperature independent other than yield strength.

In the late 1990's, Brickstad and Josefson (Brickstad and Josefson, 1998) used two-dimensional (2D) axisymmetric model to do a numerical modeling of a series of multi-pass circumferential butt-welds of stainless steel pipe up to 40 mm thick in a non-linear thermo-mechanical finite element analysis. Wen and Wen et al (Wen and Farrugia, 2001) also used a two-dimensional axisymmetric finite element (FE) model to simulate three pass pipe girth welding with wall-thickness of 19 mm.

In the mid 2000's, Deng and Murakawa (Deng and Murakawa, 2006) developed and compared the uncoupled thermo-mechanical 3D model with 2D axisymmetric Finite Element Model. Results justified the effectiveness of axisymmetric 2D model by reducing computation time drastically but still showing satisfactory results.

In the early 2000, Mochizuki et al. (Mochizuki et al., 1999) used inherent strain analysis and thermal elastic plastic analysis to predict RS in carbon steel pipe, and they verified their numerical models using neutron diffraction measurement. Today, the inherent strain method, which will be more detailed in Section 4.3.1, is vastly used in the commercial software for AM, because it reduces computation time drastically.

Some researchers have shown that the inclusion of transformation strain caused by solid-state phase transformation present in steel is critical in weld modeling due to the reason that transformation strain influence bulk distortion and RS of workpiece, with lower martensite-start temperature yielding reduced levels of RS and distortion (Dai et al., 2008; Francis et al., 2009a). Francis et al. (Francis et al., 2007) have presented a detailed review of welding RS present in steel and concluded that transformation strains present in welded steel can completely negate or erase the strain caused by thermal contraction in the welding. The negation or erasing of strain caused due to thermal contraction by transformation strain alters the distribution of bulk RS throughout a workpiece and has been shown to reduce bending stresses on the bottom of surface of base plates for bead-on-plate welds (Francis et al., 2009b). Because AM is a similar process to welding, the welding literature suggests that transformation strain also need to be included in AM models. Generally, the primary goal to do numerical modeling of welding is mitigation of distortion. In order to reduce distortion the appropriate distortion mode must be identified as first defined by Masubuchi (Masubuchi, 2013).

The out-of-plane distortion modes include angular, buckling, and longitudinal bending. Angular and buckling distortion are caused by similar mechanisms. Angular distortion is caused by transverse shrinkage in the deposition region, while buckling occurs when RS caused by longitudinal shrinkage exceeds the workpiece critical buckling strength. Both angular and buckling distortion are less common in AM than in welding as the substrates used are generally thicker than weld panels. Of the 3 possible out-of-plane modes, longitudinal bending is of primary concern in AM processes. The longitudinal bending distortion is caused by the contraction of the molten material after heating and deposition. Weld research has shown reducing the heat

input (Michaleris, 2011), balancing the RS to minimize the bending moment (Michaleris, 2011), and creating a temperature difference between parts to be welded (known as *transient differential heating*) to be effective in reducing longitudinal bending distortion levels (Deo and Michaleris, 2003).

## 1.4 Prior Work in LDED modeling

LDED is a complex process due to the process physics that involves complex interacting physical phenomena and also due to multi-scale characteristics associated with the process. Also, some of the physics occur in very short time in order of microseconds (Phase change: melting or solidification) and some physics occur in order of minutes or hours (Stress relaxation, Annealing). Physics-based modeling can provide the insight that how competing process parameters interact and can hence provide the basis for process optimization. LDED process simulation using FEM technique introduces challenges that are not present in welding or LPBF. High number of passes and processing time, along with the addition of material deposition results in increase of computation time with complexity. Length and timescale considerations compels us to split models into meso and macro-scale models as shown in **Fig 1.12** (Bayat et al., 2021a). As of now given the computing capabilities,

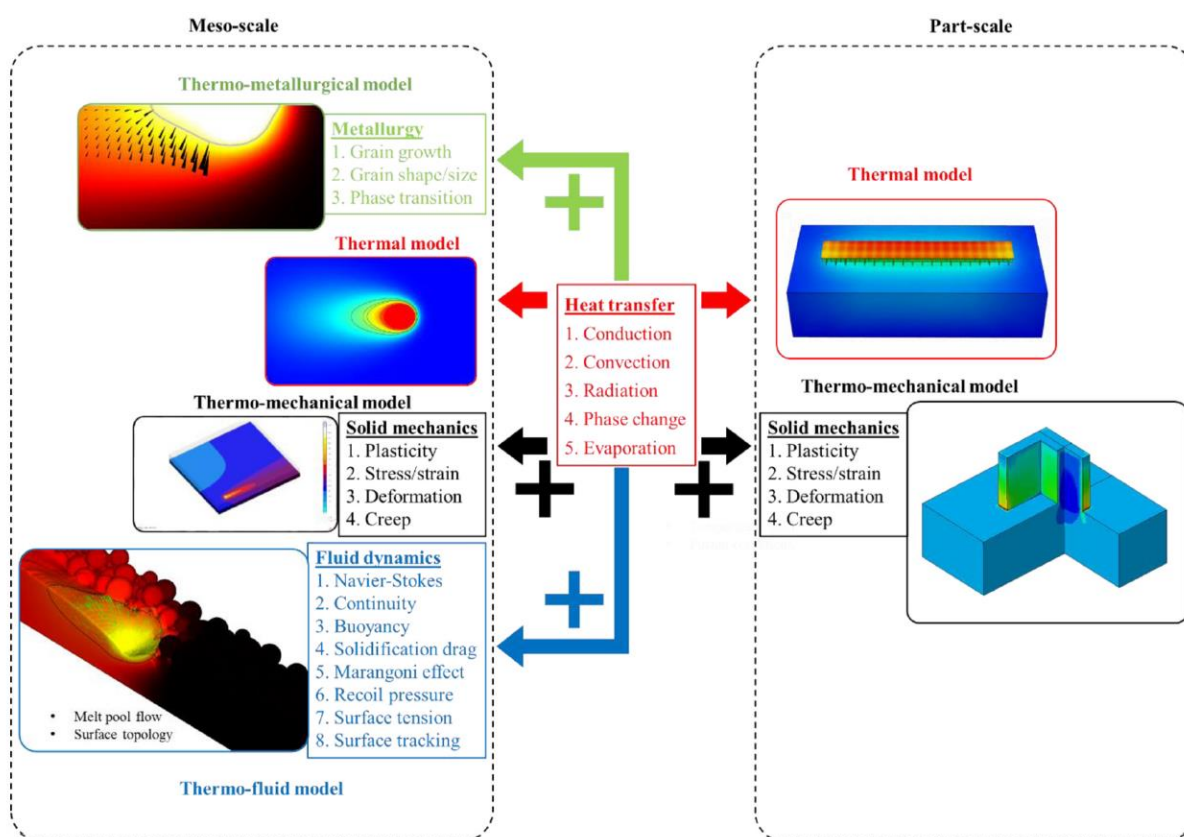


Figure 1. 12: Modeling strategies for LDED at meso & part scale (Bayat et al., 2021a)

it is almost impossible to simulate all physical phenomena including the fluid flow at melt-pool scale (meso scale) and accumulation of distortion and stresses at part scale (macro scale).

Therefore, it is imperative that when setting up the model, one specifies the required outputs and scale of the model. For example, if the objective is to study the melt-pool stability, then meso-scale would be the solution, but if the objective is to analyse the part-scale deformation, as the case for this PhD, then a mechanical model at part scale is the solution. Furthermore, such models should consider the different physical phenomenon responsible for distortions in LDED process. **Figure 1.13** presents the main phenomena and their coupling happening in LDED. The laser-material interaction leads to formation of melt-pool originated from laser energy. This results in melt-pool temperatures much higher than fusion temperature

that results in thermal expansion phenomenon. Then, the heating phase is quickly followed with the cooling down phenomenon as the laser heat source moves away. The cooling down phenomenon leads to thermal

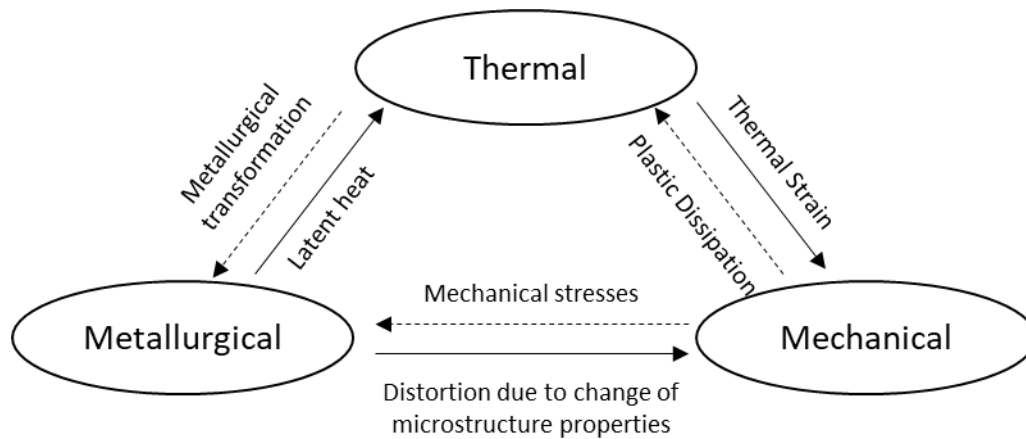


Figure 1. 13: Different physical phenomena happening in LDED. Dotted line represents weak coupling and full line representing strong coupling.

contraction/shrinkage. The thermal expansion and shrinkage phenomenon generate crucial stresses and strains that can lead to cracking and distortion respectively in the workpiece. There are other metallurgical transformations happening as well that alters the obtained deformation (due to different material properties between different phases e.g., Ti-6AlV) and mechanical properties of the workpiece. In addition, there are certain phenomenon happening during the LDED process like annealing that results in stress relaxation, which in turn results in reduction in distortion. So, the thermal expansion and shrinkage (Mechanical analysis) is strongly coupled with the amount of laser energy absorbed in the workpiece and the conduction heat transfer (Heat transfer analysis) in the workpiece respectively. Therefore, the driving force for the mechanical analysis in LDED process is "TEMPERATURE". Hence it is of utmost importance in the development of an accurate numerical model to have correct temperature field (Heat Transfer Analysis) in order to have correct distortion field (Mechanical Analysis) for the LDED workpiece. The following section presents the main mathematical formulations for meso-scale models for thermo-mechanical modeling.

## 1.4.1 Meso-scale modeling: conduction-based simulations

### 1.4.1.1 Pure thermal models

Majority of the research done in the literature related to LDED simulations is based on pure conduction models. In the conduction-based models, transient temperature analysis is done via solving the partial differential equation arising from the energy balance as shown below. Most of those models are developed based on Finite Element Method (FEM).

#### 1.4.1.1.1 Thermal Equilibrium

Assuming a Lagrangian frame  $\Omega$  and a material point located by  $r$  ( $r \in \Omega$ ) as the reference. Given thermal energy balance at time  $t$ , the governing equation can be formulated as follows:

$$\rho C_p \frac{\partial T(r, t)}{\partial t} = -\nabla \cdot q(r, t) + Q(r, t), r \in \Omega \quad (1.1)$$

Where  $T$  is temperature, time is  $t$ ,  $\nabla \cdot$  is divergence,  $q$  is heat flux,  $r$  is the relative reference coordinate, and body heat source is  $Q$ ,  $\rho$  denotes temperature dependent material density and  $C_p$  denotes temperature dependent specific heat capacity. The distribution of heat through the part is described by Fourier's conduction equation:

$$q = -k(T)\nabla T \quad (1.2)$$

Where  $k$  represents temperature dependent thermal conductivity. To solve above stated equations, it is necessary to have an initial condition, a heat input model, and thermal boundary conditions. The initial condition is usually set to the temperature of either the ambient or preheating temperature for the substrate. A two-part Neumann boundary condition is implemented consisting of the applied heat source and the surface heat losses due to both convection and thermal radiation, as detailed in the next sections.

#### 1.4.1.1.2 Heat Input models

In the conduction based thermal models, laser-material interaction is simulated via a moving surface or volumetric heat source. Numerical heat source model representing laser energy is dependent upon the laser intensity distribution in the experiment. In the literature, researchers have utilised both type of heat sources that are elaborated in the following section.

Table 1. 1: Different type of numerical heat sources used in the literature for LDED

| Name & Type                    | Expression   | References   |
|--------------------------------|--|--|
| Gaussian:<br>Surface           | $Q = \frac{AP}{\pi r_o^2} \exp\left(\frac{-2r^2}{r_o^2}\right)$  | (Alimardani et al., 2007a, 2007b; Fallah et al., 2011; Johnson et al., 2018; Labudovic et al., 2003; Madireddy et al., 2019; Manvatkar et al., 2011; Neela and De, 2009; Wang and Felicelli, 2006) |
| Top-Hat:<br>Surface            | $Q = \begin{cases} \frac{AP}{\pi r_o^2}, & -r_o \leq r \leq r_o \\ 0, & r > r_o \end{cases}$   | (Peyre et al., 2017)   |
| Conico-Gaussian:<br>Volumetric | $Q = \frac{2AP}{\pi r_o^2 H} \left(1 - \frac{z}{H}\right) \exp\left(1 - \frac{r^2}{r_o^2}\right)$  | (Biegler et al., 2020, 2018b, 2018a; Mukherjee et al., 2017; Liang Wang et al., 2008; L. Wang et al., 2008)  |
| Cylindrical:<br>Volumetric     | $Q = \begin{cases} \frac{AP}{\pi r_o^2 H}, & -r_o \leq r \leq r_o \\ 0, & r > r_o \end{cases}$   | (Lu et al., 2018a; Piscopo et al., 2019)   |
| Goldak:<br>Volumetric          | $Q = \frac{6\sqrt{3}APf_{f,r}}{\alpha_{f,r}bc\pi\sqrt{\pi}} \exp\left(-\frac{3x^2}{\alpha_{f,r}^2} - \frac{3y^2}{b^2} - \frac{3z^2}{c^2}\right)$ | (Anca et al., 2011; Erik R Denlinger et al., 2015; Denlinger and Michaleris, 2016; Goldak et al., 1984; Heigel et al., 2015; Michaleris, 2014; Xie et al., 2019, 2020a; Yang et al., 2016)         |

Alimardani et al. (Alimardani et al., 2007a), Labudovic et al. (Labudovic et al., 2003) and Manvatkar et al. (Manvatkar et al., 2011) employed a gaussian distribution surface heat flux to predict the temperature profiles and dimension of the deposited materials in the fabrication of thin wall. Largely in the literature, deposited material geometry is usually taken as input in the model. This reduces the computation time by avoiding solving the complex algorithms of geometry prediction. But due to the process physics associated with LDED, that leads to melt-pool formation surface heat source is not the ideal choice. Therefore, Wang et al. (Liang

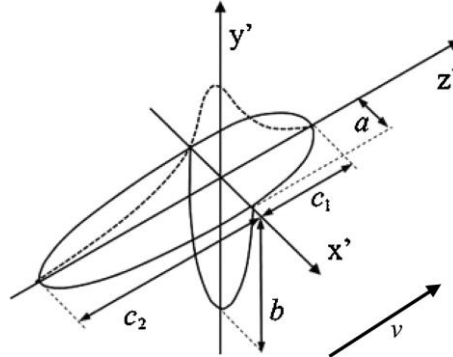


Figure 1. 14: Configuration of double ellipsoid (DE) heat source model (Yang et al., 2016)

Wang et al., 2008) employed a gaussian distribution of heat flux with conical shape to predict the temperature evolution for fabrication of simple walls of AISI 410. They demonstrated that with power program (optimization), they were able to achieve the stable melt-pool numerically and experimentally. Biegler et al. (Biegler et al., 2018a) also employed conical shape gaussian distribution of heat flux to predict the temperature evolution and melt-pool size for fabrication of Stainless Steel 316L (SS 316L) thin walls. They successfully calibrated the heat source model to achieve the same experiment melt-pool shape and dimensions. But the most commonly used and well-known heat source used for LDED simulation is Goldak's Double Ellipsoid heat source (Goldak et al., 1984). Due to the movement of laser heat source in the experiments, it has been observed that temperature gradient in the front and end of the heat source is different (Goldak et al., 1984). Therefore, combining two ellipsoids sources seemed logical that is also helpful in changing the size and shape of the heat source depending upon the process parameters as shown in **Fig 1.14** (Yang et al., 2016). Due to its versatility of modifying the numerical heat source's shape and size that replicates the experimental melt-pool size, double ellipsoid heat source model is used extensively in the literature.

#### 1.4.1.1.3 Boundary heat losses

During AM process, heat losses can occur due to thermal radiation, free convection, forced convection and conduction through fixturing bodies (clamping tools). The delivery (carrier gas) and shielding gases used in LDED process poses a big challenge to accurately model the process. To save computation time, it is a common practice to lump together thermal boundary losses into a single effective heat transfer coefficient:

$$h_{eff} = h_{free} + h_{forced} + h_{rad} \quad (1.3)$$

Where  $h_{free}$ ,  $h_{forced}$ ,  $h_{rad}$  are heat transfer coefficients of free convection, forced convection and radiation respectively. Then the total heat loss is modeled using Newton's law of cooling:

$$Q_{conv} = h_{eff}(T_s - T_{amb}) \quad (1.4)$$

Where  $Q_{conv}$  is the convective heat loss,  $h_{eff}$  is effective heat transfer coefficient,  $T_s$  is the surface temperature and  $T_{amb}$  is the ambient temperature. But, this lumping approach of heat transfer losses can account for poor

accuracy. Therefore, it is advisable to model these heat losses separately that are explained in the section below.

#### 1.4.1.1.3.1 Convection

As described in Section 1.2.1, powder particles are fed into melt-pool using an inert gas that acts as carrier gas. Convection can account for significant amount of heat losses in LDED process, because of the effect of carrier inert gas. As a result of turbulent nature of melt-pool, the carrier gas causes forced convection at the top of the melt-pool. Gouge et al. measured the forced surface in LDED process that was found to be dependent upon surface roughness and surface orientation (Heigel et al., 2016). Thus, in LDED modeling, convection mechanism is considered as a forced convection mechanism. Heigel et al. (Heigel et al., 2015) and Gouge et al. (Gouge et al., 2015) demonstrated that the value of convection coefficient  $h_{\text{forced}}$  in LDED varies as the axi-symmetric exponential decay function varies from the centre of laser beam. But, with the use of a variable coefficient, it also increases the calculation time, without significantly affecting the numerical calculation results (Yang et al., 2016).

#### 1.4.1.1.3.2 Radiation

Thermal radiation heat loss contribution becomes significantly important when temperature is high, as occurs in LDED. This heat transfer process is considered in the model by using Stefan-Boltzmann law that describes the heat-loss radiation as:

$$Q_{\text{rad}} = \varepsilon\sigma(T_s^4 - T_{\text{amb}}^4) \quad (1.5)$$

Where  $\varepsilon$  is surface emissivity and  $\sigma$  is the Stefan-Boltzmann constant,  $\sigma = 5.67 \times 10^{-8} \text{ W/m}^2\text{K}^4$ . A constant value of surface emissivity is usually taken in the Numerical Model.

#### 1.4.1.1.4 Thermal Model Validation

Thermal models for LDED are usually validated with experimental data such as melt-pool dimensions and temperature evolution (thermal cycles) during the LDED process. In situ temperature measurements can be easily done using thermocouples (Chiumenti et al., 2010; Peyre et al., 2008). Historically, thermocouples have been used specifically to validate transient thermal models as done by Peyre et al. on a 20 layer wall deposition (Peyre et al., 2008). But the use of thermocouples limits the measurement locations to only the substrate, however they provide sufficient data for model sensitivity analysis and its validation. Other researchers have therefore chosen to use optical pyrometers to collect additional temperature data such as measuring peak melt-pool temperatures that can be helpful in calibrating the numerical heat source (Lundbäck and Lindgren, 2011).

#### 1.4.1.1.5 Pros and cons of conduction-based thermal models

As discussed in the previous section, conduction based thermal models considers broad assumptions to simplify the melt-pool dynamics as it does not consider the effect of fluid dynamics, that plays a big role in the mechanism of heat transfer in the melt-pool. However, conduction-based thermal models can be effective in optimizing the process parameters with an aim of stabilising the process and understanding the process physics. Therefore, these models need to be re-calibrated depending upon the new process parameters. However, pure conduction-based models are computationally cheap and robust in handling different process parameters.

### 1.4.1.2 Thermo-metallurgical models

Conduction-based pure thermal models can be coupled to other physics for example metallurgy or mechanics to further exploit the potential of thermal model. In the thermo-metallurgical models, most researchers have studied two independent solidification parameters. At the start of the solidification, thermal gradient is calculated and at the end of solidification, solidification rate is calculated. Thermal gradient ( $G$ ) and solidification gradient are the two parameters that are first calculated. Once these two parameters are determined, the solidification growth speed  $R$  ( $m \cdot s^{-1}$ ) and morphology factor  $F$  ( $K \cdot s \cdot m^{-2}$ ) is calculated. Glicksman concluded that independent of AM technology, columnar grain structure is obtained with a higher morphology factor  $F$ , while low  $F$  value yield to equiaxed grain structure (Glicksman, 2010) as shown in **Fig 1.15**. Nie et al. employed a multi-scale FEM model with stochastic analysis to study the microstructure evolution of nickel based superalloy in LDED process (Nie et al., 2014). They found a strong dependence of microstructure evolution on cooling rate and temperature gradient. Manvatkar et al. developed a conduction-

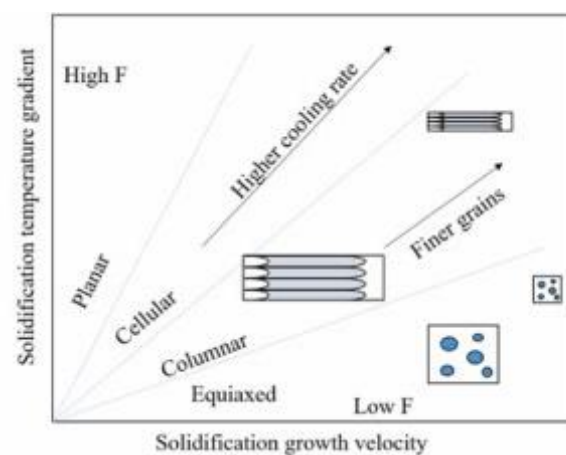


Figure 1. 15: Effect of  $G$  and  $R$  on possible grain morphology (Glicksman, 2010)

based thermal model along with a set of constitutive relations to simulate cooling rates and hardness distributions of Austenitic Stainless Steel in LDED process (Manvatkar et al., 2011). They concluded that due to the difference in cooling rate in the deposited bead, yield strength and hardness reduce from the bottom towards top layers. Huang et al. used an analytical model aiming to develop a link between the process parameters and the localized thermal characteristics and solidifications parameters (Huang et al., 2019). They studied SS 316L and Inconel 625 in LDED process. They concluded that high scanning speed with low laser power resulted in finer microstructure. Also, cooling rates ( $G \times R$ ) varies within deposits, it increases from the bottom to the top of deposited bead, that in turn leads to finer microstructure. This behaviour was noticed for both the materials. Gockel et al. developed a FEM model with an integrated approach, at first thermal model is solved, and microstructure is predicted using the solidification map of the concerned material (Gockel et al., 2014). This approach was developed for single-track deposition, but later on extended to thin-wall deposits as well (Gockel et al., 2015).

In the present work, the objective is to develop a numerical model to predict distortions of large structures. However, the metallurgical modeling requires that additional equations are solved to calculate the phase proportions, which increases the computation cost and makes the model more complex. Therefore, for reasons of simplicity, as many researchers, the metallurgical phase transformations will not be predicted in this thesis.

### 1.4.1.3 Mathematical formulation of thermo-mechanical models

The metallurgical modeling requires a lot of computation cost, however it's effects can be included in the thermo-mechanical model which is computationally faster. Hence in the conduction-based Thermo-mechanical models do not model the metallurgical effects and somehow include its effects that will be explained in the coming sections.

Conduction-based pure thermal models predict the temperature field which can be used as an input for mechanical models to simulate distortion and stress evolution. Thermo-Mechanical models can be used to predict and study the manner in which distortion accumulates in LDED build workpieces.

#### 1.4.1.3.1 Mechanical Equilibrium

The governing mechanical stress equilibrium is written as, neglecting inertia effects and gravity:

$$\nabla \cdot \sigma = 0 \quad (1.6)$$

Where  $\sigma$  denotes the stress tensor. The mechanical constitutive law can be written as:

$$\sigma = C \varepsilon_{el} \quad (1.7)$$

Where C is the 4<sup>th</sup> order stiffness tensor and  $\varepsilon_{el}$  is elastic strain. In LDED, as the material experiences a wide range of temperatures, from ambient to more than fusion temperature, it is required to consider non-linear material hardening.

Considering small deformation theory for Thermo-Elasto-Plastic model, the total strain  $\varepsilon_{to}$  is decomposed as:

$$\varepsilon_{to} = \varepsilon_{el} + \varepsilon_{pl} + \varepsilon_{tr} + \varepsilon_{th} \quad (1.8)$$

Where  $\varepsilon_{pl}$ ,  $\varepsilon_{tr}$ , and  $\varepsilon_{th}$  are plastic, phase transformation and thermal strain respectively.

#### 1.4.1.3.2 Elastic Strain

The elastic strain increases linearly with the stress in the elastic regime. In the linear elasticity framework of isotropic materials, the elastic strain can then be expressed using Hooke's Law:

$$\varepsilon_{el} = \frac{(1 + \nu)}{E} \sigma - \frac{\nu}{E} tr(\sigma) \quad (1.9)$$

Where  $\nu$  is poisson's ratio and  $E$  is Young's Modulus of the material.

#### 1.4.1.3.3 Plastic Strain

In most of the available cited literature (Denlinger and Michaleris, 2016; Gouge et al., 2018; Ren et al., 2019), plastic strain is computed by enforcing the Von Mises yield criterion and the Prandtl-Reuss flow rule:

$$f = \sigma_m - \sigma_y(\varepsilon_q, T) \leq 0 \quad (1.10)$$

Where  $f$  is the yield function,  $\sigma_m$  is Von Mises's Stress,  $\sigma_y$  is yield stress,  $\varepsilon_q$  is the equivalent plastic strain.

$$\dot{\varepsilon}_{pl} = \dot{\varepsilon}_q \mathbf{a} \quad (1.11)$$

$$\mathbf{a} = \left( \frac{\partial f}{\partial \sigma} \right)^T \quad (1.12)$$

Where  $\mathbf{a}$  is the flow vector. Apart from Von-Mises yield criterion, there is other yield criterion such as Tresca stress and Hill orthotropic plasticity that have been employed by the researchers in the literature. But the above-mentioned yield and flow rules criterion are the most popular among the researchers. To calculate the material response in the plastic regime, isotropic and kinematic models are employed. However, in AM process, kinematic hardening accounts for higher computation cost, and that's why majority of the researchers in the literature have employed isotropic hardening model. There are different isotropic hardening models employed in the literature:

- a) Perfectly Plastic
- b) Linear
- c) Power-law

Detailed discussion with explanation about these laws will be carried out in the next chapters, when mechanical model developed in the present work is explained.

#### 1.4.1.3.4 Thermal Strain

The thermal strain is calculated using temperature dependent coefficient of thermal expansion  $\alpha$ , as shown in equation 1.13, where  $T^{ref}$  is reference temperature.

$$\varepsilon_{th} = \alpha(T - T^{ref}) \quad (1.13)$$

#### 1.4.1.3.5 Phase Transformation Strain

There are many metals that can exist in more than one form of crystalline and this feature is called Allotropy. For example, pure iron, undergoes different allotropic solid-state phase transformation (BCC to FCC and reverse) during heating and cooling phases. Titanium also experiences solid-state phase transformation during heating from  $\alpha$ -phase (HCP) to  $\beta$ -phase (BCC) and during cooling, this is reversed from  $\beta$ -phase to  $\alpha$ -phase. The materials that undergo allotropic phase transformation have a considerable effect on the outcome value of distortion and RS in the workpiece and fabricated part. Longuet et al. has focused on to predict the RS and distortion in materials that undergoes phase transformation (Longuet et al., 2009). Ghosh and Choi demonstrated that for stainless steel, it is necessary to properly take into account transformational RS and strains especially at substrate/clad interface (Ghosh and Choi, 2005). Griffith et al. proved that for stainless steel 316, high temperature reached during LDED process can cause material to anneal, and thus reducing the measured RS (Schlienger et al., n.d.). Denlinger demonstrated in his Numerical Model that the effect of stress relaxation (effect of solid-state phase transformation) in Ti-6Al-4V is to oppose all other strain components, effectively rapidly eliminating all strain at temperatures above 690°C (Denlinger, 2015).

$$\varepsilon_{tr} = -(\varepsilon_{el} + \varepsilon_{pl} + \varepsilon_{th}) \quad (1.14)$$

This assumption accounts for the transformation strain and completely negate the strain components that can be attributed to the thermal contraction. The cut-off temperature is calculated by inverse simulation to fit numerical simulation results with the experimental data.

#### 1.4.1.3.6 Material deposition modeling techniques

The thermo-mechanical models for LDED are generally associated to specific numerical methods to account for the material addition process. There are different material deposition strategies that can be cited in the literature. The above-mentioned strategies are mentioned in following section.

##### 1.4.1.3.6.1 The quiet/active activation strategy

In the quiet element method, the elements depicting metal deposition regions are present from the start of the analysis. However, the properties are assigned to the metal deposition regions in such a way that the elements that are not activated (quiet elements), do not affect the analysis. For the heat transfer analysis, once the elements are turned active from quiet state, they are assigned physical material properties, and all other quiet elements thermal are assigned dummy material properties. The quiet element material properties are set to a lower value so that it minimizes the conduction into quiet elements and to adjust energy transfer to the quiet elements respectively.

$$k_{quiet}(T) = s_k k(T) \quad (1.15)$$

$$C_{p_{quiet}}(T) = s_{C_p} C_p(T) \quad (1.16)$$

Where  $k_{quiet}$  and  $C_{p_{quiet}}$  are thermal conductivity and specific heat used for quiet elements,  $s_k$  and  $s_{C_p}$  are the scaling factors used for thermal conductivity and specific heat respectively that are usually assigned very small values. Density values ( $\rho$ ) are kept same for both quiet and active elements. Different researchers have employed this material activation strategy (Chew et al., 2015; Erik R Denlinger et al., 2015; Johnson et al., 2018; Ren et al., 2019; L. Wang et al., 2008; Yang et al., 2016). The same strategy is applied for the mechanical problem as well.

The quiet element method has the following advantages (Michaleris, 2014):

- It is easily implementable in COMSOL or any other general purpose finite element codes.
- The number of elements remains fixed or constant (does not change), so the number of equations is also constant throughout the analysis. So, no additional equation re-numbering and also no solver initialisation are needed.

The quiet element method has the following disadvantages (Michaleris, 2014):

- If the scaling factors  $s_k$  and  $s_{C_p}$  do not have very small values, thermal energy can conduct into inactive elements resulting in errors (loss of accuracy). This thermal error then contributes to the mechanical error in the mechanical analysis.
- If the scaling factors  $s_k$  and  $s_{C_p}$  are too small, it can lead to convergence issues in the model.
- Because all the elements are considered from the start, for large build structures, it may result in longer computation time.

#### 1.4.1.3.6.2 The Inactive Activation Strategy

In the inactive element method, only the nodal degrees of freedom corresponding to active elements are considered and the remaining elements lying in the metal deposition region are removed from the nodal analysis. So, at each time step, new nodal degrees of freedom are added in the computational analysis as some new region become active considering activation criteria. Different researchers have demonstrated the use of the inactive activation strategy (Biegler et al., 2018a; Farahmand and Kovacevic, 2014; Labudovic et al., 2003; Lu et al., 2018a).

The inactive element method has following disadvantages:

- There are no convergence issues due to scaling factor as in the case of quiet element method.
- Computation analysis is done only for active elements.
- Only the active nodal degrees of freedom are considered at each time step leading to smaller algebraic system by Newton-Raphson linearization.

The inactive element method has the following disadvantages:

- This method is difficult to incorporate for the users into COMSOL or any other general purpose finite element codes, if it is not already included by the software developers.
- At each time step, elements are activated, so the equation numbering and solver initialization have to be repeated at each time step also. This may increase the computation cost and also negate the advantage of solving for a lesser active number of degrees of freedom.

At each time step, when new elements are activated, nodes that are shared by active elements and inactive elements may not be at the initial temperature that may result into artificial energy being fed into the model.

#### 1.4.1.3.6.3 The Hybrid Activation Strategy

The Hybrid element activation strategy is a combination of quiet and inactive activation strategy. At start, elements are initially set as inactive. Then the whole first layer is switched to quiet (dummy material), and this layer is switched to active step by step depending upon the heat input. Then these steps are repeated for layer 2 and further. In this approach, equation numbering and solver initialization is done only when each layer is activated that results into lesser computation cost. Denlinger et al. (Denlinger and Michaleris, 2016), Biegler et al. (Biegler et al., 2020) and Heigel et al. (Heigel et al., 2015) have demonstrated the practical feasibility of this approach. A lot of commercial software like Autodesk, GeonX, etc. also uses this activation strategy.

#### 1.4.1.3.6.4 Arbitrary Lagrangian Eulerian (ALE) Strategy

The Arbitrary Lagrangian Eulerian (ALE) method can also be used as to demonstrate the addition of material. In this method, mesh is stretched in such a way that it acts as deposition of material. This method can be problematic because of the mesh stretching issues. Element size is one of the most important factors determining accuracy and convergence. If the mesh element size is not optimized, it can have the above mentioned in the issues. So, in ALE method, re-meshing has to be done repeatedly after each layer is deposited. Peyre et al. (Peyre et al., 2017) has performed a thermal analysis for 5 layers and have validated the model for different process parameters. Very few other researchers have employed this strategy (Morville, 2012a; Morville et al., 2012b) because ALE Strategy can be very difficult to optimize for the complex scan pattern.

### 1.4.1.3.7 Mechanical Model Validation

Mechanical models for LDED are usually validated with co-relating experiment distortion and RS with predicted Numerical Model distortion and RS. There are two different ways of recording distortion and RS that are mentioned in the following section.

#### 1.4.1.3.7.1 Post-Process measurement

Post-process distortion measurement is the most common practise to validate Mechanical Model. If the Mechanical Model has accurately predicted the final distortion, Mechanical Model is considered to be accurate and reliable. While post-process method does not provide any insight about the distortion accumulation during the deposition process, this method is still frequently used for Mechanical model validation because it is much easier to calculate the final distortion in the fabricated part and workpiece once it is fabricated. There are different distortion measuring techniques of the final deformed shape (final shape) obtained after unclamping the workpiece:

##### a) Coordinate-measurement machine (CMM)

Pre-and post-measurements of the substrate is done using a Coordinate Measuring machine (CMM). Then changes in the substrate's profile/shape is calculated by measuring the difference between the pre-process and post-process dimensions. This difference gives the final post-process distortion measurement. Chiumenti et al. did a post-process measurement of longitudinal and transverse distortion of a 10-layer Inconel 718 wall using CMM technique. These measurements are then used for model validation (Chiumenti et al., 2010). Xie et al. also used a CMM technique to measure the distortion at the bottom face of the substrate and then compare it with the numerical model for the deposition of 5 layer high, simple wall of Ti-6Al-4V (Xie et al., 2020b)

##### b) Optical 3D scan

An optical 3D scanner is used to 3D scan the complete part/workpiece that generates a cloud of millions of points representing workpiece. This digitised data in form of points is then transformed into a digitised solid feature that is then compared with a CAD file of the workpiece. The difference between original CAD file and digitised scan gives the final post-process distortion measurement. Anca et al. validated the Thermo-Mechanical model for the mechanical response of Ti-6Al-4V using post process distortion measurements using an optical 3D scanner (Anca et al., 2011). Yang et al. also used an Optical 3D scanner to measure the final distortion measurement at the bottom face of the substrate and then compare it with the numerical model for a deposition of 5 layer high, hollow rectangular geometry of Ti-6Al-4V (Yang et al., 2016). Optical 3D scanner provides much more information than a CMM, because it gives the measurement of the complete surface/volume rather than some selected points that is a case of CMM.

The repeated thermal cycles during the deposition process leads to accumulation of RS in LDED workpieces (Fessler et al., 1996; Grum and Žnidaršič, 2004; Pratt et al., 2008; Rangaswamy et al., 2003). It has been demonstrated that RS levels are dependent on processes parameters, deposited geometry, and the number of layers (Jendzejewski et al., 2004; Jendzejewski and Śliwiński, 2007). In addition to distortion, RS measurement can also be an important feature of validating the numerical model. There are mainly 3 different techniques of measuring RS (Withers and Bhadeshia, 2001) namely:

##### a) Hole drilling method

The Hole drilling method is a destructive method consisting in drilling a small hole and measuring the resulting deformations. A numerical model is then required to identify the residual stresses from the relieved deformations. Denlinger et al. employed this method to measure the RS at the substrate for a 42-layer high, double-bead wall of Ti-6Al-4V and Inconel 625 and then compare it with the numerical model (Denlinger and Michaleris, 2016). They concluded that with an increase of dwell/cooling time, there is an increase of RS for Ti-6Al-4V, however for Inconel 625, there was no effect in the values of RS.

#### b) Neutron diffraction

Wang et al. demonstrated the effectiveness of Neutron diffraction method by measuring the RS at the fabricated part as well as substrate for the workpiece obtained with the process parameters of the substrate for a 42-layer high, double-bead wall of Inconel 625 (Wang et al., 2017a). Experiment RS results are further compared with the numerical model and results were complimentary to each other.

#### c) X-ray diffraction

Ren et al. employed X-ray diffraction measurement technique to measure the RS at a thin substrate of SS 316L for a single layer of a filled rectangle geometry with two different deposition strategies. These experiment RS measurements are then successfully compared with the numerical model and it was concluded that deposition strategy influences the RS values in the workpiece. They concluded that for a rectangular part geometry, Zig-Zag longitudinal deposition strategy gives lower RS than Zig-Zag transversal deposition strategy.

### 1.4.1.3.7.2 In-situ measurement

To improve the validation of Mechanical Model, researchers compare Numerical Model results with in-situ distortion measurement during the deposition. This provides more insight about the distortion accumulation and can also be helpful in understanding the process itself. There are mainly two different techniques to measure in-situ distortion:

#### a) Laser Displacement Sensor (LDS)

A Numerical Model validated with in-situ distortion measurements is much more reliable and versatile as compared to Numerical Model validated with post-process distortion measurement as it provides more insightful information that is temperature and time dependent. Laser Displacement Sensor (LDS) works very efficiently and is very easy to use. A laser comes out of the sensor and hit a selected surface, most commonly, substrate's bottom surface, and is reflected back to sensor. This basically gives the reference value or distance between the sensor and substrate. Usually to validate the numerical model, experiment measurement is done with a cantilever tooling so that substrate can move/deflect/distort freely at the free end of the substrate. During the LDED process, substrate starts to defect/distort at the free end and LDS placed at the bottom of the substrate captures this movement in the vertical direction and records the in-situ measurement. Plati et al. (Plati et al., 2006) compared the numerically calculated mechanical distortion results to distortion measured during the laser cladding of 1 deposition track onto a stainless steel substrate. Xie et al. also used LDS to capture the in-situ displacement and then validate the thermo-mechanical model that uses an experiment based stress relaxation model with Ti-6Al-4V (Xie et al., 2020b). Denlinger and Michaleris (Denlinger and Michaleris, 2016) used LDS to demonstrate that distortion accumulation depends upon material type (Inconel 625 and Ti-6Al-4V) and different inter-layer cooling time (dwell time of 0s, 20s, 40s). They found out that for a cantilever tooling, with a decrease in dwell time from 40s to 0s, distortion drastically reduces. However, Inconel 625 exhibits opposite behaviour, with a decrease in dwell time from 40s to 0s, distortion was increasing.

### b) Digital Image correlation (DIC)

LDS usually measures only displacements at a particular point mostly at the substrate and does not provide much information about the build-part region. Digital Image Correlation techniques can provide much more information e.g., displacement and strain evolution over a surface in different directions, but DIC techniques are difficult to use and is very expensive as well. In this technique, multiple cameras are used to capture images at a high frequency. Then particular light setting is required so that sufficient high contrast is made at the measurement location (fabricated part). Then a specialised software is required that can treat these images acquired by the cameras and then correlate these images to finally give the distortion measurements in every direction.

Biegler et al. (Biegler et al., 2018a) used 3D digital image correlation (DIC) system GOM Aramis that employs two CMOS cameras for image acquisition and a software to treat or correlate the images from a 20-layer wall of SS 316L covered by a speckle of paint. DIC measurements are done during the deposition of 10 additional layers. Ocelik et al. used 3D digital image correlation (DIC) techniques with two CCD camera and Aramis software to record and treat the images (Ocelík et al., 2009). The measurements are done to measure the strain and distortion of a substrate during LDED deposition process. The experiment results were used to validate the Numerical model depositing 10 tracks. It was found out that greater distortion accumulated during the first few deposition passes. Lundback and Lindgren (Lundbäck and Lindgren, 2011) developed a flow stress model and validated it with 40 build passes. In-situ distortion was recorded with an optical measurement system of ARAMIS by GOM allowing for measurements to be taken on multiple points of the substrate. The Numerical model was shown to capture the distortion of the first 6 passes correctly but then begins to over predict distortion.

### 1.4.1.3.8 Linking thermo-mechanical model

In the literature, it can be seen that different researchers have linked the thermal model with mechanical model in two different ways that re explained in the following section.

#### 1.4.1.3.8.1 Fully Coupled Model

The relationship between thermal and mechanical behaviour is considered bi-directional in coupled or strongly coupled. This means that thermal history affects mechanical behaviour and mechanical history affects temperature behaviour (stresses and strains affect temperature profile) as discussed at the start of the section “Thermo-mechanical model “. So, at each time step, the thermal and mechanical analysis is performed simultaneously. This strategy however increases the degree of freedom drastically and hence leading to increase in computation time. A lot of researchers have developed, implemented and used strongly coupled Thermo-Mechanical Model (Biegler et al., 2018b, 2018a, 2020; Lu et al., 2018a; Ren et al., 2019; L. Wang et al., 2008). But the strongly coupled model contributes in increasing the computation cost of the analysis. However, the mechanical history does not impact the thermal history a lot, because the plastic dissipation energy is almost negligible in LDED process (Zhang et al., 2004a). Also, the effect of change/modification of the geometry has little impact on thermal aspect. Therefore, majority of the researchers in the literature have performed a 1-way coupled analysis for LDED process.

#### 1.4.1.3.8.2 Decoupled/Weakly/Sequential/1-way coupled

In the decoupled or weakly coupled modeling, an assumption has been made that the relationship between the thermal and mechanical behaviour is uni-directional implying that the thermal history affects the

mechanical behaviour (temperature affect stress and strain profile due to temperature dependent material properties such as Young's modulus, yield stress and coefficient of thermal expansion), but that the mechanical behaviour has very little or no influence upon the thermal behaviour (stresses and strains affect temperature profile) (Lindgren, 2001). This assumption is often applicable to AM processes, or at the very least, is a fair approximation. The thermal analysis can be performed independently of the mechanical analysis because the plastic strain energy is small compared to the laser source energy, making the analyses weakly coupled (Zhang et al., 2004a).

The thermal history is first calculated by performing a 3D transient thermal analysis. The thermal results are then input into a 3D quasi-static incremental analysis which simulates the mechanical response. This strategy is more practical and is very popular among the researchers as it reduces the computation cost as compared to Fully Couple model. A lot of researchers and also the commercial software use decoupled model (Erik R Denlinger et al., 2015; Denlinger and Michaleris, 2016; Heigel et al., 2015; Johnson et al., 2018; Kiran et al., 2020; Lu et al., 2019a; Marimuthu et al., 2013; Nickel et al., 2001; Xie et al., 2019, 2020b; Yang et al., 2016).

#### 1.4.1.3.9 Distortion mitigation techniques

Researchers who have investigated distortion mitigation techniques in AM have shown that changing the laser scanning pattern can reduce distortion (levels) with shorter deposition passes (Dai and Shaw, 2002; Foroozmehr and Kovacevic, 2010; Nickel et al., 2001). However, with shorter deposition passes, it requires a greater number of deposition passes accounting the same amount of material. This problem becomes more significant for large parts with a greater number of depositions passes. RS can also be reduced by preheating the substrate and keeping it at a high bulk temperature (Jendrzewski et al., 2004; Jendrzewski and Śliwiński, 2007; Vasinonta et al., 2000) or by heating the deposition region immediately prior to deposition (*localized pre-heating*) (Aggarangsi and Beuth, 2006). But bulk substrate heating is practical only for small workpieces as it is not feasible to hold a large size substrate at a high temperature for a longer period of time. Furthermore, localized pre-heating requires modifications to the laser deposition system which can be problematic as it requires a lot of complex design changes in the LDED system. Another promising way has been recently proposed to reduce distortions. It consists of using compensation methods such that amount to performing correcting actions such as modifying the geometry of the CAD model before manufacturing. Thermo-mechanical model on original CAD file predicts the deformation that will be obtained with the original CAD file. The calculated distortions are inverted to generate a compensated geometry/CAD. Biegler et al. demonstrated that for a turbine of SS 316L fabricated with LDED process a compensated CAD geometry obtained from a transient thermo-mechanical model after a single compensation iteration is able to reduce the distortions by over 65% (Biegler et al., 2020). Afazov et al. also demonstrated the effectiveness of this method for LDED industrial Inconel 718 manifold component (Afazov et al., 2021). The part is first fabricated with the original CAD and distortion is measured by 3D optical scanner. A compensated CAD is then generated and the part is again fabricated with a reduction in distortions by over 75%.

#### 1.4.1.3.10 Pros and cons of thermo-mechanical models

Meso-scale conduction based thermo-mechanical models follows the deposition pattern, and hence they can be employed to study the effect of deposition strategy on distortion and RS. But, due to the fact that it follows laser beam, it can be used for small domains only, otherwise it will lead to high computation cost. As shown in the previous section of the LDED literature, majority of the researchers have been able to simulate up-to 50 layers with deposition structures like wall, rectangle, etc. considering the limitation of computation time

using meso-scale model. However, it has been found that meso-scale thermo-mechanical models were not employed to simulate large parts with number of layers exceeding 50.

Generally, thermo-mechanical models use an equivalent heat source representing laser energy. This source requires experiment data to calibrate it numerically. So, every time, new process parameters are introduced, same step of calibrating the equivalent heat source has to be repeated. This process of calibration for each set of experiments limits the predictive nature of the models. Therefore, some researchers have developed more detailed models that encompass the physical phenomena like re-distribution of energy due to the flow of molten metal in the melt-pool. Also, material deposition modeling can be done by employing numerical methods like free surface tracking. These two aspects are detailed in the following section.

## 1.4.2 Meso-scale modeling: flow-based simulations

As the name suggests, fluid-related variables like pressure and velocity vectors are also calculated along with temperature in the meso-scale flow-based simulations. This requires higher computation time since new equations need to be solved (momentum, continuity and equations associated with material addition). Furthermore, these equations require very fine mesh in the melt-pool region that leads to increase of computation time. Computational Fluid Dynamics (CFD) models focussing on LDED process can be divided in two categories, (a) CFD models that uses a fixed Eulerian mesh (b) CFD models with moving mesh. Since in the present research, flow-based model is not developed, therefore very brief literature review is done in the following sections.

### 1.4.2.1 CFD models with fixed Eulerian Mesh

In these types of simulations, as the melt-pool surface is considered flat that does not have any curvature, therefore the effect of surface tension forces and recoil pressure is not considered. However Marangoni effect is considered as it is one main fluid dynamic forces in the melt-pool for LDED process(Wen and Shin, 2011) .

He et al. employed a CFD model to analyse the evolution of temperature and velocity fields during laser spot welding of 304 stainless steel (He et al., 2003). They found out that heating rate is significantly dependent upon the location. Also, they concluded that the main driving force for the liquid flow is surface tension. Jiang et al. simulated a single track deposition with a flat melt-pool surface aiming to find out the influence of Marangoni effect on the temperature field and melt-pool dimensions (Jiang et al., 2020) as shown in **Fig. 1.16**. They found out that the conduction mode is the primary reason of heat transfer at the initial stage of the melt-pool. But once the melt-pool stabilises, heat convection due to Marangoni convection dominates the heat transfer mechanism in the melt-pool. Manvatkar et al. employed a CFD model with Quiet/active material

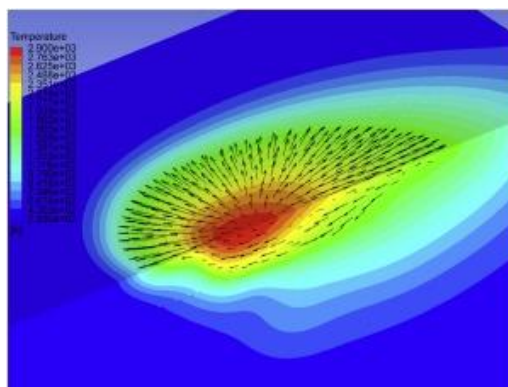


Figure 1. 16: Temperature and velocity profiles simulation assuming fixed eulerian mesh (Jiang et al., 2020)

deposition strategy to simulate multi-layer thin wall of Austenitic SS 316L in LDED process (Manvatkar et al., 2014). They found out that the melt-pool dimensions showed good agreement with the experiment results for the first few layers, but for the upper layers, they concluded that melt-pool size increases. Wei et al. studied the effect of deposition strategies on the microstructure evolution for Nickel based alloys Inconel 718 in LDED process (Wei et al., 2015). They concluded that with uni-direction deposition pattern, dendrite orientation was at an angle with  $60^\circ$  angle, but with zig-zag deposition pattern, it was at  $45^\circ$  angle.

### 1.4.2.2 CFD models with small surface deformation

In these types of simulations, a surface-tracking strategy is used that can calculate small surface deformations. Therefore, surface tension is calculated in the model since melt-pool can have a curvature owing to the fact of free surface. With this type of methodology, recoil pressure can also be accounted in the model. Wu et al. developed a laser-powder coupling model and a thermal-fluid transport model with a dynamic ALE method representing material deposition (Wu et al., 2021). Laser-powder interaction is modeled with an input laser source model and Beer-Lambert law to calculate the attenuated energy absorbed by powder during its flight. They concluded that the choice of laser beam profiles has a strong influence on the temperature gradient at the solidification interface. Morville et al developed a multi-layer 2 & 3D heat transfer and fluid flow model coupled with ALE material deposition on COMSOL for LDED process (Morville, 2012a; Morville et al., 2012b). They concluded that melt-pool dilution strongly depends upon laser power & scanning speed.

Gan et al. employed a CFD model to simulate the deposited bead-shape during LDED process for cobalt-based alloy on steel by tracking the free surface using ALE method (Gan et al., 2017b). They concluded that the simulation results of composition profiles of different alloy material showed good agreement with experiment results. Gan et al. developed another model to predict the deposited bead-shape of nickel-based powder on cast iron during LDED process (Gan et al., 2017a). However, the free shape is calculated by solving an analytical force balance equation. They found out that cooling rates declines with an increase in number of layers deposition, that results in coarser grains at the upper layers. Bayat et al. developed a CFD model on FLOW-3D commercial software to simulate the powder injection and melt-pool flow for LDED process (Bayat et al.,

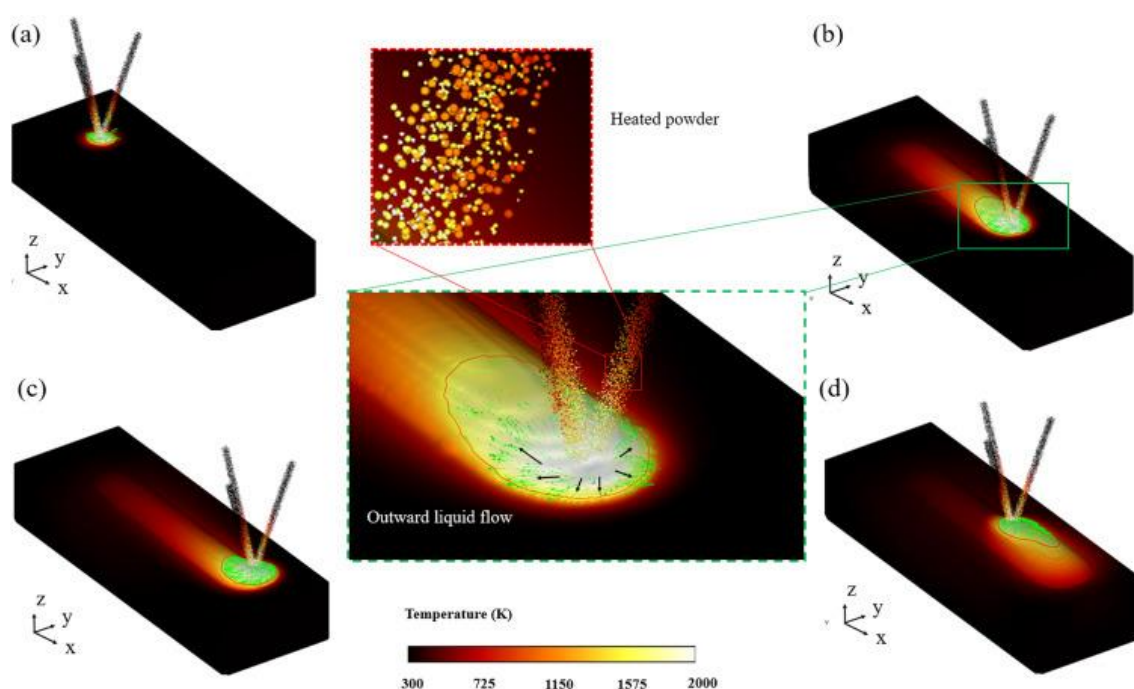


Figure 1. 17: Simulation of incoming powder and temperature evolution in the melt-pool (Bayat et al., 2021b)

2021b) as shown in **Fig. 1.17**. These combined models can be helpful in studying the effect of incoming powder velocity on the melt-pool stability or deposition shape.

The main issue with these models is the limitation of simulating only small number of layers due to the constraints of high computation time and memory requirements. *Since the main objective of the present work is to develop a model that can predict distortion of large-size part, we have focussed primarily on the development of thermo-mechanical model.*

### 1.4.3 Part-scale models

As discussed in the previous sections, meso-scale modeling that simulates the laser movement/deposition pattern are computationally expensive due to the fact of fine mesh size, small computation time-step, to fulfil the convergence criteria. Applying this methodology for a part-scale model would lead to impractical computation cost. Due to this reason, researchers have developed part-scale modeling techniques that can be broadly classified in two namely Inherent Strain Methods and Multi-scale methods. These two methods dedicated for LDED are explained in the following section.

#### 1.4.3.1 Inherent Strain Methods

The main idea of the inherent strain (IS) method is to avoid solving computationally expensive transient thermo-mechanical analysis for LDED process and instead solve it with a quasi-static mechanical analysis that is much computationally faster. This is done in two sequential steps, at first a local (small domain) thermo-mechanical model is solved that tracks the laser heat source. The local thermo-mechanical model yields local deformation that is called "Inherent Strains". Then the second step is to apply these heat source induced inherent strains with layer-by-layer approach on part-scale model in a quasi-static mechanical analysis. IS methodology is first introduced for welding technology in 1970's (Ueda et al., 1975; Ueda and Fukuda, 1989a). In the literature, IS method is also called applied plastic inherent strain method and different researchers have employed IS methods with different variants in calculating Inherent Strains. Because of the similarities between welding and LDED process (heat source induced material deposition that leads to melting and solidification), IS methods are also applied to LDED process. But there are dissimilarities as well between welding and LDED processes, especially the multi-track/layer features found in LDED process. This leads to different and complex evolution of strains as compared to welding. Just because of these dissimilarities, original IS methods did not yield accurate results when applied on LDED process (Bayat et al., 2021a). Hence, some modifications were done to the original IS method that is more suitable for LDED process. These modifications are mainly focussed on the calculation of heat source induced inherent strains for local thermo-mechanical model, however the part-scale quasi-static model is kept same that follows the layer-by-layer deposition approach. Liang et al. proposed a Modified Inherent Strain (MIS) approach especially for LDED (Liang et al., 2018a). In the original IS method, inherent strain is considered to be the plastic strain in the part at cooled down state. But in the MIS method, besides the general plastic strain at cooled down temperature, elastic strain is also added that accounts for elastic deformation in the already deposited layers during the deposition of subsequent layers (Liang et al., 2018a) as shown in **Fig. 1.18**. They validated the MIS method with experimental results obtained with deposition of thin wall structures and rectangle of Ti6Al4V material on cantilever tooling.

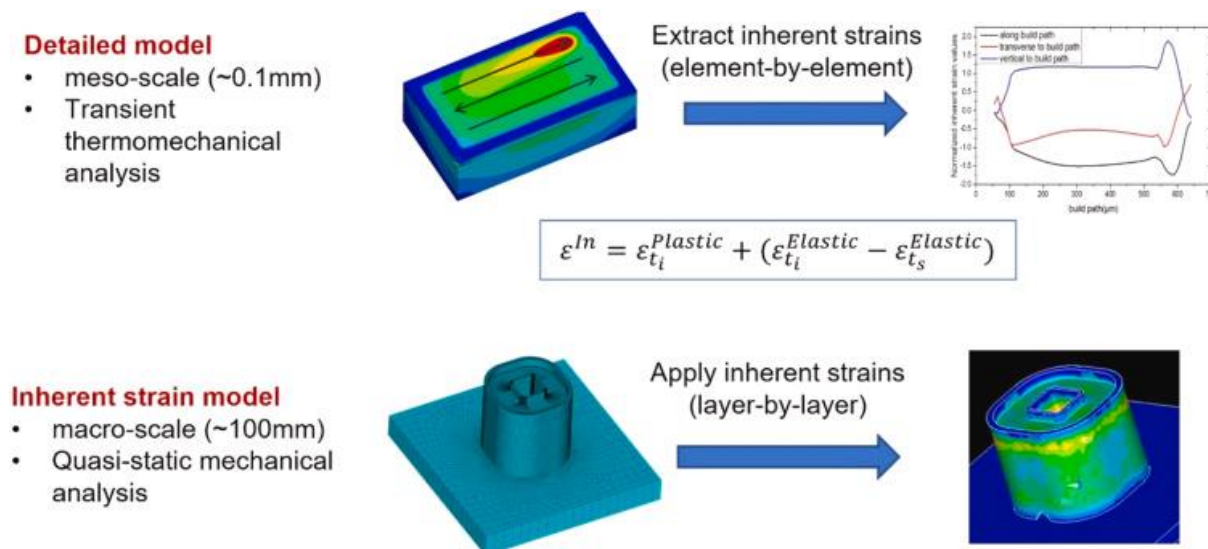


Figure 1. 18: Illustration of the modified illustration model with an addition of elastic strains in the inherent strain calculation (Bayat et al., 2021a)

Most of the work in the literature concerning IS methods is done on the PBF process (Alvarez et al., n.d.; Chen et al., 2019a; Cheng et al., 2019; Li and Anand, 2020; Liang et al., 2019; Tran et al., 2020a). **Also, most of the commercial software that provide part-scale simulation tools e.g., MSC Simufact, Autodesk Netfabb, ANSYS, Dassault Simulia etc. are dedicated for PBF. These simulation tools employ IS methods. For LDED, very few works were found in the literature. So, there is no guideline how to employ Inherent Strain-based methods for LDED accurately.**

### 1.4.3.2 Multi-Scaling methods

Lumping/Combining multiple layers together and then heating it is a multi-scaling technique that is also used for part-scale modeling. In this method, build-part that should be divided into same number of layers as in the experiments, are merged to form a block called a meta-layer. The number of layers that are combined together is user-dependent and represent the meta-layer's thickness. Only one meta-layer is activated at once, a uniform heat source is applied on the meta-layer for a process-dependent time period that initiates heating phenomenon in the meta-layer. Then the second meta-layer is activated and the same process of applying uniform heat source for a given period is repeated. Here also, most of the work in the literature that

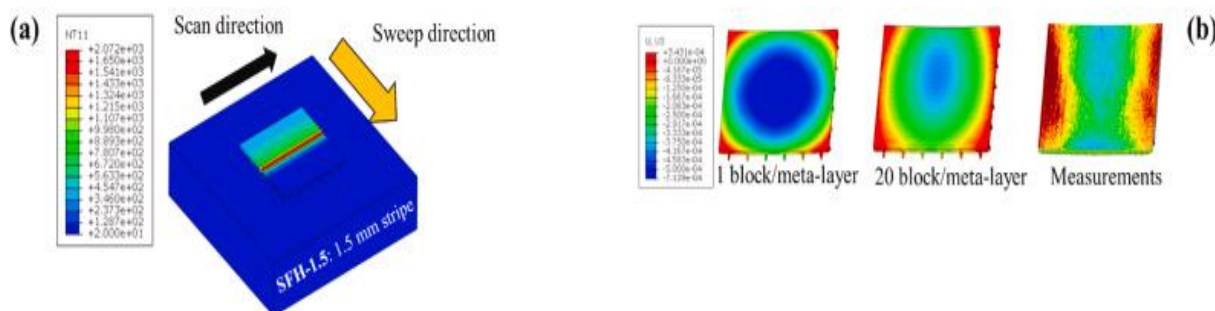


Figure 1. 19: Temperature distribution during a meta-layer width activation simulation. (b) final deformation obtained with different meta-layer widths (Bayat et al., 2020)

employs lumped layers activation is found in the PBF. Chiumenti et al. employed and compared different heat lumping (heating) strategies, point-by-point, hatch-by-hatch, layer-by-layer and finally 4 layer-by-4 layer (Chiumenti et al., 2017). They concluded that hatch-by-hatch heating can be a good balance between computation time and accuracy. Bayat et al. also studied the effect of lump heating (activation sequence) on the thermal and mechanical analysis for PBF process (Bayat et al., 2020). They defined new hatch width that

is a variable with 5 different hatch width within a meta-layer. So, they analysed 5 different meta-layer widths and concluded that with different meta-layer widths, they had different results. A meta-layer width of 20 blocks resulted in a good agreement with experimental results as shown in **Fig. 1.19**.

Part-scale modeling can also be done at different scales in different models. Because in the above-mentioned model, part-scale simulation is performed in a single model itself. But some researchers have developed different models for different scales that involves different physics. Chie et al. developed 3 models at 3 different scales (Chao Li et al., 2018; Li et al., 2017, 2016) each involving different physics. The first model (micro-scan model) follows the laser beam in pure thermal conduction-based model. The second model is a thermo-mechanical model (meso-layer hatch model) that employs an equivalent heat source that leads to identical temperature obtained in the first model and extract the average stress. Finally, in the third model (part-scale) that is a mechanical model, average stress extracted from the second model is applied on the part-scale model to calculate the final deformation and stresses.

For the LDED, Chiumenti et al. simplified the deposition strategy and used a meta-layer with a thickness of 4 layers (Lu et al., 2019a). They concluded that the local temperature history is lost, but the average temperature values show good agreement with the experiment results. Also, for distortion results, for the first few layers, simulation results showed a lot of discrepancies, but for the subsequent layers deposition, simulation results were in agreement with the obtained experiment results. With lumped heating meta-layer strategy, they were able to achieve a reduction of computation time of 77%.

### 1.4.3.3 Other techniques to reduce computation time

It is of utmost importance to reduce the computation time because the part size in LDED is significantly large and conventional models leads to impractical computation time (days to months depending upon part-size). There are other numerical tools such as mesh optimisation, hyper reduction of the model, analysis on eulerian frame etc. that can be helpful in reducing the computation cost of the numerical analysis. The most important and often used is mesh optimisation technique that is discussed in this section.

#### 1.4.3.3.1 Adaptive mesh

High temperature gradients and the plastic strains induced due to it are mostly present in the current deposition layer or penetrated to the previously deposited layer. Therefore, it requires high resolution of mesh size at the high temperature gradient zone (current & previous deposition layer), however it does not require the same fine mesh size at the remaining domain of the workpiece. Conventionally, a fixed fine uniform mesh size is chosen all over the deposited/fabricated part for the complete duration of the numerical analysis. This drastically increases the computation time and memory requirements. Therefore, different researchers have worked on the dynamic/adaptive meshing models that will refines the mesh at the high temperature gradient zone while coarsening the mesh size anywhere else during the simulation of deposition process. Lindgren et al. were among the first ones to develop adaptive mesh strategy for welding process (Lindgren et al., 1997). They concluded that computation time was reduced up-to 60% and higher gains are expected on case of longer weld beads. But with the introduction of mesh coarsening, computation error starts to accumulate as well. Runnemalm et al. improved the adaptive mesh strategy by introducing an error indicator that predicts the critical zone that needs to be refined (Runnemalm and Hyun, 2000).

Hajjalizadeh et al. showed a comparison between conventional and adaptive mesh-based model (mesh coarsening algorithm) for a 18-layer L shape part of AISI 304L (Hajjalizadeh and Ince, 2019) as shown in **Fig 1.20**. They concluded that with an adaptive mesh, computation time can be reduced up-to 3 times as compared to conventional uniform static mesh. This time reduction will be more influential as the part size and number of layers increases.

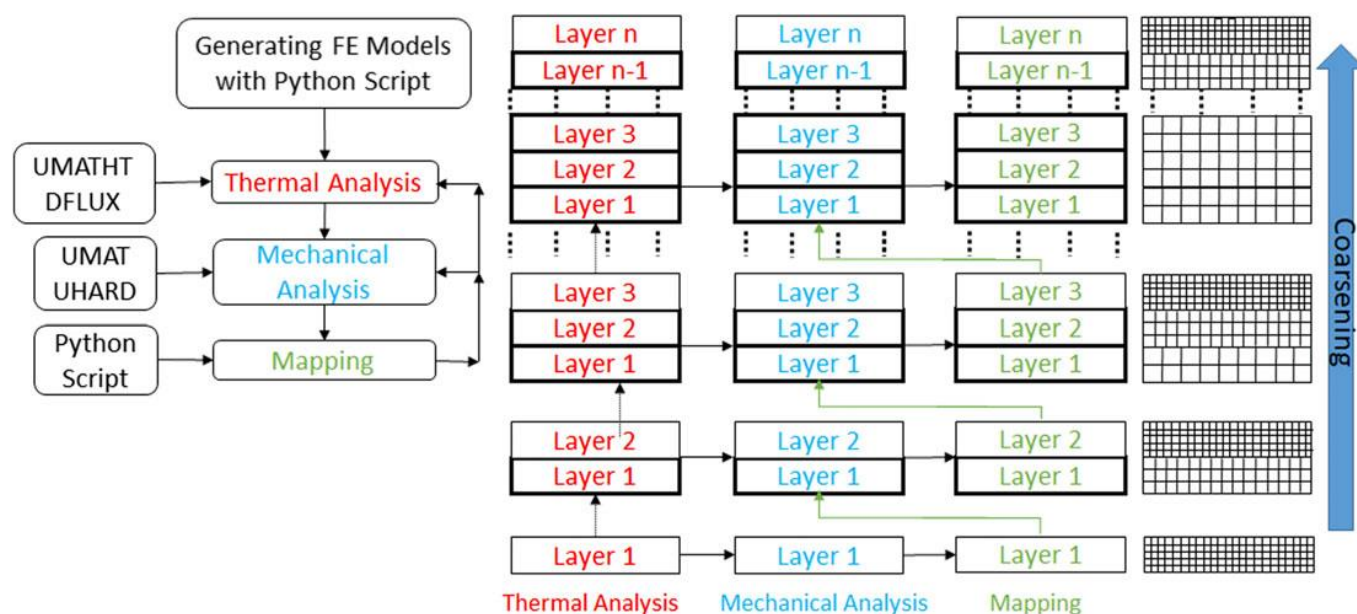


Figure 1. 20: Sequence of adaptive mesh-based FEM (Hajjalizadeh and Ince, 2019)

Denlinger et al. also used a Hybrid material activation model with adaptive mesh-based model (mesh coarsening algorithm) to simulate a 3.8m size part of 107 layers high of Ti-6Al-4V (Denlinger et al., 2014). They also conclude that computation time was practical (116h) for such a large-size part and is drastically reduced using adaptive mesh. Adaptive mesh is really helpful in reducing the computation time for the complete simulation of the deposition process, however coarsening strategy can also result in computation accuracy (Baiges et al., 2021). This loss of accuracy can kill the original idea of refining the mesh in the high temperature gradient zone. Therefore, they introduce two corrective terms that compensate for the loss of accuracy originated due to mesh coarsening.

#### 1.4.3.3.2 Model with Eulerian approach

A conventional model employs a transient thermal model with Lagrangian frame with a time discretisation to model the moving laser heat source. A steady-state analysis utilised a Eulerian reference frame for the moving laser heat source and the material moves through the mesh. Hence, the analysis with Eulerian reference frame can be done with one-time step (quasi-stationary) that reduces the computation time exponentially (Gu and Goldak, 1994). In addition, this type of analysis does not need a fine resolution of mesh that also contributes in reducing computation time. This type of analysis was first introduced for welding simulation that reduced the computation time. Zhang et al. compared simulation with both Eulerian & Lagrangian reference frame and concluded that a Quasi-static analysis with Eulerian frame is two times faster than a transient analysis with Lagrangian frame for the LDED process (Zhang and Michaleris, 2004). Ding et al. also demonstrated the effectiveness of this approach by comparing the two approaches for deposition of mild steel for a Wire + Arc Additive manufacturing process (WAAM) (Ding et al., 2011). They also concluded that with quasi-stationary analysis, computation is done 5-times faster than a transient analysis.

## 1.5 Identification of needs or Research Gap

This state of the art has made it possible to carry out an assessment of the various works aimed at developing numerical models of the LDED process. The interest of simulation tools for these processes no longer needs to be demonstrated. However, the development of robust and fast models is still a necessity, in particular, to control the accumulation of distortions for producing large parts. Reducing the calculation times of thermomechanical models requires reflection in the various choices made at each stage of the model.

In this way, a work can be done on the choice of the equivalent heat sources. The state of the art has shown that different heat sources (Goldak Double Ellipsoid, Goldak Simple Ellipsoid, Top-Hat 3D, Gaussian 3D) have been used for LDED simulation. Most of the researchers have used Goldak Double Ellipsoid Heat Source and validated their model with a set of process parameters. However, majority of the thermo-mechanical models are validated for few layers that are in the range of 20-50. Also, these models were mostly validated with post-process distortion or stress results. It has been proven, that in-situ distortion accumulation is a complex phenomenon that depends upon process parameters and therefore thermo-mechanical should be validated with in-situ distortion results for large-scale part. This will justify the robustness and versatility of the model dedicated for LDED.

So, after doing the literature review, several needs have been identified:

1. Identification of suitable metal deposition modelling strategy dedicated for LDED.
2. Optimization of heat losses parameters (radiation and convection) has to be done, so that computation time can be reduced by not taking time dependent values of convection coefficient and emissivity.
3. For the Numerical Model Validation, the number of deposition tracks and layers that need to be investigated should be in large numbers:
  - a) With an increase in the number of passes, it causes a greater accumulation of heat that can expose shortcoming of the model, if it is not accurately modelled.
  - b) With higher deposition time and a higher number of passes and layers, it can cause errors, if the Numerical Model does not predict the evolution of distortion accumulation.
4. Thermo-mechanical models have to be validated using in situ measurements:
  - a) In-situ measurement methods capture information that would go unreported when using only post-process measurements and can be used to optimize the unknown process parameters.
  - b) Time dependent distortion data can help in better understanding of the mechanical response because it provides an insight in the evolution of distortion accumulation throughout the build for the whole deposition and cooling process.
5. Mechanical models have to be validated using post-process measurements:
  - a) Information pertaining to part distortion can be gathered in all 3 dimensions.

# Chapter 2: Metal deposition modeling

|   |    |
|---|----|
| Chapter 2: Metal deposition modeling .....                        | 33 |
| 2.1 Introduction.....   | 34 |
| 2.2 Experiment Set-Up (PIMM) .....                                | 34 |
| 2.3 Meso-scale conduction-based pure thermal model for LDED.....  | 35 |
| 2.3.1 Thermal Analysis .....                                      | 36 |
| 2.3.2 Thermal and initial boundary Conditions.....                | 36 |
| 2.3.3 Latent Heat of Fusion and Marangoni Flow .....              | 38 |
| 2.3.4 Heat source model.....                                      | 39 |
| 2.4 Numerical implementation.....                                 | 40 |
| 2.4.1 FEA solver.....   | 40 |
| 2.4.2 FEM Mesh .....  | 40 |
| 2.4.3 Model calibrations and boundary conditions .....            | 41 |
| 2.5 Material Modeling .....                                       | 42 |
| 2.5.1 Quiet/Active Material Activation Method.....                | 42 |
| 2.5.2 Hybrid Activation Method.....                               | 50 |
| 2.5.3 Arbitrary Lagrangian Eulerian (ALE) Moving Mesh Method..... | 53 |
| 2.6 Conclusions.....  | 56 |

## 2.1 Introduction

*The objective of the present work is to develop a thermo-mechanical model for large parts fabricated by LDED process. To achieve this objective with practical computation time, CFD models cannot be employed. Therefore, keeping this in mind, in this work pure thermal model will be utilized. Also, as LDED is a material addition process, metal deposition modeling can be a critical aspect in the development of a numerical model that can predict the thermal response with desirably low computation time for complex part-geometries. Therefore, main aim of this chapter is to investigate and develop the most-suitable metal deposition model for LDED process.*

The development of the all the numerical models in the PhD is done on COMSOL Multiphysics® 5.6. This software is chosen due to the fact that the IRDL lab (host lab for PhD) has a proven expertise of developing detailed numerical models on COMSOL representing different physical phenomenon occurring in welding (Courtois, 2014), LDED (Morville, 2012b) and WAAM technologies (Cadiou, 2019).

The knowledge and expertise gained by the lab gave me the confidence of choosing COMSOL software as a test bench to carry out the research work for the present work. Also, this software gives the opportunity to the developers or users of generating exportable applications that can be really useful for industrial applications. Since this Ph.D. is done with industry and academic collaboration with the main objective of developing numerical tools that can assist the industry in LDED technology, therefore it was an easy choice to select COMSOL for the development of process simulation for LDED.

The main objective of this chapter is to investigate the best metal deposition modeling strategies for LDED resulting in the least computation time and errors. In this respect, different techniques are developed, implemented, validated with experimental results, and then finally compared to each other:

- a) Quiet/Active
- b) Hybrid
- c) Arbitrary Lagrangian-Eulerian (ALE)

A detailed discussion is done about these metal deposition models in the following sections. The work carried out in this chapter was at the very start of the thesis, before setting up the experiment procedures at Irepa Laser. Therefore, to validate these models, the comparisons were done with the experimental data obtained from the literature work done at the PIMM lab in Paris. This work is a well-documented publication allowing the experiment work to be re-done numerically and can be helpful in validating the numerical model (Peyre et al., 2017). Also, the material used in Peyre's work is Ti-6Al-4V, which is not the chosen material in this Ph.D. So, it provides an opportunity to validate the numerical model for more than one material and proves its versatility in handling different materials.

## 2.2 Experiment Set-Up (PIMM)

LDED tests were done on an industrial Optomec 850 LENS machine using Ti-6Al-4V powders with a range of 45-75  $\mu\text{m}$ . Single wall structures were fabricated on a 62 mm long, 2 mm wide, and 10 mm thick Ti-6Al-4V substrate (matching material) using a LDED process. A detailed explanation of the experiment is presented in reference (Peyre et al., 2017). The orientation of the substrate used for the deposition process is shown in **Fig 2.1**. This particular orientation of substrate is chosen to capture the high thermal evolution near the deposition or melt-pool region using a thermocouple. Thermocouple is positioned at a location of 3 mm down from the top surface of the substrate and centred at the substrate as shown in **Fig 2.1**.

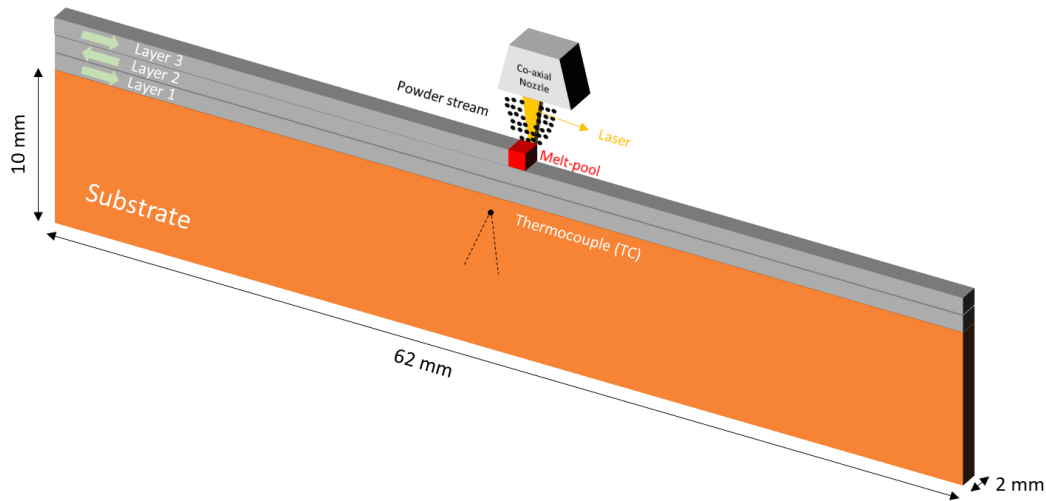


Figure 2. 1: Building Strategy and dimensions used in the literature experiment

Two different process parameters are considered of 400 and 600 W laser power with a fixed laser scan speed of 200 mm/min. The mass feed rate is constant at 2.5 g/min. Deposition is done with a zig-zag strategy as shown in **Fig 2.1**. The laser spot size was measured to be 1.7 mm in diameter at the part surface. Laser and powder are co-focussed at the substrate with laser having a top-hat intensity distribution and incoming powder having gaussian distribution at the co-focussed point. Dwell time of 10s was used for each layer to expose the part to cooling time. Therefore, in the present work also, effect of laser power is analysed by fixing the laser scan speed and inter-layer dwell time. Along with the thermocouple, a fast camera was also used to capture the melt-pool recordings that is further analysed to measure the melt-pool dimensions which are presented in **Table 2.1**.

Table 2. 1: Experiment measurements of wall and melt-pool dimensions (Peyre et al., 2017)

| Parameter               | Case 1: P = 400 W - $V_S = 200$ | Case 2: P = 600 W - $V_S = 200$ |
|-------------------------|---------------------------------|---------------------------------|
| Deposition Layer Width  | 2.5 mm                          | 3.3 mm                          |
| Deposition Layer Height | 1.08 mm                         | 0.92 mm                         |
| Melt-pool length (MP-L) | 3.3 mm                          | 4.2 mm                          |
| Melt-pool height (MP-H) | 1.5 mm                          | 1.75 mm                         |

The in-situ measured temperature and melt-pool dimensions from Peyre's work are used to calibrate and validate our thermal model developed on COMSOL *Multiphysics*® 5.6 with modeling approach explained in **Section 3**.

The modeling approach laid out for heat transfer analysis in **Section 2.1** is applied to simulate the experiments performed in the literature for Ti6Al4V wall builds done with different sets of experiments in an attempt to capture the thermal behavior of the sample.

## 2.3 Meso-scale conduction-based pure thermal model for LDED

As discussed in Chapter 1, meso-scale flow-based model cannot be used for simulating multi-layer large part deposition. Therefore, in the present work, at first a meso-scale pure conduction-based thermal model is first

developed to model the heat transfer phenomenon. It is coupled with a metal deposition model to represent material addition during LDED process. To simplify the model, following assumptions are made:

- Geometry of the layer is known
- No metallurgy
- No fluid-flow

At first, in this section, a brief summary is provided of how the finite element method (FEM) for transient thermal model is developed and implemented.

### 2.3.1 Thermal Analysis

In the Heat Transfer module of COMSOL, assuming a Lagrangian frame  $\Omega$  and a material point located by  $\mathbf{r}$  ( $\mathbf{r} \in \Omega$ ) as the reference, given thermal energy balance at time  $t$ , the governing equation can be formulated as follows:

$$\rho(T)C_p(T)\frac{\partial T(\mathbf{r}, t)}{\partial t} = -\nabla \cdot \mathbf{q}(\mathbf{r}, t) + Q(\mathbf{r}, t), \mathbf{r} \in \Omega \quad (2.1)$$

where  $\rho$  is the material density,  $C_p$  is the specific heat capacity,  $T$  is the temperature,  $t$  is the time,  $Q$  is the heat source, and  $\mathbf{q}$  is the heat conduction flux vector, calculated as:

$$\mathbf{q} = -k(T)\nabla T(\mathbf{r}, t) \quad (2.2)$$

Where  $k$  is the thermal conductivity of the material. Material properties such as density, specific heat and thermal conductivity are taken as temperature dependent from the literature and is fed manually as a function of temperature. Temperature dependent material properties are taken from literature (Mills, 2002a) as shown in **Fig 2.2**. Linear interpolation is used to calculate the values between the given temperature dataset in the figure. Also, temperatures beyond the fusion temperature, thermal properties are considered constant.

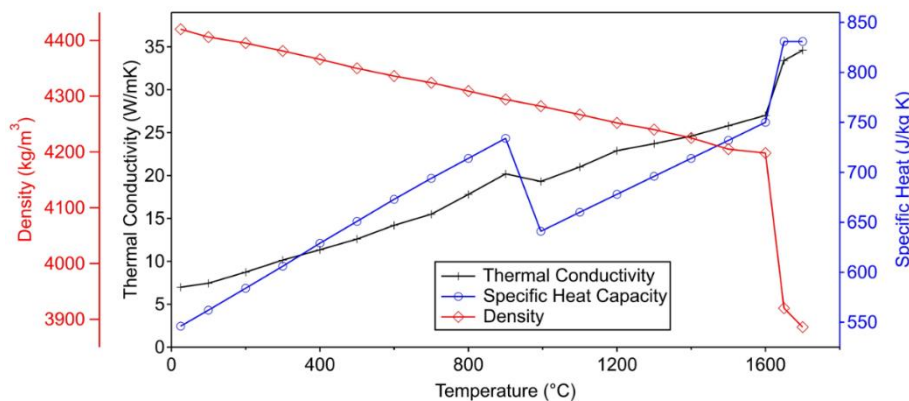


Figure 2. 2: Temperature dependent thermal properties of Ti-6Al-4V (Mills 2002)

### 2.3.2 Thermal and initial boundary Conditions

To solve above stated equations in FEM, it is necessary to have an initial condition. The initial condition is set to the temperature of the ambient temperature.

$$T(\mathbf{r}, 0) = T_0(\mathbf{r}, 0) \quad \mathbf{r} \in \Omega \quad (2.3)$$

In the LDED process, heat losses are occurring due to the thermal radiation, free convection and forced convection. In the model, convective heat loss is accounted by introducing the convective heat flux option in the heat transfer module.

$$q_{conv} = h (T - T_{amb}) \quad (2.4)$$

where  $h$  is the convective heat transfer coefficient. Ideally, convective heat transfer coefficient should be temperature dependent. But, it's difficult to obtain correct data in the literature for this parameter. Therefore, we will use a constant value for this parameter.

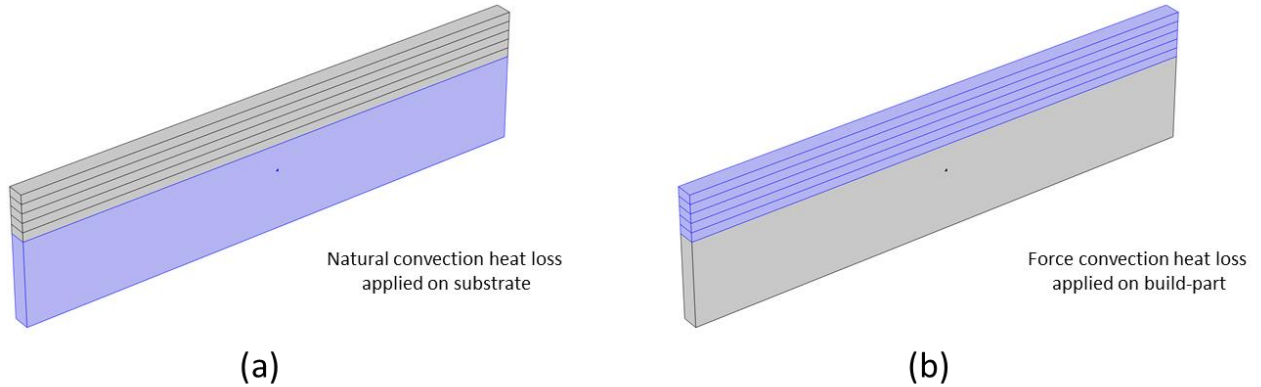


Figure 2. 3: Description of model showing different surfaces over which natural and forced convection heat loss is applied

To account for forced convection on the deposited metal, higher value of convective heat transfer coefficient is taken on the deposited regions as shown in **Fig 2.3**. Therefore, in the model, another convective heat flux is introduced that accounts for forced convection on build regions:

$$q_{conv} = h_{forced} (T - T_{amb}) \quad (2.5)$$

where  $h_{forced}$  is the forced convective heat transfer coefficient. Here also, ideally this coefficient should be dependent upon the current position of the nozzle i.e., dependent upon space and time. And should be applied to the powder stream diameter. However for the sake of simplicity, in the model, an average value of  $h_{forced}$  per layer is taken that takes into account the global position per layer and time of the nozzle. Build region is discretized/divided in different domains in model. And each layer in the model is assigned with a different domain number. It would be really time consuming and impractical to assign each layer domain with  $h_{forced}$ . Therefore, an if condition is used to assign  $h_{forced}$  in the build region as follows:

$$if(dom == domain(t), h_{forced}, h) \quad (2.6)$$

Where a function  $domain(T)$  is formulated. This function stores the generated domain and surface number as a function of time, therefore taking the time into account. And **dom** is a specific software generated identifier for different domains of the CAD. So, the condition simply works if the user programmed nozzle location is at layer 1, only layer 1 is assigned with  $h_{forced}$  and all the surfaces of the other domains are assigned with natural convection coefficient  $h$ . During the dwell period or cooling time between successive layers, forced convection is inactive. And if the local position is at layer 2, only layer 2 is assigned with  $h_{forced}$  and all other domains are assigned with natural convection coefficient  $h$ . Hence, the time dependent average  $h_{forced}$  is employed in the model. The behaviour of  $domain(t)$  function is represented in the **Fig 2.4**, that explains how

this function applies the  $h_{forced}$  on the domain of current deposition layer during the complete deposition process. The values chosen for  $h$  and  $h_{forced}$  are given in the Model Calibration section.

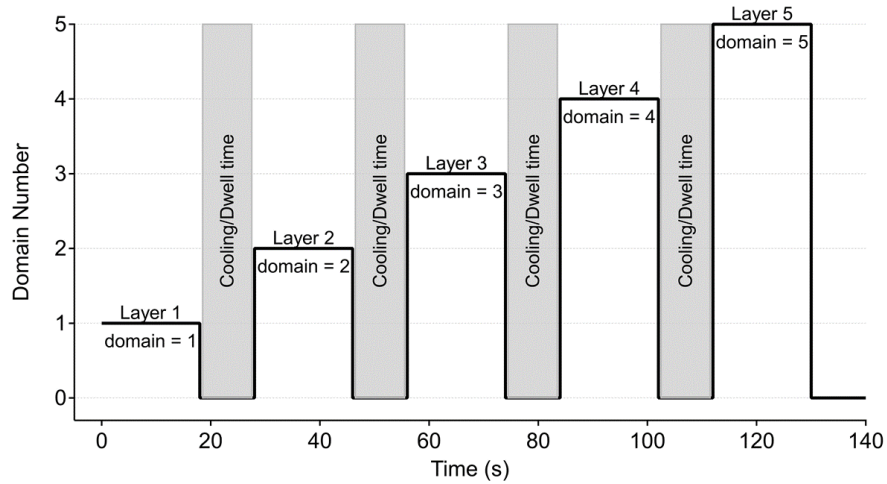


Figure 2. 4: Schematic of analytical function domain(t) and its evolution during the deposition process

Thermal radiation  $q_{rad}$  is accounted for using the Stefan–Boltzmann law and is applied on all the surfaces of substrate and build-part shown in **Fig 2.3**:

$$q_{rad} = \varepsilon \sigma (T^4 - T_{amb}^4) \quad (2.7)$$

where  $\varepsilon$  is the surface emissivity,  $\sigma$  is the Stefan–Boltzmann constant,  $T$  the surface temperature of the workpiece, and  $T_{amb}$  is the ambient temperature. Again, surface emissivity should be temperature dependent, but for the same reason as above, it is taken as a constant. The above equation is introduced in model by utilising the surface to ambient radiation heat loss feature under the heat transfer module.

### 2.3.3 Latent Heat of Fusion and Marangoni Flow

The developed model is a conduction-based pure thermal model, however to account for the effect of melting and solidification during the metal deposition in LDED process, temperature dependent specific heat capacity of the material is modified (Ren et al., 2019; Yan et al., 2017).

$$C_p^*(T) = \frac{L_f}{T_m - T_{amb}} + C_p(T) \quad (2.8)$$

Where  $C_p^*(T)$  is modified temperature dependent specific heat,  $T_m$  is melting temperature, for Ti-6Al-4V,  $L_f$  (J/kg) is latent heat of fusion equals to 365 KJ/kg, and it is spread over a temperature ranging from 1600 °C to 1700 °C.

Also, in order to take the convective redistribution of heat in the melt-pool due to the fluid flow into account, a higher value of thermal conductivity is considered, hence avoiding integrating complex analytic form in the model which goes hand in hand with calculation time. Therefore a simplified form was chosen to represent this phenomenon by introducing an enhanced thermal conductivity (Lampa et al., 1997; Ren et al., 2019).

$$k^*(T) = \begin{cases} k(T), & T < T_m \\ 2.5 \times k(T), & T \geq T_m \end{cases} \quad (2.9)$$

Where  $k^*(T)$  is enhanced thermal conductivity. Both  $C_p^*(T)$  and  $k^*(T)$  replaces the original specific heat and thermal conductivity in **Eq. 2.1** and **2.2** respectively.

## 2.3.4 Heat source model

As discussed in Chapter 1, Double Ellipsoid (DE) heat source is most commonly used to represent input laser energy, as it can be tuned to the process parameters. This feature provides great flexibility to model the input laser energy by modifying the shape and size of the numerical heat source (DE). In Chapter 1, we discussed that the lasers employed in LDED process usually operate in continuous mode with a gaussian or top-hat intensity distribution. Therefore, in the numerical model, equivalent heat source representing input laser energy should also be of same intensity distribution (gaussian or top-hat) leading to the correct melt-pool temperature and dimensions. However, equivalent heat source parameters need to be calibrated with experiment data obtained in the same conditions. This calibration of source parameters also plays a role in choosing the equivalent heat source for the model. For example, Gaussian 3D, Top-hat (2D) heat source requires very few parameters that need to be calibrated. On the contrary, Goldak's Double Ellipsoid (DE) heat source requires much more parameters and can prove to be tricky if process parameters are changed each time. Therefore, in the present work, different equivalent heat sources with both gaussian and top-hat distribution is implemented that are presented below.

### 1. Gaussian Double Ellipsoid (DE)

The schematic/orientation of DE heat source model is presented in **Fig 2.5**.

$$Q_{DE} = \frac{6\sqrt{3}APf_{f,r}}{a_{f,r}bc\pi\sqrt{\pi}} \exp\left(-\frac{3(x - V_s t)^2}{a_{f,r}^2} - \frac{3y^2}{b^2} - \frac{3z^2}{c^2}\right) \quad (2.10)$$

The laser power is  $P$  and the laser absorption efficiency is  $A$ . The value for laser power  $P$  is based on process parameter. The value of  $A$  is calibrated using the method of reverse calibration by iteratively fitting the

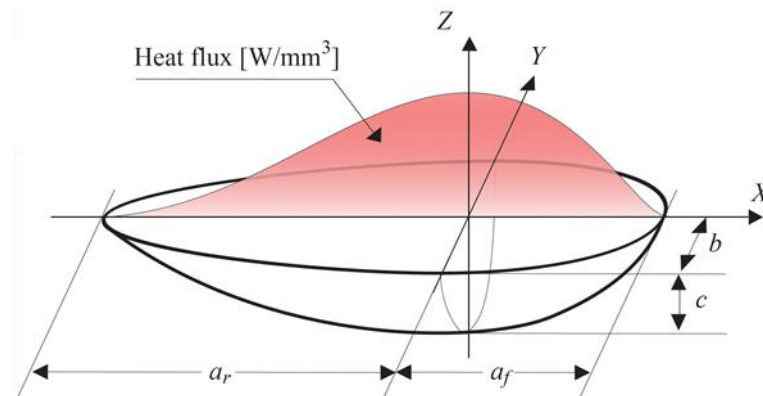


Figure 2. 5: Schematic of DE heat source model

simulated temperature field at thermocouple location to match the experiment results described in Ref. (Erik R Denlinger et al., 2015).  $x$ ,  $y$  and  $z$  are the local coordinates with the origin centred at the two ellipsoids where the DE heat source reaches the maximum intensity and with a moving velocity  $V_s$ , parameters  $a_{f,r}$ ,  $b$  and  $c$  represent the respective length of the longitudinal, transverse and through the depth semi-axes of the DE parallel to the local  $x$ ,  $y$  and  $z$  axes. Generally,  $a_f + a_r$  is taken as the melt-pool length,  $b$  is taken as the half width of the deposition bead and  $c$  to the melt pool depth. In the literature, different lengths are taken for the front ellipsoid  $a_f$  and rear ellipsoid  $a_r$  of the heat source.  $f$  is a weighting fraction, that determines the energy partition among the front and rear ellipsoid.

### 2. Gaussian 3D exponential volume (G-3D)

This heat source assumes a gaussian distribution over the deposition surface (XY plane) and follows the Beer-Lambert law during energy absorption through the layer thickness (Z axis) (Mishra et al., 2018).

$$Q_G = \frac{2AP}{\pi r^2 D} \exp\left(-\frac{2((x - Vt)^2 + y^2)}{r^2}\right) \exp\left(\frac{-|z|}{D}\right) \quad (2.11)$$

Where  $x, y$  are local coordinates,  $|z|$  is the absolute value of  $z$  coordinate,  $r$  is the laser beam spot radius and  $D$  is the penetration depth that needs to be calibrated with melt-pool depth measurement.

### 3. Top-Hat 2D (TH-2D)

This heat source assumes a uniform distribution over the laser spot size and corresponds to laser having uniform distribution rather than gaussian.

$$Q_{TH} = \begin{cases} \frac{AP}{\pi r^2}, & -r \leq \sqrt{(x - V_s t)^2 + y^2} \leq r \\ 0, & \sqrt{(x - V_s t)^2 + y^2} > r \end{cases} \quad (2.12)$$

Different simulations are performed using these different heat sources and comparisons were done in terms of peak temperatures obtained in the melt-pool, melt-pool sizes and computation time. A detailed comparison of the results obtained using the above-mentioned heat sources is presented in the results section (Section 4.4).

## 2.4 Numerical implementation

### 2.4.1 FEA solver

For all methods studied here to model material deposition, the FEM analysis is performed using solver (PARDISO) with the implicit Backward Differentiation Formula (BDF) time stepping method. Adaptive time stepping method is employed rather than strict formulation with maximum time step of  $R/v_s$  for all simulations performed. The solver is further adapted specifically to model additive manufacturing technologies in the present work. All simulation cases are performed on an Intel Xeon W-2275, 16 cores, with 128 GB RAM workstation.

### 2.4.2 FEM Mesh

**Fig. 2.6** displays the 3D finite element mesh, generated in CM5.6, used for the thermal model employing Quiet/Active and Hybrid Activation method. The same mesh is used for all experiment cases and different equivalent heat Source models (DE, G-3D, TH-2D) used in the present work. The mesh contains 10,944 Hex-8 elements and 14,535 nodes. Hex-8 elements were chosen because it has been proved that Hex-8 elements gives more accurate results as compared to linear tetrahedral elements for the plastic deformation (Benzley et al., 1995). Therefore, to have same mesh for thermal & mechanical analysis in future work, Hex-8 elements were used. The elements for the deposited material are allotted as 4 per laser spot size and 2 per deposition thickness, making the elements  $0.5 \text{ mm} \times 0.5 \text{ mm} \times 0.54 \text{ mm}$  in volume for experiment case 1 ( $P = 400 \text{ W}$ ,  $V_s = 200 \text{ mm/min}$ ), but varies for other experiment case P600 V200 as track geometry changes. The mesh is coarsened at the substrate as it moves away from the wall builds. The mesh at the substrate is highlighted in

different colours. A mesh convergence study was done using three different mesh strategies to confirm the accuracy of thermal analysis that is presented in the Appendix (Chapter 2).

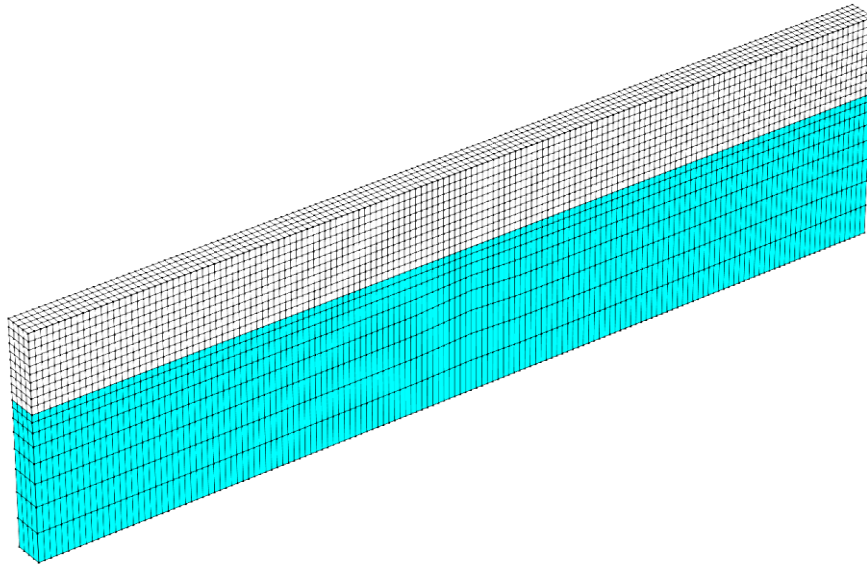


Figure 2. 6: Finite Element Mesh used for Quiet/Active and Hybrid Activation method (blue mesh represents the substrate and white mesh the layers)

### 2.4.3 Model calibrations and boundary conditions

To simplify the model, deposited wall build is considered to be a flat rectangular shape with constant layer height and width. This is different from the experiments as layer height changes in the few first layers and then reaches a uniform layer thickness as the process physics stabilise. The dimensions of the layer are taken from the experiment data mentioned in Table 2.1. As discussed previously in **Chapter 1**, to develop an accurate meso-scale conduction-based pure thermal model, certain input parameters have to be calibrated against experiment results. The laser absorption efficiency ( $A$ ) is taken as 0.35 with reverse calibration of fitting simulated temperature field to experiment results at thermocouple location iteratively as suggested in (Michaleris, 2014). Also, for all experiment cases, as laser spot size is 1.7 mm, laser spot size radius is taken as 0.85 mm. The double ellipsoid heat source dimensions parameters are dependent on experiment cases but follow the same rule i.e., front ellipsoid length  $a_f = 1.1 \text{ mm}$  and  $a_r = 2a_f$ ,  $b = \text{Track width}/2$  and  $c = \text{Layer Height} + \text{Meltpool depth}$ , that represent the double ellipsoid dimensions to be almost equal to experiment melt-pool dimensions for each experiment case. Track width, height and melt-pool depth are taken from the experiment data and is then fed in the DE heat source parameters. Emissivity ( $\epsilon$ ) is temperature dependent, but mean value of 0.6 is taken as widely reported in the literature (Michaleris, 2014). The convective heat transfer ( $h$ ) coefficient is temperature dependent, but a mean value is taken at the substrate  $h = 5 \text{ (W.m}^{-2}\text{.K}^{-1}\text{)}$  and to consider the effect of forced convection due to the powder carrying argon gas at the wall builds, average convective heat transfer coefficient of  $h = 25 \text{ (W.m}^{-2}\text{.K}^{-1}\text{)}$  is taken as widely reported in the literature that it can be in the range of  $h = 20 - 60 \text{ (W.m}^{-2}\text{.K}^{-1}\text{)}$  (Heigel et al., 2015). Temperature dependent properties like thermal conductivity, specific heat and density for Ti6Al4V are taken from the literature (Mills, 2002a).

The **Section 3** gives details of the modeling of heat transfer mechanism employed for LDED process. The **Section 4** highlights the numerical implementation and calibrations of the model. However, metal deposition modeling is not explained until now. In the further section, detailed analysis of the metal deposition modeling techniques developed and implemented are presented.

## 2.5 Material Modeling

The material deposition in LDED can be of hundreds or thousands of layers depending upon the part-size. Therefore, computation time and accuracy can be greatly influenced with the modeling technique employed for metal deposition. As discussed in **Chapter 1**, different strategies/techniques are reported in the literature for modeling metal deposition:

1. Quiet/Active
2. Inactive
3. Hybrid
4. ALE (Arbitrary Lagrangian Eulerian)

All these above-mentioned strategies are successfully developed, implemented and compared in the present work to investigate the best strategy suitable for LDED process.

### 2.5.1 Quiet/Active Material Activation Method

The translating laser heat flux is applied on the top surface of the domains representing deposition material for all numerical heat sources employed in the present work. The elements that represent the wall builds are pre-existing at the beginning of the analysis as shown in **Fig. 2.7**. Therefore, the computation domain consists of substrate and all the deposition layers from the start of computation analysis. But their material properties

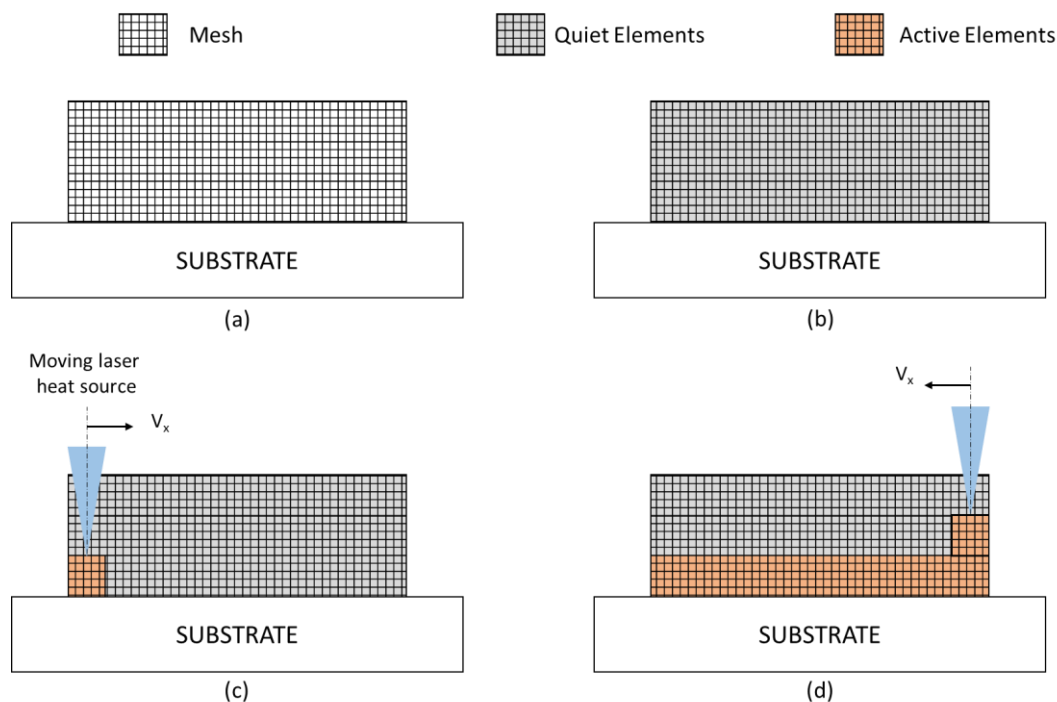


Figure 2. 7: (a) Meshing: Computation domain at start of computation  
 (b) Quiet Material assigned to all layers  
 (c) Material switch from dummy to active material (1<sup>st</sup> layer)  
 (d) Material switch from dummy to active material (2<sup>nd</sup> layer)

are rescaled in such a way that it does not affect the computational analysis. But as the laser advances, an analytical expression (**Eq. 2.15**) accordingly activates the thermo-physical properties of the activated domain from quiet/dummy to active/metal material properties. In the present work, the thermal conductivity  $k$  and specific heat  $C_p$  are set to very low values to minimize the heat transfer from active to quiet elements, as follows:

$$k_{quiet} = s_k k \quad (2.13)$$

$$C_{P_{quiet}} = s_{C_P} C_P \quad (2.14)$$

where  $k_{quiet}$  and  $C_{P_{quiet}}$  are the respective thermal conductivity and specific heat for the quiet elements;  $s_k$  and  $s_{C_P}$  are the appropriate scaling factors that are usually assigned very small values, for instance,  $10^{-4}$  is employed in the present work. Density values ( $\rho$ ) are kept same for both quiet and active elements. The properties of an element are switched from “quiet” to “active” when any Gauss point of the element is consumed by the heat source volume (Eq. (2.13)).

$$\exp\left(-\frac{3(x-v_s t)^2}{a_f r^2} - \frac{3y^2}{b^2} - \frac{3z^2}{c^2}\right) \geq 5\% + \text{solid.wasactive} \quad (2.15)$$

This means that if the evaluated heat source value at any Gauss point is greater than 5% of the peak intensity, the element will be activated by switching material from quiet to active. This activation criteria with a limit to 5% peak intensity value is well calibrated and used by most of the researchers in the literature (Erik R Denlinger et al., 2015). With further increase of this limit e.g., 10%, will shrink the activation domain (melt-pool/deposited metal) and results in much higher temperatures at the interface zone between active and quiet elements. This can lead to some convergence issues in the solver. On the contrary, decrease in this limit of 5% can result in activation of some elements with a temperature lower than fusion temperature, that is not the case in physical phenomenon. Therefore, this particular activation criteria with calibrated intensity limit for activation is logical related to experiment. The deposition strategy is manually programmed and is integrated in all heat sources that allows it to replicate the experiment deposition strategy. Eq. 2.15 will then activate the material from quiet to active material state following the experiment deposition strategy. In COMSOL *Multiphysics*® 5.6, the activation node is available in Solid Mechanics module with an activation expression and Eq. 2.15 is put as the activation criteria. Finally in the activation feature *solid.wasactive* command is also added along with Eq. 2.15. This command justifies that once the element is activated from quiet to active state, it can never turn back to quiet state in a scenario, where deposition strategy is a zig-zag scan and some elements are re-deposited again.

### 2.5.1.1 Quiet/Active Model results and discussion

#### 2.5.1.1.1 Double Ellipsoid (DE) Heat source model

As shown in Fig 2.8(a), Quiet/Active metal deposition model is implemented successfully. During the deposition of layer 1, following the deposition strategy, elements are activated from quiet to active state.

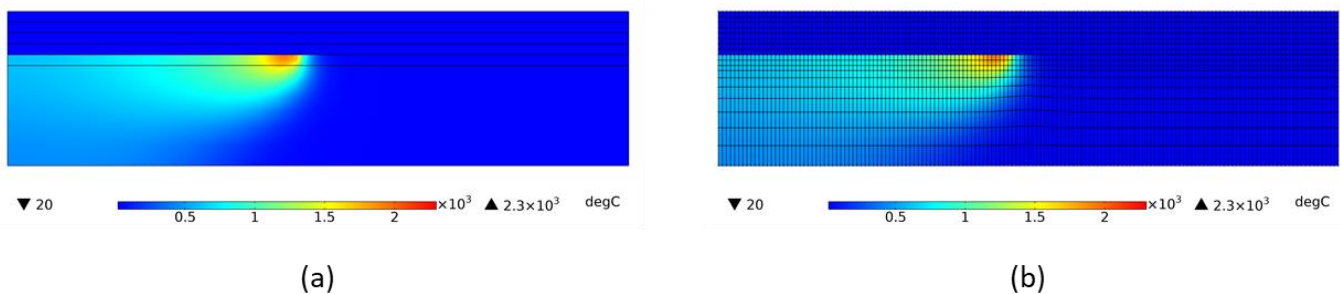


Figure 2. 8: (a) Temperature field with Quiet/Active method  
(b) Representation of Computation domain using Quiet/Active method in Heat transfer analysis

Quiet elements present in layer 1 and layers above do not affect the heat transfer mechanism due to its low thermal conductivity. Therefore, the metal deposition is correctly represented in the COMSOL *Multiphysics*® 5.6 model. **Fig 2.8(b)** represents the computation domain (mesh) at the deposition of layer 1, and it can be seen that the deposition region is a part of the computation analysis from the start.

**Fig 2.9** shows the complete process simulation chain starting from CAD, metal deposition modeling following the trajectory and finish this step repeatedly for all layers.

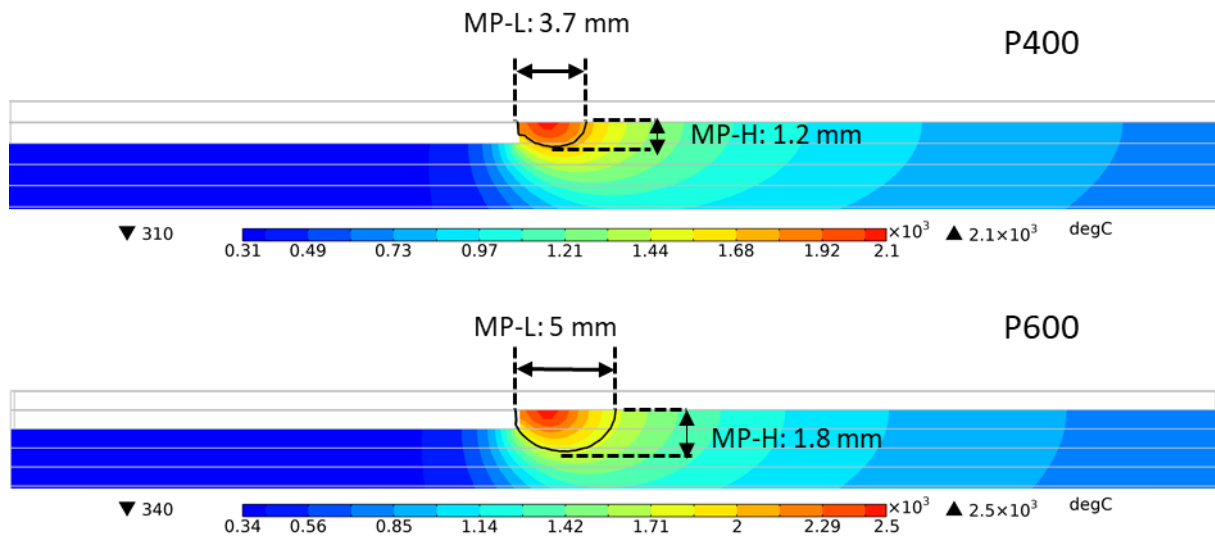


Figure 2. 9: Estimation of melt-pool dimensions employing DE heat source and using Quiet/Active method for experiment case 1 ( $P = 400\text{ W}$ ,  $V_s = 200\text{ mm/min}$ )

**Fig 2.10** shows melt-pool contours and the analysis of melt-pool dimensions in the thermal model. In the **Fig 2.10**, only active elements are shown and quiet elements are hidden. With the increase of laser power, peak temperatures and melt-pool dimensions are increasing and is in accordance to the physical process.

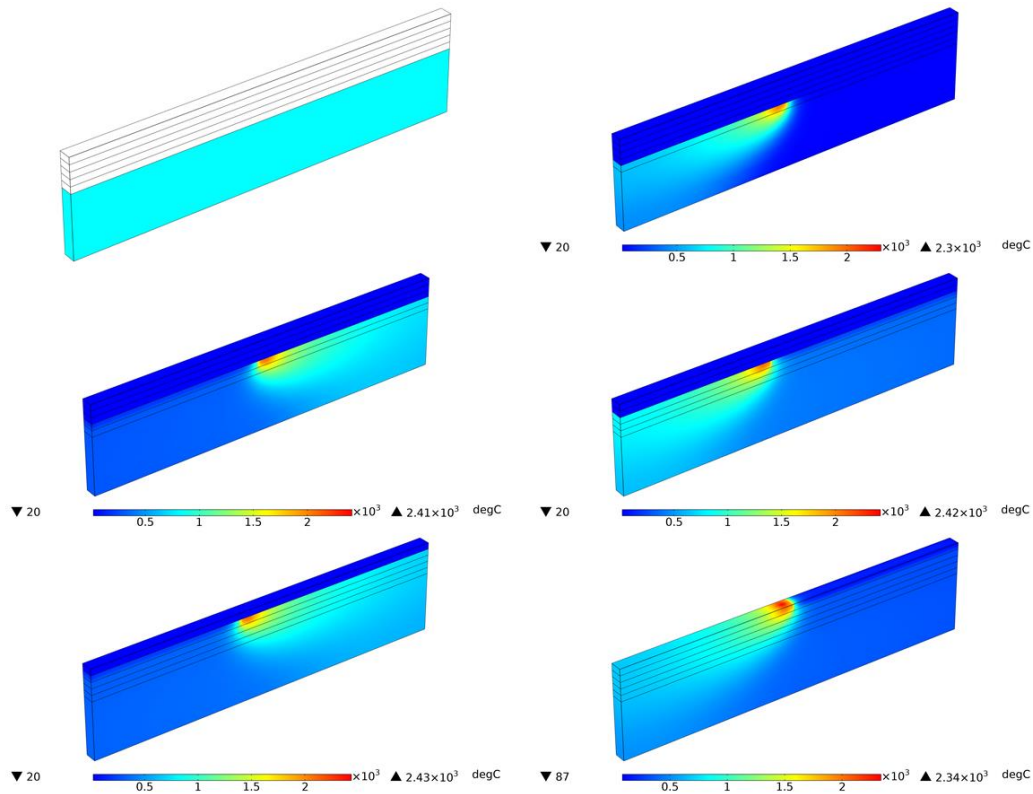


Figure 2. 10: Description of the modeling chain from design to process simulation using Quiet/Active Method for experiment case 1 ( $P = 400 \text{ W}$ ,  $V_s = 200 \text{ mm/min}$ )

To verify the thermal model's accuracy, temperature evolution predicted by the model at the node of thermocouple location is compared with the in-situ experiment results obtained by the thermocouple. Also,

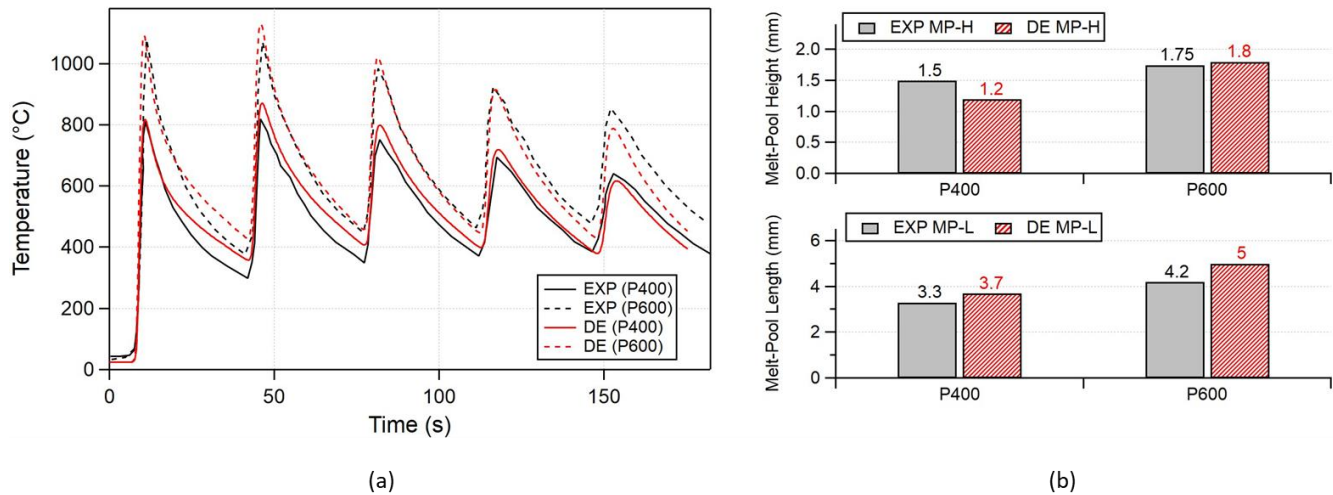


Figure 2. 11: Comparison of Numerical model employing DE heat source using Quiet/Active method with experiment results (a) Temperature evolution at TC location (b) Melt-pool dimensions

the melt-pool dimensions obtained with the model is compared with the experiment measurements that were given in **Table 2.1**. This comparison is shown in **Fig 2.11**. As it can be seen in **Fig 2.11(a)**, with an increase of laser power from 400 to 600W, peak temperatures obtained at the thermocouple location is also increasing. During the inter-layer dwell time of 15s, temperatures are cooled down. The effect of laser power on melt-pool dimensions is also well predicted by the model presented in **Fig 2.11(b)**. The effect of laser power and inter-layer cooling time is well captured by the thermal model with good accuracy. *The computation time for*

this analysis using DE heat source for 5 layers was 14 min. The Quiet/Active material activation method with DE heat source (laser absorptivity value  $A$ : 0.35) gives correct results for temperature evolution as shown in **Table 2.2**, melt-pool dimensions and peak-temperatures obtained in the melt-pool seems realistic as they are well below the evaporation temperature of Ti6Al4V (2860°C).

Table 2. 2: Computation thermal error at thermocouple location for Quiet/Active method employing DE heat source

| Experiment case | Quiet Active Method: Error (%) |  |
|-----------------|--------------------------------|--|
|                 | Double Ellipsoid (DE)          |  |
|                 | A = 0.35                       |  |
| P400            | 11.7                           |  |
| P600            | 12.4                           |  |

### 2.5.1.1.2 Gaussian 3D exponential volume heat source (G-3D)

Using Quiet/Active method, other heat sources are also analysed to find out the suitable heat source for LDED process. Gaussian 3D (G-3D) and Top-Hat 2D (TH-2D) heat sources are employed and same thermal analysis is performed. The analytical expressions of the numerical heat sources are given in **Eq. 2.11 & 2.12**.

Model calibrations section gives details about the heat source calibration for DE and all other calibrations related to heat transfer mechanism. The laser absorption efficiency is calibrated with reverse-simulation strategy and taken as 0.35. For the volumetric gaussian (G-3D) and surface top-hat heat (TH-2D) source, the laser absorption efficiency needs to be calibrated again. However, the material activation criteria and its intensity limit of 5% for activation remains the same as given in **Eq. 2.15**.

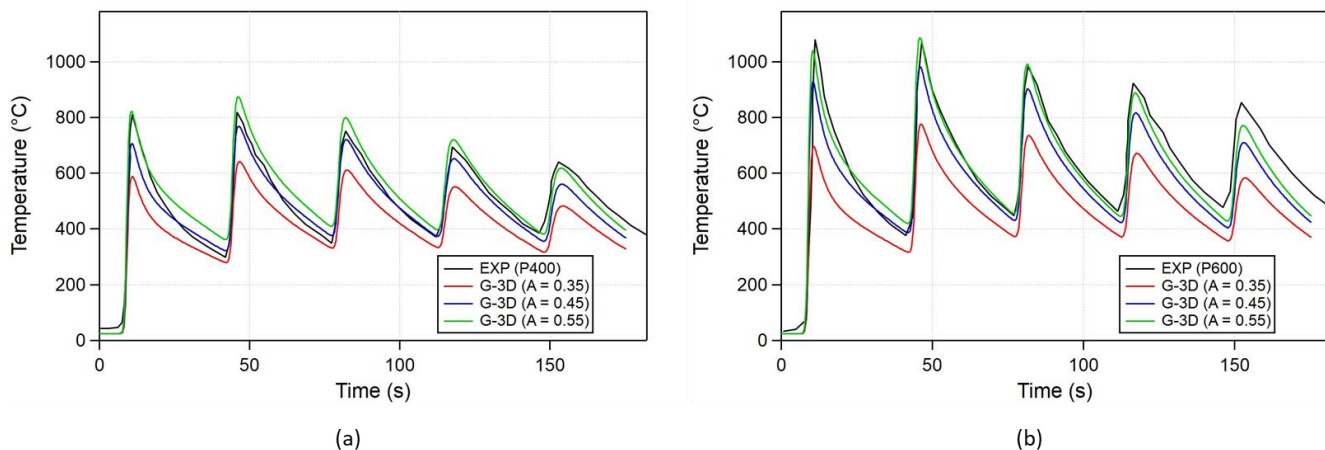


Figure 2. 12: Comparison of temperature evolution at thermocouple location between numerical model employing G-3D heat source with different laser absorption efficiency using Quiet/Active method with experiment results (a)  $P = 400$  W (b)  $P = 600$  W

As it can be seen in **Fig 2.12(a)**, using the same laser absorption efficiency  $A$  (DE: 0.35) with Gaussian 3D heat source, temperature evolution shifts downwards due to the change of heat intensity in the heat source. Then, iteratively different  $A$  values are employed until a correct fit with experiment results is obtained. With  $A = 0.55$ , G-3D seems to give correct results and peak temperatures are almost identical to DE heat source as shown in **Table 2.3**. The computation time for this analysis using G-3D was 11 min which is 22% faster than the analysis using DE heat source. This is due to the fact that DE heat source use two ellipsoid equation with a user-define different gaussian distribution for two ellipsoids of different lengths.

Table 2. 3: Computation thermal error at thermocouple location for Quiet/Active method employing G-3D heat source

| Experiment case | Quiet Active Method: Error (%) |          |          |
|-----------------|--------------------------------|----------|----------|
|                 | G-3D                           |          |          |
|                 | A = 0.35                       | A = 0.45 | A = 0.55 |
| P400            | 20.2                           | 10.2     | 12.5     |
| P600            | 24.7                           | 13.7     | 12.8     |

The lengths and intensity distribution defines numerical heat source shape to exact melt-pool shape, on the contrary G-3D is a simple gaussian distribution that does not replicate the exact melt-pool shape or the intensity distribution. This is clearly observed when melt-pool dimensions predicted by G-3D are analysed. **Fig. 2.13** presents the melt-pool dimensions obtained with G-3D heat source for P400 and P600. Results with  $A = 0.35$  value are not presented because peak temperatures obtained are less than melting temperature that leads to no formation of melt-pool. However, the effect of laser power can be clearly noticed with an increase of melt-pool dimensions, which is well captured by the model. But numerical model is over-predicting the melt-pool lengths by huge magnitude as it is not considering the effect of laser movement and experiment obtained melt-pool shape. Due to the laser movement, melt-pool temperatures (thermal gradient) at the front end are different to the rear end (Goldak et al., 1984). That's why DE heat source is versatile and robust to accommodate this phenomenon and also acquire the melt-pool shape. G-3D heat source works correctly for the global thermal analysis for  $A = 0.55$ , but for the local melt-pool thermal analysis even with  $A = 0.55$ , it does not work as efficiently as DE heat source and over-predicts the melt-pool lengths.

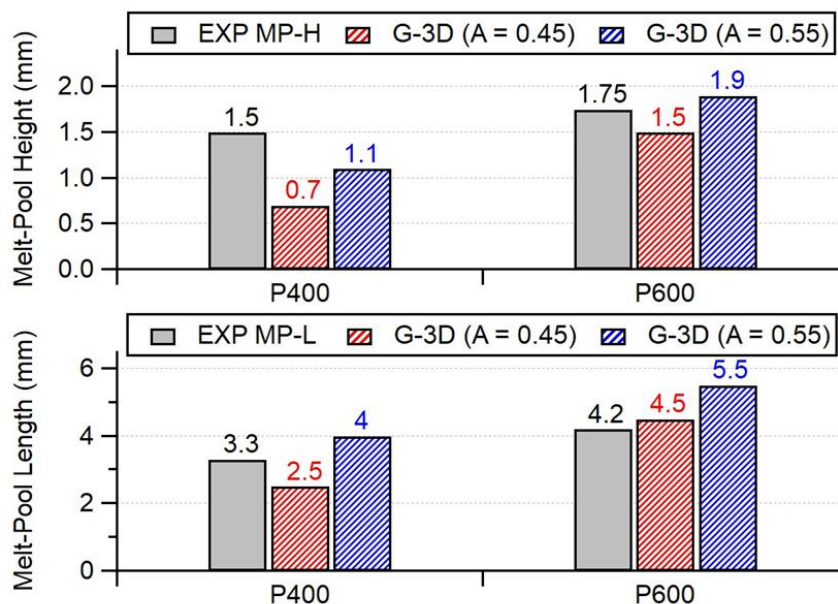


Figure 2. 13: Comparison of melt-pool dimensions between numerical model employing Gaussian 3D (G-3D) heat source with different laser absorption efficiency using Quiet/Active method and experiment results

### 2.5.1.1.3 Top-Hat 2D (TH-2D)

Finally, surface top-hat 2D (TH-2D) heat source is employed. As it can be seen in **Fig 2.14**, using the same laser absorption efficiency  $A$  (DE: 0.35) with Top-hat 2D heat source, temperature evolution shifts upwards due to the change of heat intensity in the heat source. Surface heat source is applied at the top of layer 1, and due to its surface intensity feature, heat intensity distribution is done at the surface i.e., top face of layer 1, rather than over a volume. This leads to higher thermal energy accumulation at the top surface leading to higher temperatures recorded at the thermocouple location. This also leads to un-realistic melt-pool temperatures reaching above the evaporation temperature.

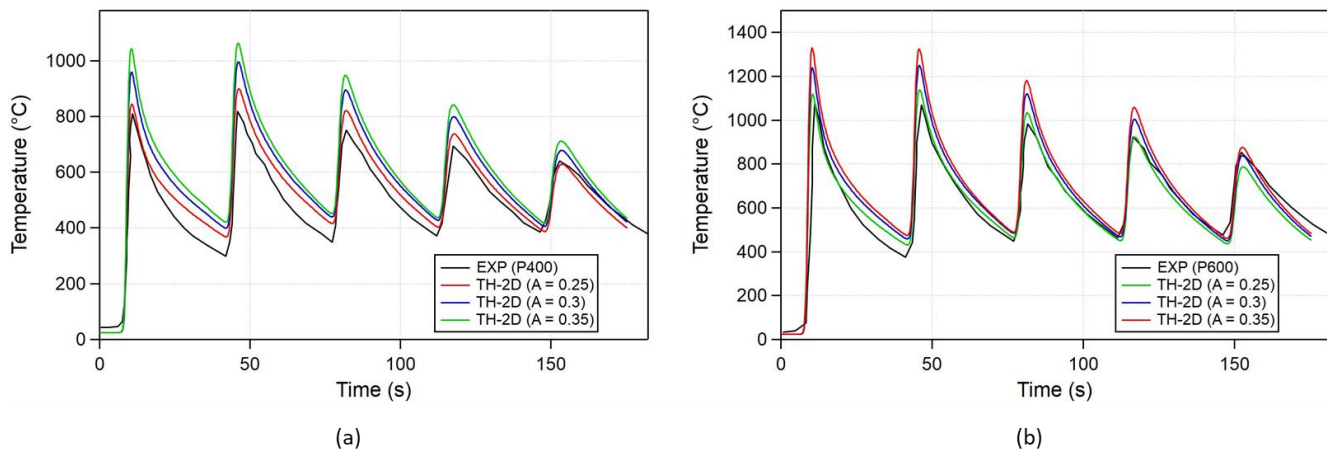


Figure 2. 14: Comparison of temperature evolution at thermocouple location between numerical model employing TH-2D heat source with different laser absorption efficiency using Quiet/Active method with experiment results (a)  $P = 400$  W (b)  $P = 600$  W

Therefore, different  $A$  values are employed iteratively until a correct fit with experiment results is obtained. With  $A = 0.25$ , TH-2D seems to give correct results as shown in **Table 2.4**, however peak temperatures obtained in the melt-pool are still above the evaporation temperature with lower  $A = 0.25$  that is un-realistic.

Table 2. 4: Computation thermal error at thermocouple location for Quiet/Active method employing TH-2D heat source

| Experiment case | Quiet Active Method: Error (%) |          |          |
|-----------------|--------------------------------|----------|----------|
|                 | TH-2D                          |          |          |
|                 | A = 0.35                       | A = 0.45 | A = 0.55 |
| P400            | 13.7                           | 21.0     | 26.9     |
| P600            | 13.2                           | 18.54    | 23.18    |

The effect of surface heat source can also be seen in the obtained melt-pool dimensions presented in **Fig. 2.15**. With the increase of  $A$ , melt-pool dimensions are increasing drastically and over-predicting by huge magnitude. The model with  $A = 0.25$  gives correct temperature evolution at the thermocouple location, but even with this value, melt-pool dimensions predicted are much higher than experiment results. The computation time for this analysis using TH-2D was 13 min which is 7% faster than the analysis using DE heat source. It is evident that surface heat source (TH-2D) is not suitable for LDED process due to the fact that obtained melt-pool is volumetric in nature and can be in mm's in-magnitude.

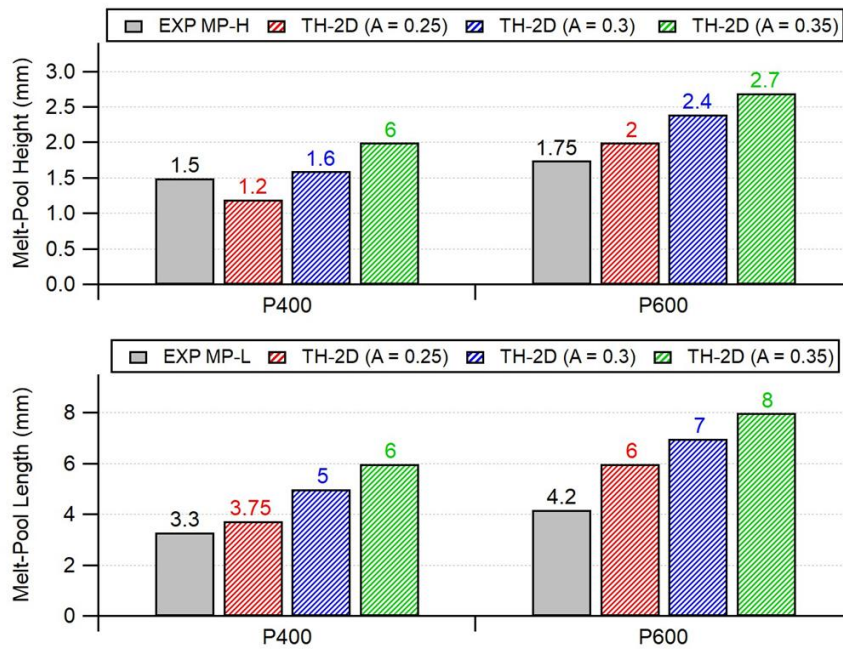


Figure 2. 15: Comparison of melt-pool dimensions between numerical model employing TH- 2D heat source with different laser absorption efficiency using Quiet/Active method and experiment results

Implementation of Quiet/Active material activation strategy in COMSOL Multiphysics® 5.6 is relatively the simplest. DE heat source seems to be working correctly for LDED process. However, all the deposition region is a part of computation domain from the start of computation analysis thereby increasing the computation time. To overcome this issue, Hybrid activation strategy is implemented as explained in the next section.

## 2.5.2 Hybrid Activation Method

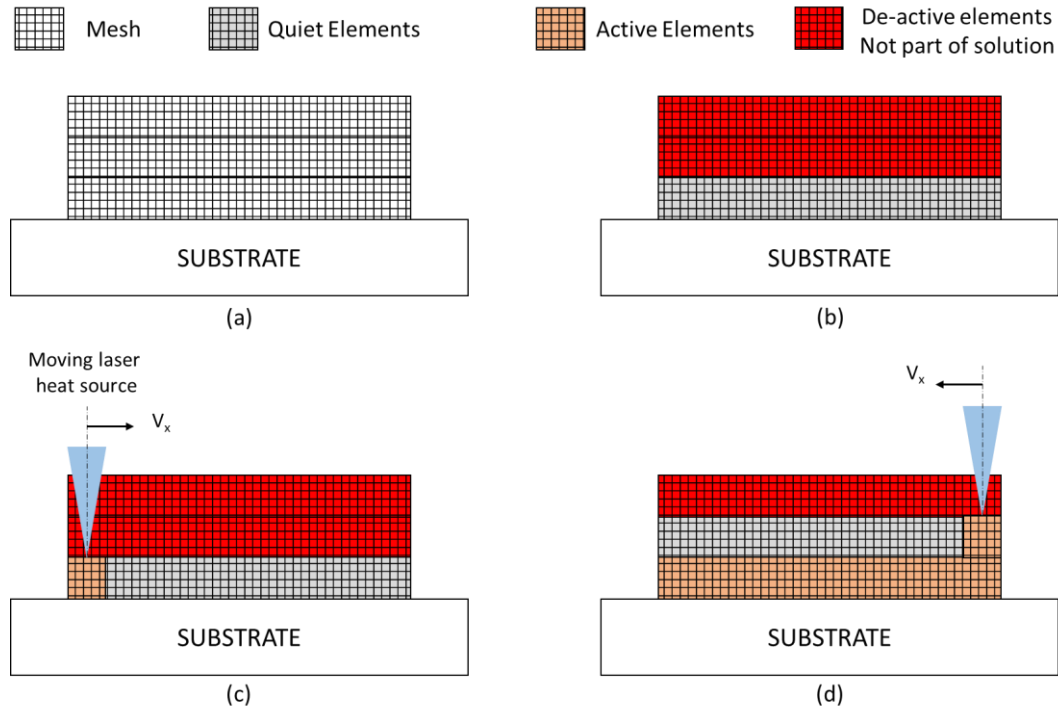


Figure 2. 16: (a) Meshing: Computation domain at start of computation is only substrate  
 (b) Quiet Materials Assigned to 1st layer and all other layers are de-activated (not part of computation domain)  
 (c) Material Switch Quiet/Active (1<sup>st</sup> layer), all other layers are de-active  
 (d) Material Switch Quiet/Active (2<sup>nd</sup> layer), Layer 1 already activated, all other layers are de-active

To overcome the problem stated in Quiet/Active Material Activation Strategy, Hybrid Activation method is developed and implemented in COMSOL Multiphysics® 5.6 that takes the advantage of Quiet/Active and Element Birth material activation strategy. At the start of the computational analysis, only substrate is considered in the computation domain. Then 1<sup>st</sup> layer is added to the computation domain and the 1<sup>st</sup> layer is assigned with Quiet material Properties. Then, according to the activation criteria that follows the laser scan, material state is switched from quiet to active. After the deposition of 1<sup>st</sup> layer, 2<sup>nd</sup> layer is added to computation domain and is assigned Quiet material properties and then switched to active once the activation criteria given in **Eq. 2.15** are fulfilled. This cycle is repeated until all the layers are numerically computed. A detailed schematic of Hybrid Method is shown in **Fig. 2.16**.

### 2.5.2.1 Hybrid Activation model results and discussion

Fig 2.17 shows the complete process simulation chain starting from CAD, metal deposition modeling following the trajectory and finish this step repeatedly for all layers. Here, it can be seen clearly that Hybrid Activation

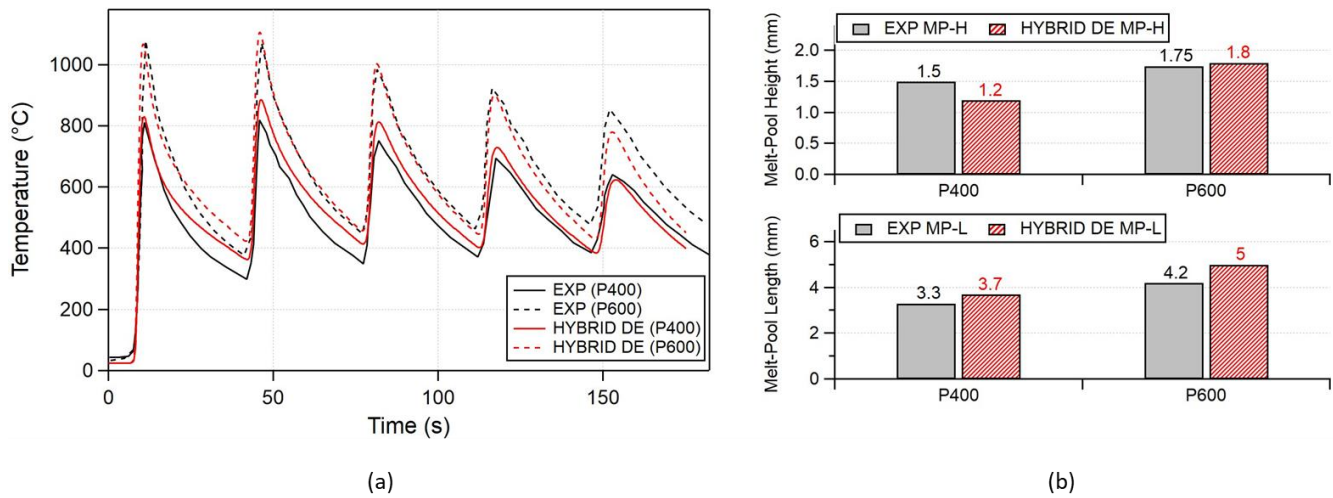


Figure 2. 18: Comparison of Numerical model employing DE heat source using Hybrid Activation method with experiment results (a) Temperature evolution at TC location (b) Melt-pool dimensions

method is correctly in COMSOL Multiphysics® 5.6. As shown in Fig. 2.17 (top-right), during the deposition of layer1, only layer 1 and substrate is part of the computation domain. During layer 2 deposition as shown in Fig. 2.17 (middle-left), now layer 2 is also a part of computation domain and material is activated from quiet to active given the activation criteria is fulfilled. This process is repeated for layer 3, 4, and 5, until the process is finished.

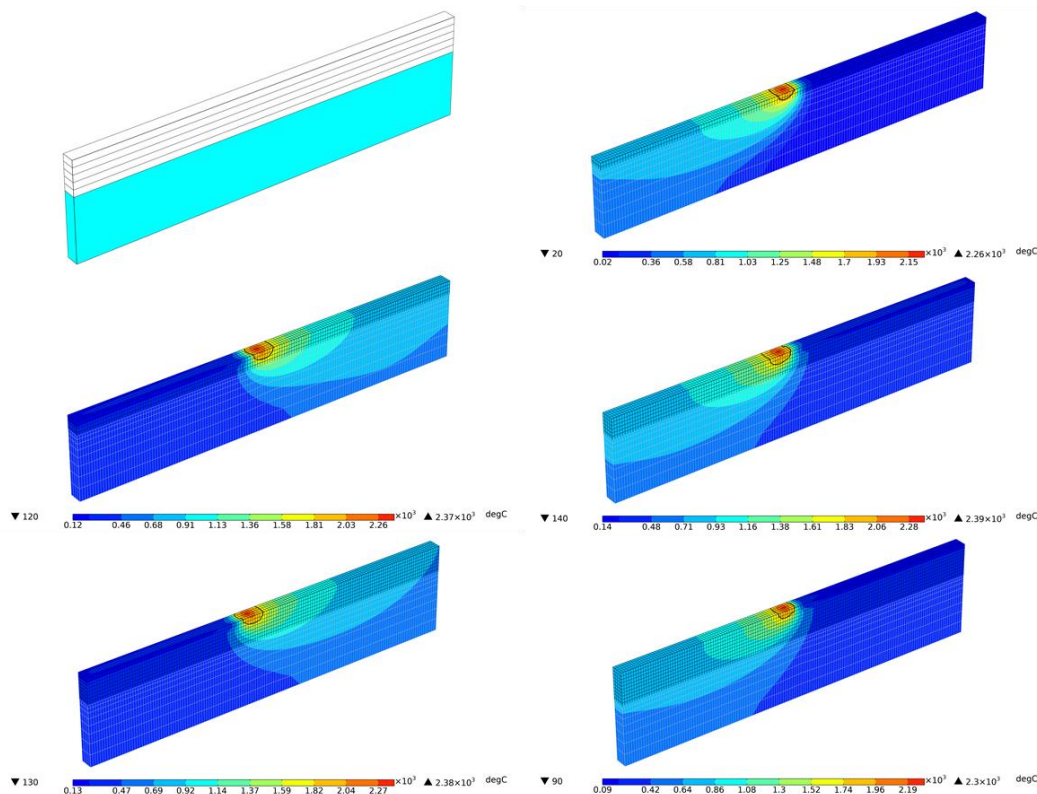


Figure 2. 17: Description of the modeling chain from design to process simulation using Hybrid Activation Method. Substrate mesh is shown in grey color and deposition layer's mesh is shown in black color to identify layers build-up.

To verify the thermal model's accuracy using Hybrid Activation method, numerical model's results is compared with experiment results. This comparison is shown in **Fig 2.18**. As discussed previously, DE heat source is the most suitable for LDED, therefore for Hybrid activation method, only DE heat source is employed. As it can be seen in **Fig 2.18**, numerical model is correctly predicting the temperature evolution at thermocouple location and melt-pool dimensions as shown in **Table 2.5**.

Table 2. 5: Computation thermal error at thermocouple location for Hybrid activation method employing DE heat source

| Experiment case | Hybrid Activation Method: Error (%) |
|-----------------|-------------------------------------|
|                 | Double Ellipsoid (DE)               |
|                 | A = 0.35                            |
| P400            | 12.5                                |
| P600            | 11.9                                |

It can be observed that Hybrid activation model with DE heat source have the same identical results as obtained with Quiet/Active method using DE heat source. Both methodologies use the same quiet/active activation method with DE heat source. The only difference is the computation domain. However, the *computation time for this analysis using DE heat source was 16 min for 5 layers*, that is 14% higher than Quiet/Active method. It is contrary to the expectation, because, in the literature, it has been demonstrated that this methodology leads to reduction in computation time, because at every computational time step, only present layer and already activated layers are part of computation domain. The elements that are not activated present in all the layers above the present layer are not part of computation domain. This results in reduction of computation time and can be reduced much higher if the number of layers in the fabricated part is high i.e., in LDED technology. However, in COMSOL Multiphysics® 5.6 this methodology is implemented, but involves a lot of manual work for the implementation. Also, the model is implemented in such a way that it takes a lot of memory storage and does not result in drastic reduction of computation time.

As shown in **Fig 2.19**, the thermal analysis computation is done at once, but this study internally is divided in different study steps. For example, **Study Step 1: LAYER 1** is thermal analysis done for the layer 1 deposition over substrate + layer 1 computation domain. Once this study step is finished, then **Study Step 2: LAYER 2** thermal analysis is done for the layer 2 deposition over substrate + layer 1 & 2 computation domain. Now these two Study steps are done under Study 1 tree, but these study steps have different unique solvers and each solution is stored in different solution store. Therefore, to have a single solution store, that contains the complete solution for the thermal analysis for deposition of layer 1 and 2, these two solutions are then combined with **Study Step 3: LAYER 1 + 2** as shown in **Fig 2.19**. This combine feature is accessible in COMSOL

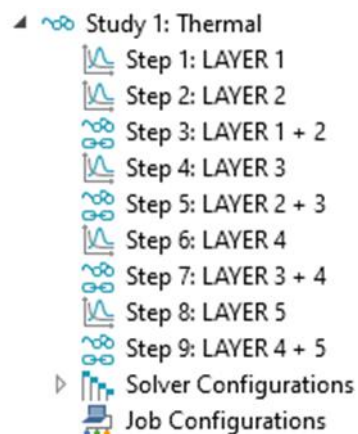


Figure 2. 19: Study Steps employed for Hybrid Activation Model in COMSOL Multiphysics® 5.6

Multiphysics® 5.6 with the name of **COMBINE SOLUTIONS** under the **Study 1: Thermal** tree. Now, this process of unique study step for a respective layer and then combining the present solution with the solution of preceding layer is repeated for the remaining solutions. This was the only way; the author could implement Hybrid Activation method in COMSOL Multiphysics® 5.6 in the present work. Since, in the thermal analysis for **Study Step 1: Thermal**, 5 different solvers are used that takes time for the initialisation and each time solutions have to be combined that also leads to increase of computation time for the analysis. And due to multiple combine solutions, the thermal analysis starts to consume a lot of memory storage on the hard-disk. That's the reason why the computation time was 16 min using Hybrid Activation method which is higher than Quiet/Active method, and it loses its advantage of lesser computation domain due to the above stated reasons as compared to Quiet/Active method which has higher computation domain.

Therefore, Hybrid Activation model as implemented in this work is not feasible for higher number of layers, requiring higher number of study steps equal to number of layers need to be launched and this will lead to memory storage issues. However, Hybrid Activation method can be implemented much easier in other commercial software such as Abaqus or in-house build FEM codes. Furthermore, it is well documented in the literature, that Hybrid Model drastically reduces the computation time as compared to Quiet/Active method. But somehow, author did not find any other way to implement this methodology in COMSOL Multiphysics® 5.6.

### 2.5.3 Arbitrary Lagrangian Eulerian (ALE) Moving Mesh Method

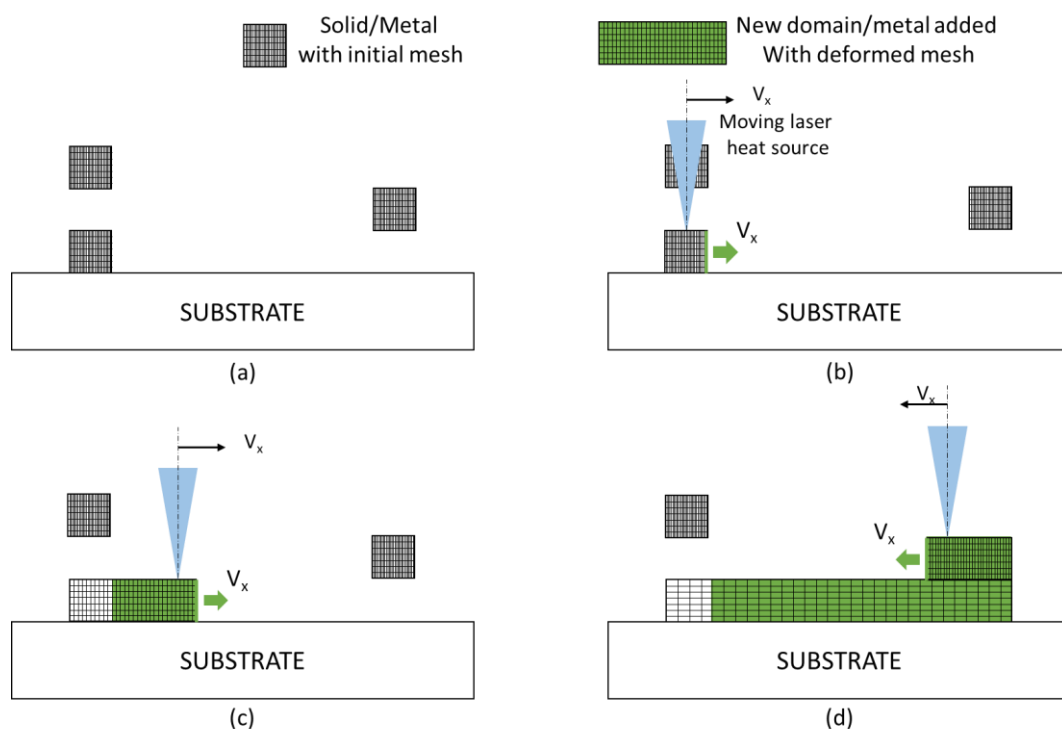


Figure 2. 20: (a): Initial CAD or Original Geometry Model  
 (b) Mesh velocity equal to laser scan speed is prescribed at the side surface  
 (c) Deformed mesh in 1st layer relates to material addition  
 (d) Deformed mesh in 2nd layer relates to material addition

In COMSOL Multiphysics® 5.6, Deformed geometry interface can be used under the Deformed Mesh physics branch. Deformed geometry can be used to study how physics changes when the geometry (represented by mesh, in this interface) changes due to the externally imposed geometry change. The deformed geometry

change can be used in the cases where the original model shrinks or grows by removal or addition of material respectively. In the deformed geometry interface, to account for the boundary's shape changes of the concerned domain and process physics, software employs Arbitrary Lagrangian Eulerian (ALE) method to solve this multi-physics problem. To test this particular functionality, layers are constructed from the initial cuboids that are stretched in the deposition direction of the laser heat source. It has to be noted that Peyre et al. also uses the same method, but to represent material deposition, they impose a vertical displacement of the nodes falling under the moving heat source (Peyre et al., 2017). However, this requires the very important (computation time consuming) re-meshing strategy especially when the number of layers starts to increase.

As shown in **Fig. 2.20**, at the beginning start of each layer/track, a small block equals to laser spot size are designed that represents layer 1 in the original CAD file or original geometric model. Under the deformed geometry interface, all surfaces in the layers are prescribed zero displacement in Y & Z direction. This will not allow the mesh elements to move/deform in Y and Z direction. Then, a process dependent mesh velocity ( $V_{200}$ ) is prescribed in  $\pm X$  direction i.e., deposition strategy on the vertical surface of each block as shown in **Fig 2.20**. A function ***ON-OFF(t)*** is then created that stores the automatic generated surface identifier and mesh velocity as a variable. Only five surface numbers are stored in this function because mesh velocities are assigned to 5 vertical surfaces of 5 blocks representing layers. For example, prescribe mesh velocity for each layer is valid during the active layer's deposition time and all other times, the mesh velocity is assigned zero velocity. This function takes the deposition time and surface identification for all layers into account. As shown in **Fig 2.20(c)**, as the mesh velocity is prescribed on the first layer, it starts to deform in the deposition direction representing metal deposition or material addition. This deformation will continue until the if condition of the function ***ON-OFF(t)*** is satisfied. At the end of layer 1's deposition, function ***ON-OFF(t)*** returns zero value (prescribed mesh velocity) for layer 1. Then the function returns layer 2's surface, this leads to the deformation of layer 2 in the deposition direction that represents metal deposition or material addition as shown in **Fig 2.20(d)**. This process is repeated until all layers are deposited.

The heat transfer modeling is done in the same way as explained in the previous sections of Quiet/Active and Hybrid Activation model. DE heat source is used to model laser heat source and all other heat losses are modeled accordingly.

ALE method elongates the mesh elements in the prescribed  $\pm X$  direction. The optimised meshing strategy explained in **Section 4.2: FEM Mesh**, that takes 4 elements per laser spot size and 2 elements per layer thickness is also taken for the analysis. This element size is found to be sufficient for the thermal analysis and is well documented in the literature. This element size allows a fine balance between sufficiently fine and too fine element size. In the model, the aspect ratio of the mesh elements is shrunk/compress along XZ plane to anticipate for the deformation during the deposition process. The meshing strategy is taken in such a way that the maximum element size is less than 0.5 mm. This element size (same as Quiet/Active or Hybrid Model) is sufficiently high for the melt-pool region to provide smooth and stable evolution of temperature without any convergence issues.

### 2.5.3.1 ALE model results and discussion

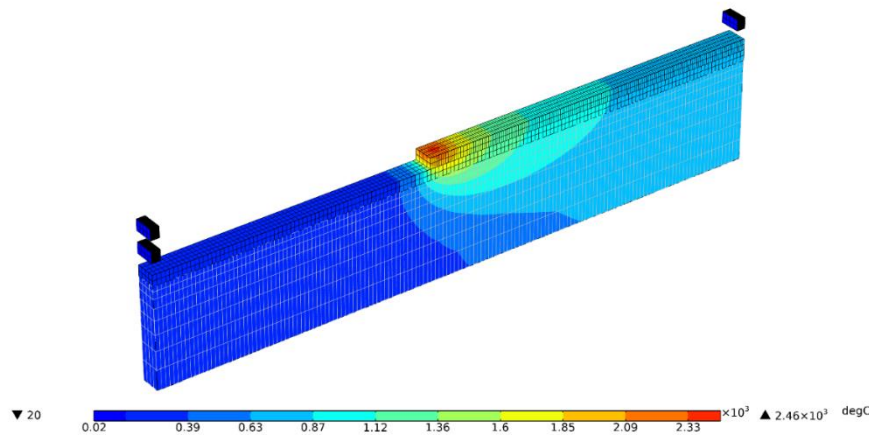


Figure 2. 21: Heat transfer analysis during 2nd layer deposition with ALE method implemented correctly

As shown in **Fig 2.21**, ALE method for metal deposition is implemented successfully in COMSOL *Multiphysics*® 5.6. During the deposition of layer 2, following the deposition strategy, mesh for the current layer i.e., 2, are elongating and mesh elements for layer 1 have already elongated/deformed representing metal deposition. The deformed geometry interface seems to be correctly coupled with heat transfer physics.

The thermal model with DE heat source is implemented and working correctly. **Fig 2.22** shows the complete process simulation chain starting from CAD, metal deposition modeling following the trajectory and finish this step repeatedly for all layers using ALE method.

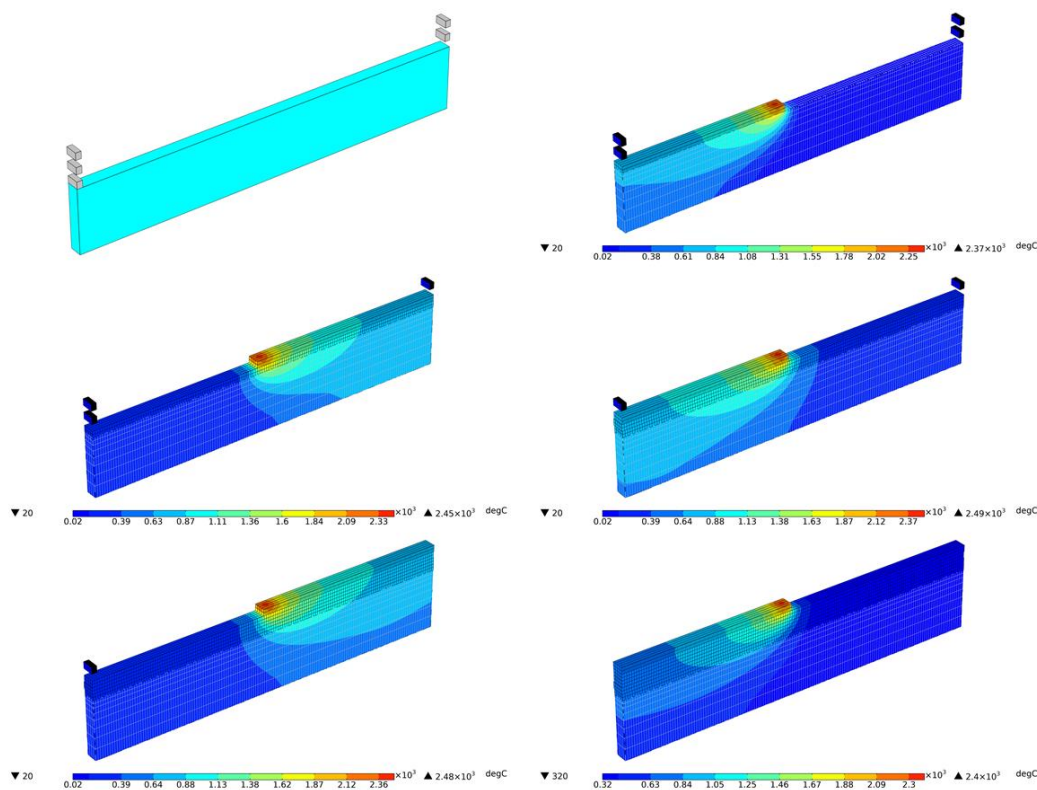


Figure 2. 22: Description of the modeling chain from design to process simulation of 5 layers using ALE Method using DE heat source for  $P = 400 \text{ W}$  and  $V_s = 200 \text{ mm/min}$

To verify the thermal model's accuracy using ALE method, numerical model's results is compared with experiment results. This comparison is shown in **Fig 2.23**. As discussed previously, DE heat source is the most suitable for LDED process, therefore for ALE method, only DE heat source is employed. As it can be seen in **Fig**

2.23, numerical model is correctly predicting the temperature evolution at thermocouple location and melt-pool dimensions.

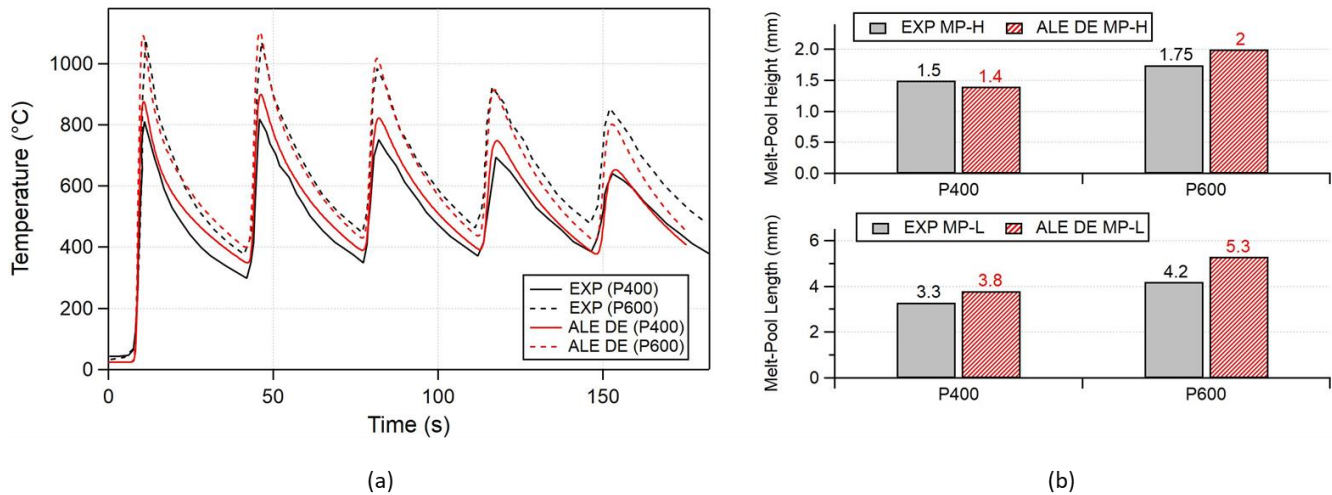


Figure 2. 23: Comparison of Numerical model employing DE heat source using ALE method with experiment results (a) Temperature evolution at TC location (b) Melt-pool dimensions

The thermal results obtained with ALE method are almost the same as obtained in Quiet/Active and Hybrid Activation method as shown in **Table 2.6**.

Table 2. 6: Computation thermal error at thermocouple location for ALE method employing DE heat source

| Experiment case | ALE Method: Error (%) |
|-----------------|-----------------------|
|                 | Double Ellipsoid (DE) |
|                 | A = 0.35              |
| P400            | 14.2                  |
| P600            | 11.9                  |

However, the computation time for this analysis using DE heat source for 5 layers was 19 min, that is 36% higher than Quiet/Active method. This is due to the fact that geometry deformation is done using the ALE method that is inherently expensive by nature. Also, ALE method involves a lot of manual handling like mesh definition, mesh velocities and takes a big effort to solve the analysis without convergence issues. For the mechanical model, mesh optimisation will be even more difficult and it will have potential issues in convergence for mechanical analysis. For LDED process, that involves large deposition length, ALE method is not robust & versatile enough to handle all these complex phenomena.

## 2.6 Conclusions

As LDED is a material addition process, it is a necessity to have a robust and versatile metal deposition model to perform a thermal or thermo-mechanical analysis. In this chapter, different metal deposition models were investigated to find out the suitable model for LDED. Thermal model with different numerical heat source and metal deposition strategies are developed, analyzed and compared with literature experiment results. Following conclusions are done:

- Volumetric heat source is essential to model laser heat source for LDED process as the obtained layer thickness is in millimeters. Surface heat source is not capable to obtain the correct thermal fields for LDED process.

- Volumetric DE heat source is the best choice for LDED process that correctly captures the melt-pool dimensions and shape. Also, thermal fields obtained in the melt-pool are correctly distributed and stable.
- Quiet/Active material activation method is the easiest to develop and implement in COMSOL *Multiphysics*® 5.6. It yields accurate results and is robust enough to handle complex multi-physics phenomenon for large parts without having memory issues.
- Hybrid activation method's implementation in COMSOL *Multiphysics*® 5.6 requires a lot of manual handling. It yields accurate results, but also creates memory issues and will be impossible to use for LDED parts that is the aim of the present research.
- ALE method as applied in COMSOL to our layer-configuration seems to be not suitable for large-part simulation.

*Therefore, it is concluded that for this thesis work, Quiet/Active Material activation method with Double Ellipsoid heat source model should be employed for thermo-mechanical model.*

# Chapter 3: Thermal Model for LDED<sup>1</sup>

|   |    |
|---|----|
| Chapter 3: Thermal Model for LDED.....                | 58 |
| 3.1 Introduction.....                                 | 59 |
| 3.2 Modeling approach.....                            | 59 |
| 3.2.1 Thermal analysis .....                          | 59 |
| 3.2.2 Heat source models .....                        | 60 |
| 3.3 Experiment Set-Up.....                            | 62 |
| 3.3.1 Temperature measurement.....                    | 65 |
| 3.3.2 Melt-pool measurement.....                      | 65 |
| 3.3.3 Microstructure analysis.....                    | 66 |
| 3.4 Numerical implementation.....                     | 68 |
| 3.4.1 FEA solver.....                                 | 68 |
| 3.4.2 FEM mesh .....                                  | 68 |
| 3.4.3 Material deposition modeling.....               | 68 |
| 3.4.4 Model calibration and boundary conditions.....  | 69 |
| 3.5 Modeling results and discussion.....              | 69 |
| 3.5.1 Model with Double Ellipsoid heat source .....   | 69 |
| 3.5.2 Model with Elongated Ellipsoid heat source..... | 73 |
| 3.5.3 Correction Factor .....                         | 78 |
| 3.5.4 Correlation .....                               | 81 |
| 3.6 Conclusions.....                                  | 84 |

---

<sup>1</sup> The work presented in this particular chapter has already been published: Vaibhav Nain, Thierry Engel, Muriel Carin, Didier Boisselier, and Lucas Seguy. 2021. "Development of an Elongated Ellipsoid Heat Source Model to Reduce Computation Time for Directed Energy Deposition Process." *Frontiers in Materials* 8: 512. <https://doi.org/10.3389/fmats.2021.747389>.

## 3.1 Introduction

The objective of the present chapter is to develop a thermal model for LDED process with Stainless Steel 316L (SS 316L) material. The thermal model should also take into account the large-part size feature possible in LDED. Therefore, the proposed model also justifies its feasibility to model large-part size. Finally, this model is compared with experiment results carried out at Irepa Laser for different process parameters, to justify model's versatility and accuracy. SS 316L material is chosen as it is one of the primary materials currently used in the LDED industry. Also, within PAMPRDO project framework, only SS 316L material is used for the development of LDED process. This present work comes under the PAMPROD project and is also funded under this project. Therefore, in this chapter, a detailed explanation is presented in the development of thermal model dedicated for LDED process that has the possibility of simulating large-size parts.

In the previous Chapter i.e., Chapter 2, it has been demonstrated that Double Ellipsoid (DE) equivalent heat source works efficiently to model input laser energy for LDED process and is validated with literature experiment results for Ti-6Al-4V. Also, it has been concluded in Chapter 2 that for the present work, to model metal deposition for LDED process, Quiet/Active material activation is the most practical numerical strategy in terms of features like computational accuracy, speed, and ease of implementation in FEM codes. Therefore, in Chapter 3, for a part-scale conduction-based thermal model, at first a DE heat source model with Quiet/Active material activation method is developed, then calibrated and finally validated for deposition of wall structures of SS 316L experiment results. In addition, to simulate large part size for LDED process, Elongated Ellipsoid (EE) line heat source is developed, calibrated, and validated with the experiment results. EE model demonstrates its capability of simulating large-part by reducing computation time drastically along with taking the deposition strategy into account that plays a big role in the accumulation of distortion in the workpiece.

## 3.2 Modeling approach

The methodology in the proposed numerical model focus on the thermal fields, simplifies the melt-pool fluid and powder dynamics to reduce computational cost. The developed LDED model discretizes the continuous physical process of laser metal deposition into a combination of simulation steps, in which laser travel is considered sequential step-by-step. During each time step, the thermal analysis is performed and the resulting temperature field is saved. The proposed numerical model architecture can be applied to simulate any multi-bead or multi-layer parts.

### 3.2.1 Thermal analysis

As specified in Chapter 2, assuming a Lagrangian frame  $\Omega$  and a material point located by  $\mathbf{r}$  ( $\mathbf{r} \in \Omega$ ) as the reference, the governing equation for computing temperature field can be formulated as follows:

$$\rho(T)C_p(T)\frac{\partial T(\mathbf{r}, t)}{\partial t} = -\nabla \cdot \mathbf{q}(\mathbf{r}, t) + Q(\mathbf{r}, t), \mathbf{r} \in \Omega \quad (3.1)$$

where  $\rho$  is the material density,  $C_p$  is the specific heat capacity,  $T$  is the temperature,  $t$  is the time,  $Q$  is the heat source, and  $\mathbf{q}$  is the heat conduction flux vector, calculated as:

$$\mathbf{q} = -k(T)\nabla T(\mathbf{r}, t) \quad (3.2)$$

Where  $k$  is the thermal conductivity of the material. The latent heat of fusion is taken into account using the same method mentioned in chapter 2, by modifying the specific heat capacity. The thermal conductivity is also modified in the melt pool with an enhancement factor of 2.5 for all experiment cases as specified in Chapter 2. Also, as explained in Chapter 2, losses due to convection and radiation are taken into account and done in the same way as Chapter 2. The values of heat transfer coefficient and emissivity are discussed in Section 3.4.4.

Temperature dependent material properties are taken from literature (Mills, 2002b) as shown in **Fig 3.1**. Linear interpolation is used to calculate the values between the given temperature dataset in the figure. Also, temperatures beyond the fusion temperature, thermal properties are considered constant.

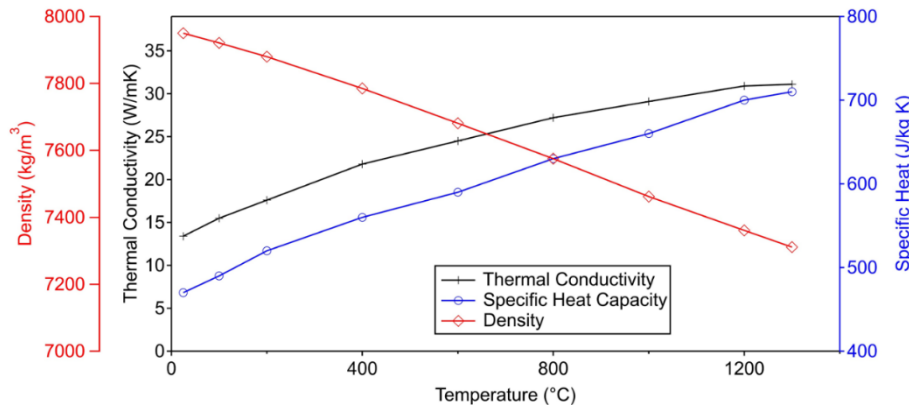


Figure 3. 1: Temperature dependent thermal properties of SS 316L (Mills 2002)

## 3.2.2 Heat source models

In Chapter 2, different types of heat sources (Volumetric DE & Gaussian 3D, and Surface Top-Hat) were studied and it was shown that the DE heat source gives a better agreement with experiment results (melt-pool dimensions and temperature evolution) for Ti-6Al-4V. Therefore, in Chapter 3 for this work, DE heat source is applied for SS 316L as well. Other types of heat sources are also studied such as the Single Ellipsoid (SE) heat input model (Goldak) that can be used to describe an equivalent to the laser heat source (Goldak et al., 1984) as:

$$Q_{SE} = \frac{6\sqrt{3}AP}{abc\pi\sqrt{\pi}} \exp\left(-\frac{3(x - v_s t)^2}{a^2} - \frac{3y^2}{b^2} - \frac{3z^2}{c^2}\right) \quad (3.3)$$

The laser power is  $P$  and the laser absorption efficiency is  $A$ . The value for laser power  $P$  is based on measurement, as will be discussed in Section 3.3. The value of  $A$  is calibrated using the method of reverse calibration by iteratively fitting the simulated temperature field at thermocouple location to match the experiment results described in (Erik R Denlinger et al., 2015).  $x$ ,  $y$  and  $z$  are the local coordinates with the origin centred at the ellipsoid where the heat source reaches the maximum intensity and with a moving velocity  $v_s$ , parameters  $a$ ,  $b$  and  $c$  represent the respective length of the longitudinal, transverse and through the depth semi-axes of the ellipsoid parallel to the local  $x$ ,  $y$  and  $z$  axes. Generally,  $a$  is taken as the melt-pool length,  $b$  is taken as the half width of the deposition bead and  $c$  to the melt pool depth (Erik R Denlinger et al., 2015).

It has been shown previously that, using single ellipsoid heat source predicts a lower temperature gradient at the front and a higher temperature gradient at the trailing edge as compared to the experiments (Goldak et al., 1984). Therefore, as mentioned in Chapter 2, double ellipsoid heat source can be more computationally accurate. Here we recall the expression of the double ellipsoid (DE) Heat Input model initially proposed by (Goldak et al., 1984):

$$Q_{DE} = \frac{6\sqrt{3}APf_{f,r}}{a_{f,r}bc\pi\sqrt{\pi}} \exp\left(-\frac{3(x-v_s t)^2}{a_{f,r}^2} - \frac{3y^2}{b^2} - \frac{3z^2}{c^2}\right) \quad (3.4)$$

where  $f$  is a weighting fraction, that determines the energy partition among the front and rear ellipsoid. Typically, different values are employed in the front and rear of the heat source for the longitudinal axis length  $a$  (Goldak et al., 1984). The orientation of the double ellipsoid (DE) heat source and coordinate system are depicted in Fig 2.5. For the single ellipsoid (SE) heat source the lengths of two ellipsoids are equal ( $a_f = a_r$ ), hence depicting a single ellipsoid.

To accurately model the motion or movement of laser (input heat source), the simulation time increments should be small enough in such a way that the numerical heat source should move less than or equal to half of laser spot size i.e., spot size radius in one-time step (Irwin and Michaleris, 2016). Therefore, in the present work for all cases using Double Ellipsoid Heat Source, computation time-step does not exceed  $R/v_s$ , where  $R$  is laser spot size radius and  $v_s$  is laser source/travel speed. In LDED, track length is big and with the specified computation time increment, it can lead to high computation time. Therefore, to reduce the computation time, an elongated ellipsoid line heat input model can be used that averages the single ellipsoid heat source over its path (Irwin and Michaleris, 2016).

$$Q_{AVERAGE} = \frac{1}{\Delta t} \int_{t_0}^{t_0 + \Delta t} Q_{SE} dt \quad (3.5)$$

where  $t_0$  is the time at beginning of the increment and  $\Delta t$  is the duration of time increment over which SE model is averaged. But this averaging over its path will result in large thermal gradients at the edges of each segment especially when the linear segment is large ( $v_s \Delta t \gg a$ ) (Irwin and Michaleris, 2016). Therefore, to smooth out the discontinuities at the segment edges, elongated ellipsoid model is developed where peak value of the heat input is at the middle of the sub-track or segment. Power density of elongated ellipsoid at the beginning and end of each segment is half of its peak value that results in smooth distribution over successive linear segments. Thus, Elongated Ellipsoid (EE) line heat input model is also used in present work to describe the laser heat source (Irwin and Michaleris, 2016):

$$Q_{EE} = \frac{6\sqrt{3}AP}{\hat{a}bc\pi\sqrt{\pi}} \exp\left(-\frac{3(x-v_s(t+\frac{1}{2}\Delta t))^2}{\hat{a}^2} - \frac{3y^2}{b^2} - \frac{3z^2}{c^2}\right) \quad (3.6)$$

where the length of each elongated ellipsoid sub-track or segment  $\hat{a}$  is (Irwin and Michaleris, 2016):

$$\hat{a} = \frac{v_s \Delta t}{2} \sqrt{\frac{3}{\log 2}} \quad (3.7)$$

The main difference between equations (3.3) and (3.6) are the introduction of elongated length  $\hat{a}$  in place of  $a$ , that stretches the heat distribution in the local  $x$  direction and additional  $(1/2)\Delta t$  which shifts the peak heat input from the end to the middle of the linear segment or sub-track (Irwin and Michaleris, 2016). Also, the double ellipsoid heat source moves continuously along the path replicating laser movement in experiments with computation time step less than  $R/v_s$ , the elongated ellipsoid heat source also move continuously along the path, but enables bigger time steps equal to  $\Delta t$  that results in reduction of computation time. A comparison of the energy distribution with three different heat source models SE, DE and EE is shown in Fig 3.2. A detailed analysis of the Elongated Ellipsoid Heat Source and its functioning is the presented in the reference work (Irwin and Michaleris, 2016).

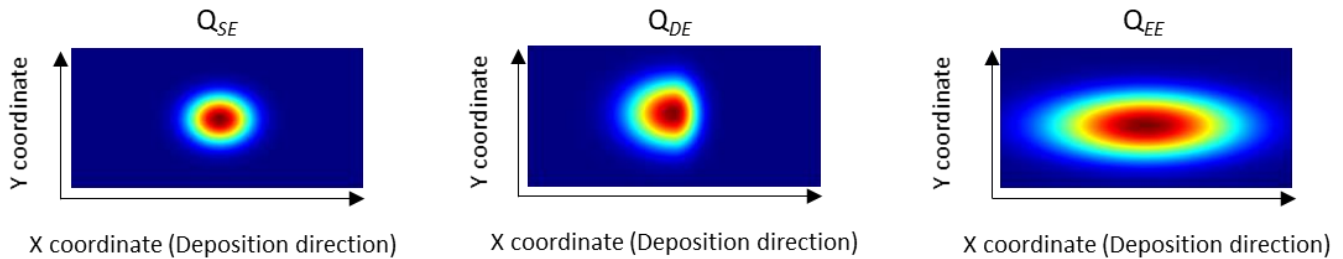


Figure 3. 2: Illustration of power densities of different heat source model

Elongated Ellipsoid heat source model allows the simulation of an entire heat source scan in one time increment instead of hundreds of time increment if using Double Ellipsoid or Single Ellipsoid Heat Source. However, taking large time increments also leads to increase in errors as well (Irwin and Michaleris, 2016). Therefore, the track scan is divided into several linear segments (sub-tracks), for each of which, heat source is applied in one simulation time increment.

### 3.3 Experiment Set-Up

In Chapter 2, experiments were done (literature) with a vertical substrate and thermocouple is placed close to the substrate's top face in order to capture high temperature peaks. However, this is not a representative tooling in the regular LDED process. Therefore, in the present work, the experiments are performed with a conventional tooling of the substrate so that the numerical model can perform and demonstrate its versatility. The modeling approach laid out in Section 2 is applied to simulate the experimental results acquired for SS 316L wall builds done with different sets of experiment in an attempt to capture the thermal behaviour. A detailed explanation of the experiment is provided here. Single wall structures were fabricated on a 100 mm long, 50 mm wide, and 3 mm thick SS 316L substrate (matching material) using a laser-directed energy deposition process. In-house developed MAGIC machine is used for DED system equipped with a 2 kW Diode laser by IPG laser system. Laser and powder are co-focussed at the substrate with laser having a top-hat intensity distribution and incoming powder having gaussian distribution at the co-focussed point.

For all experiment cases, the depositions are performed at a scan speed of 1 m/min with zig-zag deposition strategy and a powder deposition rate of 13 g/min Stainless Steel 316L powder feedstock (Oerlikon, grain size 45-106  $\mu\text{m}$ ). The laser beam spot size was measured to be 2.2 mm in diameter at the part surface. Fig. 3.3(a) shows the schematic of substrate & planned wall build and Fig. 3.3(b) shows DED system with nozzle Fig. 3.3(c), co-axial infra-red camera Fig. 3.3(d) and fixture clamps and Fig. 3.3(e) shows the wall build for case 1.

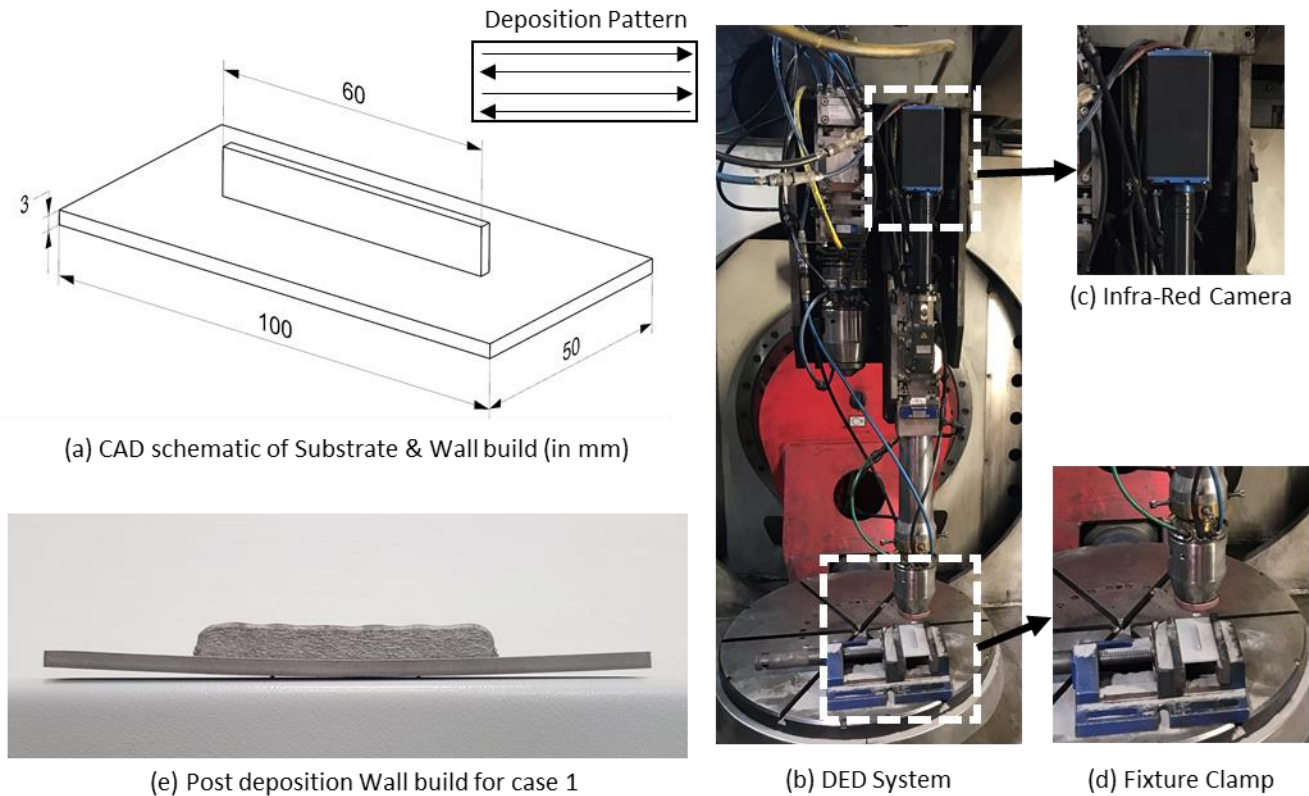


Figure 3. 3: Illustrations of CAD, Experiment Set-Up with sensors and deposited wall

Each wall build is 20 layers high, 1 bead wide, with a longitudinal zig-zag deposition strategy. For the first set of experiments, effect of waiting time between successive layers (dwell time) is studied by fixing laser power 800W and changing the dwell time after the deposition of each layer. Dwell times of 0, 5, 10 and 30 s were used for each layer to expose the parts to different cooling times. Effect of dwell time plays a critical role in industrial LDED part application, because it allows to achieve process stability by obtaining uniform heat temperature in the workpiece at the start of deposition of a new layer. If LDED process is employed without dwell time, deposition of new layer starts at a region that has much higher temperature and can lead to issues like varying height, over-heating zones etc. Also, it adversely impacts the microstructure, stresses and distortion. Therefore, it is well established practise in LDED to employ dwell time. For the numerical model, it provides a good opportunity to demonstrate that model is well calibrated to model heat losses accounting for cooling phenomenon during dwell period.

In the second set of experiments, effect of laser power is studied by keeping a dwell time of 10s and varying the laser power to 800, 1000, 1200 and 1400W. Laser scan speed is set to 1m/min in both tests. Laser power also plays a critical role in LDED process in the industry because it influences the material deposition rate and is widely used to augment the material deposition rate to deposit large-part for LDED process. Therefore, numerical model, it provides a good opportunity to demonstrate that model is well calibrated to model different melt-pool temperature and conduction-heat transfer in the workpiece. **Table 3.1** summarizes the sets of experiments and cases.

Table 3. 1: Description of the cases and process parameters used in the present work

| Experiment Set 1: Effect of dwell time (scan speed 1 m/min)  |                |                 |
|--|----------------|-----------------|
| Case   | Dwell time (s) | Laser Power (W) |
| D1: D0 P800  | 0              | 800             |
| D2: D5 P800  | 5              | 800             |
| D3: D10 P800   | 10             | 800             |
| D4: D30 P800   | 30             | 800             |
| Experiment Set 2: Effect of Laser Power (scan speed 1 m/min) |                |                 |
| Case   | Dwell time (s) | Laser Power (W) |
| P1: D10 P800   | 10             | 800             |
| P2: D10 P1000  | 10             | 1000            |
| P3: D10 P1200  | 10             | 1200            |
| P4: D10 P1400  | 10             | 1400            |

For the first set of experiment (effect of dwell time), wall dimensions such as track width and height do not vary at all as shown in Fig 3.4 (a) & (c). However, for the second set of experiments (effect of laser power), track width and height are increasing with an increase in laser power as shown in Fig 3.4 (b) & (d). With different process parameters, wall dimensions are also varying. Track width and height are varying with change of laser power, however there is no change with change of dwell time.

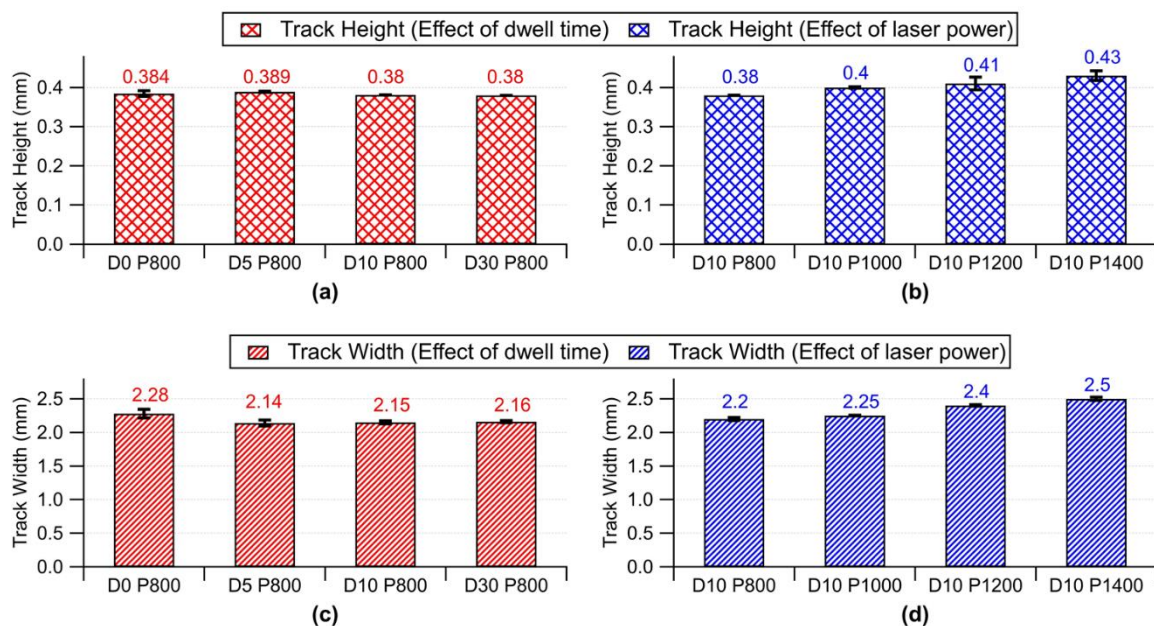


Figure 3. 4: Wall dimensions obtained with different experiment cases

### 3.3.1 Temperature measurement

*In situ* temperature is measured at two different locations on the bottom face of substrate, as shown in **Fig. 3.5**, using Omega GG-K-30 type K thermocouples (TC) of 250  $\mu\text{m}$  diameter. The thermocouples have a measurement uncertainty of  $\pm 0.75\%$ . TC 1 and TC 2 are located on the bottom surface of the substrate along the deposition path. At these positions, thermocouples record the peak temperature gradient as they are perfectly aligned to the deposition path and not placed transversally to the center axis. However, as will be discussed in Chapter 5, more experiments are done with TC placed transversal to the center axis to capture the temperature gradient along the transversal axis as well. The thermocouple signals are read by National Instruments modules 9213. The module record data in Signal Express at a sampling rate of 200 Hz.

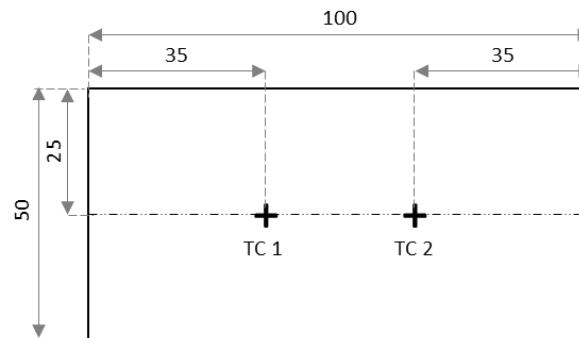


Figure 3. 5: Thermocouple location at bottom of substrate

Substrate thickness is chosen as 3 mm that allows the surface temperature measurement to be sufficiently high enough to have a certain sensitivity with change of process parameters. Thermocouple are placed at the bottom face of the substrate just below the deposition zone (centred on the deposition axis) so that it can capture the maximum thermal evolution. Thermocouple are placed at the bottom face instead of top face of the substrate so that it can be protected from the adverse effects of carrying gas argon and incoming powder flow. Incoming argon and powder hamper the positioning of thermocouple near the deposition zone as it leads to removal of thermocouple contact with the substrate. Also, incoming argon gas creates unwanted noise signal if thermocouple is placed near the deposition zone. One solution is to provide safety brackets around the thermocouple to protect it from the powder splashes and argon. This solution however makes the experiment data acquisition procedure more complicated that is contrary to the objective of this work. The main idea is to develop a simple, fast and repeatable procedure for different process parameters to acquire experiment data.

### 3.3.2 Melt-pool measurement

An Infra-Red imaging camera (NIT system) is used to capture the melt-pool radiation and the images are analysed with the Igor pro software to estimate the melt-pool dimensions and their variations. Image acquisition was done at a sampling rate of 200 fps that makes a movie of about 26 thousand images to manage as shown in **Fig. 3.6**. Interesting parts (construction periods) are extracted from the film and analysed with an Analyse Particles Image routine in order to give the evolution of the melt-pool width (MP-W) and the melt-pool length (MP-L) all over the process, expressed in pixel and based on a specific contour level (L).

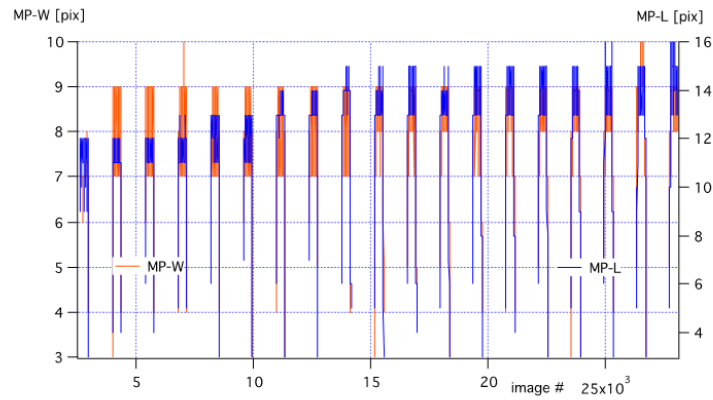


Figure 3. 6: Image analysis during deposition of 42 layers

In **Fig. 3.6**, we see that both dimensions are stabilized after about 8 layers. The contour level (L) is taken in accordance with the measured melt-pool width (MP-W) knowing the pixel size ( $231\mu\text{m}$ ), and the melt-pool length (MP-L) is deduced from that (**Fig. 3.7a & 3.7b**). **Fig. 3.7a** represents a typical thermal image of the melt pool and **Fig 3.7b** the transverse center profile (reference) and longitudinal center profile of the thermal image. We can notice that the transverse profile is quite symmetrical while the longitudinal profile is somewhat elongated to the rear of the melt-pool (blue curve). This is to connect with the double ellipsoid distribution of the source heat source.

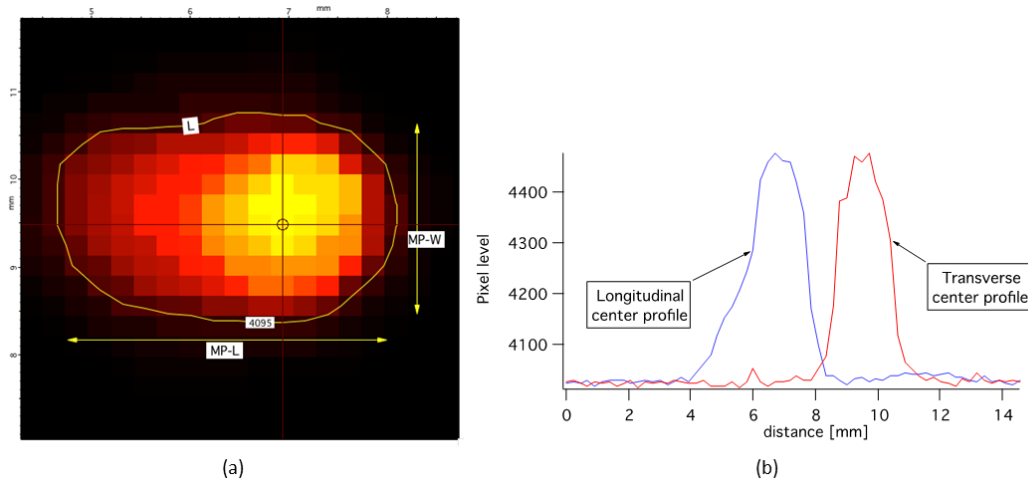


Figure 3. 7: Typical dimensions of in-situ melt-pool length and width based on the contour level L

### 3.3.3 Microstructure analysis

Measurement of melt-pool dilution is done post the deposition process. Sample is cut at two different locations, surface is polished and chemically etched with Oxalic Acid reagent. Once the desirable level of polishing is achieved, then the sample is analyzed in the microscope to measure melt-pool dilution. The laser penetration depth was measured for each case by sectioning as recommended in (Goldak et al., 1984) and illustrated in the macrograph shown in **Fig. 3.8**.

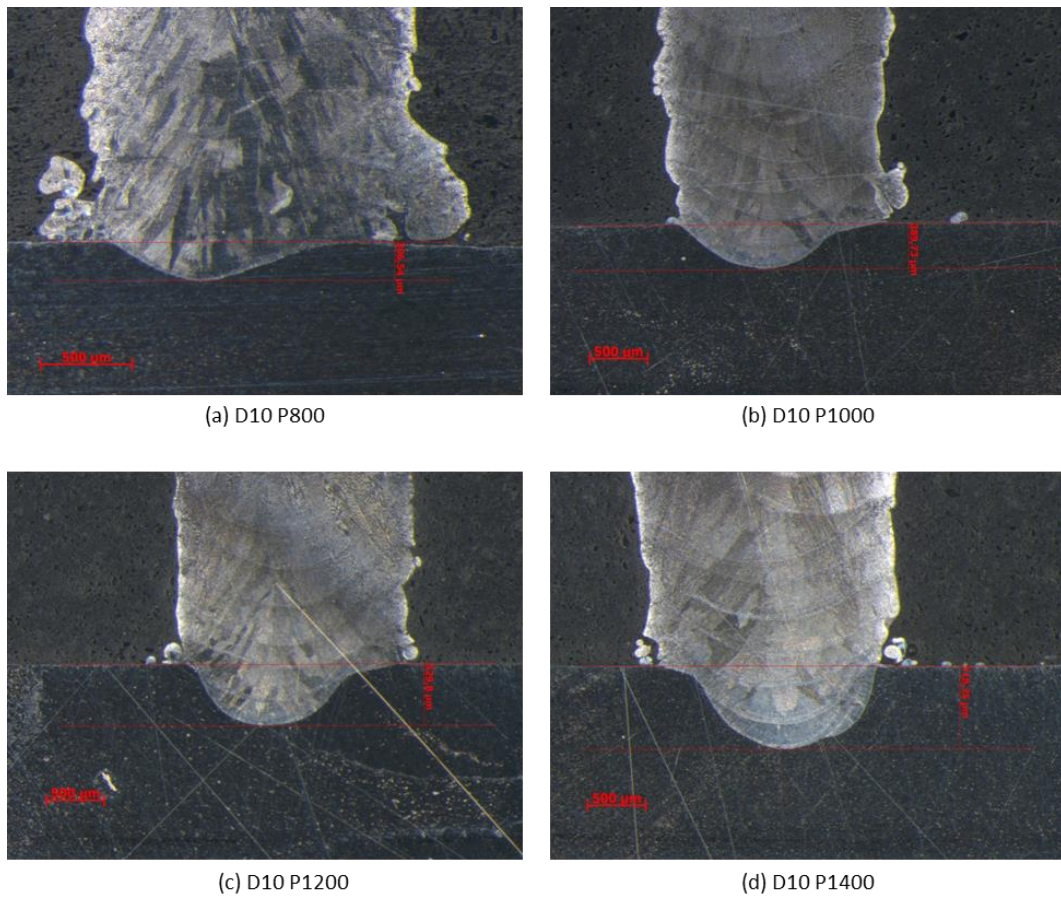


Figure 3. 8: Melt-pool dilution analysis for experiment cases (effect of laser power)

The melt-pool dimensions obtained from image analysis and micro-structure analysis are presented in Fig 3.9. These values given in the Fig 3.9 are then used to calibrate the values of numerical heat source parameters as discussed in previous section.

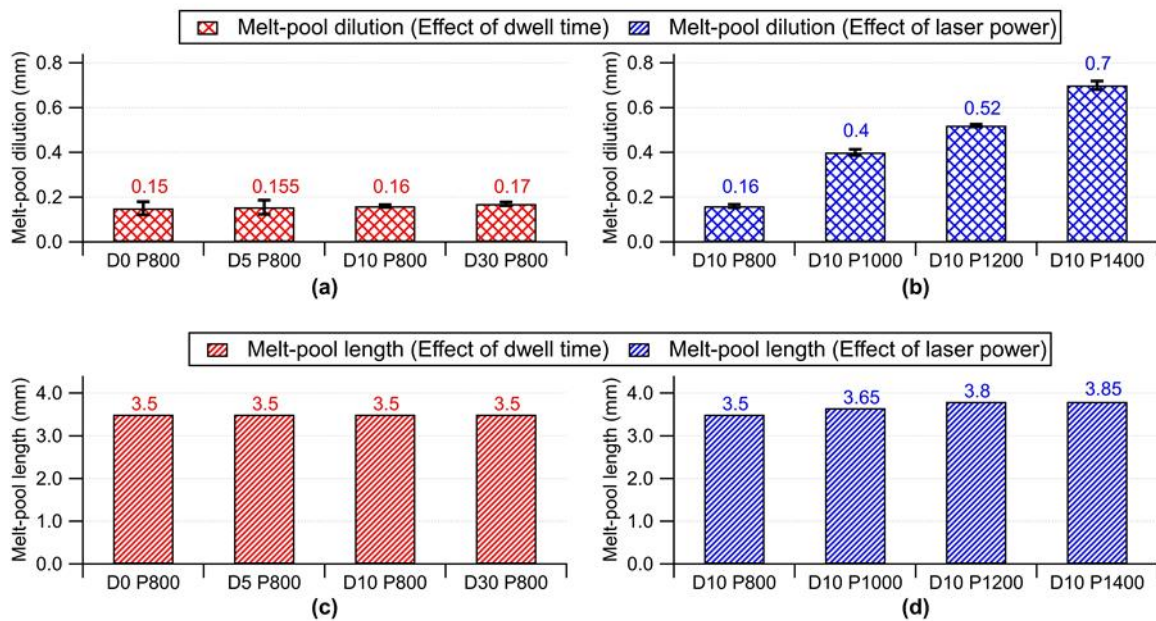


Figure 3. 9: Experimental measurement of melt-pool dimensions for all experiment cases

## 3.4 Numerical implementation

### 3.4.1 FEA solver

The FEM analysis is performed using COMSOL Multiphysics based solver (PARDISO) with the implicit Backward Differentiation Formula (BDF) time stepping method. Adaptive time stepping method is employed rather than strict formulation with maximum time step of  $R/v_s$  for DE and  $\Delta t$  for EE heat sources. The solver is further adapted specifically to model additive manufacturing technologies in the present work. All simulation cases are performed on an Intel Xeon W-2275, 16 cores, with 128 GB RAM workstation.

### 3.4.2 FEM mesh

**Fig. 3.10** displays the three-dimensional finite element mesh, used for the thermal model. The same mesh is used for all cases and for different Heat Source models used in the present work. The mesh contains 33,852 Hex-8 elements and 49,790 nodes. Hex-8 elements were chosen because it has been proved that Hex-8 elements gives more accurate results as compared to linear tetrahedral elements for the plastic deformation (Benzley et al., 1995), therefore to have same mesh for thermal & mechanical analysis in future work, Hex-8 elements were used. The elements for the deposited material are allotted as 3 per laser spot size and 2 per deposition thickness, making the elements  $0.75 \text{ mm} \times 0.75 \text{ mm} \times 0.19 \text{ mm}$  in volume for experiment case 1, but varies for different experiment cases as track geometry changes. The mesh is coarsened at the substrate as it moves away from the wall builds. A mesh convergence study was done using three different mesh strategies to confirm the accuracy of thermal analysis.

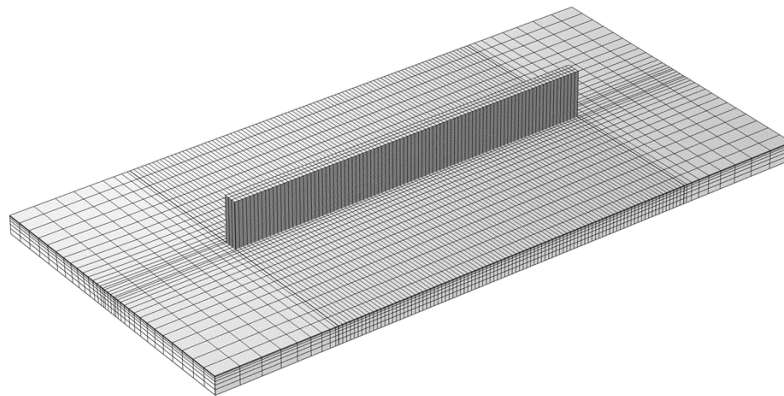


Figure 3. 10: Finite Element Mesh of substrate and wall builds

### 3.4.3 Material deposition modeling

As explained in Chapter 2, the “quiet” element activation method is used to simulate the deposition of material during the DED process. The elements that represent the wall builds are pre-existing at the beginning of the analysis as shown in **Fig. 3.10**.

For the elongated ellipsoid line heat input model, material activation is done in the same way of heat source intensity as explained above, but in this case only the activation domain is larger over the deposition path. If the evaluated heat source value at any Gauss point is greater than 50% of the peak intensity, the element turned to active state. The activation criteria of 50% in the deposition direction is explained in the further

sections. Material is activated in the form of sub-track that takes one time increment to activate the particular sub-track and moves to activate the next sub-track in next time increment.

$$\exp \left( -\frac{3(x - v_s(t_0 + \frac{1}{2}\Delta t))^2}{\hat{a}^2} \right) \geq 50\% \quad (3.8)$$

### 3.4.4 Model calibration and boundary conditions

To simplify the model, deposited wall build is considered to be a flat rectangular shape with constant layer height and width. This is contrary to the experiments as layer height changes in the few first layers and then reaches a uniform layer thickness. As discussed previously, to develop an accurate thermal model, certain input parameters have to be calibrated against experiment results. The laser absorption efficiency ( $A$ ) is taken as 0.4 with reverse calibration of fitting simulated temperature field to experiment results at thermocouple location iteratively as suggested in (Michaleris, 2014). Also, for all experiment cases, as laser spot size is 2.2 mm, laser spot size radius is taken as 1.1 mm. The double ellipsoid heat source dimensions parameters are dependent on experiment cases but follow the same rule i.e., front ellipsoid length  $a_f = W/2$  and  $a_r = 2a_f$ ,  $b = W/2$  and  $c = H + MP_D$ , that represent the double ellipsoid dimensions to be almost equal to experiment melt-pool dimensions for each experiment case. Emissivity ( $\epsilon$ ) is temperature dependent, but mean value of 0.6 is taken as widely reported in the literature (Biegler et al., 2018a). The convective heat transfer ( $h$ ) coefficient is temperature dependent, but a mean value is taken at the substrate  $h = 5 (W.m^{-2}.K^{-1})$  and to consider the effect of forced convection due to the powder carrying argon gas at the wall builds, average convective heat transfer coefficient of  $h = 25 (W.m^{-2}.K^{-1})$  is taken as widely reported in the literature that it can be in the range of  $h = 20 - 60 (W.m^{-2}.K^{-1})$  (Heigel et al., 2015). At the clamped surfaces, the substrate is in contact with metallic fixtures clamps shown in Fig 1 (d). In the numerical model, to reduce the computation time, fixtures clamp is not included, therefore for these surfaces, a higher heat loss is modelled through conductive to convective equivalent heat loss expression similar to Newton's law of cooling Eq. 2.4. The thermal conductance at the contact surfaces is thus  $h = 150 (W.m^{-2}.K^{-1})$  to model the conductive heat transfer from substrate to the metallic fixture clamps as suggested in (Lu et al., 2019a).

## 3.5 Modeling results and discussion

### 3.5.1 Model with Double Ellipsoid heat source

The Quiet/Active material activation is well implemented in the model as can be seen in Fig. 3.11. Indeed, during the deposition of the current layer, quiet elements of the current layer and elements above are not activated and hence do not contribute to the heat transfer, as the material properties of quiet elements are assigned to a dummy material. For example, as shown in Fig 3.11(a), during the deposition of 5<sup>th</sup> layer, material activation is done correctly and the heat transfer is not getting affected as the quiet elements of 5<sup>th</sup> layer and layers above have very low thermal conductivity. Also, it can be noticed in Fig 3.11(a) and Fig 3.11(b) very clearly that the peak temperatures in the melt-pool and melt-pool dimensions (length & depth) is increasing as number of deposition layers is increasing from 5<sup>th</sup> to 10<sup>th</sup> layer. However, peak temperature and melt-pool dimensions have stabilised after the deposition of 10-15<sup>th</sup> layer as 15<sup>th</sup> and 20<sup>th</sup> layer are experiencing the same peak temperature and melt-pool dimensions. This justifies the claim of stabilising/saturating temperature after the deposition of first few layers and there is no further increase of temperature or melt-

pool dimensions. The current deposition elements and previously deposited layer elements are correctly activated from quiet to active once the activation criteria are satisfied that depends upon the laser travel (Equation 2.15). The input heat source absorptivity and heat losses parameters are kept same for all experiment cases as discussed in previous section Model Calibration. Double Ellipsoid heat source dimensions are dependent on experiment cases and is taken following the rule explained in the previous section Model Calibration. The thermal response of the workpiece is calculated by the DE model and compared to the experimental measurements.

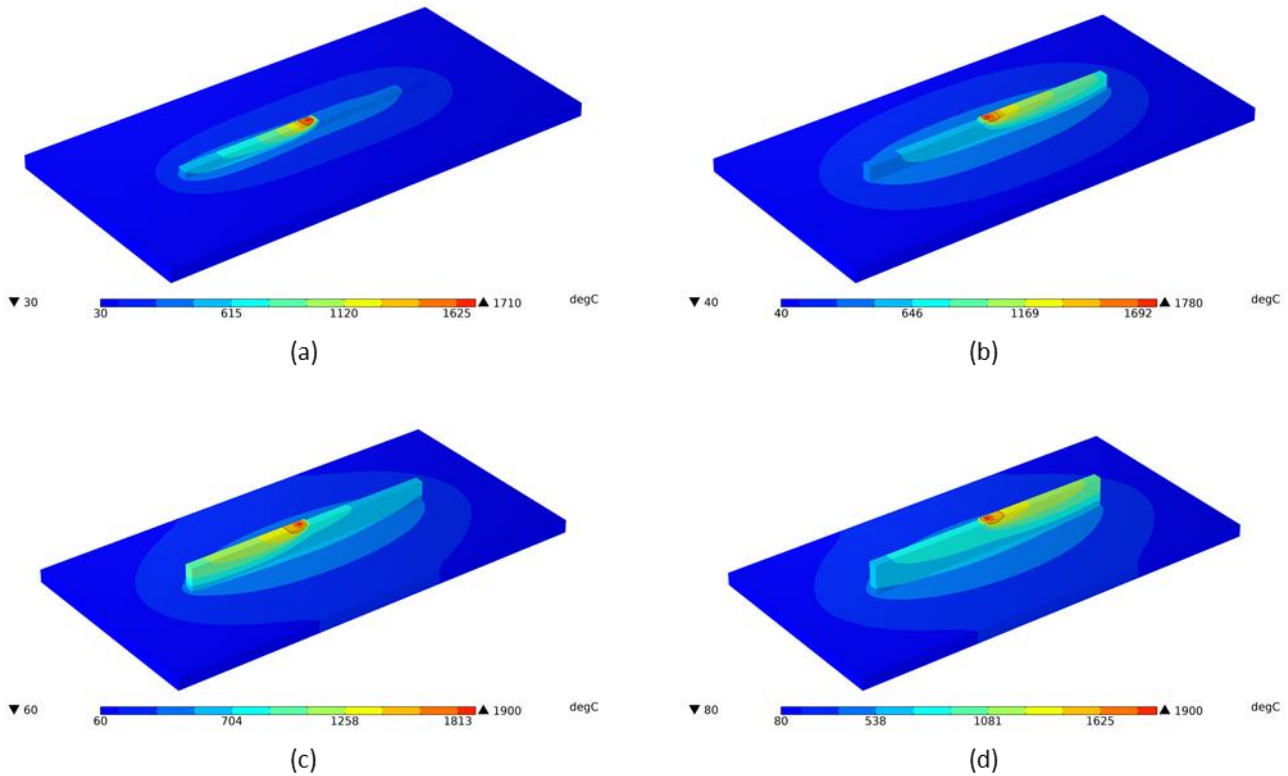


Figure 3. 11: Material deposition using Quiet/Active material activation coupled with temperature distribution for (a) 5<sup>th</sup> layer (b) 10<sup>th</sup> layer (c) 15<sup>th</sup> layer (d) 20<sup>th</sup> layer (final layer)

Fig. 3.12 shows the comparison between experimental results, as measured by thermocouples 1 and 2, and the numerical results at the corresponding nodes in FEM analysis for experiment set 1 (effect of dwell time). As explained in the previous section, due to the experiment set-up, because thermocouple 1 and 2 are at different locations on the substrate but along the deposition line, they record almost same thermal histories with a time offset. Therefore, only Thermocouple 1 results are presented. However, the results obtained from both thermocouples are presented in the Appendix (Chapter 3). Furthermore, it can be seen from the results (Appendix) that both thermocouples record the same temperature evolution, however with a time shift/gap arising due to the scanning speed. This also justifies that thermocouples are aligned and positioned correctly at the desired locations. The thermal response can be classified in 4 different zones depending upon the thermal history. In zone 1, peak temperature for successive build layers increases as layers are building up, in zone 2, peak temperature for successive layers stabilises and there is no further increase of temperature, and in zone 3, peak temperature for successive build layers starts to decrease due to the fact that heat source is moving vertically away from the thermocouple locations and fabricated material starts to increase that also conducts heat leading to the less heat transfer or temperature gradient. In zone 4, once the process is finished, temperature rapidly reduces with respect to time.

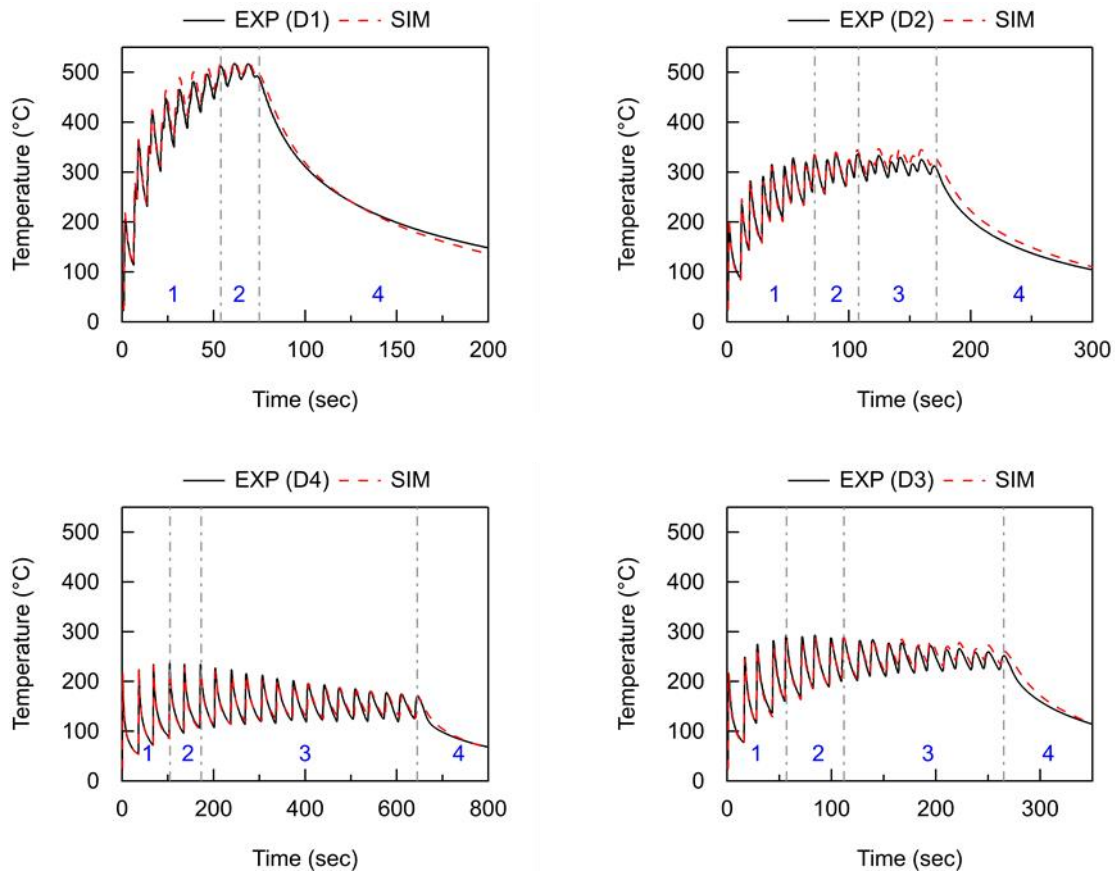


Figure 3. 12: Experiments v/s Simulation using Double Ellipsoid (DE) heat source for experiment cases D1-D4 (Effect of dwell time)

In the experiment set 1, analysis of effect of dwell time is studied, as shown in **Fig. 3.12**. Peak temperature starts to decrease as dwell time increases from 0 s to 30 s. Longer dwell times results in lower peak temperatures of 230 °C with the 30s dwell time (D4), while with 0 s dwell time (D1) exceeding 500 °C. Therefore, dwell time has a strong influence on temperature evolution as well as the peak temperatures obtained during the deposition process. For experiment set 1, analysis of effect of dwell time, it is observed that thermal response is changing drastically, not just in terms of peak temperatures, but also in terms of thermal evolution. **Table 3.2** that counts the number of peaks (or layers) observed in the different zones (Z1 to Z4), the number of layers under Zone 1 are decreasing with an increase of dwell time, depicting peak temperature is stabilising at much earlier deposition stage (number of layers). But, the number of layers under Zone 2 and 3 are increasing with an increase of dwell time, depicting that stabilised peak temperature are maintained for longer duration of deposition. Numerical model with calibrated parameters captures the temperature evolution trend and peak temperatures correctly with change of dwell time.

Table 3. 2: Classification of layers deposition process according to temperature gradient for experiment cases (Effect of dwell time)

| Experiment Case | Number of layers |        |        |
|-----------------|------------------|--------|--------|
|                 | Zone 1           | Zone 2 | Zone 3 |
| D1              | 18               | 2      | 0      |
| D2              | 9                | 4      | 7      |
| D3              | 5                | 4      | 11     |
| D4              | 4                | 2      | 14     |

In experiment set 2, analysis of effect of laser power is studied, as shown in **Fig. 3.13**. Peak temperature keeps on increasing as laser power increases from 800 W to 1400 W. Higher laser power results in higher peak temperatures of 480 °C with 1400 W laser power (P4), and only 280 °C with 800 W laser power (P1). Therefore, laser power has a strong influence on peak temperature, but does not influence the trend of temperature evolution obtained during the deposition process.

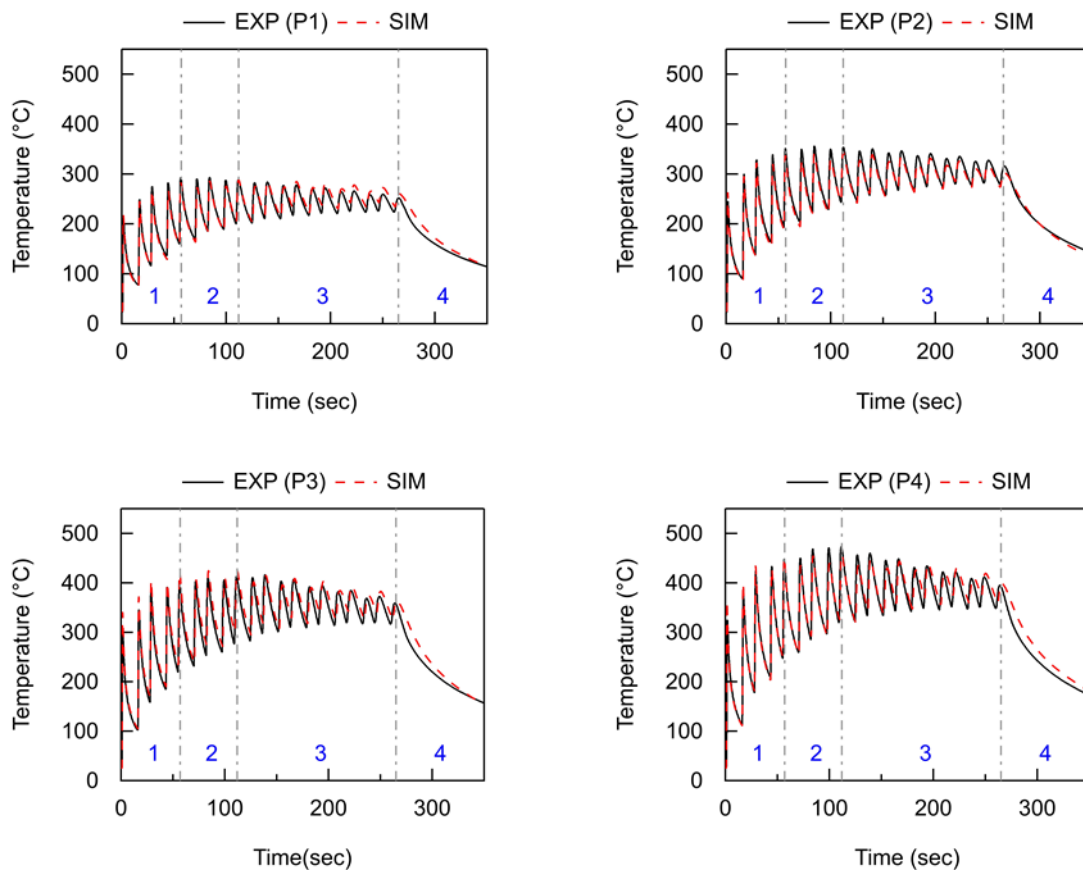


Figure 3. 13: Experiments v/s Simulation using Double Ellipsoid (DE) heat source for experiment cases P1-P4 (Effect of laser power)

For experiment set 2 (analysis of effect of laser power), it is observed that thermal response is changing peak temperatures drastically, but does not influence the thermal gradient. As it can be seen in **Table 3.3**, number of layers under Zone 1, 2 and 3 remains same depicting that temperature trend is lifted upwards (increase of peak temperature). Higher peak temperatures are recorded because of the increase of laser power, but the thermal gradient remains the same. As can be seen in Table 5, peak temperature is stabilised at 5<sup>th</sup> layer, stabilises for next 4 layers and then starts to decrease as heat source is moving vertically away from thermocouple locations for all experiment cases (P1-P4).

Table 3. 3: Classification of layers deposition process according to temperature gradient for experiment cases (Effect of laser power)

| Experiment Case | Number of layers |        |        |
|-----------------|------------------|--------|--------|
|                 | Zone 1           | Zone 2 | Zone 3 |
| P1              | 5                | 4      | 11     |
| P2              | 5                | 4      | 11     |
| P3              | 5                | 4      | 11     |

|    |   |   |    |
|----|---|---|----|
| P4 | 5 | 4 | 11 |
|----|---|---|----|

The results of the transient thermal analyses are in close agreement with the experimental results as can be seen in **Fig. 3.12 and 3.13**. Errors between experiment and simulation results are calculated by comparing instances in time.

$$\% \text{ Error} = \frac{100 \sum_{i=1}^n \left| \frac{(T_{exp})_i - (T_{sim})_i}{(T_{exp})_i} \right|}{n} \quad (3.9)$$

where  $n$  is the total number of simulation time increments between the beginning and end of the deposition,  $i$  is the current time increment,  $T_{sim}$  is the simulated temperature, and  $T_{exp}$  is the measured temperature. The largest error at thermocouple is found to be 3.91%.

**Table 3.4** shows the computation time & percent error at both thermocouples TC1 and TC2 for all cases. For experiment set 1 (D1 to D4), it can be clearly seen that with the increase of dwell time, that leads to increase in number of time increments leading to increase in computation time. For experiment set 2 (P1 to P4), it can be observed that with an increase in laser power, that leads to an increase in simulation peak temperature at the melt-pool region i.e., higher thermal gradient, that leads to slight increase of computation time.

Table 3. 4: Cases examined for Thermal Model Validation (Double Ellipsoid)

| Case | Run Time (min) | % Error |      |
|------|----------------|---------|------|
|      |                | TC 1    | TC 2 |
| 1    | 98             | 2.49    | 1.55 |
| 2    | 135            | 3.41    | 3.37 |
| 3    | 175            | 3.09    | 3.41 |
| 4    | 324            | 3.57    | 3.97 |
| 5    | 175            | 3.09    | 3.41 |
| 6    | 177            | 3.16    | 2.42 |
| 7    | 180            | 3.93    | 2.57 |
| 8    | 182            | 2.81    | 2.53 |

### 3.5.2 Model with Elongated Ellipsoid heat source

To reduce the computation time, elongated ellipsoid model is used to reduce the number of simulation time steps by dividing the complete track in number of linear sub-tracks, with each sub-track is solved in one computation time step. For the sake of comparison of different lengths that are chosen, a dimensionless time increment size  $K_E$  is used.

$$K_E = \frac{v_s \Delta t}{a} \quad (3.10)$$

In DE model, to have a continuous movement of the DE heat source that do not skip any elements over its deposition path, it requires to have  $K_E \leq 1$ . This implies that with this parameter  $K_E = 1$ , DE heat source moves a distance of laser spot beam diameter (laser spot size) because for SE,  $a$  represents melt-pool length. Hence,  $K_E$  parameter provides an idea of how large the computation time increments are taken for the computation analysis using EE heat source model in comparison with the analysis using DE or SE heat source model.

Different track size (sub-track) is chosen for material activation presented in **Table 3.5** and a comparison is done with the experiment results to make a compromise between computation speed and accuracy.

Table 3. 5: Elongated Ellipsoid (EE) heat source parameters used in the present work

| $K_E$ | Computation time step FEM ( $\Delta t$ )<br>(s) | EE length ( $\hat{a}$ )<br>(mm) | No. of sub-tracks per layer<br>(Wall Length/ $\hat{a}$ ) |
|-------|---|---------------------------------|--|
| 0.5   | 0.066   | 1.14                            | 52   |
| 1     | 0.132   | 2.28                            | 26   |
| 4     | 0.538   | 9.15                            | 8  |
| 8     | 1.057   | 18.31                           | 4  |
| 27    | 3.564   | 61.79                           | 1  |

As shown in **Table 3.5** and **Fig 3.14**, 5 different simulation time increments are chosen, where  $K_E = 0.5$  represents heat source movement of  $R$  with a time step of  $R/v_s$ , hence the ellipsoid is not elongated and that is same as in the case of double ellipsoid (DE) heat source. With  $K_E = 4$  value, it represents heat source averaging over a linear-segment (EE length of sub-track) of  $8R$  with a computation/simulation time step of  $8R/v_s$  and  $K_E = 27$  represents heat source averaging over a linear-segment (EE length of sub-track) of  $54R$  with a simulation/computation time step of  $54R/v_s$ , that is averaging over the complete track, activating the complete track and performing heat transfer analysis in 1 simulation time increment.

Each sub-track of length  $\left(\hat{a} = \frac{v_s \Delta t}{2} \sqrt{\frac{3}{\log 2}}\right)$  is activated in 1 computation time step size of  $\Delta t = (K_E \times a)/v_s$ .

Therefore, higher the value of parameter  $K_E$ , higher the size of computation time step and lesser the number of computation time steps required to finish the analysis.

The size of computation time step in the computation model/analysis depends upon the parameter  $K_E$ , that in turn depend upon the size of elongated ellipsoid (EE) length. With  $K_E = 0.5$ , with each computation time increment ( $\Delta t$ ) of 0.066 s, heat source is moving or activating a segment ( $\hat{a}$ ) of 1.14 mm. This will require 52 computation time steps to activate the complete layer. Then with  $K_E = 1$ , with each computation time increment ( $\Delta t$ ) of 0.132 s, heat source is moving or activating a segment ( $\hat{a}$ ) of 2.29 mm. This will require 26 computation time steps to activate the complete layer. So, with an increase in further values of  $K_E$ , size of computation time step and sub-track segment is increasing that is further reducing the number of computation time steps to activate/finish the complete layer.

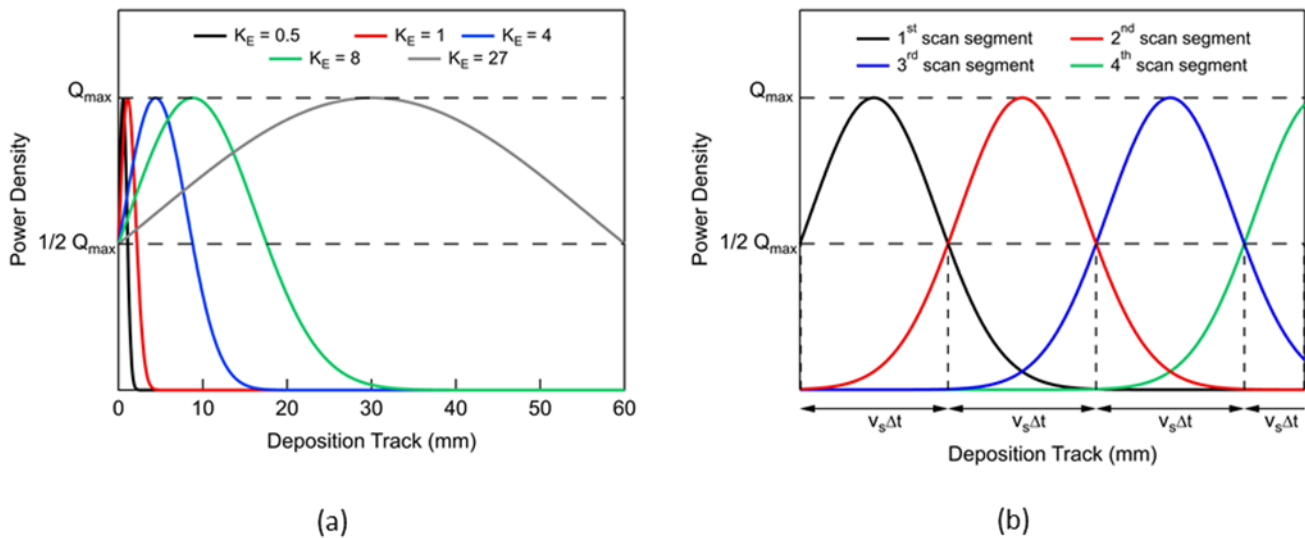


Figure 3. 14: (a) Illustration of  $K_E$  (sub-track sizes) at first computation time step of Elongated Ellipsoid (EE) heat Source  
(b) Power Intensity for subsequent sub-tracks of an elongated ellipsoid (EE) with  $K_E = 8$  over the deposition track

With  $K_E = 4, 8$  and  $27$ , computation time steps in the analysis becomes 0.538, 1.057 and 3.564 s. With such high computation time steps, the adaptive solver in the model takes multiple iterations (small time-steps) within a computation time increment/step to avoid convergence issues. These small time-steps are not stored in the solution but it helps in avoiding any convergence problems during the analysis. So, the solver stores the output at every computation time step mentioned in **Table 3.5** that depends upon the choice of  $K_E$ . It is further explained in this section, that with an increase in  $K_E$  that leads to increase in EE length, heat distribution intensity is centred at the EE sub-track with a 50% of the intensity at the edges of each EE sub-track. The increase of EE length (dependent upon  $K_E$ ), its movement over the deposition path and how its source intensity distribution is spread is shown and explained in **Fig 3.14**.

The movement of the elongated ellipsoid heat source is such that there is a smooth distribution of power intensity over the successive scan segments. The power intensity at the start and end of each scan segment is half of its peak value, resulting in a smooth distribution over the successive segments of a track as shown in **Fig. 3.14(b)**. This is the reason why activation criteria for elongated ellipsoid (EE) heat source model are 50% that accounts for the half of its peak value in the deposition direction. With  $K_E = 0.5$ , EE length ( $\hat{a}$ ) is equal to  $R$  and with further increase in  $K_E$  values, EE length ( $\hat{a}$ ) increases as presented in **Table 3.5**. Implementation of EE heat source is done in COMSOL correctly as shown in **Fig 3.15**. It can be seen in **Fig 3.15**, that with higher value of  $K_E$  results in large deposit of material (sub-track  $\hat{a}$ ) from the start of the calculation.

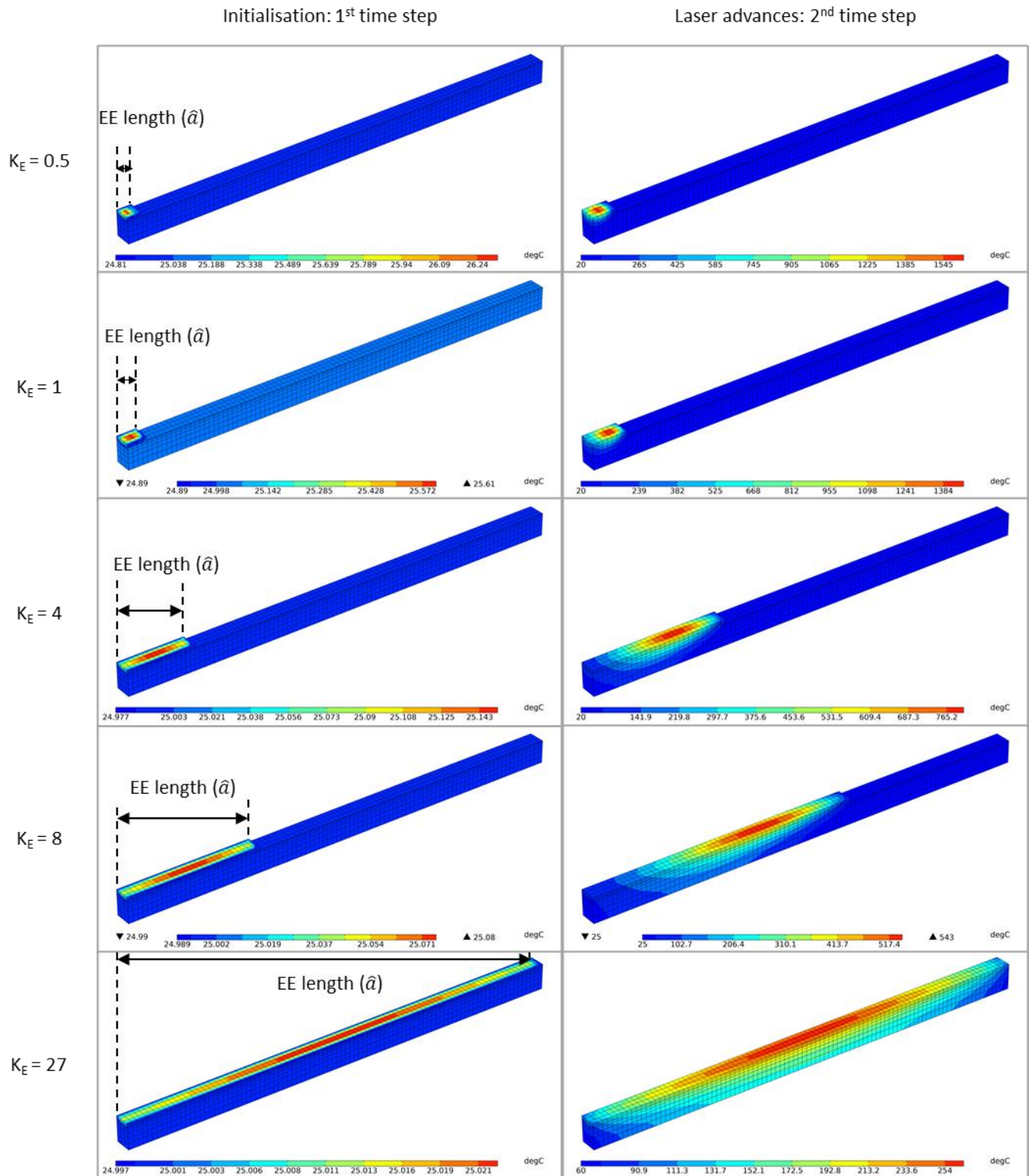


Figure 3. 15: Illustration of EE heat source with different  $K_E$  values and its effect on temperature distribution

With an increase in  $K_E$ , heat intensity distribution over the length is same however peak intensity value is lowered. This leads to lowering of the peak temperatures with an increase in  $K_E$ . This relation of lowering of peak temperature with an increase in  $K_E$  is almost directly proportional. But computation time steps required to finish the computation analysis is reduced drastically. Increasing the parameter  $K_E$  helps in reducing the total computation time, but it also leads to the increase of computation error. Thus, effect of sub-track size ( $\hat{a}$ ) activation on temperature evolution at thermocouple location is shown in Fig 3.16.  $K_E$  of 0.5 ( $\Delta t = R/v_s$ ) gives the same accurate results as we observed with Double Ellipsoid (DE) heat source with a simulation time step of  $R/v_s$ .

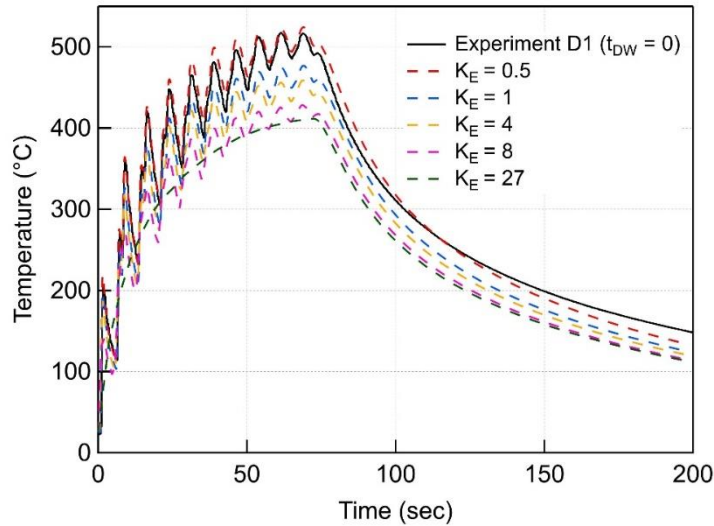


Figure 3. 16: Effect of  $K_E$  (sub-track sizes) on temperature evolution at Thermocouple location in experiment Case 1

As explained in the section further, computation error increase with  $K_E$ , while computation time drops, as shown in Fig. 3.17. For all experiment cases, simulation is performed to find out the effect of  $K_E$  on computation time and accuracy. Fig. 3.17 shows the results for D1-D4 (effect of dwell time). For case D1, with increase in  $K_E$  from 0.5 to 27, computation time reduces drastically from 90 to 35 min, but leads to an increase of error from 2% to 22%. For case D2, with respect to increase of  $K_E$ , computation time reduction is more drastic from 130 min to 36 min and computation error increases from 3% to 21%. For case D3 and case D4 as well, computation time reduction is more as dwell time is increasing but computation error is also increasing.

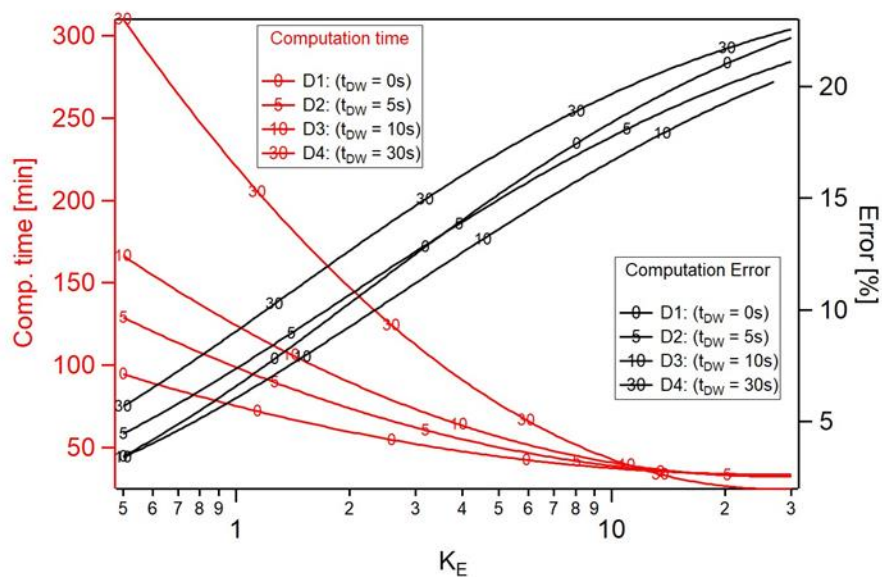


Figure 3. 17: Effect of  $K_E$  on computation time and accuracy of the numerical model with the EE heat source for experiment cases D1-D4 (effect of dwell time)

Fig. 3.18 shows the results for all cases P1-P4 (effect of laser power). For case P1-P4, with increase in  $K_E$  from 0.5 to 27, computation time reduces from 175 min to 25 min, but leads to an increase of error from 2% to 21%. Computation time reduction is exponential (3-4 times reduction) when  $K_E$  is increased from 0.5 to 4. But then the trend in computation time becomes linear when  $K_E$  is increased from 4 to 27 (not even half). Computation error increases linearly with an increase in  $K_E$ . So, an intelligent compromise needs to be done to reduce the computation time but also keeping in mind the computation error as well. In this work, the objective is that computational error should be less than 10%, that is well accepted in the scientific and

industrial community. Keeping this in mind,  $K_E = 4$  seems to satisfy both the objectives of reducing the computation time drastically but also keeping computation error less than 10%. Further increase of  $K_E$  results in computation time reduction, but computation error exceeds 20% when  $K_E = 27$ . However, with the introduction of elongated ellipsoid (EE) heat source, it is noticed that there is a drop-down of the temperature at melt-pool scale (local scale) as well as part scale (global scale) e.g., thermocouple locations that is far away from the deposition region as shown in **Fig. 3.5**. This modification of the thermal behaviour (especially, melt-pool scale) will surely impact the local mechanical response of the sample. Therefore, same analysis has been

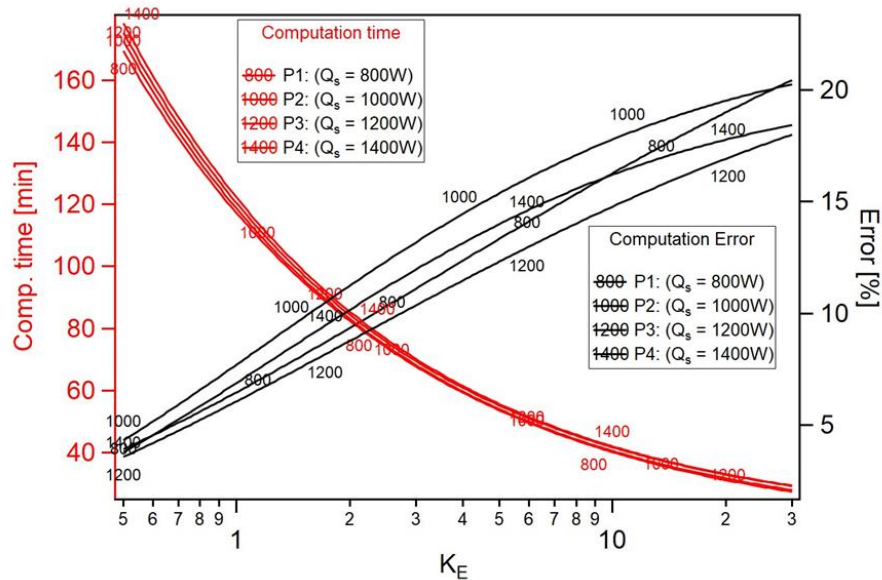


Figure 3. 18: Effect of  $K_E$  on computation time and accuracy of the numerical model with the EE heat source for experiment cases P1-P4 (effect of laser power)

performed in next chapter (Chapter 4) to verify if the optimised value of  $K_E$  found in thermal analysis is also valid for mechanical response e.g., distortion and residual stresses. This analysis will be presented in Chapter 4 dedicated to the Mechanical Model for LDED process.

### 3.5.3 Correction Factor

Due to the increase in  $K_E$  (sub-track length as well), computation time reduces exponentially, but it also leads to increase in computation errors. To compensate those errors, a variable source correction factor  $K_Q$  is introduced that leads to an increase in source intensity in elongated ellipsoid model, as shown in the following equation:

$$Q_{EE} = \frac{6\sqrt{3}APK_Q}{\hat{a}bc\pi\sqrt{\pi}} \exp\left(-\frac{3(x + v_s(t_0 + \frac{1}{2}\Delta t))^2}{\hat{a}^2} - \frac{3y^2}{b^2} - \frac{3z^2}{c^2}\right) \quad (3.11)$$

With the introduction of  $K_Q$ , distribution and peak intensity over the ellipsoid are increased artificially. Thus, the correct value of  $K_Q$  should be dependent upon the value of  $K_E$ , so calibration of source correction factor is done with respect to different sub-track size for all experiment cases. Then for the correct value of correction factor that should be dependent upon the size of sub-track ( $K_E$ ), calibration of correction factor is done with respect to sub-track size ( $K_E$ ) for all cases.  $K_E = 0.5$  does not elongate the ellipsoid. So, to analyse the effect of correction factor, values of  $K_E$  starting from 1 to 27 is used, because  $K_E = 0.5$  using Elongated Ellipsoid does averaging over a sub-track of  $R$ , i.e., SE or DE with a simulation time step of  $R/v_s$  i.e., conventional simulation increment.

As it can be seen in **Fig. 3.19**, for experiment cases D1-D4 (effect of dwell time), with an increase in  $K_E$ , computation error increases as we have seen in the previous section (EE with no source correction factor  $K_Q$  is represented by black bar).

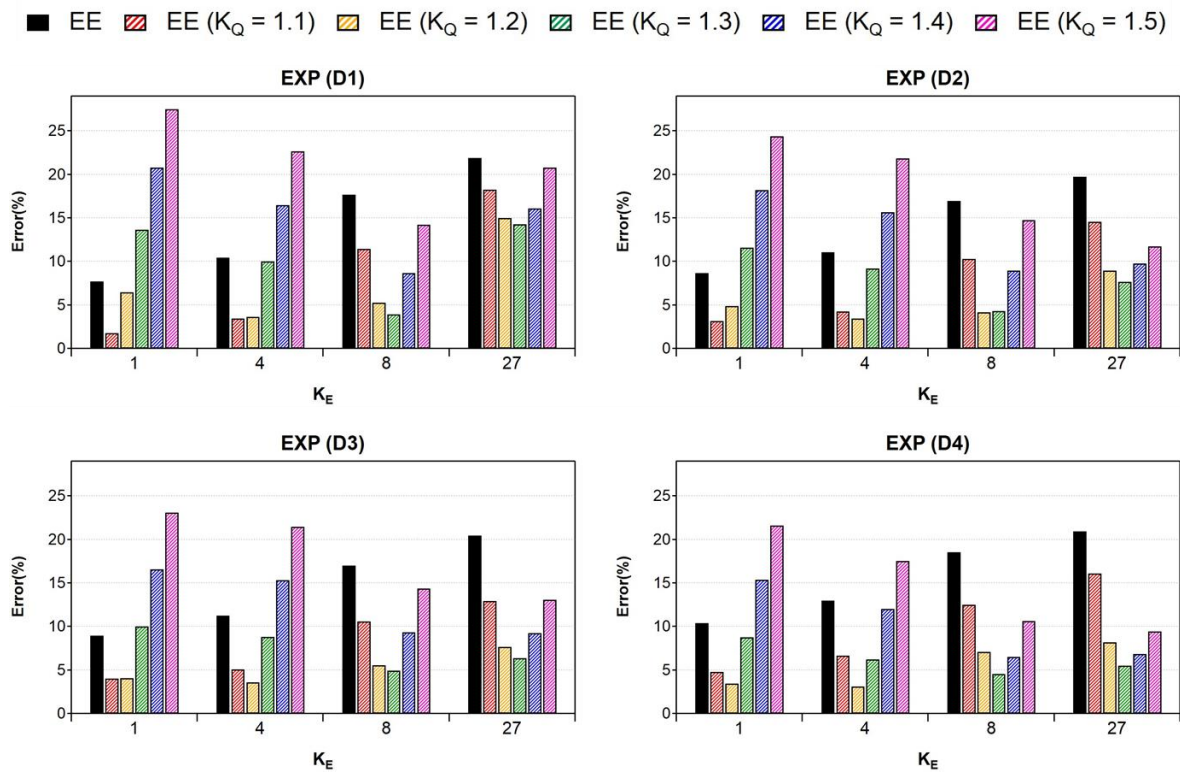


Figure 3. 19: Effect of  $K_Q$  on computation accuracy for experiment cases D1-D4 (effect of dwell time)

- For all experiment cases D1-D4, with  $K_E = 1$ ,  $K_Q = 1.1$  &  $1.2$  is sufficient enough to compensate for the EE length ( $\hat{a}$ ) as the elongated length is not too big. Further increase in  $K_Q$  starts to over-compensate the averaging effect as the increase in EE length is not too much.
- For all experiment cases D1-D4, with  $K_E = 4$ ,  $K_Q = 1.1$ ,  $1.2$  &  $1.3$  is sufficient enough to compensate for the EE length ( $\hat{a}$ ). Here the EE length ( $\hat{a}$ ) starts to get big and therefore  $K_Q = 1.3$  value is required. Further increase in  $K_Q$  starts to over-compensate as the increase in EE length is not too much.
- For all experiment cases D1-D4, with  $K_E = 8$ ,  $K_Q = 1.1$  underpredicts the temperature values and is not sufficient enough to compensate.  $K_Q = 1.2$ ,  $1.3$  &  $1.4$  is sufficient enough to compensate for the EE length ( $\hat{a}$ ). Further increase in  $K_Q$  starts to over-compensate as the increase in EE length is not too much.
- For all experiment cases D1-D4, with  $K_E = 27$ ,  $K_Q = 1.1$  underpredicts the temperature values and is not sufficient enough to compensate.  $K_Q = 1.2$ ,  $1.3$  &  $1.4$  is sufficient enough to compensate for the EE length ( $\hat{a}$ ). Further increase in  $K_Q$  starts to over-compensate as the increase in EE length is not too much.

This trend of increasing  $K_Q$  value with an increase in  $K_E$  value can be clearly noticed. This is occurring to compensate for the increase in computation error with an increase in  $K_E$ . Therefore, there is a direct relation between  $K_E$  and  $K_Q$ , that is helpful in achieving the second objective to reduce the computation error. With the introduction of  $K_Q$ ,  $K_E = 8, 27$  can also be utilised as computation error falls below 10% which was not the case previously. For different  $K_E$  value,  $K_Q$  value that results in minimum computation error is identified for each experiment case. This will be used further to extract the  $K_Q$  value depending upon  $K_E$  value that results in minimum computation error.

As it can be seen in Fig. 3.20, for experiment cases P1-P4 (effect of laser power), with an increase in  $K_E$ , computation error increases as we have seen in the previous section (EE with no source correction factor  $K_Q$  is represented by black bar).

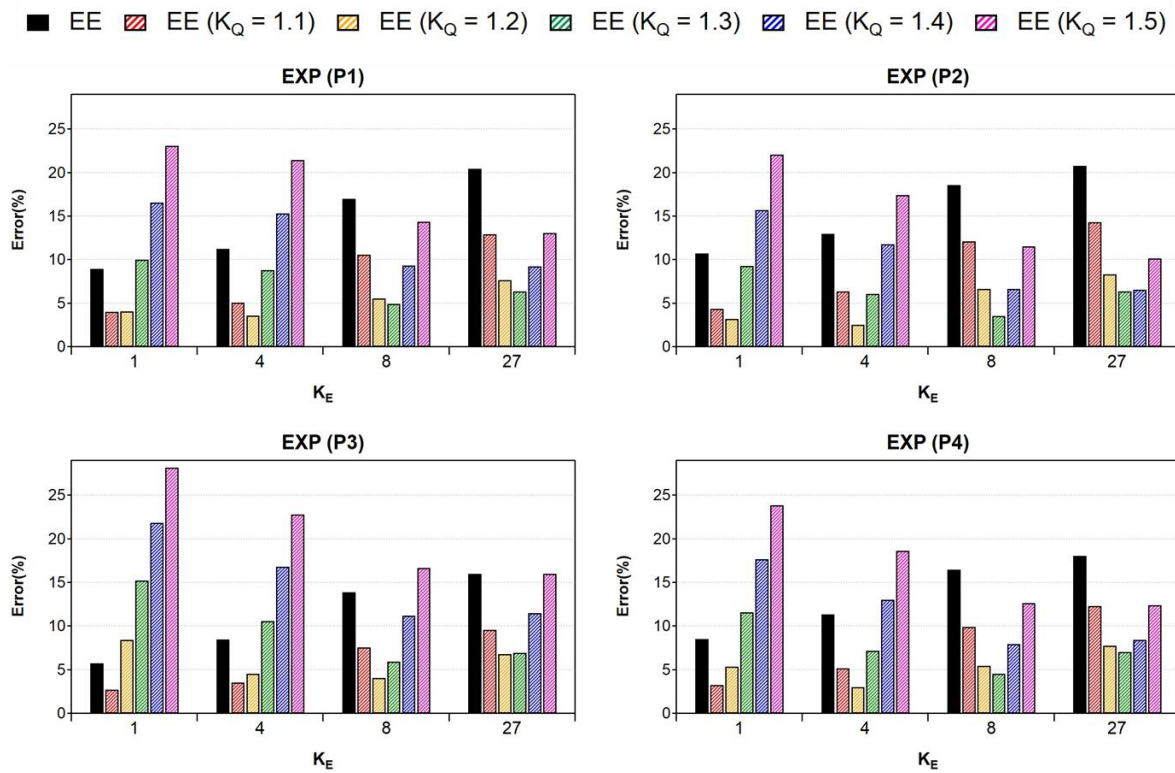


Figure 3. 20: Effect of  $K_Q$  on computation accuracy for experiment cases P1-P4 (effect of laser power)

- For all experiment cases P1-P4, with  $K_E = 1$ ,  $K_Q = 1.1$  & 1.2 is sufficient enough to compensate for the EE length ( $\hat{a}$ ) as the elongated length is not too big. Further increase in  $K_Q$  starts to over-compensate the averaging effect as the increase in EE length is not too much.
- For all experiment cases P1-P4, with  $K_E = 4$ ,  $K_Q = 1.1$ , 1.2 & 1.3 is sufficient enough to compensate for the EE length ( $\hat{a}$ ). Here the EE length ( $\hat{a}$ ) starts to get big and therefore  $K_E = 1.3$  value is required. Further increase in  $K_Q$  starts to over-compensate as the increase in EE length is not too much.
- For all experiment cases P1-P4, with  $K_E = 8$ ,  $K_Q = 1.1$  underpredicts the temperature values and is not sufficient enough to compensate.  $K_Q = 1.2$ , 1.3 & 1.4 is sufficient enough to compensate for the EE length ( $\hat{a}$ ). Further increase in  $K_Q$  starts to over-compensate as the increase in EE length is not too much.
- For all experiment cases P1-P4, with  $K_E = 27$ ,  $K_Q = 1.1$  underpredicts the temperature values and is not sufficient enough to compensate.  $K_Q = 1.2$ , 1.3 & 1.4 is sufficient enough to compensate for the EE length ( $\hat{a}$ ). Further increase in  $K_Q$  starts to over-compensate as the increase in EE length is not too much.

For experiment cases P1-P4 (effect of laser power), same relation is established between  $K_E$  and  $K_Q$ . In this set of experiments also,  $K_E = 8, 27$  can now be used in heat transfer analysis as computation error falls below 10%. So, with the introduction of  $K_Q$ , computation error is reduced along with reduction of computation time (due to  $K_E$ ) as higher values of  $K_E$  yields desired accurate results. With the introduction of source correction factor, there is no significant impact on the computation time of analysis.

For experiment case D1, EE heat source with  $K_E = 4$ , and with the introduction of source correction factor  $K_Q$  using EE heat source model, temperature evolution at thermocouple location shifts upwardly due to the increase of heat intensity as shown in **Fig 3.21**.  $K_Q$  values of 1.1 and 1.2 seems to be well compensating the effect of  $K_E$  that leads to underprediction of temperature evolution, but with further increase of  $K_Q$  values of 1.3, 1.4 and 1.5, it can be seen that it over-compensates the thermal error generated due to  $K_E$ , and starts to yield higher computation error. Therefore, a correlation between  $K_E$  and  $K_Q$  should be established for different process parameters that yields minimum computation error for elongated ellipsoid (EE) heat source.

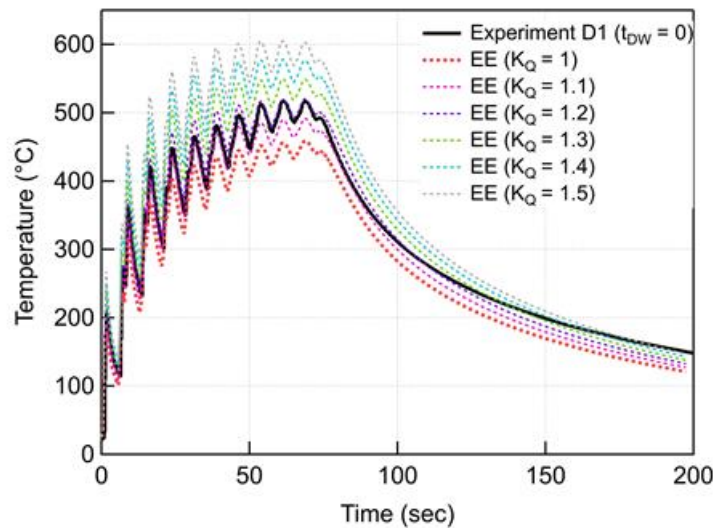


Figure 3. 21: Effect of source correction factor ( $K_Q$ ) on temperature evolution at thermocouple location for  $K_E = 4$  (sub-track size) for experiment case D1

### 3.5.4 Correlation

With the introduction of  $K_E$ , computation time can be reduced. In addition, with the introduction of  $K_Q$ , computation error originated due to introduction of  $K_E$  can be reduced. Now the objective is to identify the  $K_Q$  value that yields to the minimum computation error for the corresponding  $K_E$  value. Results presented in **Fig 3.19 & 3.20** are analysed to identify the relation between  $K_E$  and  $K_Q$  that leads to minimum computation error. Once the data analysis is finished, a surface plot is created that is more helpful in identifying  $K_Q$  value corresponding to  $K_E$  value leading to minimum computation error as shown in **Fig. 3.22 & 3.23**.  $K_E$  values are presented on log axis to represent the increase in values from 0.5 to 27. Log axis is chosen as  $K_E$  values used in the present work are 0.5, 1, 4, 8 and 27. Increase in the  $K_E$  values is not linear and therefore log axis is chosen to represent the data.  $K_E = 1, 4, 8$  and 27 value are represented with a black vertical line. This makes the identification of these values on the graph very easy. Then computation errors obtained with different combination of  $K_E$  and  $K_Q$  are drawn as contour level on the surface plot. Each contour level (showing computation error) is highlighted with its value e.g., 5, 6, 7 and 10. This highlights the computation domain that falls under a give computation error. This computation domain gives different combination of  $K_E$  and  $K_Q$  that will yield a computation error less than the drawn contour of computation error. It can be noticed very clearly that for contour level of 10 (computation error), change of  $K_Q$  values follow the same trend as discussed earlier.  $K_Q$  value increases with an increase in  $K_E$  value and then starts to stabilise with further increase in  $K_E$  value from 15-30. This trend is noticeable for both experiment cases D1-D4 i.e., effect of dwell time in **Fig 3.22** and P1-P4 i.e., effect of laser power in **Fig 3.23**.

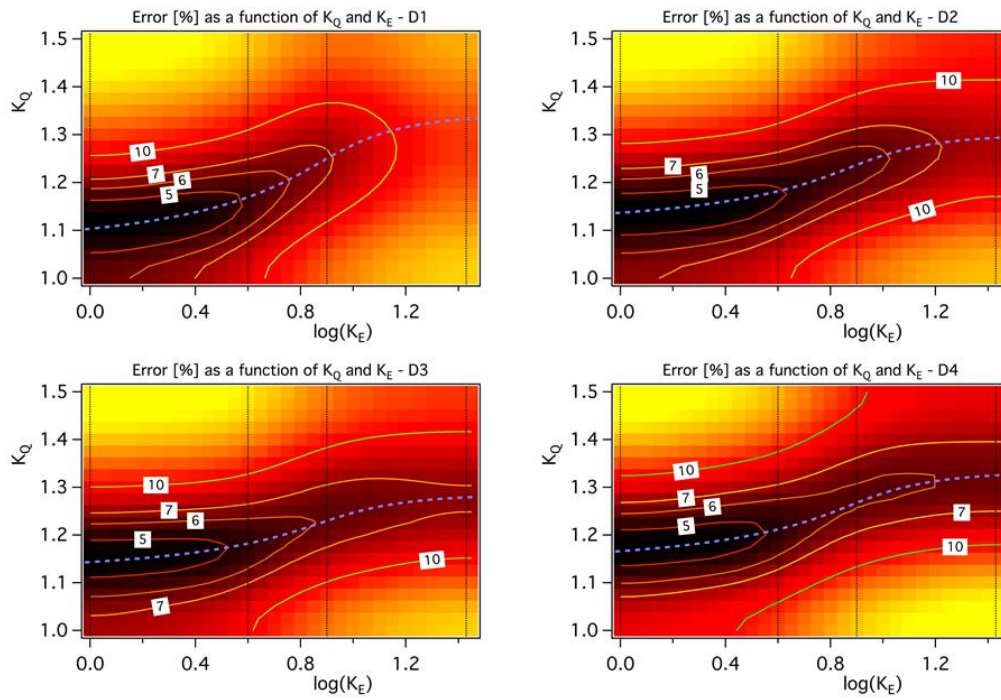


Figure 3. 22: Domain of computation accuracy as a function of  $K_E$  and  $K_Q$  for the experiment cases D1-D4 (effect of dwell time). The minimum error is pointed out with a blue dashed line

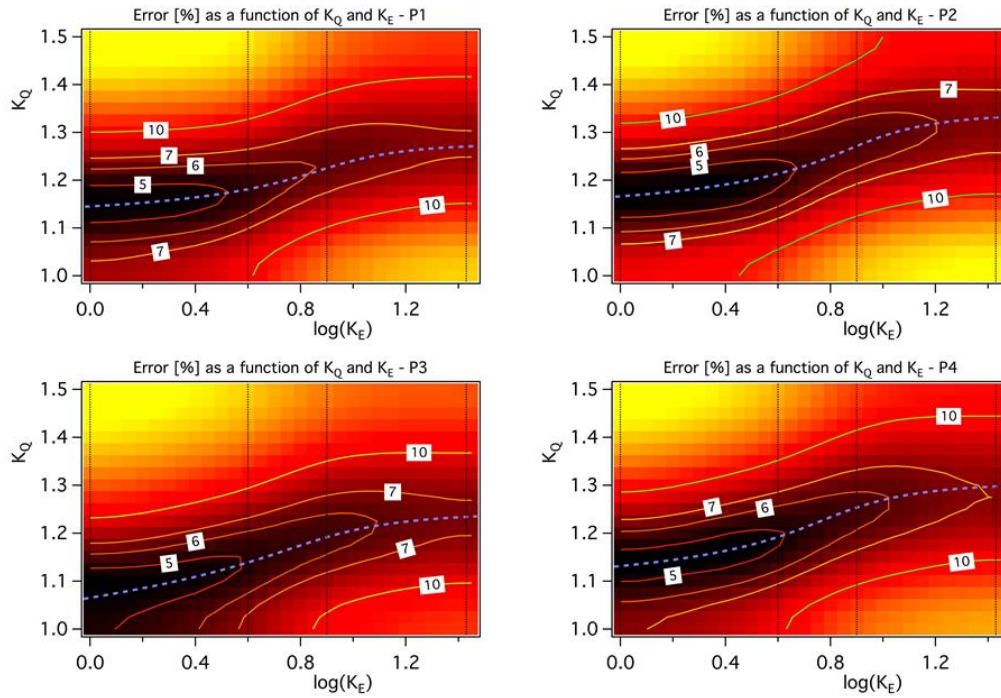


Figure 3. 23: Domain of computation accuracy as a function of  $K_E$  and  $K_Q$  for the experiment cases P1-P4 (effect of laser power). The minimum error is pointed out with a blue dashed line

Once  $K_Q$  value is identified for each corresponding  $K_E$  value, then these results for all experiment cases are plotted in two different graphs. This is done to identify the relation between  $K_E$  and  $K_Q$ . For all experiment cases D1-D4 and P1-P4, it can be seen in **Fig. 3.24** that for most experiment cases, with an increase of  $K_E$  from 0.5 to 8, there is also an increase in correction factor from  $K_Q = 1$  to 1.25, that leads to minimum computation error for temperature history at thermocouple location. But with further increase of  $K_E$  from 8 to 27, further increase in values of  $K_Q$  is not a necessity. Therefore, a correlation between  $K_E$  and  $K_Q$  is recommended in this work that yield to minimum computation error with different process parameters e.g., dwell time and laser power. This relation is highlighted in grey color in **Fig 3.24**.

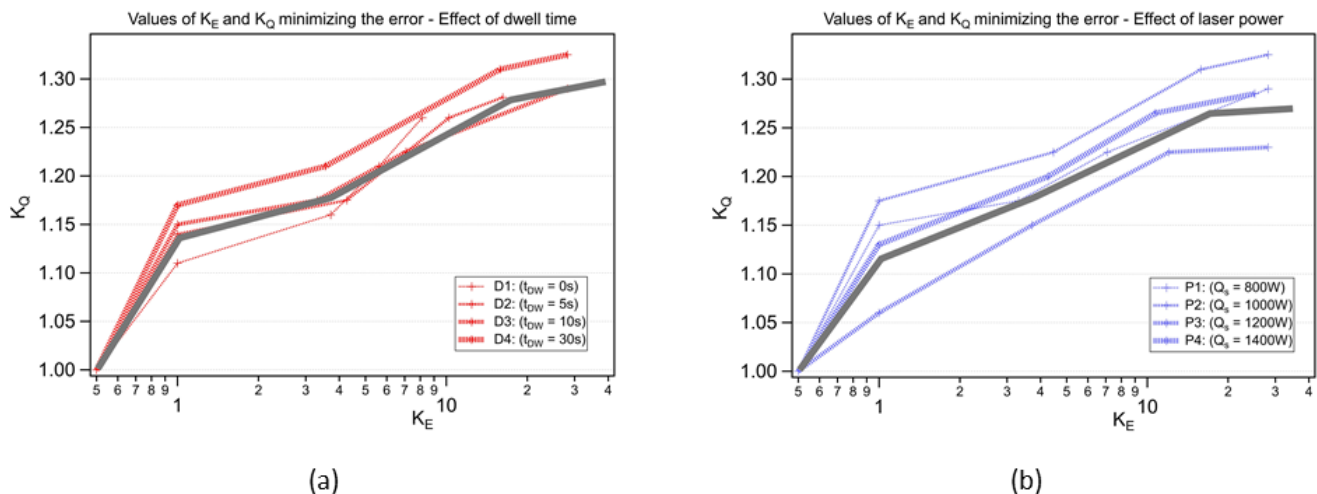


Figure 3. 24: Identification of a source correction factor ( $K_Q$ ) for different sub-tract sizes ( $K_E$ ), for different experiment cases. Recommended correlation between these parameters is pointed out in grey line

## 3.6 Conclusions

This chapter has made it possible to develop a thermal model on the basis of the model presented in Chapter 2, to recall the numerical model that is used to simulate metal deposition. In this chapter, however, emphasis is done on the choice of equivalent heat source and its impact on computation time to simulate large-parts. In addition, an experimental set-up was developed to study the fabrication of one bead wall with 20 layers made of 316 stainless steel. A series of experiment were carried out to build walls with four different laser powers and four dwell times, keeping the laser scan speed and powder mass flow rate constant. All these experiments were instrumented with thermocouples and infra-red imaging camera. These experimental data were compared to the calculated temperatures by the model. The main conclusions of this chapter are following:

- Double Ellipsoid heat source model with small time increments ( $\leq R/v_s$ ) correctly predicts temperature evolution with an average computation accuracy of more than 96%, but leads to high computation time due to thousands of simulation time increments.
- Elongated Ellipsoid heat source model with different  $K_E$  values significantly reduces computation times (up to 10 times) while yielding average computation accuracy of more than 75-95%.
- A source correction factor ( $K_Q$ ) for Elongated Ellipsoid (EE) heat source model is presented that reduces the average computation error within 5% at thermocouple location.
- A correlation is then found that is helpful in finding the co-relation between simulation time increments, computation time and error. Correlation is shown to be dependent of variables laser power and dwell time.
- Thermal model with DE heat source and EE heat source with different  $K_E$  and  $K_Q$  works efficiently for different process parameters justifying the versatility of the model.
- EE model can be used to simulate large-part size as it unlocks the issue of computation time by preserving computation accuracy with the introduction of source correction factor.

*In the next chapter i.e., Chapter 4, a thermo-mechanical model is developed that is dedicated for LDED process. Both DE and EE heat source models are employed and a detailed comparison study is done to demonstrate the pros and cons of these models especially features like computation time and accuracy.*

# Chapter 4: Mechanical Model for LDED<sup>2</sup>

|  |     |
|--|-----|
| Chapter 4: Mechanical Model for LDED.....                          | 85  |
| 4.1 Introduction.....  | 86  |
| 4.2 Modeling approach.....   | 87  |
| 4.2.1 Thermal analysis .....                                       | 87  |
| 4.2.2 Mechanical Analysis.....                                     | 88  |
| 4.3 Experiment Set-Up of a SS 316L wall build by LDED process..... | 100 |
| 4.3.1 Temperature measurement.....                                 | 101 |
| 4.3.2 In-situ distortion measurement .....                         | 101 |
| 4.3.3 Post-process line distortion measurement.....                | 101 |
| 4.4 Numerical implementation.....                                  | 102 |
| 4.4.1 FEA solver.....  | 102 |
| 4.4.2 FEM mesh .....   | 102 |
| 4.4.3 Material deposition modeling.....                            | 102 |
| 4.4.4 Model calibration and boundary conditions.....               | 103 |
| 4.5 Results and discussion .....                                   | 103 |
| 4.5.1 Comparison of temperature evolution .....                    | 103 |
| 4.5.2 Comparison of in-situ distortion evolution .....             | 105 |
| 4.5.3 Comparison of post-process line distortion results .....     | 113 |
| 4.6 Simulation Speed-up.....                                       | 115 |
| 4.7 Conclusions.....   | 120 |

---

<sup>2</sup> The work presented in this particular chapter has already been published: Vaibhav Nain, Thierry Engel, Muriel Carin, and Didier Boisselier. "Conventional Meso-Scale and Time-Efficient Sub-Track-Scale Thermomechanical Model for Directed Energy Deposition." *Materials* (2022). <https://doi.org/10.3390/ma15124093>

## 4.1 Introduction

*The objective of the present chapter is to develop a thermo-mechanical model for LDED process with Stainless Steel 316L (SS 316L) material. The thermo-mechanical model takes into account the elastoplastic behavior along with stress relaxation phenomenon inhibited by material in LDED. Also, the proposed model aims to simulate the distortions during the manufacturing of large-parts. Therefore, the feasibility of the proposed model to simulate large-part size is analysed. In addition, as for the thermal model, specific experiments have been carried out at Irepa Laser in order to compare numerical and experimental results. To better understand the emergence of distortions during additive manufacturing process, in-situ distortion trend and accumulation are measured using a laser displacement sensor. To cross-check the proposed model's accuracy, it is also validated with post-process distortion measurements. To justify model's versatility and accuracy, different process parameters are used for the experiments and then numerical model's results are successfully compared with these experiment results.*

In the last chapter i.e., Chapter 3, it has been demonstrated that thermal model with DE heat source coupled with Quiet/Active material activation strategy works accurately for LDED process. The effectiveness of EE heat source to successfully reduce the thermal computation time (up-to a factor of 10) by keeping the acceptable computation error levels (less than 10%) is also established. Therefore, in this chapter, the same methodology (DE and EE heat source with Quiet/Active material activation strategy) is extended to mechanical model. An important point needs to be reminded here that the thesis's objectives is to develop a thermo-mechanical model to predict the global response of the deposited part, local aspects are not studied in detail. However, if the stated objectives of the research are to develop a model that can also predict the cracking phenomenon, then choice of the constitutive law, type of work hardening laws (linear, non-linear, perfect plasticity etc.), type of hardening (isotropic or kinematic) need to be reconsidered. So, this is not the case of the present research that is carried out in the context of the PhD. It has been proven in the literature that Elasto-plastic (EP) model with isotropic hardening works correctly for SS 316L material in AM process. Depradeux shows that an Elasto-plastic model with kinematic hardening gives a better agreement when comparing the residual stresses, however, better agreement is obtained with an isotropic hardening in terms of distortions (Depradeux, 2004). Cambon has proven that EP model with isotropic hardening coupled with stress relaxation model yields similar stresses those obtained with Elasto-Visco-Plastic model mixed hardening (isotropic and kinematic hardening) for SS 316L (Cambon, 2021). As the main objective is to develop a thermo-mechanical model capable of simulating large-parts within acceptable computation time. Therefore, in this chapter, main objective is to develop a simplified thermo-mechanical model with Elasto-Plasticity (Voce Non-linear Isotropic hardening law) with instantaneous stress relaxation (SR) temperature model that also accounts thermal cycles induced stress relaxation for SS 316L in LDED process. It is a well-established fact that most metals like SS 316L exhibits non-linear hardening (Cambon, 2021; Depradeux, 2004), therefore Voce non-linear hardening law is chosen to model work hardening. Also, to simplify the thermo-mechanical model, isotropic hardening is chosen instead of kinematic hardening. Finally, to simplify the stress-relaxation modeling, an instantaneous SR model is chosen. The prescribed (SR) temperature is calibrated by doing inverse calculation and comparing with in-situ distortion results. As for, numerical model's heat source parameters, boundary heat losses and instantaneous stress relaxation temperature values are calibrated with one-set of experiment results. Then the calibrated thermo-mechanical model is verified with different experiment results obtained with other set of experiments with varying inter-layer dwell times and number of beads. Thermo-mechanical model is validated with in-situ temperature and distortion experiment data obtained during the fabrication of 42 layers high, single and double beads wall on a cantilever substrate with 0, 5 and 10s inter-layer dwell time. The

thermo-mechanical model is further validated with post-process distortion results. Also in Chapter 3 (findings have been published in (Nain et al., 2021) have demonstrated that thermal model with an elongated ellipsoid (EE) heat source works efficiently by considerably reducing the computation time for pure thermal model. Therefore, in the present chapter for a thermo-mechanical model, effectiveness of this approach (EE heat source) is also demonstrated by efficiently predicting temperature and distortions history with drastic reduction in computation time.

## 4.2 Modeling approach

The proposed thermo-mechanical model focusses primarily on thermal and mechanical fields. The geometry of the different layers of deposited wall is supposed to be known from the experiments. The effect of the melt-pool flow is modeled using an enhanced thermal conductivity. The numerical model discretizes the continuous physical process of material deposition in a combination of successive simulation steps, in which laser travel is considered sequential step-by-step. The numerical simulations of the LDED process are done sequentially: firstly, a 3D transient thermal analysis is performed to obtain the temperature field assuming a weak thermal-mechanical coupling. Then, thermal results are applied as a thermal load to a 3D quasi-static mechanical analysis to simulate the mechanical response. Thermo-mechanical model for LDED can be considered as weakly coupled (1-way coupling) due to the fact that the laser energy source in thermal analysis is much higher than the plastic strain energy in mechanical analysis (Zhang et al., 2004b). The whole model is built on COMSOL Multiphysics software.

### 4.2.1 Thermal analysis

The thermal model being identical to that presented in chapters 2 & 3, it will not be detailed here. This model is based on the resolution of equations 2.1, 2.2, associated with a double ellipsoid source term (Eq 3.2) initially. An elongated ellipsoid source (Eq 3.4) will also be studied at the end of the chapter in order to illustrate the gain in computation time on a complete thermomechanical model. The initial boundary conditions, convective and radiative heat losses are also identical to the formulation explained in chapters 2 & 3 and is based on the equations 2.4, 2.5 and 2.7. The natural and forced convective coefficient values are kept the same along with emissivity values as well. Also, specific heat capacity is modified using the same method (Eq 2.8) mentioned in chapter 2. Finally, enhanced thermal conductivity factor of 2.5 is kept for thermal conductivity beyond melting temperature (Eq. 2.9) given in chapter 2.

Temperature dependent material properties for SS 316L are employed in the model and are presented in **Fig 4.1** (Biegler et al., 2018b). As in chapter 3, linear interpolation is used to calculate the values between the given temperature dataset and properties are kept constant beyond the fusion temperature. The temperature dependent thermo-mechanical properties are taken from (Biegler et al., 2018b) that is different from the material properties used in chapter 2 (Mills, 2002b). The main reason of using material properties from (Biegler et al., 2018b) in this chapter is that it provides complete thermo-mechanical properties for SS 316L, and this database is used in a commercial software MSc Simufact. On the other hand, material properties from (Mills, 2002b) only provides thermal material properties that is not sufficient for the thermo-mechanical model. However, there is little difference in thermal material properties between these two different sources and a superimposition of the datasets is provided in the Appendix (Chapter 4).

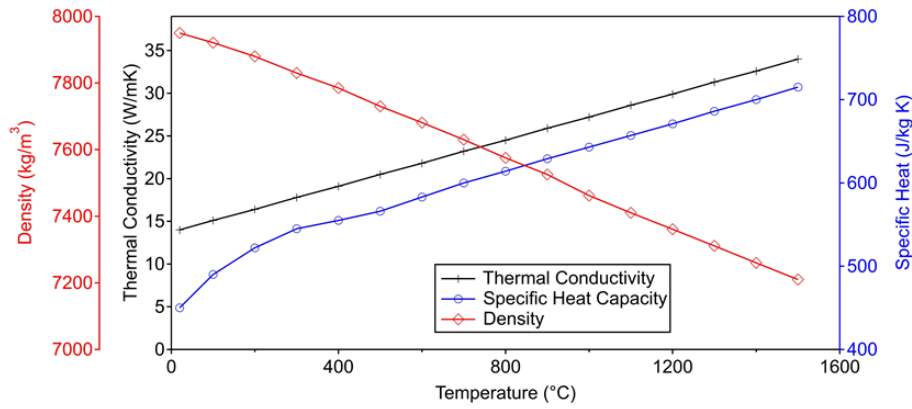


Figure 4. 1: Temperature dependent thermal properties of SS 316L (M. Biegler et al. 2018)

## 4.2.2 Mechanical Analysis

The governing mechanical stress equilibrium equation can be given as:

$$\nabla \cdot \sigma = 0 \quad (4.1)$$

The mechanical constitutive law where stress-strain relation of material is described using Hooke's law of linear elastic material as:

$$\sigma = C \varepsilon_e \quad (4.2)$$

Total strain  $\varepsilon$ , considering small deformation theory and Thermo-Elasto-Plasticity, is decomposed additively in elastic  $\varepsilon_e$  and inelastic part  $\varepsilon_{in}$ :

$$\varepsilon = \varepsilon_e + \varepsilon_{in} \quad (4.3)$$

### 4.2.2.1 Elastic Strain

The elastic strain increases linearly with the stress in the elastic regime. In the linear elasticity framework of isotropic materials, the elastic strain can then be expressed using Hooke's Law:

$$\varepsilon_{el} = \frac{(1 + \nu)}{E} \sigma - \frac{\nu}{E} tr(\sigma) \quad (4.4)$$

Where  $\nu$  is poisson's ratio taken as 0.3 and  $E$  is temperature dependent Young's Modulus of the material given in Fig 4.2 (Biegler et al., 2018b).

Inelastic strain includes thermal  $\varepsilon_{th}$  and plastic strain  $\varepsilon_{pl}$  in the numerical model.

$$\varepsilon_{in} = \varepsilon_{th} + \varepsilon_{pl} \quad (4.5)$$

### 4.2.2.2 Thermal Strain

The thermal strain is calculated using temperature dependent coefficient of thermal expansion  $\alpha$  given in **Fig 4.2** (Biegler et al., 2018b), as shown in equation below, where  $T_{ref}$  is reference temperature.

$$\varepsilon_{th} = \alpha (T - T_{ref}) \quad (4.6)$$

Where  $T_{ref}$  is the reference temperature. The plastic strain is calculated by employing the Von-Mises yield criterion and isotropic non-linear hardening model.

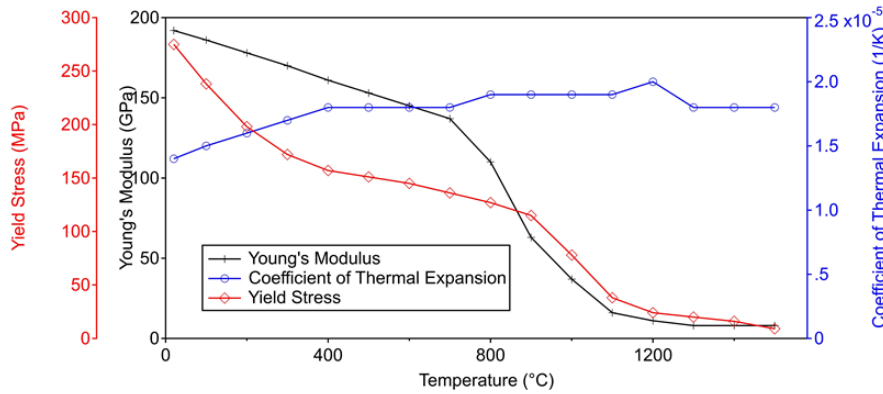


Figure 4. 2: Temperature dependent mechanical properties of SS 316L (M. Biegler et al. 2018)

The material properties presented are coherent with other literature sources such as (Cambon, 2021). A detailed comparison of material properties from different sources is presented in the Appendix (Chapter 4).

### 4.2.2.3 Plastic Strain

Plastic strain is computed by enforcing the Von Mises yield criterion and the Associated flow rule:

$$F = \sigma_{vm} - \sigma_y(\varepsilon_{eq}, T) \leq 0 \quad (4.7)$$

Where  $F$  is the yield function,  $\sigma_{vm}$  is Von-Mises's stress,  $\sigma_y$  is yield stress, and  $\varepsilon_{eq}$  is the equivalent plastic strain. To calculate the material response in the plastic regime, isotropic model is used, as kinematic model requires much higher computation cost. However, hardening behaviour is calculated using Non-linear hardening rule instead of linear hardening, as most metals exhibit non-linear hardening behaviour. Voce hardening law is used to model non-linear isotropic hardening as presented in **Eq. 4.12**

$$\sigma_y(\varepsilon_{eq}, T) = \sigma_{y0}(T) + \sigma_{sat}(1 - e^{-\beta\varepsilon_{eq}}) \quad (4.8)$$

Where  $\sigma_{y0}$  is the temperature-dependent initial yield stress given in **Fig 4.2** (Biegler et al., 2018b),  $\sigma_{sat}$  and  $\beta$  is saturation flow stress and saturation exponent respectively. The saturation flow stress  $\sigma_{sat}$  determines the capacity of yield surface to expand in the stress space.

As given in **Eq. 4.12**, the isotropic hardening is exponentially related to the equivalent plastic strain and it can be loosely interpreted that if  $\varepsilon_{eq} = 0$ , material returns to its yield point and regains its elastic behaviour, however the plastic transformation is kept. This feature of  $\varepsilon_{eq} = 0$  will be used in the model to represent the effects of annealing and is explained more in detail in the next section.

The values of these two parameters  $\sigma_{sat}$  and  $\beta$  are extracted by reverse-fitting the results from stress-strain data presented in the literature work (Biegler et al., 2018a) in comparison to results yielded by Voce Hardening law for different temperature as shown in Fig 4.3.

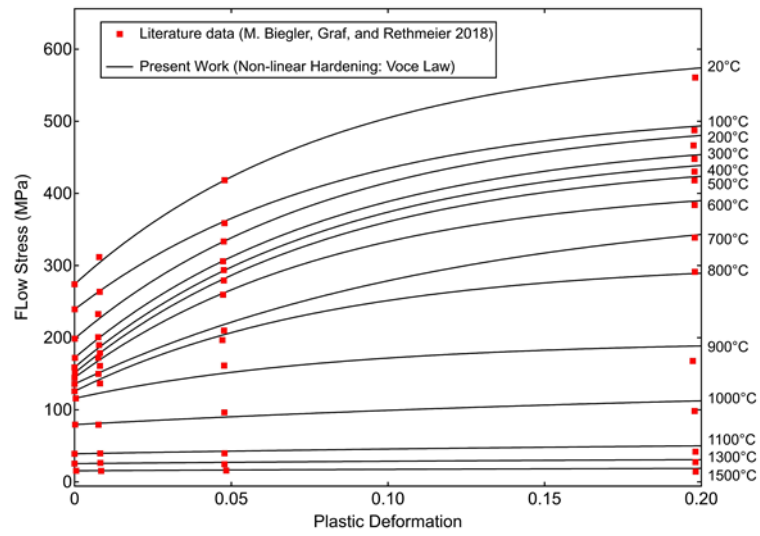


Figure 4. 3: Comparison of temperature dependent flow curves from the literature to the flow curves yielded by Voce hardening law by reverse fitting the data with different  $\sigma_{sat}$  and  $\beta$  values

To obtain the above reverse data-fitting of the plastic deformation, extracted values of  $\sigma_{sat}$  and  $\beta$  are given in Table 4.1:

Table 4. 1: Temperature dependent values of the parameters employed in Voce Non-Linear Hardening Law for SS 316L

| Temperature | $\sigma_{sat}$ (MPa) | $\beta$ |
|-------------|----------------------|---------|
| 20          | 330                  | 12      |
| 100         | 280                  | 12      |
| 200         | 310                  | 12      |
| 300         | 310                  | 12      |
| 400         | 308                  | 12      |
| 500         | 300                  | 12      |
| 600         | 270                  | 12      |
| 700         | 260                  | 12      |
| 800         | 180                  | 12      |
| 900         | 80                   | 12      |
| 1000        | 60                   | 4       |
| 1100        | 20                   | 4       |
| 1300        | 10                   | 4       |
| 1500        | 6                    | 4       |

The implementation of the previous-mentioned stress relaxation method ( $\sigma$  and  $\varepsilon_{eq} = 0$  if  $T > T_{anneal}$ ) in COMSOL and comparison of this technique with different stress relaxation techniques available in literature is explained in the coming sections.

#### 4.2.2.4 Annealing

The effect of phase transformation due to solid-state phase transformation in steel, Ti-6Al-4V and other materials that leads to stress relaxation (SR) in LDED is well studied (Denlinger and Michaleris, 2016). Also, liquefaction of the material (feedstock) contributes to the stress relaxation in LDED (Biegler et al., 2018a). Finally, due to the process physics governing LDED, fabricated component experiences multiple thermal heating and cooling cycles for a considerable amount of time, leading to annealing induced stress relaxation, and has been extensively studied (Wang et al., 2018, 2017b). Hence, it is convenient to consider the stress relaxation in LDED that alters the mechanical behaviour of the material during the fabrication.

Denlinger et al. (Erik R Denlinger et al., 2015) proposed an instantaneous stress relaxation model for Ti-6Al-4V in Electron Beam DED to account for transformation strain and stress relaxation. The model works by setting both plastic strain and stress to zero if the computed temperature goes beyond inversely calibrated prescribed relaxation temperature. Also, Denlinger et al. (Denlinger and Michaleris, 2016) demonstrated that an instantaneously stress relaxation model for Ti-6Al-4V predicts correct distortion accumulation that is consistent with experiment results for LDED technology as well. Some other researchers have also used the same methodology of using an instantaneously stress relaxation model for Ti-6Al-4V for LDED process (Heigel et al., 2015; Lu et al., 2018b). But in the LDED or AM process, the actual relaxation behaviour is a time transient temperature dependent gradual process (Yan et al., 2018). Xie et al. (Xie et al., 2020b) developed an experiment-based stress relaxation model for Ti-6Al-4V for LDED. Experiment-based methodology is coherent to the physical stress relaxation behaviour of the material that is dependent on time and temperature in LDED.

Griffith et al. (Griffith et al., 1998) has concluded that during the deposition of H13 tool steel in LDED process, sufficient high temperature is reached to cause material to anneal that leads to stress relaxation. Qiao et al. employed a dynamic stress relaxation model to represent stress relaxation by reducing the equivalent plastic strain that depends upon time duration at which metal experiences high temperature during multi-pass butt welding for dissimilar metal (Qiao et al., 2014). Kim et al. has investigated experimentally and numerically that during the deposition of Stainless Steel 316L (SS 316L) in Powder bed fusion (PBF) AM technology, there is a significant stress relaxation due to thermal cycles induced from subsequent deposition of layers (Kim et al., 2019). Biegler et al. has proposed to reset the material's plastic and stress history above solidus temperature to account for stress relaxation due to liquefaction of SS 316L deposition in LDED (Biegler et al., 2018a).

Cambon has compared different hardening models with and without stress relaxation (Cambon, 2021). She has demonstrated that a model with isotropic hardening that takes into account stress relaxation gives stresses that are very similar to those obtained with mixed hardening (isotropic and kinematic hardening) for SS 316L. However, temperature interval chosen for the relaxation greatly influences the level of residual stresses particularly in the case of isotropic hardening that tends to overpredicts the stress levels.

In the numerical model, effect of phase transformation is neglected as the Stainless Steel 316L remains austenitic at all temperatures (Yadollahi et al., 2015). However, to account for the effects of annealing induced dynamic stress relaxation (SR) (that depends upon temperature and time) during LDED process, the instantaneously stress relaxation (SR) is proposed in the numerical model.

For multi-pass welding, Lee et al. have defined an annealing temperature beyond which material loses its plasticity history (work hardening) instantaneously so that the equivalent plastic strain becomes 0 if temperature exceeds the defined annealing temperature (Lee et al., 2008). Once the workpiece is cooled down below annealing temperature, the plasticity regime starts again. They have employed annealing temperature of 900°C and 950°C for carbon and stainless steels respectively. Deng et al. also used an annealing temperature of 900°C beyond which material loses its plasticity history instantaneously for multi-pass welding of stainless-steel tubes. Finally, Shan et al. also set an annealing temperature at 1100°C for SS 316L for a single bead weld (Shan et al., 2009).

As explained with different literature works, there are different ways to implement stress relaxation techniques in the FEM codes. The most common method is to employ an instantaneously stress relaxation temperature that is calibrated with experiment data. Dynamic stress relaxation models and experiment-based stress relaxation models can be more accurate but contributes in increasing the computation time and efforts respectively.

Therefore, in the context of the present work, for the sake of simplicity, we have chosen isotropic hardening with instantaneous stress relaxation temperature beyond which equivalent plastic strain is set to 0. Once the material starts to cool down further from stress relaxation temperature, plasticity regime starts. Stress relaxation temperature is carefully chosen/calibrated after comparing with the experiment data for 1 set of process parameters. The aim is to produce same distortion results obtained during the experiments for a particular set of process parameters. This helps us in determining the calibrated stress relaxation temperature. Once the stress relaxation temperature is chosen, then FE model is compared with different experiment results obtained with different sets of process parameters to justify the accuracy and versatility of the FE model. Stress ( $\sigma$ ) and each strain contribution considered in the model ( $\epsilon_{el}$ ,  $\epsilon_{pl}$  and  $\epsilon_{th}$ ) is negated if average calculated temperature of an element exceeds the calibrated stress relaxation temperature  $T_{relax}$ . The stress relaxation temperature is calculated by reverse-data fitting as advised in the literature (Erik R Denlinger et al., 2015). As stress relaxation feature is not available directly in COMSOL, here is the detail of how the different stress relaxation techniques are implemented in the model.

#### 4.2.2.4.1 Elastic Strain and Stress-free state

To account for the annealing induced SR in the model that leads to stress-free state of the material, relaxation strain should completely negate the elastic, plastic and thermal strain when the temperature is greater than SR temperature. Also, the annealed state refers to complete removal of residual stresses as well. Beyond the high temperature i.e., 1000°C,  $\epsilon_{el}$  and  $\sigma = 0$ , i.e., equivalent plastic strain and residual stresses are put to zero value. In the absence of a correct implementation in COMSOL, this artificial solution is found in the context of the present work.

To achieve this material state ( $\sigma = 0$ , stress-free) in the COMSOL model, elastic strain contribution should be re-set to zero, as stress is calculated by Hooke's law that depends upon elastic strain given in Eq. 4.6. However, it is not possible to directly put  $\epsilon_{el} = 0$  in COMSOL because this feature is not available in the module. This is because elastic strain is the internal state variable calculated by the solver at the back-end of the analysis, so it's not possible to directly put a condition on elastic strain in the COMSOL. To implement  $\epsilon_{el} = 0$  that leads to  $\sigma = 0$ , first a new state variable is created that stores the temperature field at all computation nodes and is updated before each time step. Then another state variable feature with correct state variables name of elastic strain (eel: elastic strain identifier in COMSOL) is defined to track the contribution of elastic strain depending upon temperature. These two steps of defining state variable is shown in Fig 4.4.

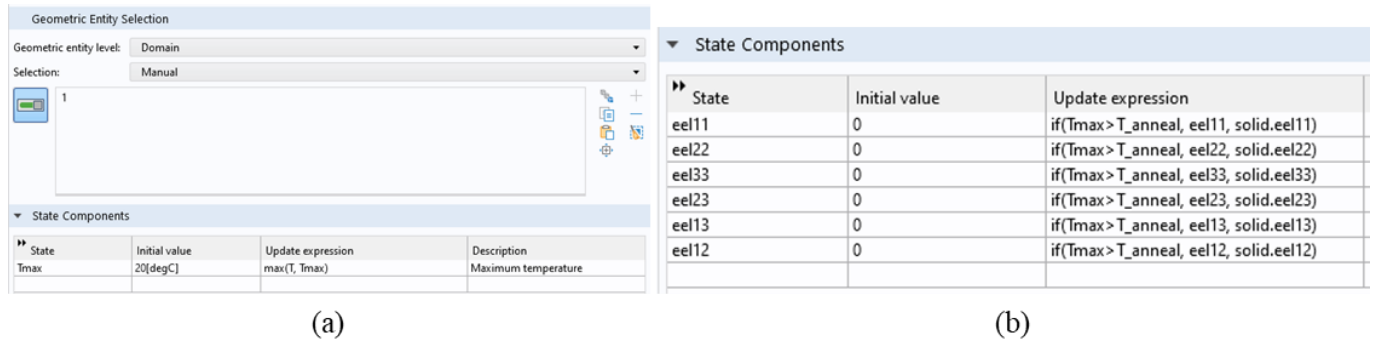


Figure 4. 5: (a) Creating of temperature dependent state variable ( $T_{max}$ )  
 (b) Defining elastic strain (internal state variable on COMSOL) that depends upon  $T_{max}$

Then in the update expression of  $\epsilon_{el}$ , “if” condition is used forcing the solver to re-set the  $\epsilon_{el} = 0$ , if the calculated temperature is higher than SR (annealing) temperature. Otherwise, if calculated temperature is lower than SR temperature, solver is calculating and storing the  $\epsilon_{el}$  in a conventional way. Now to implement this condition and calculate elastic strain in the modified way, an “External Strain” node under “Linear Elastic material” node is used as shown in Fig 4.5. This feature in COMSOL allows to add the external strain defined by the user. This feature is used to implement and calculate the elastic strain in a modified way as explained previously.

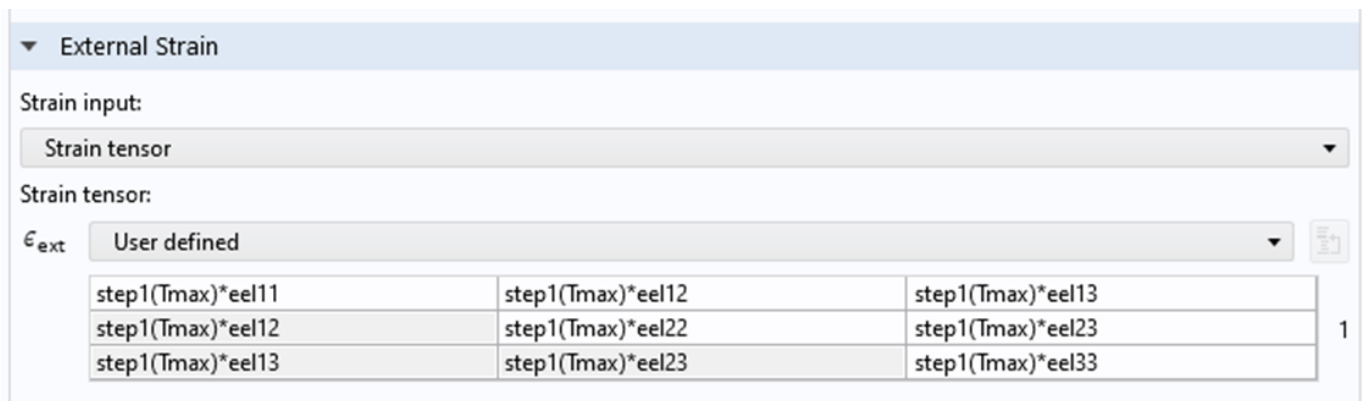


Figure 4. 4: Implementation of elastic strain contribution with relaxation condition as external strain feature in COMSOL

A step function is used at the SR temperature (annealing temperature) to smooth out the transition ( $5^{\circ}\text{C}$  interval at  $T_{relax}$ ) that yields zero elastic strain above SR temperature and some values (calculated but not zero) below SR temperature.

The above implementation in the model will yield  $\epsilon_{el} = 0$  and that in turn yield  $\sigma = 0$  when calculated temperature in the analysis exceeds SR temperature, that correctly represents annealing induced SR in the material during LDED.

#### 4.2.2.4.2 Plastic Strain and Equivalent Plastic Strain

“Equivalent plastic strain” is a scalar measure of the plastic deformation and it does not include the tensorial information that is available/calculated with the components of “Plastic Strain Tensor”. By putting  $\epsilon_{eq} = 0$  leads to re-set the plastic deformation history by keeping the plastic deformation while the material regains its elastic behaviour (yield surface is re-set so that material behaviour goes back to onset of plasticity). This modeling strategy provides more physical results, on the contrary when re-setting the “plastic strain tensor” components to zero ( $\epsilon_p = 0$ ). This re-setting of  $\epsilon_p = 0$  does not co-relate to any physical phenomenon. Because the solver has to compensate the lost plastic deformation with huge elastic strains that is not a correct physical representation of the relaxation phenomenon.

Therefore, it seems more logical to re-set  $\boldsymbol{\varepsilon}_{eq} = \mathbf{0}$  and do not modify the plastic strain tensor in the model. In the model, a condition ( $T > T_{relax}$ ) is set that forces the solver to put  $\boldsymbol{\varepsilon}_{eq} = \mathbf{0}$  if calculated temperature exceeds SR temperature. Now to implement this condition in the COMSOL, “Set variable” feature available under the “Plasticity” node available with “Linear Elastic material” branch is used as shown in **Fig 4.6**. Then a basic if condition is used to implement the above condition of  $\boldsymbol{\varepsilon}_{eq} = \mathbf{0}$  if calculated temperature exceeds SR temperature.



Figure 4. 6: Implementation of equivalent plastic strain condition in COMSOL that removes the deformation history by re-setting the yield surface to the on-set of plasticity of the material

By putting  $\boldsymbol{\varepsilon}_{eq}$  to zero, the plastic evolution/regime of the material is removed and the current state of the material is set to be at the yield state, hence replicating a relaxation phenomenon for the material. This implies that the material deformation remains but due to condition of  $\boldsymbol{\varepsilon}_{eq} = \mathbf{0}$ , it implies that if the material is to deform further, the hardening law will start/commence from the initial yield stress.

#### 4.2.2.4.3 Thermal Strain

Finally, in the numerical model, the thermal strain contribution is negated by introducing a simple if condition in the **Eq. 4.6**, with new thermal strain formulation presented in **Eq. 4.9**.

As explained in Elastic Strain negation modeling, a new state variable  $T_{max}$  is created that stores the updated/calculated temperature at each simulation time step for all mesh points/nodes. As given in Eq. 4.13, when calculated temperature is lower than annealing temperature ( $T < T_{anneal}$ ), thermal strain is calculated in a traditional manner ( $\alpha(T) \times (T - T_{ref})$ ). However, when calculated temperature is greater than annealing temperature ( $T \geq T_{anneal}$ ), a minimum function between  $T_{max}$  and  $T_{anneal}$  will always yield  $T_{anneal}$  and this will always lead to a maximum thermal strain contribution of ( $\alpha(T_{anneal}) \times (T_{anneal} - T_{ref})$ ) and will give the same uniform value no matter how high the temperature reaches at the mesh points/nodes. In this way, in the numerical model, thermal strain contribution is negated if calculated temperature is higher than stress relaxation temperature.

$$\varepsilon_{th} = \begin{cases} \alpha(\min(T_{max}, T_{anneal})) \times (\min(T_{max}, T_{anneal}) - T_{ref}), & T \geq T_{anneal} \\ \alpha(T) \times (T - T_{ref}), & T < T_{anneal} \end{cases} \quad (4.9)$$

The above modeling strategy of thermal strain is implemented in COMSOL by introducing “External Strain” node under “Linear Elastic material” node is used as shown in **Fig 4.7**. This feature in COMSOL allows to add the external strain defined by the user. This feature is used to implement and calculate the thermal strain in a modified way as explained previously.



Figure 4. 7: Implementation of elastic strain contribution with relaxation condition as external strain feature in COMSOL

As explained in Chapter 1, the temperature input for the Mechanical analysis is fed by Thermal analysis which are performed sequentially. So, a thermal analysis is done first that stores the temperature field for all computation time steps. Then, sequentially, a mechanical analysis is performed with temperature field as an input from thermal analysis. Hence, in this way, modified thermal strain that negates the contribution above SR temperature is calculated.

## 4.2.2.5 Satoh Test

### 4.2.2.5.1 Principle

In order to validate the implementation of the above explained thermo-mechanical model in COMSOL, the “Satoh” type test was simulated. This test, was first proposed in 1972 by the Japanese researchers Kunihiro Satoh (Satoh and Ohnishi, 1969) and is commonly used to validate the proper integration of thermo-metallurgical and mechanical models in computer codes (Depradeux, 2004; Ramard, 2018; Tran Van, 2018).

During this test, a cylindrical specimen is heated then cooled in a controlled and homogeneous manner, while preventing axial displacements. This results in an evolution of homogeneous but complex stresses, which can go as far as plasticity and therefore very dependent on the thermomechanical behaviour of the material. The Satoh testing conditions are shown in **Fig 4.8**. It is composed of a heating stage up to 1100°C with a rate of 91.66°C/s following by a cooling of 10°C/s. This thermal cycle is similar to the one proposed in (Depradeux, 2004), who gives also experimental data obtained for a stainless steel 316L, presented in the following section.

$$\varepsilon = \varepsilon_{el} + \varepsilon_{pl} + \varepsilon_{th} = 0 \text{ (EP model)}$$

$$\varepsilon = \varepsilon_{el} + \varepsilon_{vp} + \varepsilon_{th} = 0 \text{ (EVP model)}$$

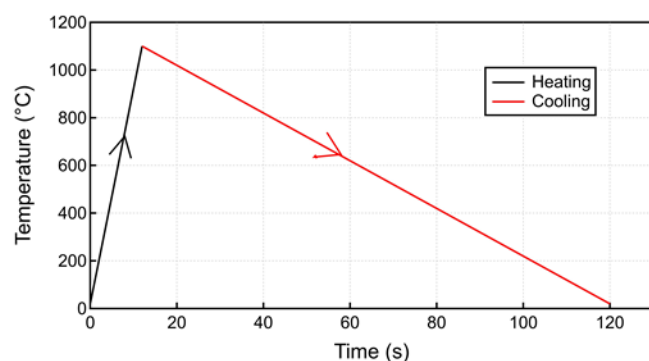
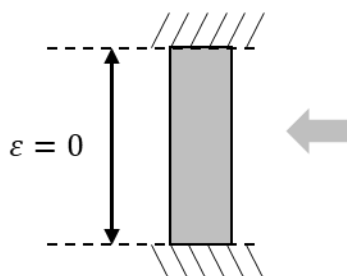


Figure 4. 8: Mechanical constraints and thermal cycle for SATOH test

#### 4.2.2.5.2 Experiment results

The axial stress response of the material for the above SATOH test conditions measured by (Depradeux, 2004) is presented in Fig 4.9. At the start, due to the temperature increase that leads to thermal expansion, but due to the constraints, part is restrained that leads to elastic compression to compensate for the thermal effects. But with further increase of temperature leads to material yielding and there is a drop in stress values with further increase in temperature. This is due to the drop of Elastic Modulus values and yield limit that are dependent upon temperature. At the end of heating phenomenon, stress still remains in compressive state. During the cooling phenomenon, material starts to contract and undergoes elastic recovery that leads to tension stress response. The tension stress increases progressively until the material yields.

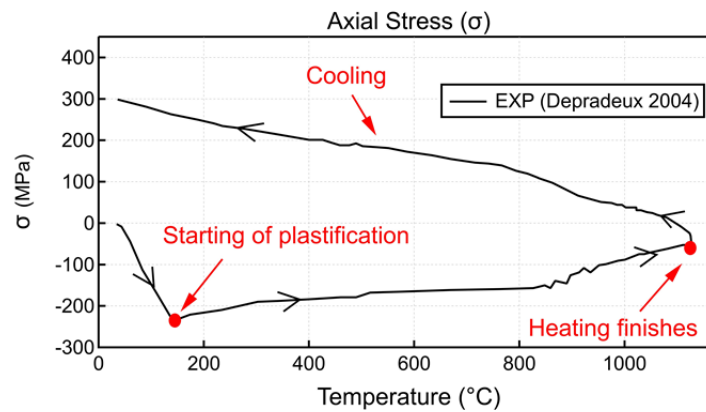


Figure 4. 9: Axial stress obtained in the experiment for SATOH test

This type of thermal loading is representative of LDED process with one thermal cycle (1 layer). It is also possible to impose repeated thermal cycles to simulate cases representative of a multi-pass welding or an additive manufacturing process and to analyse the effect of the cycles on the residual stresses or the type of work hardening (isotropic, kinematic).

This type of simple but very complete test is therefore particularly interesting for validating the implementation of a behaviour law and the parameters associated with it, as well as the analysis of the formation of residual stresses in the context of LDED.

#### 4.2.2.5.3 Numerical results with Elasto-plastic and Elasto-Visco-plastic model

In the context of this thesis, this test was simulated on the one hand, to test different laws of behaviour and on the other hand, to integrate in a simple way the phenomena of stress relaxation at high temperature. At first, a simulation is done with conventional model without relaxation as explained in previous section. The conventional models tested for SATOH test are of 2 types:

1. Thermo-Elasto-Plastic (EP) model with isotropic hardening (Voce law)
2. Thermo-Elasto-Visco-Plastic (EVP) model with Isotropic and Kinematic hardening (Chaboche law)

The temperature dependent material properties and all the parameters of the EVP law (7 parameters) are taken from the literature (Tran Van, 2018). A detailed explanation of transient EVP model that takes into account rate-dependence of the material hardening is presented in the literature (Tran Van, 2018). EVP model with Kinematic hardening is employed to compare the results with EP model with isotropic hardening that is developed in the present work. The material parameters of the EP model correspond to the values given in Fig 4.2 and Table 4.1, presented previously.

The main objective of performing this study (SATO test) is to confirm the correct implementation of the thermo-mechanical behaviour in COMSOL software for complex thermal cycle. Both EP (Isotropic hardening) and EVP models (Isotropic and Kinematic hardening with viscous effects) are then loaded with the SATOH test conditions. The calculations are done on a 2D axial-symmetric model with a single element of 4 nodes since temperature and stresses are homogenous in this test. Temperature is considered uniform and follows the conditions shown in Fig 4.8. The numerical results of obtained stresses with two models are shown in Fig 4.10 in comparison with experiment data.

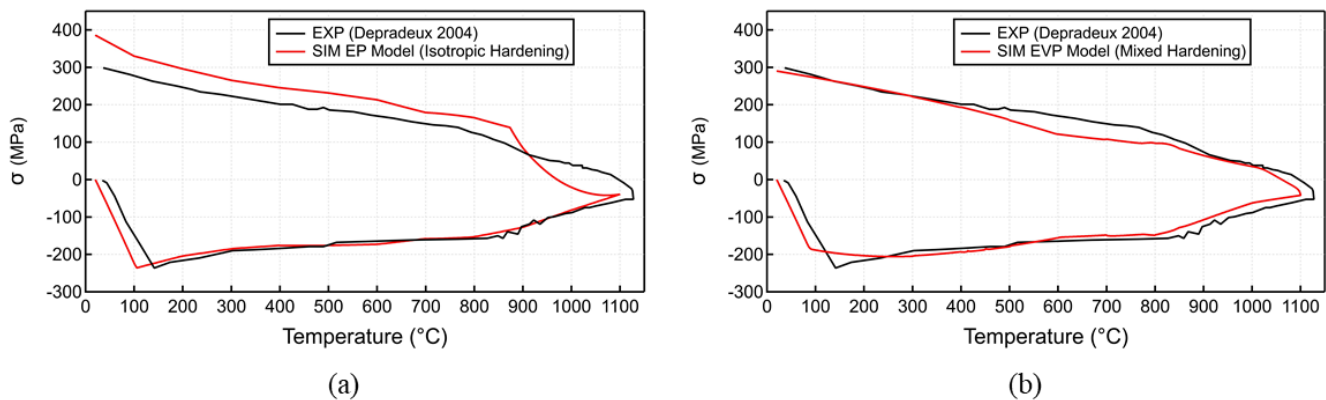


Figure 4. 10: Evolution of stress as a function of temperature for numerical model (SIM) compared to experiment results (EXP)  
 (a) Elasto-Plastic (EP) model with Isotropic Hardening (b) Elasto-Visco-Plastic (EVP) model with Mixed hardening

It can be seen clearly that the stresses obtained with both numerical models have a global shape, that is similar to the results obtained for standard SATOH test. Both models correctly capture stress magnitude and stress states, however the EVP model is more accurate as compared to EP model that slightly over-predicts the stress magnitude upon cooling, and gives a residual stress with an error of 30%. But it was observed that EVP model with mixed hardening is almost two times computationally expensive than EP model with isotropic hardening.

Now, the other phenomenon that needs to be tested is Annealing induce stress relaxation, that was not considered in the previous SATOH test. The stress relaxation modeling strategy that is proposed in Section “Annealing” needs to be verified. So, the Thermo-Elasto-Plastic model with stress relaxation modeling for LDED process is first tested in COMSOL for a SATOH test. With this analysis, it is much easier to understand the above-mentioned modeling strategy.

#### 4.2.2.5.4 Numerical results with annealing phenomenon

##### a) Stress and Elastic Strain

When build part experiences high temperature for a certain duration in LDED process, annealing phenomenon (stress-free state) takes place. So physically, it is a dynamic phenomenon that depends upon time and temperature. But as discussed earlier in Section 2.2.4 “Annealing”, to simplify the model, it is a common practise to impose temperature dependent instantaneous stress relaxation condition. For SATOH test, in EP model, a **SR temperature of 800°C** is selected as a trial, and then SR condition is imposed as explained in Section “Annealing”. However, this value of SR temperature needs to be calibrated for additive manufacturing experiments with the physical part fabrication. The stress and elastic strain results obtained with a conventional and SR model is shown in Fig 4.11. Same thermal loading that is considered in SATOH test (Fig 4.8) is employed.

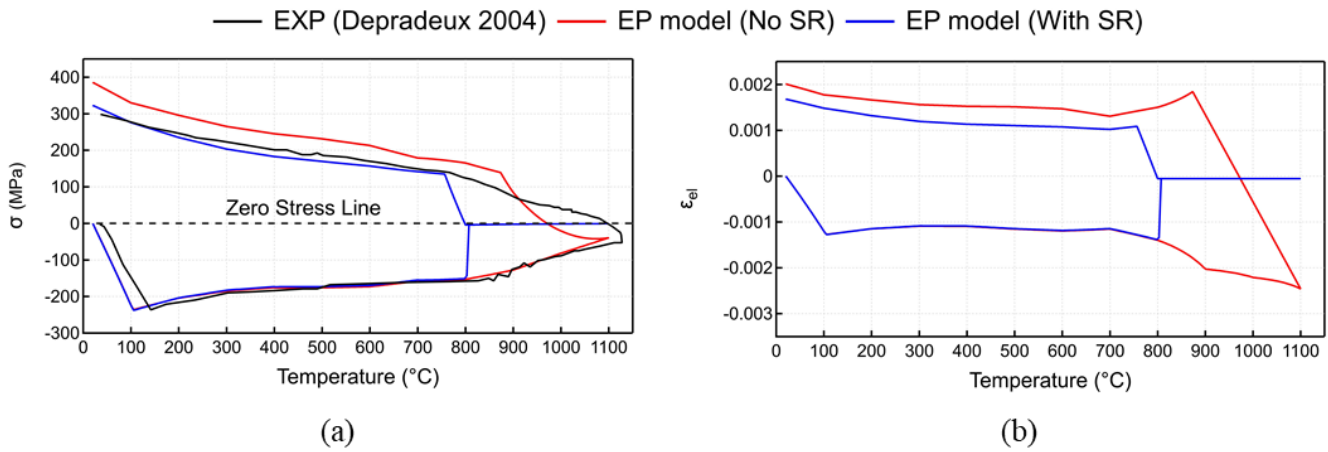


Figure 4. 11: Comparison of mechanical results between Experiment data and numerical results obtained with EP model without stress relaxation (SR) & EP model with SR (a) Stress (b) Elastic Strain

The model with SR yields zero stress and strain results once the calculated temperature exceeds pre-set SR temperature ( $800^{\circ}\text{C}$ ) i.e., ( $T > T_{anneal}$ ). It is worth noting that the SR model gives almost the same final value of stress (around 300 MPa) as obtained in the experiments (300 MPa). Also, the implementation of stress-free state is done correctly in the COMSOL model. Assigning a complete stress-free state beyond  $T_{anneal}$  is not realistic with the experiment data, however it allows to find consistent stress results upon cooling. This methodology of obtaining stress-free state is easy to develop and implement in any FE codes.

#### b) Plastic Strain and Equivalent Plastic Strain

As explained in **Section “Annealing”**, the plastic strain contribution for temperature exceeding SR temperature ( $T_{anneal} = 800^{\circ}\text{C}$ ) should be negated, rather than putting plastic strain equals to zero, as this is not a physical phenomenon. Also, by re-setting equivalent plastic strain to zero brings back the material to its yield state and relieving stresses. Both these objectives are successfully implemented and is shown in **Fig 4.12 and 4.13**.

Evolution of plastic strain and equivalent plastic strain are plotted over temperature as well as time, so that the SR condition can be easily understood and interpreted. It can be observed in **Fig 4.12(a)**, that during heating from  $20^{\circ}\text{C}$  to  $T_{anneal}$ , plastic strain magnitude starts to increase until  $T_{anneal}$ . With further increase

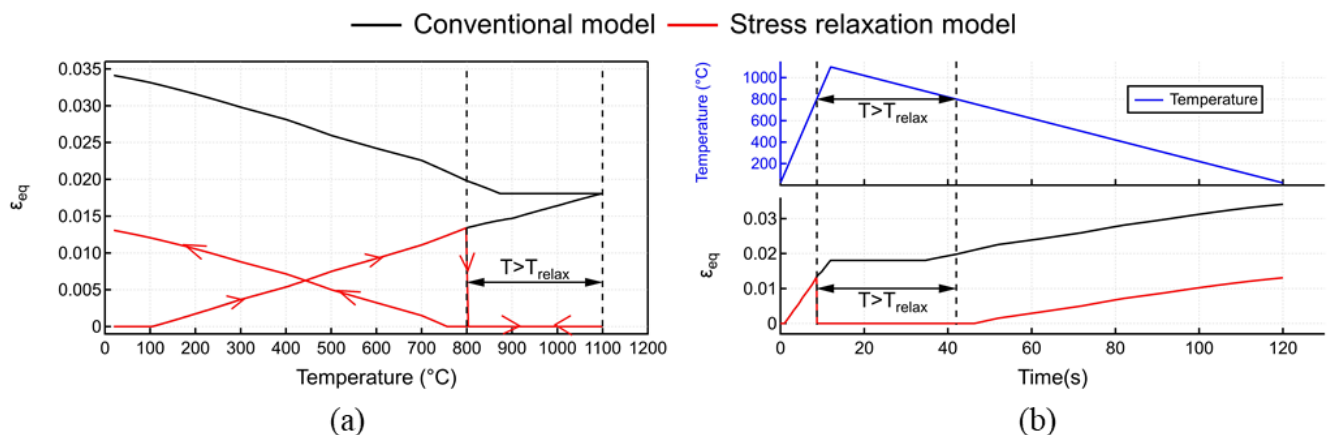


Figure 4. 12: Comparison of equivalent plastic strain obtained with conventional model & stress relaxation model Equivalent Plastic strain plot over (a) Temperature (b) Time

in temperature above  $T_{anneal}$  to  $1100^{\circ}\text{C}$  (peak value), and upon cooling from  $1100^{\circ}\text{C}$  to  $T_{anneal}$ , there is no contribution of plastic strain as it keeps constant values as shown in **Fig 4.12(b)** with  $T > T_{anneal}$  zone is highlighted with dotted lines. The magnitude of plastic strain starts to decrease progressively upon cooling when temperature falls down from  $T_{anneal}$  and progressively decreases until it reaches room temperature

(20°C). Equivalent plastic strain that defines the material hardening evolution is also implemented correctly as shown in Fig 4.13. Arrows signs are used to represent the path history of the evolution of equivalent plastic strain as shown in Fig 4.13(a). During the duration of  $T > T_{anneal}$ , equivalent plastic strain is equal to zero as shown in Fig 4.13(b), justifying the material has kept the plastic deformation but has returned to its yield limit.

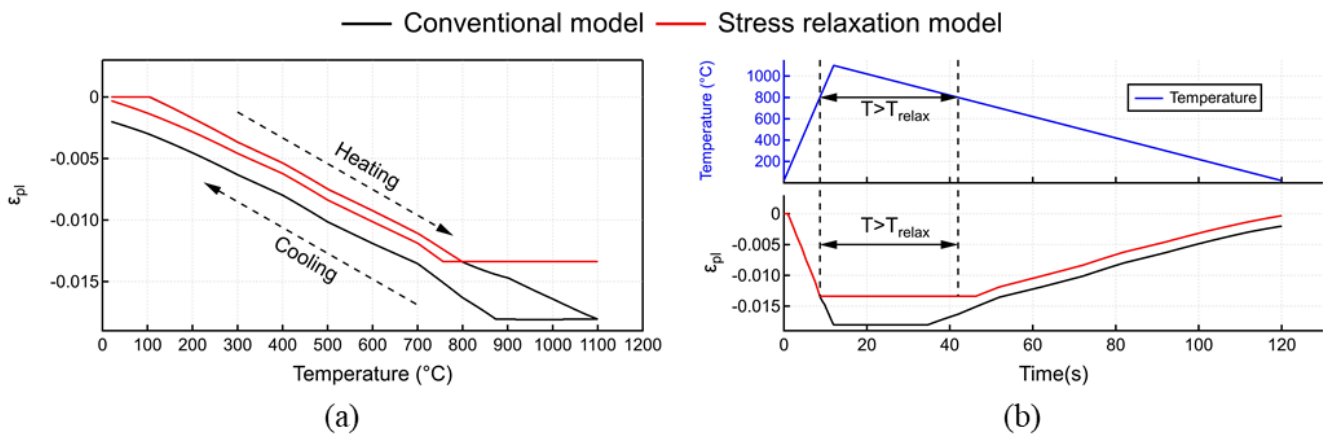


Figure 4. 13: Comparison of plastic strain obtained with EP model without SR and EP model with SR  
Equivalent Plastic strain plot over (a) Temperature (b) Time

### c) Thermal Strain

The modeling strategy of negating the contribution of thermal strain is explained Section "Annealing". The implementation of negation of thermal strain contribution if  $T > T_{anneal}$  is correctly implemented in COMSOL as presented in Fig 4.14.

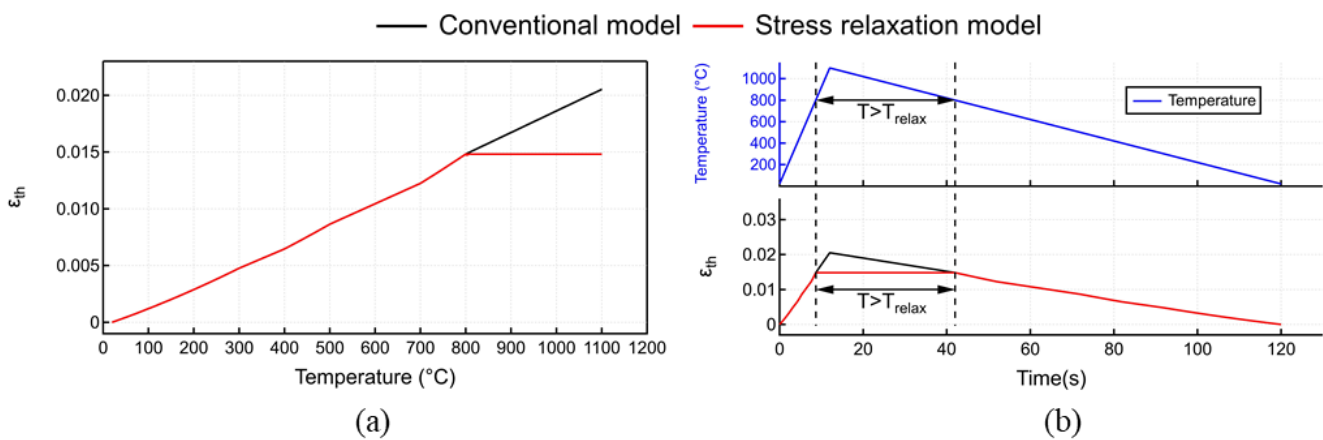


Figure 4. 14: Comparison of thermal strain obtained with conventional model & stress relaxation model  
Thermal strain plot over (a) Temperature (b) Time

Thermal strain calculation is directly proportional to temperature, therefore thermal strain keeps on increasing and decreasing when temperature increases and decreases respectively in a conventional model. However, with SR model, when  $T > T_{anneal}$ , the thermal strain values remain constant and do not contribute in the analysis for this duration. Hence, the objective of negating the contribution of different strains when  $T > T_{anneal}$  is successfully achieved and SR model is implemented correctly in COMSOL.

For part scale simulations, same idea of conventional and SR model is employed. But, at first, a detailed description of experiment set-up is provided in next section. In the literature, more complex thermal cycle (repeated heating & cooling cycle) is employed for SATOH test to represent multi-layer deposition to analyse stress accumulation (Depradeux, 2004). The proposed EP model with SR successfully handles this repeated thermal cycle and results are provided in Appendix (Chapter 4). As employed by many researchers in the

literature especially for SS 316L (Cambon, 2021; Depradeux, 2004), EP model is chosen by keeping in mind the main objective of the thesis i.e., simulation of large parts. However, more emphasis is required to identify the experimentally calibrated SR temperature for EP model.

### 4.3 Experiment Set-Up of a SS 316L wall build by LDED process

The numerical modeling approach explained in the previous **Section 2** is applied to simulate the thermo-mechanical responses during the deposition of SS 316L. A detailed explanation of the experiment set-up and process parameters is provided in this section. Single and double adjacent beads thin wall structures of SS 316L were deposited on a substrate measuring 100 mm long, 50 mm wide, and 3 mm thick of the same material as build wall with LDED process. In-house developed machine named MAGIC is used for LDED system that is equipped with a 2kW Diode laser by IPG laser system. To achieve the process stability, laser and powder are co-focussed on the top surface of the substrate. Laser and incoming powder have top-hat and gaussian distribution respectively.

All the experiments were performed with a scanning speed of 1m/min with a zig-zag deposition strategy. Powder deposition rate of 13 g/min for SS 316L powder feedstock (Oerlikon, grain size 45-106  $\mu\text{m}$ ) was chosen. The diameter of the laser beam spot size was 2.2 mm in diameter at the top-surface of the substrate. **Fig. 4.15(a)** shows the schematic of substrate's dimensions along with clamping conditions & planned wall build for experiment case 1. **Fig. 4.15(b)** shows the in-situ measurement locations for thermocouple and laser displacement sensor at the bottom face of the substrate. **Fig. 4.15(c)** shows the tooling with substrate fixed to clamp and laser displacement sensor attached to the tooling, **Fig. 4.15(d)** shows the wall build obtained for experiment case 1 along with a schematic of deposition direction. In-plane deposition for 2-bead wall is also zig-zag approach that is shown in **Fig. 4.19(b)**. Each wall build is 42 layers high, with a longitudinal zig-zag deposition strategy. Effect of waiting time (dwell time) between successive layers is analysed keeping laser power 800 W and laser scan speed 1m/min fixed. 0, 5, and 10 s dwell time were taken between the deposition

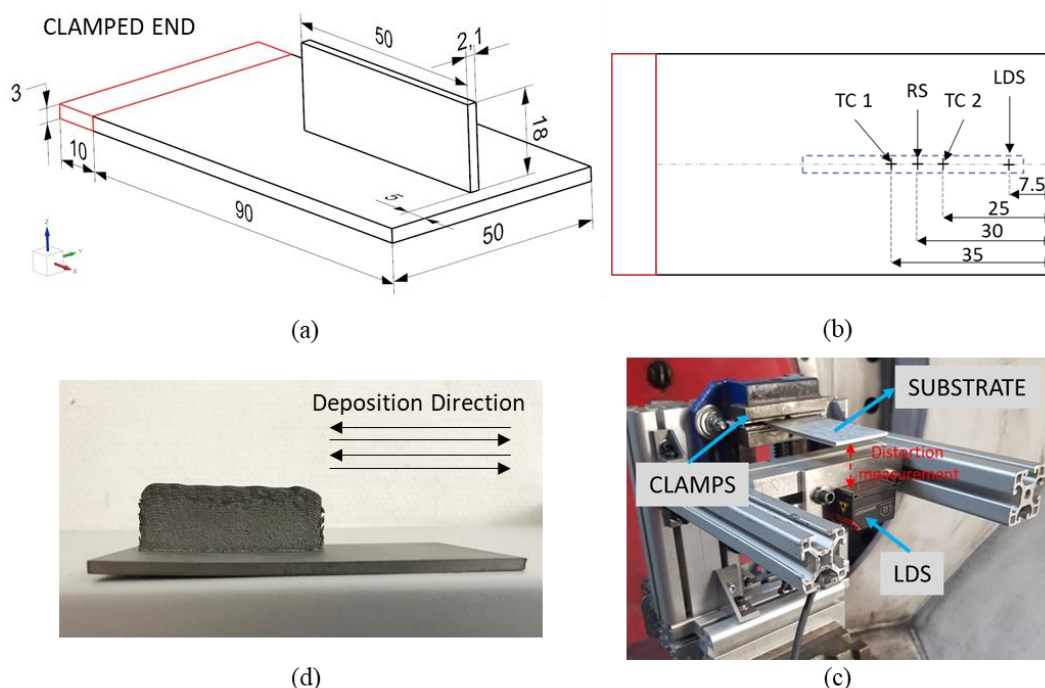


Figure 4. 15: (a) Substrate and build wall dimensions (in mm), (b) Measurement locations at substrate, (c) Experimental set-up of in-situ measurement (d) Post-Process build wall along with depiction of deposition strategy

of successive layers to expose the workpiece to different cooling time. Effect of dwell time is studied on two different wall builds, single and double bead wall. Experiment cases with different process parameters is summarised in **Table 4.2**.

Table 4. 2: Description of the cases and process parameters used in the present work

| Case | No. of beads | Dwell Time (s) | Wall Length (mm) | Wall width (mm) | Wall height (mm) |
|------|--------------|----------------|------------------|-----------------|------------------|
| 1    | 1            | 0              | 50               | 2.1             | 18               |
| 2    | 1            | 5              | 50               | 2.1             | 18.1             |
| 3    | 1            | 10             | 50               | 2.1             | 18.2             |
| 4    | 2            | 0              | 50               | 3.4             | 23.2             |
| 5    | 2            | 5              | 50               | 3.4             | 23.5             |
| 6    | 2            | 10             | 50               | 3.4             | 23.6             |

### 4.3.1 Temperature measurement

Omega GG-K-30 type K thermocouples of 250  $\mu\text{m}$  diameter are employed to measure the *in-situ* temperature. Two different locations are chosen at the bottom face of the substrate to record the temperature evolution as shown in **Fig. 4.15(b)**, so that they fall under the deposition path of the laser on the top surface of the substrate. Type of Thermocouples, data acquisition system (DAQ) and its acquisition frequency are kept same as explained in Section 3.1 “Temperature measurement” of Chapter 3.

### 4.3.2 In-situ distortion measurement

The experimental set-up and tooling are designed to clamp the substrate from one end and let it distort at the free end during and after the deposition process as shown in **Fig 4.15(c)**. A Micro-Epsilon 1420 Laser Displacement Sensor (LDS) with a linear accuracy of  $\pm 20 \mu\text{m}$  was attached to the tooling to record the in-situ deflection of the substrate in the build direction i.e., z-direction. The exact measurement location of the LDS sensor is shown in **Fig 4.15(b)**. The LDS optical signals are read and converted by RS422/USB converter into a USB data packet. The Micro-Epsilon sensor TOOL software records data at a sampling rate of 250 Hz.

### 4.3.3 Post-process line distortion measurement

After the deposition process is finished and the workpiece is cooled down, workpiece is scanned with a Faro 3D Laser Scan Arm V3 Optical scanner with a scanning accuracy of 65  $\mu\text{m}$ . Once the laser scanning is finished, Geomagic Control software is used to process the data obtained from the laser scanning. Then the scanned data is compared with the workpiece CAD file that acts as a reference design in Geomagic control. Then distribution is measured and analysed experimentally at the line of bottom surface of the substrate. The comparison of laser scanned data of the deposited wall to the workpiece’s CAD is shown in **Fig. 4.16(a)**. Distortion is analysed and measured at the centre line of the bottom face of the substrate as shown in **Fig. 4.16(b)**.

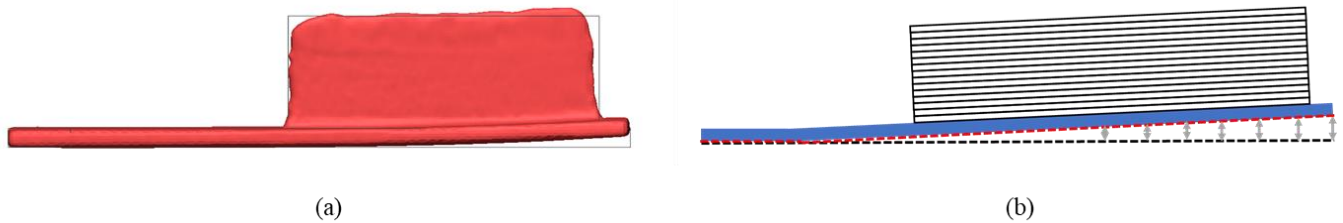


Figure 4. 16: (a) Experimental Optical 3D scanned data superimposed on reference CAD for Case 4  
(b) Schematic showing the location for measurement of post-process line distortion

## 4.4 Numerical implementation

### 4.4.1 FEA solver

COMSOL Multiphysics based solver (PARDISO) is employed to perform the FEM analysis. To reduce the computation time, adaptive time stepping method is used rather than strict formulation. Computation time step of  $R/v_s$  is taken during the material deposition period and  $3R/v_s$  during the dwell time period. This feature of adaptive time stepping should be noted when comparing with experimental results in the coming section. All simulations are done on a workstation equipped with 16 cores, 128 GB RAM and an Intel Xeon W-2275 processor.

### 4.4.2 FEM mesh

Three-dimensional finite element meshes of both single and double bead walls, generated in COMSOL Multiphysics is presented in Fig. 4.17. Same mesh is used for the thermal model as well as mechanical model. The mesh for single bead wall contains 48,370 Hex-8 elements and 60,480 nodes. Mesh for double bead wall contains 78,708 Hex-8 elements and 91,854 nodes. The mesh elements for the wall builds are taken as 2 per laser radius and 1 per layer thickness. A coarse mesh is used for the substrate as the heat source moves away from the wall builds.

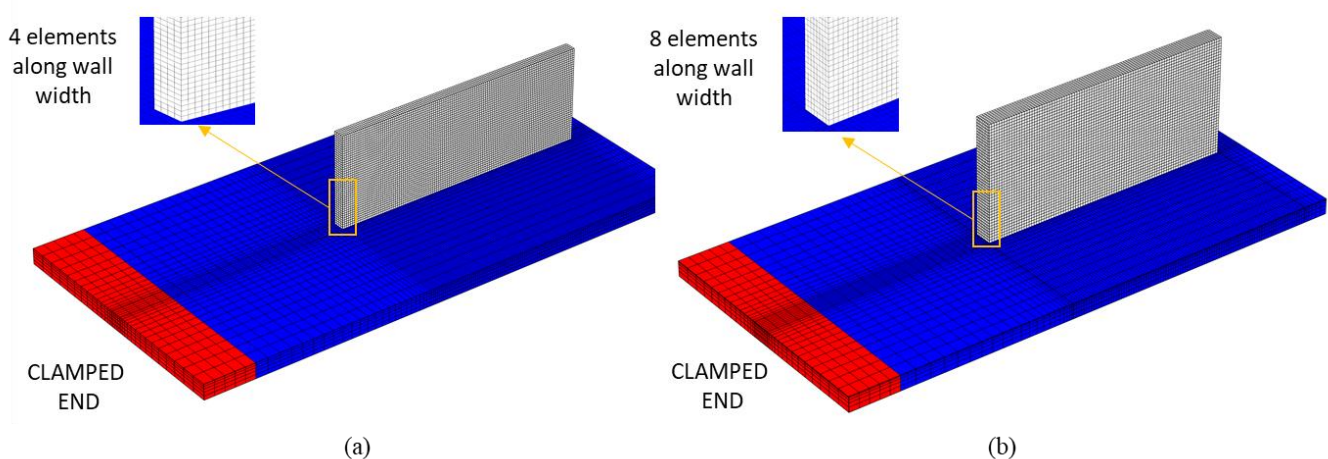


Figure 4. 17: FE meshes used for numerical simulation of LDED process: (a) 1-bead wall; (b) 2-bead wall

### 4.4.3 Material deposition modeling

Material deposition modeling is done in the same way as explained in detail in Section 4.4.1 “Quiet/Active Material Activation Method” of Chapter 2.

## 4.4.4 Model calibration and boundary conditions

As explained in Chapters 2 & 3, layer geometry is simplified, parameterisation of numerical heat source (DE) and the effect of forced convection & heat loss due to conduction heat transfer from deposited part to substrate is considered in the same way with same parameters values.

## 4.5 Results and discussion

### 4.5.1 Comparison of temperature evolution

Thermal model predicts the thermal response of the workpiece which is compared to the experimental measurements for all cases. **Fig. 4.18** shows the experimental results, as measured by thermocouple 1 (TC1), compared to numerical results at nodes corresponding to the thermocouple locations for all experiment cases. In order to highlight the deposition process, all the graphs have a double scale X axis. As explained in the previous section (**Experiment Set-up**), indeed thermocouples 1 and 2 are at different locations on the bottom face of substrate, however they are along the deposition line. Hence, they record almost same temperature evolution but with a time offset. Therefore, for this reason, only thermocouple 1 results are presented in the graphs. However, recorded data from both thermocouples is presented in Appendix (Chapter 4).

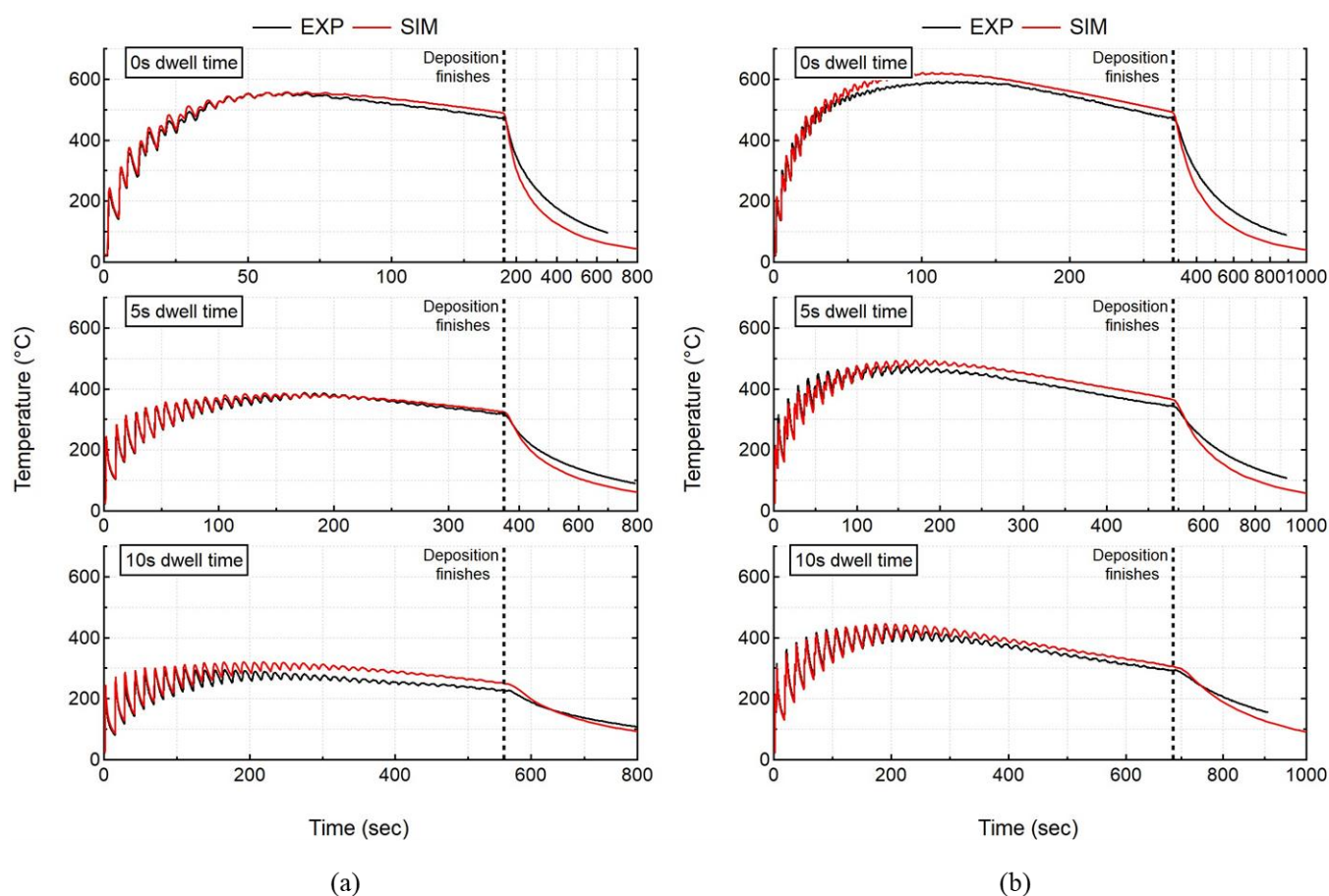


Figure 4. 18: Comparison of numerical results (SIM) with recorded In-situ thermal history (EXP) of thermocouple 1 for all cases. (a) 1 bead wall (b) 2 bead wall

Shorter dwell time ( $t_{DW}$ ) results in higher peak temperatures exceeding 550°C (Case 1) and 600°C (Case 4) for single and double beads wall respectively. Increase of  $t_{DW}$  results in lower peak temperature exceeding 250°C (Case 3) and 450°C (Case 6) for both single and double bead wall respectively, since the already deposited material has more time to cool down before switching the laser on again. Increase in number of beads in wall builds leads to higher deposited volume, that also plays a significant role in the thermal evolution in the workpiece. Increase in number of beads results in higher peak temperatures for all  $t_{DW}$  cases. Single bead wall experiences peak temperatures of 550, 390 and 270°C for 0, 5 and 10s respectively. However, double bead wall experiences higher peak temperatures of 600, 500 and 420°C for 0, 5 and 10s respectively. For double bead wall, there is no dwell time between the first and second bead deposition, thereby depositing second bead beside first bead without allowing it cool down. The single wall also experiences the same phenomenon where layer 1 (1 bead) does not have cooling time as layer 2 (1 bead) start depositing above layer 1 without allowing it to cool. But double bead wall deposits more volume as compared to single bead wall that leads to different thermal evolution in the workpiece. This can be observed in **Fig. 4.19**, that shows the comparison of temperature evolution at the TC1 location during the deposition of first two layers for single and double bead walls. Temperature obtained at the end of second layer is much higher for double bead wall as compared to single bead wall. This trend is followed for the deposition of the complete wall as well.

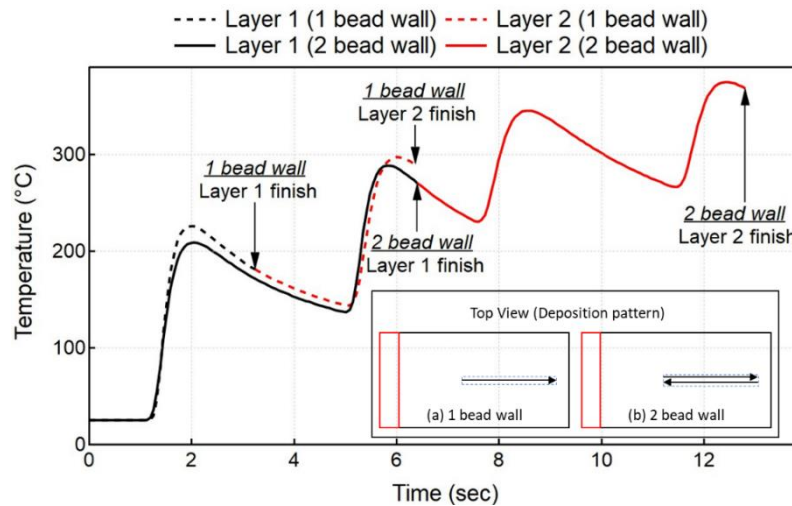


Figure 4. 19: Comparison of temperature evolution between 1 and 2 bead walls at TC1 during the deposition of first two layers

It can be noticed that 1 & 2-bead wall experiences same temperature evolution for the first 1-2 seconds, but then 2-bead wall records lesser temperature magnitude. This is due to the fact that TC are placed at the centre of deposition width for both experiment cases. Therefore, for 1-bead wall, it is placed at the centre (symmetric to bead width) that experiences peak intensity, but for 2-bead, it is not symmetric to the first bead deposition and that's why it records less temperature peak as it experiences lesser intensity. The thermal results of the transient heat transfer analysis are in close agreement with the experimental results of thermocouple presented in **Fig. 4.7**. Average deviation between experiment and simulation results are calculated by comparing computation instances in time This is why, simulation results are linearly re-sampled over time.

$$\text{Average deviation} = \frac{\sum_{i=1}^n |(T_{exp})_i - (T_{sim})_i|}{n} \quad (4.10)$$

where  $n$  is the total number of simulation time increments between the start and end of computation analysis,  $i$  is the current time increment,  $T_{exp}$  is the measured temperature, and  $T_{sim}$  is the simulated temperature. The largest average deviation at thermocouple 1 is found to be 13.2°C for case 3. **Table 4.3** shows the computation

time & average deviation at thermocouple 1 for all experiment cases obtained for the 42 layers wall of 50 mm deposition length. As it can be seen in **Fig 4.18** that during the cooling period, numerical results shows some discrepancies as compared to thermocouple measurements. A better agreement could be achieved by employing a complex (location and time dependent) convective heat transfer coefficient as suggested by (Heigel et al., 2015).

Table 4. 3: Experiment cases examined for thermal model validation via thermocouple

| Case | No. of beads | Dwell Time (s) | Computation time | Average deviation (°C) |
|------|--------------|----------------|------------------|------------------------|
| 1    | 1            | 0              | 4 h 42 min       | 4.2                    |
| 2    | 1            | 5              | 5 h 41 min       | 5.2                    |
| 3    | 1            | 10             | 7 h 22 min       | 13.2                   |
| 4    | 2            | 0              | 8 h 36 min       | 5                      |
| 5    | 2            | 5              | 9 h 5 min        | 6.4                    |
| 6    | 2            | 10             | 10 h 20 min      | 6.6                    |

## 4.5.2 Comparison of in-situ distortion evolution

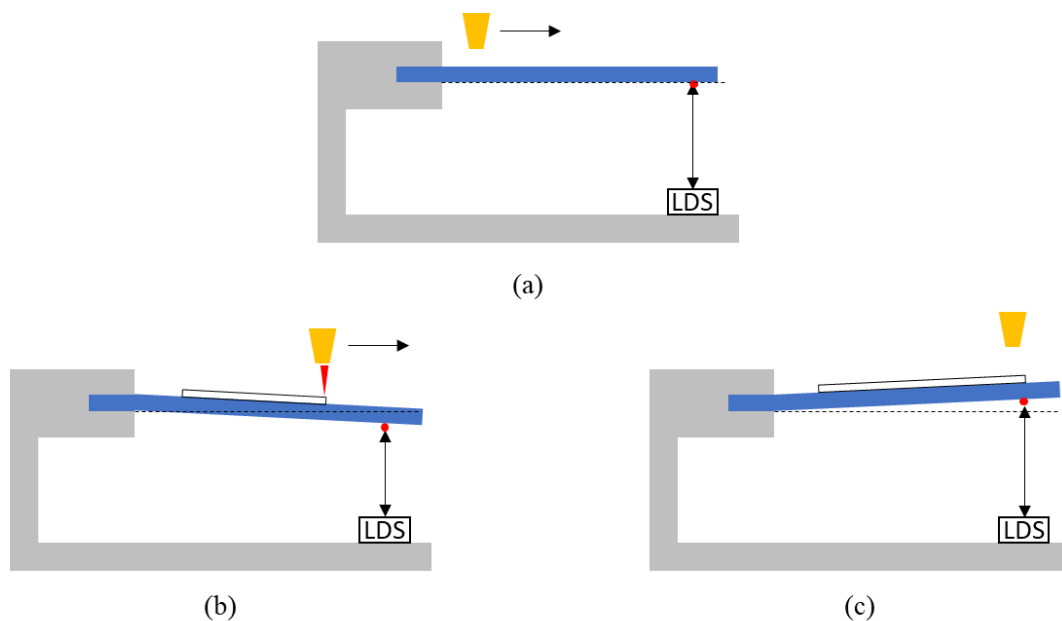


Figure 4. 20: Schematic showing substrate response during LDED process  
(a) Pre-deposition process (b) During deposition process (c) During cooling

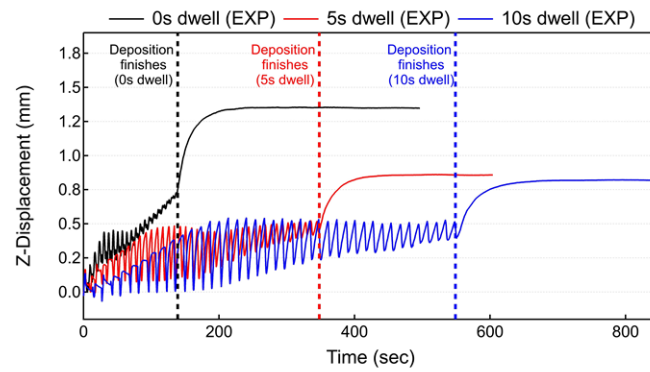
### 4.5.2.1 Experiment results

In-situ distortion measurement provides an important information concerning the process physics that would remain hidden if only post-process measurements are used for the analysis. However, for analysing the in-situ results, it is mandatory to understand the evolution of the substrate during the LDED process and to identify different phenomenon. A schematic illustrating these different phenomenon or stages in the evolution of distortion during LDED process is shown in **Fig 4.20**. **Fig 4.20(a)** shows the undeformed substrate before the deposition process along with a schematic representing experiment set-up for cantilever tooling. **Fig 4.20(b)**

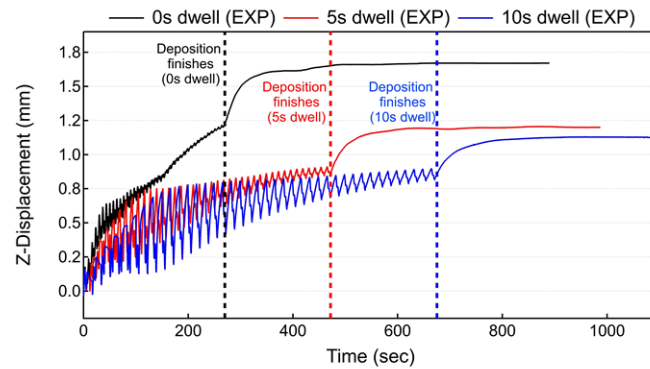
is representing the substrate's response during the start of the deposition that leads to downward distortion of the free end of the substrate. Laser-powder is co-focussed on the substrate's top face and their interaction leads to material fusion with high melt-pool temperature. Due to the high thermal diffusivity of SS 316L, bottom face of the substrate also experiences increase of temperature, but much below than the fusion temperature. This causes larger thermal expansion at the top surface relative to the bottom surface of the substrate causing the substrate to distort downwards as shown in **Fig 4.20(b)**. The downward distortion of the substrate is recorded by LDS as a decrease in distortion values. Once the layer deposition is finished, melt-pool and substrate begin to cool, leading to contraction, causing the free-end of the substrate to deflect upwards as shown in **Fig 4.20(c)**. The upward deflection of substrate is recorded by LDS as an increase in distortion values. The distortion cycle of substrate's downward and upward deflection for each layer follows the same behaviour pattern for the subsequent layers until the process is finished. Once the process is finished, workpiece is still at a relatively higher temperature. Upon cooling, substrate sharply deflects upwards recording a sharp rise in positive values recorded by LDS. This kind of cantilever tooling is very famous among the researchers as it allows to record sufficient level of displacement magnitudes that can be useful to validate the mechanical model. Same pattern of substrate response has been recorded by different researchers in the literature for the cantilever tooling for different materials (Cambon, 2021; Erik R. Denlinger et al., 2015; Denlinger and Michaleris, 2016; Xie et al., 2020b).

#### 4.5.2.1.1 Effect of dwell time on in-situ distortion measurement

In-situ distortion measurements during LDED process is successfully recorded for all experiment cases for single and double bead wall ranging for dwell times ranging from 0, 5 and 10s as shown in **Fig 4.21**. Once the deposition process is finished, the build-part and substrate are at much higher temperature. Therefore, to analyse the workpiece response upon cooling from high temperature to room temperature, the acquisition was done until the build-part is completely cooled down. It can be noticed in **Fig 4.21**, for all experiment cases, once the deposition process is finished, there is a sharp vertical rise of substrate justifying the effect of thermal contraction. After this sharp vertical rise, substrate's movement stabilises as the thermal gradient decreases because workpiece temperature stabilises as well. So, the substrate's displacement follows the basic (simplified) principle of upward and downward movement upon thermal expansion (heating) and contraction (cooling) respectively. With an increase in dwell time, the upward and downward distortion phenomenon or magnitude becomes more prominent. For all experiment cases independent of dwell time and number of beads, it is observed that distortion trend and accumulation is consistent throughout the deposition process. However, distortion magnitude accounting for each layer starts to decrease after the deposition of 20-22 layers as the heat source keeps moving up from the substrate.



(a)



(b)

Figure 4. 21: In-situ distortion accumulation recordings for all experiment cases (effect of dwell time)  
 (a) 1 bead wall (b) 2 bead wall

As can be seen in **Fig 4.21**, for SS 316L with cantilever tooling, an increase of dwell time results in decrease of distortion for both single (**Fig 4.21a**) and double beads wall (**Fig 4.21b**). Effect of dwell time is more influential when dwell time is increased from 0 to 5 s leading to sharp fall in final distortion values from 1.347 mm to 0.858 mm (36%) and 1.67 mm to 1.2 mm (28%) for single bead and double bead wall respectively. However, with further increase of dwell time from 5 to 10 s leads to lesser level of distortion from 0.858 mm to 0.817 mm (5%) and 1.2 mm to 1.125 mm (6%) for single bead and double bead wall respectively. This leads to a conclusion that effect of dwell time surely impacts the distortion trends and magnitude, however dwell time's effect diminishes with further increase of dwell time from 5 s. Finally, it can be concluded with the experiment results presented that the dwell time makes it possible to minimise distortions for LDED process.

#### 4.5.2.1.2 Effect of number of beads on in-situ distortion measurement

Also, increasing the number of beads results in an increase of distortion values for all dwell time cases as shown in **Fig 4.22**. Effect of number bead is influential for all dwell time ranging from 0 to 10 s leading to sharp increase in final distortion values. With an increase in number of beads from 1 to 2 beads, distortion values have a sharp increase from 1.347 mm to 1.67 mm (24%) for 0s dwell time. For 5s dwell time also, distortion values have a sharp increase from 0.858 mm to 1.2 mm (40%). Finally, for 10 s dwell time, this trend is repeated with a sharp increase from 0.817 mm to 1.125 mm (38%).

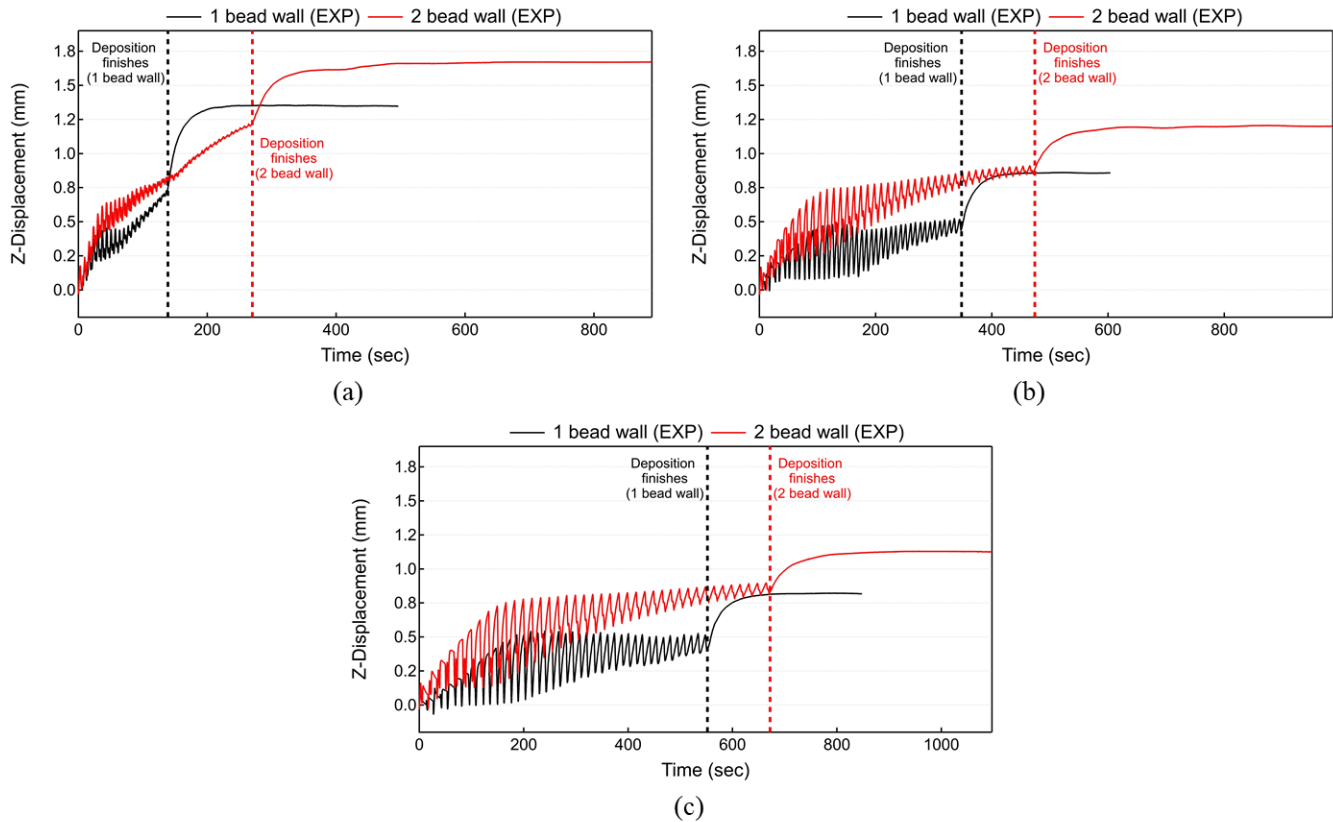


Figure 4. 22: In-situ distortion accumulation recordings for all experiment cases (effect of number of beads)  
 (a) 0s dwell time (b) 5s dwell time (c) 10s dwell time

#### 4.5.2.2 Numerical model results

Workpiece is experiencing repeated thermal expansion and shrinkage behaviour due to the repeated thermal cycle of heating and cooling respectively. This leads to the continuous accumulation of distortion throughout the process. **Fig. 4.23** shows the final calculated deformed configuration (Z-displacement) for single bead wall with no dwell time (Case 1) obtained EP model with stress relaxation.

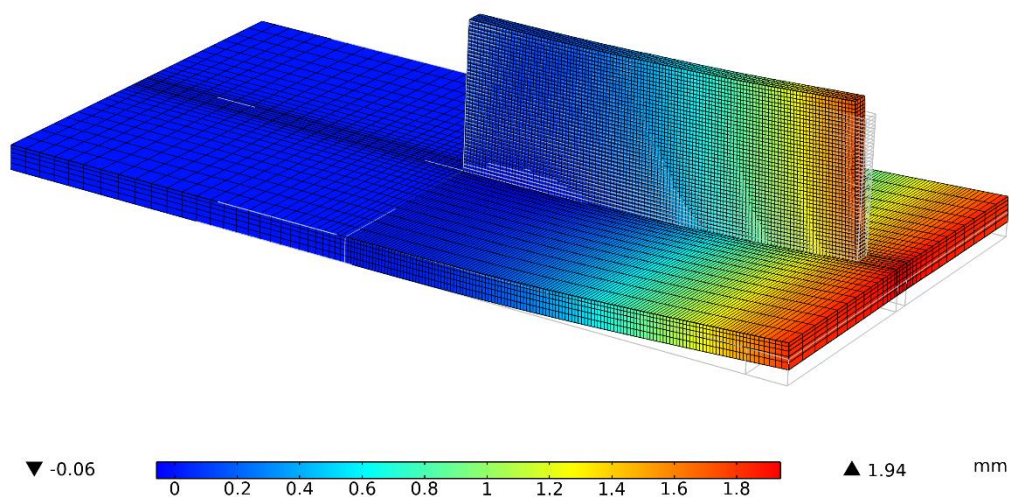


Figure 4. 23: Mechanical Model showing the final deformed configuration for Case 1

### 4.5.2.2.1 Effect of stress relaxation in LDED process modeling

The mechanical response of the workpiece is calculated by the mechanical model and then compared to the experimental measurements for all cases. Fig. 4.25 and Fig 4.26 shows the experimental results of in-situ distortion at the free-end of the substrate measured by LDS, compared to numerical results at node corresponding to the LDS location for all experiment cases. As discussed previously, distortion is caused by expansion and shrinkage during material heating and cooling phenomenon respectively. The numerically calculated in-situ distortion is done at a node corresponding to the LDS measurement location during the experiment. Before proceeding directly to the numerical results, annealing induced stress relaxation (SR) temperature ( $T_{relax}$ ) needs to be calibrated. So, for experiment case 1 (single bead with 0s dwell time), iterative simulations are done to reverse-fit the numerical distortion results with experiment LDS data as shown in Fig 4.24.

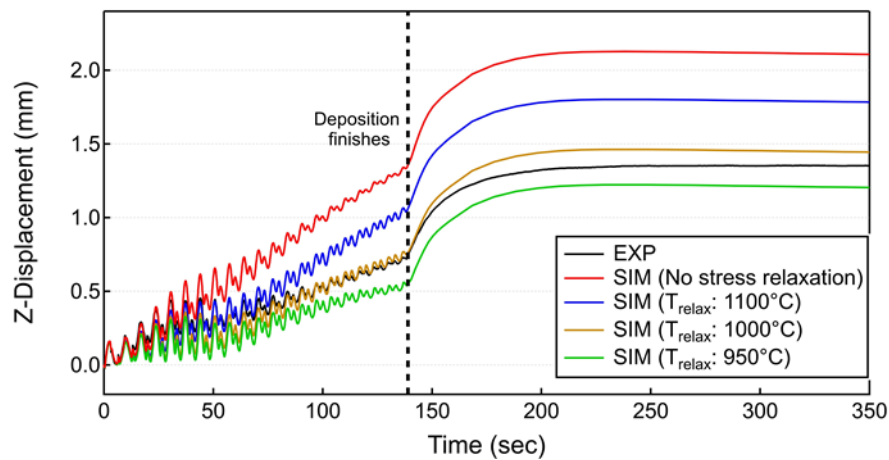


Figure 4. 24: Effect of stress relaxation temperature on numerical distortion accumulation at LDS location for experiment case 1

It can be noticed that numerical model without SR (red curve) significantly over-predicts the numerical distortion accumulation in comparison with experiment distortion data (black curve). Then different  $T_{relax}$  are considered with  $T_{relax} = 1100^{\circ}\text{C}$  (blue curve) also over-predicting the distortion accumulation in comparison with experiment distortion results. With  $T_{relax} = 1000^{\circ}\text{C}$  (dark-orange curve), numerical distortion curve correctly fits the experiment distortion curve with a computation error of less than 5%. With  $T_{relax} = 950^{\circ}\text{C}$  (green curve), numerical distortion under-predicts the experiment results, signifying that further drop of  $T_{relax}$  will result in more computation errors as numerical model will under-predict more. It can be concluded that the numerical model's response is very sensitive to  $T_{relax}$  and  $T_{relax} = 1000^{\circ}\text{C}$  yields correct mechanical response. Therefore, for the sake of consistency, it has been decided that for all further simulations of single and double bead (0,5 and 10 s dwell time), same  $T_{relax} = 1000^{\circ}\text{C}$  is employed for numerical model that employs instantaneous stress relaxation model.

Fig. 4.25 shows the numerical distortion results (SIM) with and without stress relaxation (SR) compared with experimental results (EXP) for 1 bead wall. Both models correctly capture the distortion trend throughout the deposition correctly. However, the numerical model without stress relaxation does not capture the distortion magnitude correctly as it predicts significantly higher levels of distortion as compared with experiment data for all cases. It captures the distortion magnitude correctly for first few layers, but then starts to overpredict

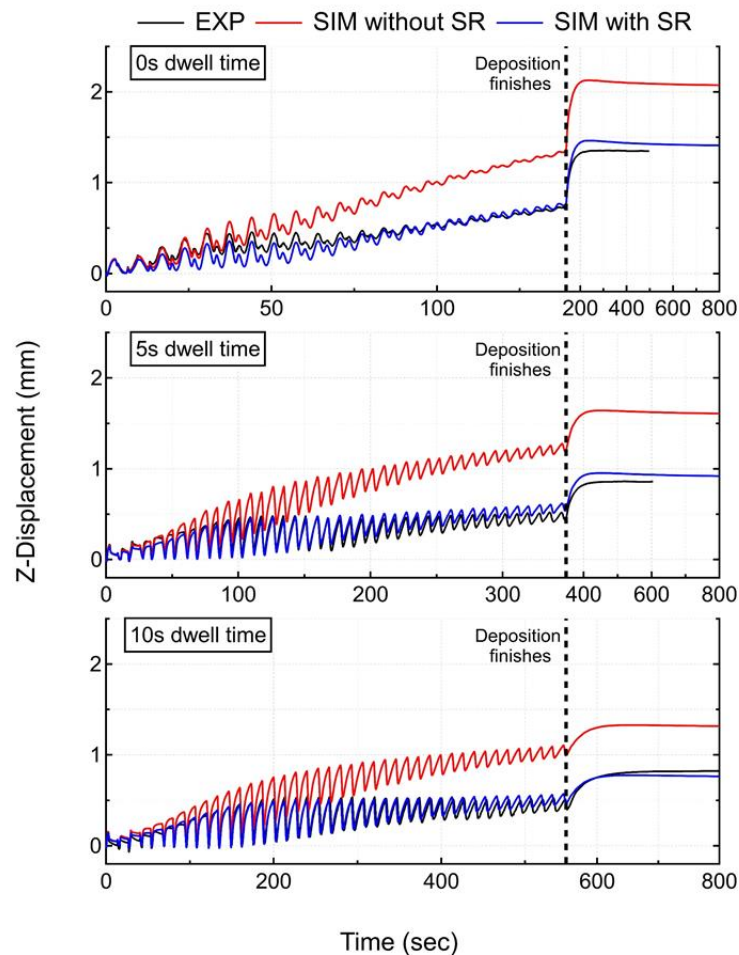


Figure 4. 25: Comparison of numerical results (SIM with and without stress relaxation (SR)) with recorded In-situ distortion accumulation of LDS (EXP) for different dwell times for 1 bead wall deposition

for the subsequent layer's deposition suggesting the effect of annealing and liquefaction induced stress relaxation in LDED. Unlike, the numerical model without stress relaxation, the numerical model with stress relaxation correctly captures both the distortion trend and magnitude for the complete deposition process. This justifies the need for including the effect of liquefaction and annealing induced stress relaxation in the numerical model.

The conclusions drawn from the comparison done for 1 bead wall is also validated with 2 bead wall results as shown in **Fig 4.26**. Here also, model without SR captures the distortion trend but fails to capture the magnitude correctly as it significantly overpredicts the distortion. On the contrary, model with proposed SR correctly captures both distortion and magnitude. Here also, it can be noticed that for the first few layers, model without SR performs correctly, but as the number of layers deposition keeps on increasing, it starts to accumulate error by overpredicting the distortion magnitude. This can be due to the fact that the model without SR excludes the effect of annealing and liquefaction induced stress relaxation in LDED. This phenomenon of SR present in LDED is double checked for both single and double bead wall experiment cases.

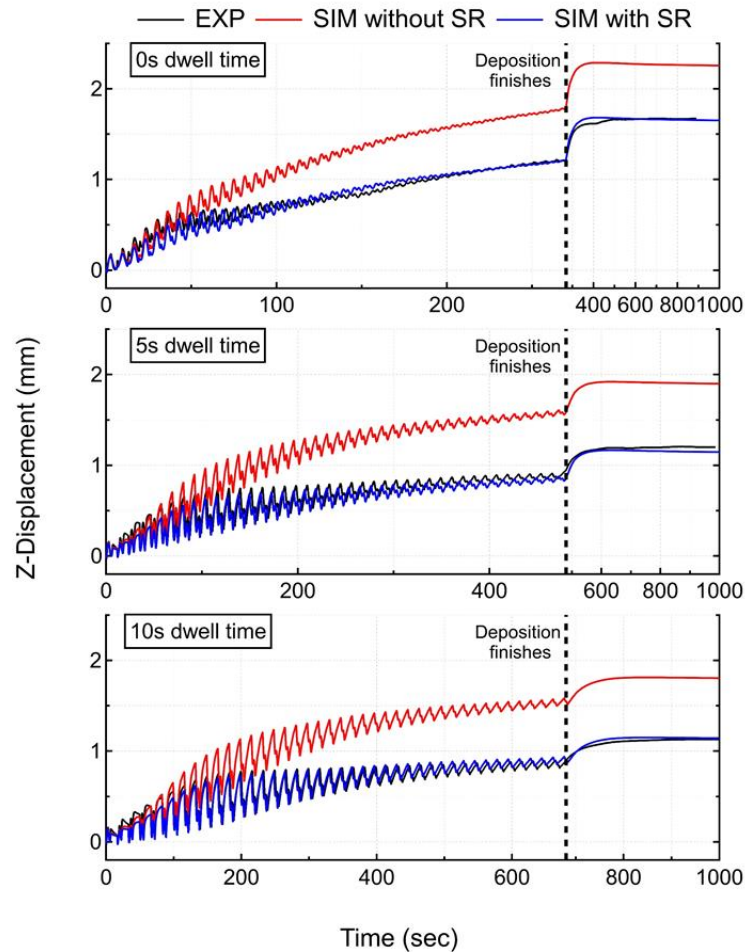


Figure 4. 26: Comparison of numerical results (SIM with and without stress relaxation (SR)) with recorded In-situ distortion accumulation of LDS (EXP) for different dwell times for 2 bead wall deposition

The numerical model with stress relaxation captures the thermal expansion and shrinkage trends correctly and in close agreement with the experiment results for all cases. **Table 4.4** shows the computation time, average deviation (averaged over all LDS measured values) and final error (last measurement recorded by LDS) at LDS location for all experiment cases.

Table 4. 4: Experiment cases examined for mechanical model validation via LDS

| Case | No. of beads | Dwell Time (s) | Computation time | Average deviation (mm) |         | Error (%) |         |
|------|--------------|----------------|------------------|------------------------|---------|-----------|---------|
|      |              |                |                  | No SR                  | With SR | No SR     | With SR |
| 1    | 1            | 0              | 10 h 45 min      | 0.185                  | 0.029   | 52.9      | 3.9     |
| 2    | 1            | 5              | 16 h 7 min       | 0.25                   | 0.06    | 85.3      | 4.9     |
| 3    | 1            | 10             | 18 h 37 min      | 0.17                   | 0.042   | 57.8      | 9.4     |
| 4    | 2            | 0              | 24 h 19 min      | 0.12                   | 0.069   | 34.7      | 1.8     |
| 5    | 2            | 5              | 28 h 41 min      | 0.27                   | 0.049   | 57.5      | 5.8     |
| 6    | 2            | 10             | 29 h 55 min      | 0.313                  | 0.041   | 58.9      | 0.3     |

#### 4.5.2.2.2 Relaxation phenomenon during LDED

With the increase in number of deposition layers, due to the thermal accumulation phenomenon, temperature of the build part and substrate increases. This phenomenon is shown in **Fig 4.27** depicting the areas/domain that are above the relaxation temperature i.e., 1000°C (see the colour legend) during (a) 1<sup>st</sup> layer, (b) 20<sup>th</sup> layer and (c) 42<sup>nd</sup> layer.

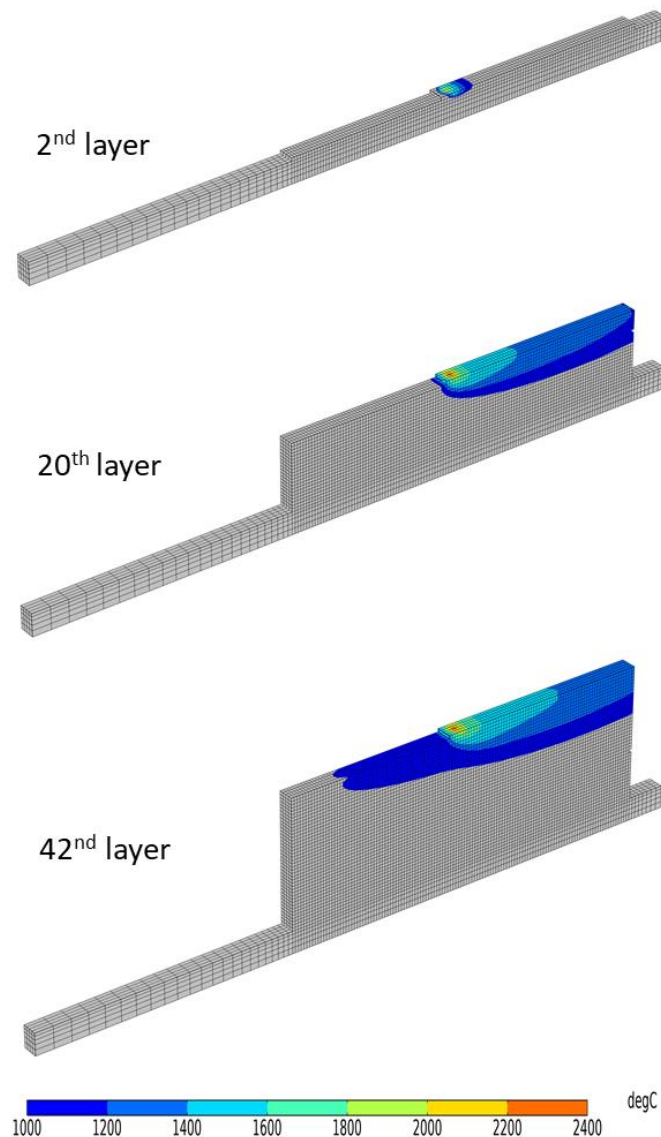


Figure 4. 27: Depiction of temperature field highlighting stress relaxation domain

The coloured area in **Fig 4.27** highlights the domain where calculated temperature is higher than the calibrated relaxation temperature. Therefore, in the coloured area of the deposited material, in the proposed model relaxation phenomenon takes place. As can be seen in **Fig 4.27**, during the deposition of 2<sup>nd</sup> layer, there is very small domain where the relaxation takes place. However, as the number of deposition layers increases, domain representing temperature above relaxation temperature grows significantly during the deposition of 20<sup>th</sup> layer. This phenomenon of domain enlargement with an increase in deposition layers can be noticed during the deposition of last or 42<sup>nd</sup> layer. Therefore, it can be concluded that the relaxation behaviour plays a significant role on the distortion during the deposition of multiple layers, which is an inherent feature of LDED process. Hence, for the development of an accurate thermo-mechanical model, annealing induced stress relaxation phenomenon need to be incorporated in the model.

## 4.5.3 Comparison of post-process line distortion results

### 4.5.3.1 Experiment results

Once the LDED process is finished and the workpiece is allowed to cool, then the workpiece is removed from the tooling's clamp and a 3D scanning is done to obtain the part-level distortion. Once the scanning is finished, then it is superimposed with the original CAD file/geometry. Then a comparative analysis is done between scanned file and CAD file on the Geomagic Control software to measure the global distortion. These results provide additional information to analyse the distortion pattern all over the workpiece. Also, these experiment results are used to validate the numerical model. The post-process optical 3D scanning results for all experiment cases are presented in **Fig 4.28**.

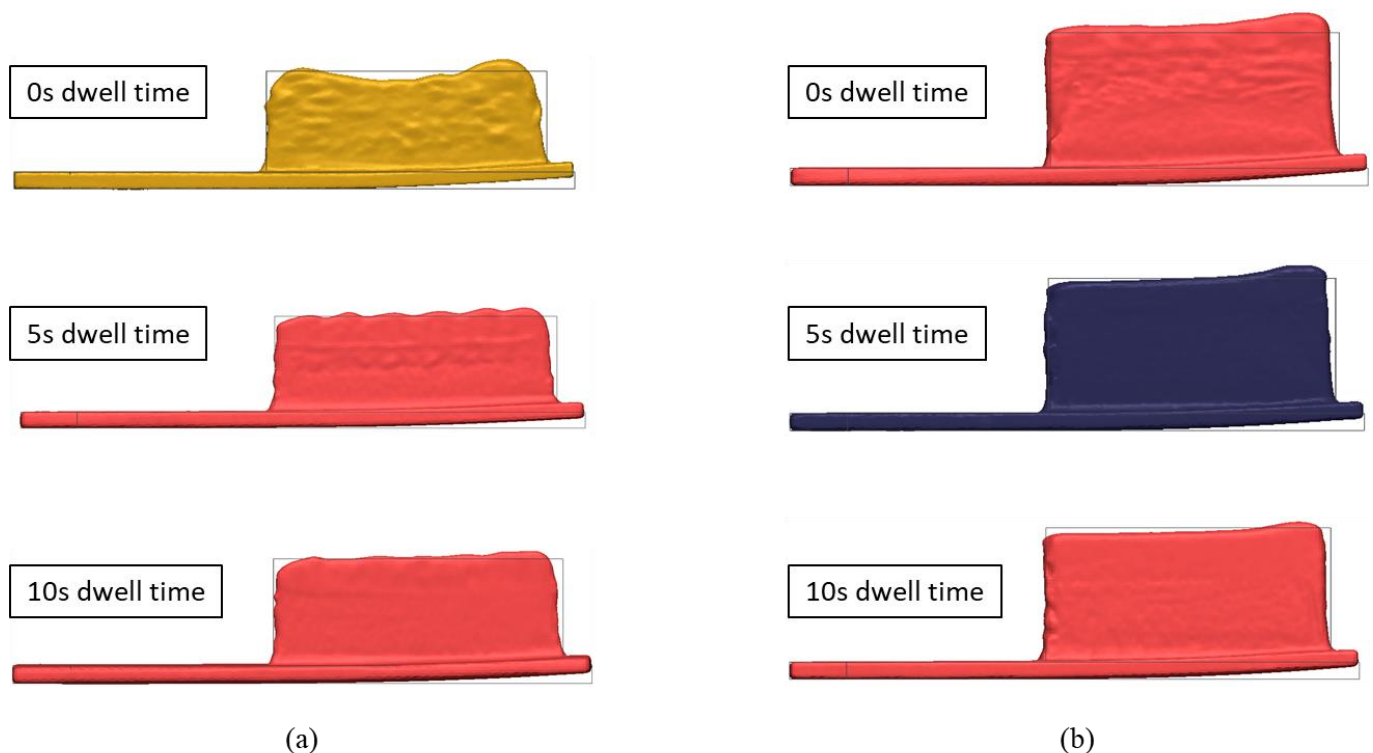


Figure 4. 28: Comparison of Post-Process 3D scan with reference CAD geometry for all experiment cases  
(a) 1 bead wall (b) 2 bead wall

The global distortion pattern of the substrate remains same for all experiments case with maximum distortion at the free end. For 1 bead wall, and 0s dwell time, material deposition is not smooth as it leads to more material deposition at the deposition ends. However, with an increase in dwell time, material deposition is smoother and uniform.

With an increase in dwell time, it can be noticed in **Fig 4.28** that distortion at the free end of the substrate is decreasing. Also, with an increase in number of beads, it leads to an increase in distortion at the free end. These post-process distortion results are coherent with the in-situ LDS results discussed in the previous sections.

### 4.5.3.2 Numerical model results

Once the numerical analysis of the deposition is finished, unclamping of the substrate is also simulated by removing the fixed constraint. However, to simulate the unclamping process, 2-3 points are clamped to give initial and sufficient boundary condition for the solver to initialise correctly, otherwise workpiece has the possibility to rotate and deflect un-symmetrically. The unclamping numerical analysis takes few seconds to finish and it was noticed that there was not a big difference in distortion results between two models pre-clamped and post-clamped removal model. The workpiece final numerical deformation obtained after the clamp removal is presented in **Fig 4.29** for all cases.

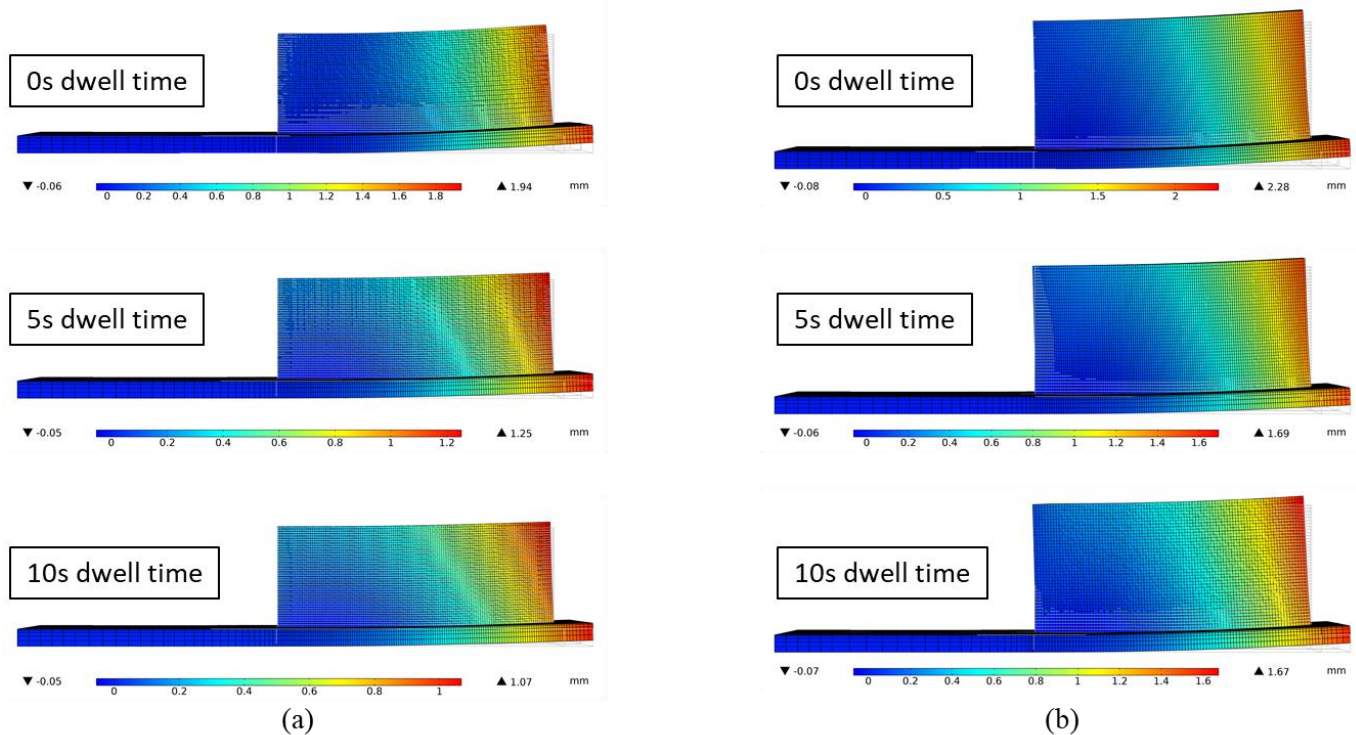


Figure 4. 29: Comparison of Post-Process 3D scan with reference CAD geometry for all experiment cases  
(a) 1 bead wall (b) 2 bead wall

The numerical model is predicting the same material response found in the experiment as we discussed earlier in the previous section i.e., with an increase of dwell time, distortion value at the free-end is decreasing and with an increase in number of beads, distortion value at the free-end is increasing. The mechanical model's calculated distortions at part scale show good agreement with experiment post-process distortions measured by Optical scanner as shown in the previous section in **Fig. 4.28** for all experiment cases.

The numerical model with stress relaxation correctly captures the post-process distortion shape and magnitude for all cases as shown in **Fig. 4.30**. The numerical model without stress relaxation significantly over-predicts the distortion for all cases. Hereby justifying the need of including stress relaxation in the numerical model. As was observed with in-situ distortion, post-process distortion also follows the same trend that, an increase of dwell time results in decrease of post-process distortion for both single and double bead wall. Also, an increase in number of beads results in an increase of post-process distortion values for all dwell time cases. These trends are well captured by the numerical model and hence shows its versatility. The final measurement recorded by LDS sensor before workpiece was unclamped is marked on the **Fig. 4.30**. This comparison highlights the fact that LDS sensor and Optical 3D scanner gives consistent values of distortion.

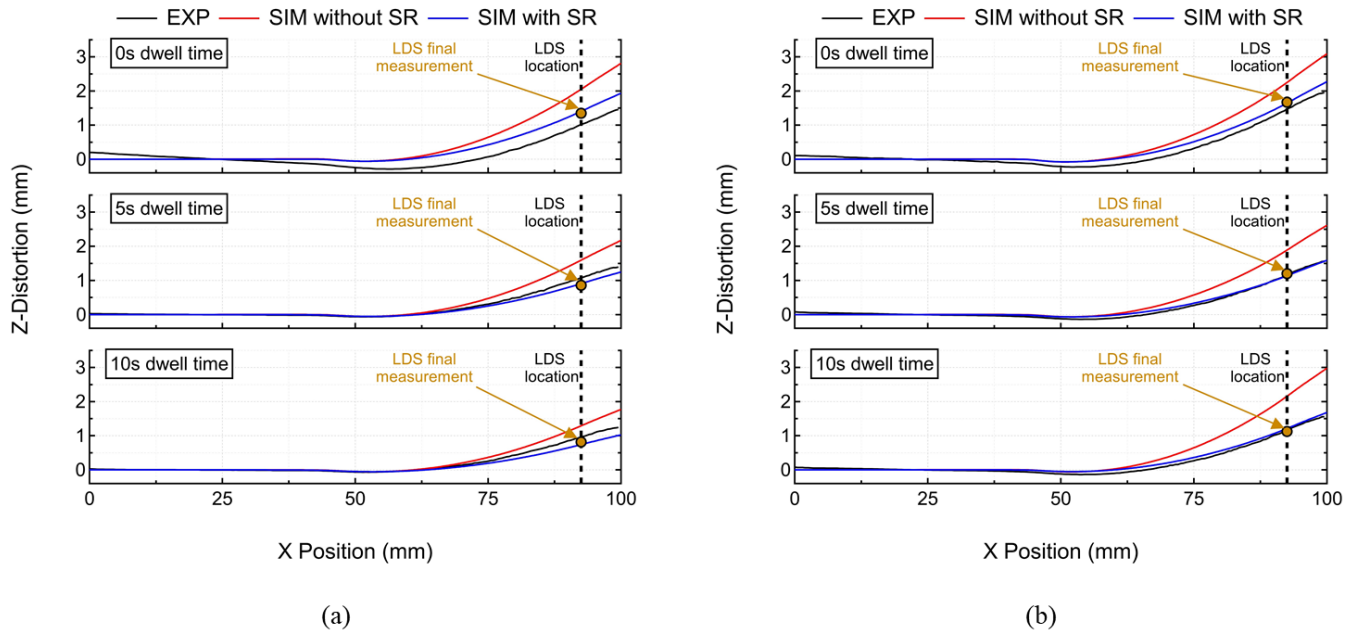


Figure 4. 30: Comparison of numerical results (SIM with and without stress relaxation (SR)) with experimental post-process line distortion results of Optical scanner (EXP) for different dwell times.

(a) 1-bead wall, (b) 2-bead wall

## 4.6 Simulation Speed-up

Due to the feature of big track size in LDED and combined with the specified computation time increment of  $R/v_s$ , this leads to high computation time given in **Table 4.3 and 4.4**. Therefore, to reduce the computation time, as discussed in **Chapter 3**, an elongated ellipsoid (EE) line heat input model is employed that averages the heat source over its deposition path (Irwin and Michaleris, 2016).

$$Q_{EE} = \frac{6\sqrt{3}AP}{\hat{a}bc\pi\sqrt{\pi}} \exp\left(-\frac{3(x + v_s(t + \frac{1}{2}\Delta t))^2}{\hat{a}^2} - \frac{3y^2}{b^2} - \frac{3z^2}{c^2}\right) \quad (4.11)$$

where the length of each EE sub-track or segment  $\hat{a}$  is (Irwin and Michaleris, 2016):

$$\hat{a} = \frac{v_s \Delta t}{2} \sqrt{\frac{3}{\log 2}} \quad (4.12)$$

Instead of taking hundreds of computation time steps employing DE heat source, with EE model, large computation time steps are possible in the analysis. However, employing such large computation time increments leads to large computation average deviation as well (Irwin and Michaleris, 2016). Therefore, it is recommendable to divide the deposition scan (track length) into multiple successive linear scans (sub-tracks) along the deposition path. For each individual linear scan, EE source is applied in one computation time increment. Hence, different track sizes (sub-track) are chosen and investigated for EE source as done in Chapter 3 and published in (Nain et al., 2021). Material activation from quiet to active state is done in with the same procedure as explained in previous Chapter 3. The dimensionless number  $K_E$ , introduced in Chapter 3, is also used in order to make a comparison of different elongated lengths (sub-track).

$$K_E = \frac{v_s \Delta t}{a} \quad (4.13)$$

Goldak's double ellipsoid or any other heat source model requires  $K_E \leq 1$  to simulate the continuous motion of heat the source without skipping over some elements. **Table 4.5** presents different elongated lengths and parameters used in the present work.

Table 4. 5: Elongated Ellipsoid (EE) heat source model parameters used in this chapter

| $K_E$ | Computation time step FEM ( $\Delta t$ )<br>(s) | EE length ( $\hat{a}$ )<br>(mm) | No. of sub-tracks per layer<br>(Wall Length/ $\hat{a}$ ) |             |
|-------|---|---------------------------------|--|-------------|
|       |   |                                 | 1 bead wall  | 2 bead wall |
| 4     | 0.528   | 9.15                            | 6  | 12          |
| 8     | 1.056   | 18.3                            | 3  | 6           |
| 12    | 1.584   | 27.46                           | 2  | 4           |

With an increase of  $K_E$ , length of elongated ellipsoid ( $\hat{a}$ ) increases that leads to reduction of computation time steps. However, it also leads to averaging of laser energy over larger domains that reduces the peak intensity

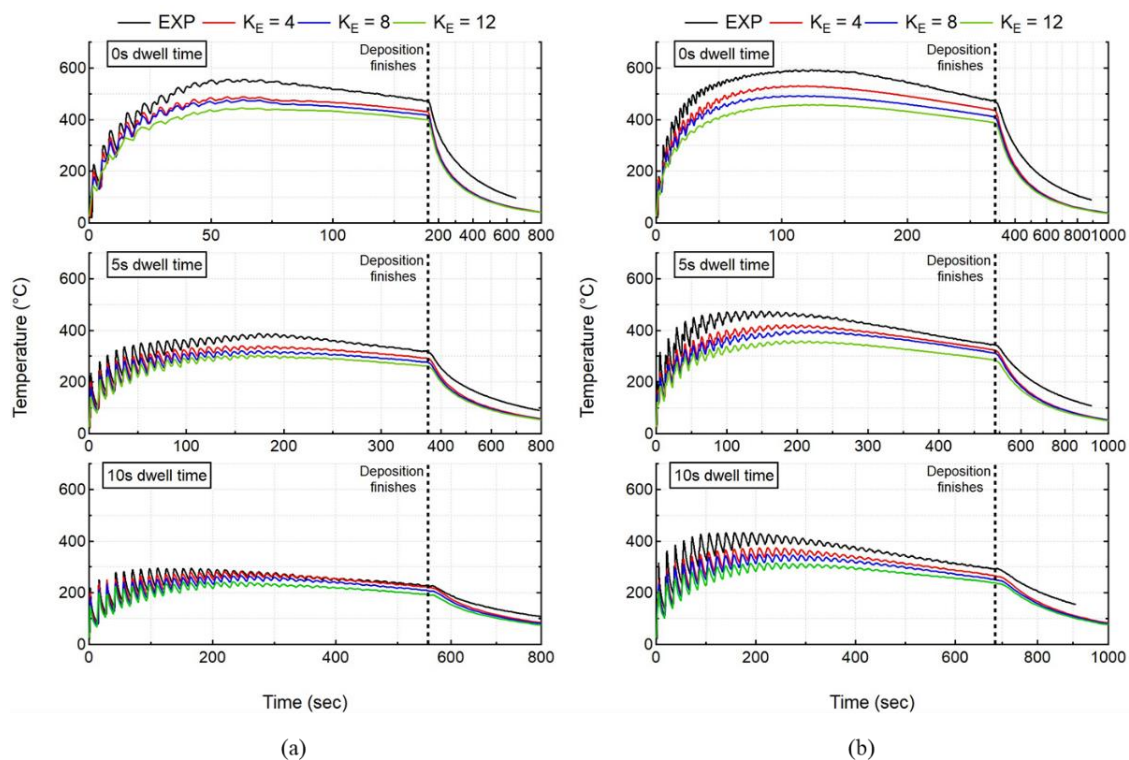


Figure 4. 31: Comparison of numerical results using Elongated Ellipsoid with recorded In-situ thermal history of thermocouple 1 for all cases. (a) 1-bead wall, (b) 2-bead wall

of the elongated ellipsoid heat source, that leads to an increase in computation average deviation. For all cases, with different  $K_E$  values, numerical model can capture the trends of temperature evolution, however the mean and peak temperature values have reduced that is proportional to  $K_E$  as shown in **Fig. 4.31**.

It can be noticed, that with an increase in  $K_E$ , computation average thermal deviation at the thermocouple location (global level) starts to increase as shown in **Fig. 4.31**. This trend of increasing computation average thermal deviation with increase of  $K_E$  also happens at the melt-pool level as well.

However, with the introduction of  $K_E$ , computation time is reduced drastically up-to a factor of 5-10 as presented in **Fig.4.32**. A comparison of computation time for thermal analysis is done between Double Ellipsoid (DE) and Elongated Ellipsoid (EE) with different  $K_E$ . With an increase in  $K_E$ , computation time starts to decrease for all experiment cases. Considering all experiment cases,  $K_E = 4$  and 8 seems to give better thermal results with maximum average thermal deviation of  $100^\circ\text{C}$  with  $K_E = 8$ . For all experiment cases, average deviation for in-situ temperature results at thermocouple location is less than  $100^\circ\text{C}$  using elongated ellipsoid for  $K_E = 4$  and 8 values.

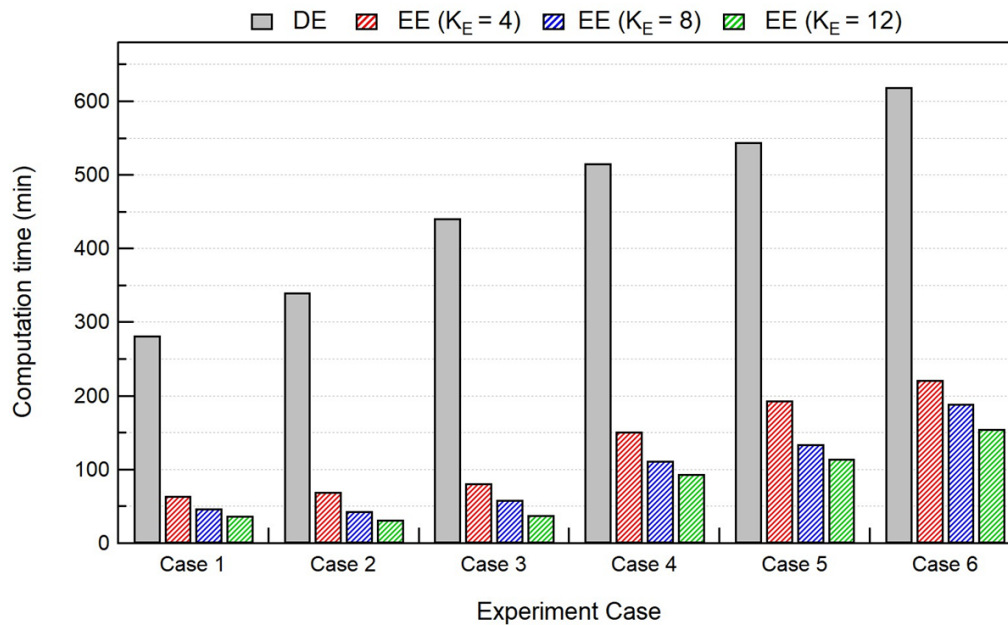


Figure 4. 32: Comparison of computation time for thermal analysis between DE and EE heat source with different elongated length

For the mechanical analysis, as explained in the previous section that the layer deposition/fusion leads to lowering of the substrate. This movement is recorded as decrease in distortion values as explained in the previous section. Due to the elongated ellipsoid length ( $K_E$ ), peak temperature obtained during the layer deposition are reduced significantly. This leads to reduction in the phenomenon of lowering of the substrate that accounts for decrease in distortion. Also, the cooling phenomenon is altered due to the lower temperature field obtained with different  $K_E$  values. For all cases as shown in **Fig. 4.33**, with different  $K_E$  values, numerical model can capture the in-situ distortion evolution, however the magnitude of the distortion values changes with respect to  $K_E$ . Considering all experiment cases,  $K_E = 4$  and 8 seems to give acceptable distortion results with an exception in Case 4 that results in maximum average distortion deviation of 0.56 mm with  $K_E = 8$ . For all other cases, average deviation for in-situ distortion is less than 0.25 mm using elongated ellipsoid for  $K_E = 4$  and 8 values.

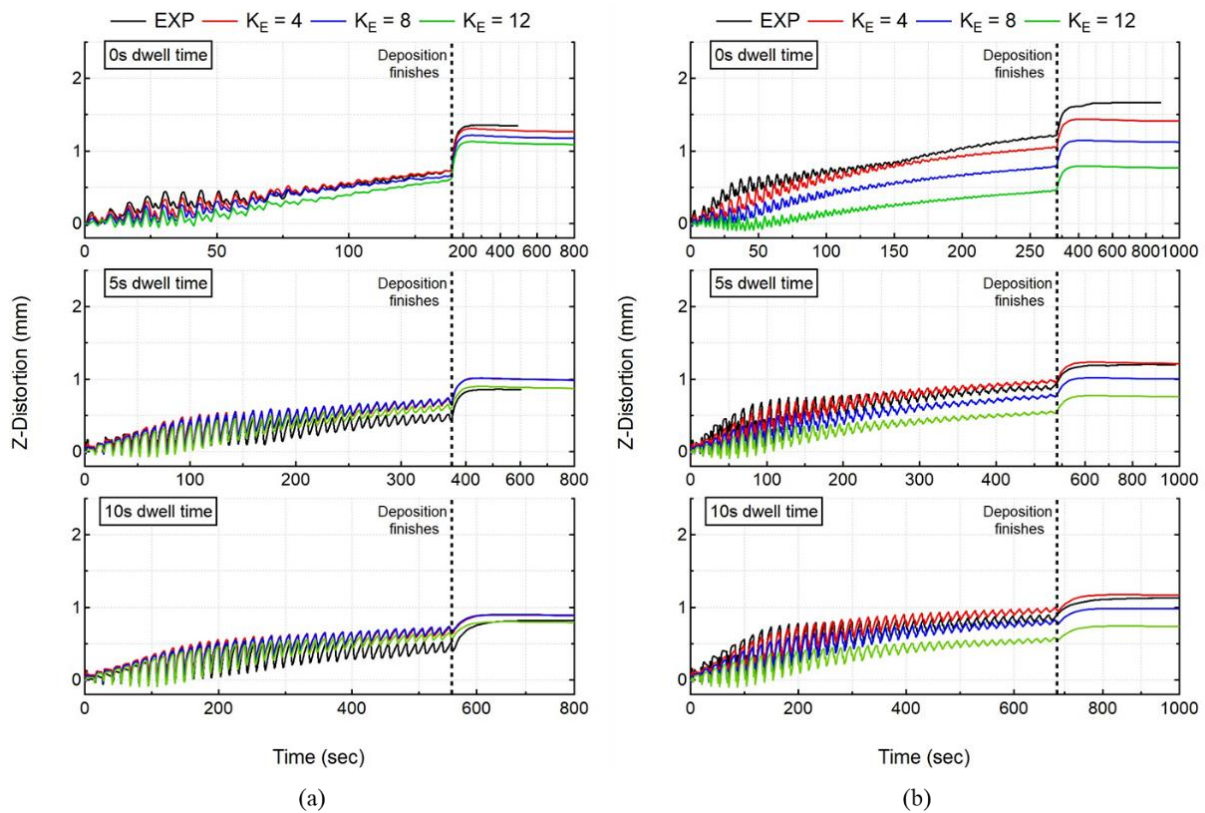


Figure 4.33: Comparison of numerical results using Elongated Ellipsoid with recorded In-situ distortion accumulation of LDS for all cases. (a) 1-bead wall, (b) 2-bead wall

$K_E$  of 4, 8 and 12 values are chosen for the analysis for EE model that is different in comparison to Chapter 3 where  $K_E$  of 0.5, 1, 4, 8 and 27 values are chosen. The main reason is for Chapter 3,  $K_E = 0.5$  was chosen as EE models functions like Single Ellipsoid (SE), therefore it acted as a reference to justify that an EE model with  $K_E = 0.5$  yields same results as a conventional DE model. Then  $K_E = 1, 4$ , and 8 were chosen to analyse the effect of elongated lengths on computation time and accuracy. With  $K_E = 27$ , elongated length became the total length of the deposited layer, so model was activating layer at once (Multi-scale approach). This value was chosen as it was interesting to analyse how the model responds if the activation is done layer-by-layer. Therefore, in this Chapter,  $K_E$  of 4, 8 and 12 values are chosen as it is consistently doubling the elongated lengths from 9.15 (1/6 of deposited layer length), 18.3 (1/3 of deposited layer length) to 27.46 (1/2 of deposited layer length) respectively. With further increase in  $K_E$  such as 25, elongated ellipsoid length will be equal to deposition layer length. So, this starts to function as layer-by-layer activation approach (Multi-scale approach), that is not the objective of this chapter. Multi-scale and Inherent Strain methods are discussed in final chapter i.e., Chapter 6.

Computation error is calculated with the final recorded value by the LDS and the predicted value by the EE model and is presented in **Table 4.6**. It is highlighted in different colours that EE model yielding errors less than 10% (green), 10-20% (orange) and more than 20% (blue). With an exception of Case 4, for all other cases, EE model with  $K_E = 4$  and 8 values result in error below 20%, that can be an acceptable value.

Table 4. 6: Computation error yielded by EE model for final distortion value recorded by LDS

| Case | Error (%) |           |            |
|------|-----------|-----------|------------|
|      | $K_E = 4$ | $K_E = 8$ | $K_E = 12$ |
| 1    | 6.4       | 13.1      | 19.8       |
| 2    | 13.9      | 13.6      | 0.2        |
| 3    | 6         | 6.9       | 5.1        |
| 4    | 16.1      | 33.5      | 54.5       |
| 5    | 1.4       | 17.2      | 37.5       |
| 6    | 2.5       | 14.1      | 35.6       |

However, with the introduction of elongated ellipsoid, reduction in computation time follows the same trend as thermal analysis. As shown in **Fig. 4.34**, for the mechanical analysis, computation time is reduced up-to a factor of 5-10 with  $K_E = 4$  and 8 values.

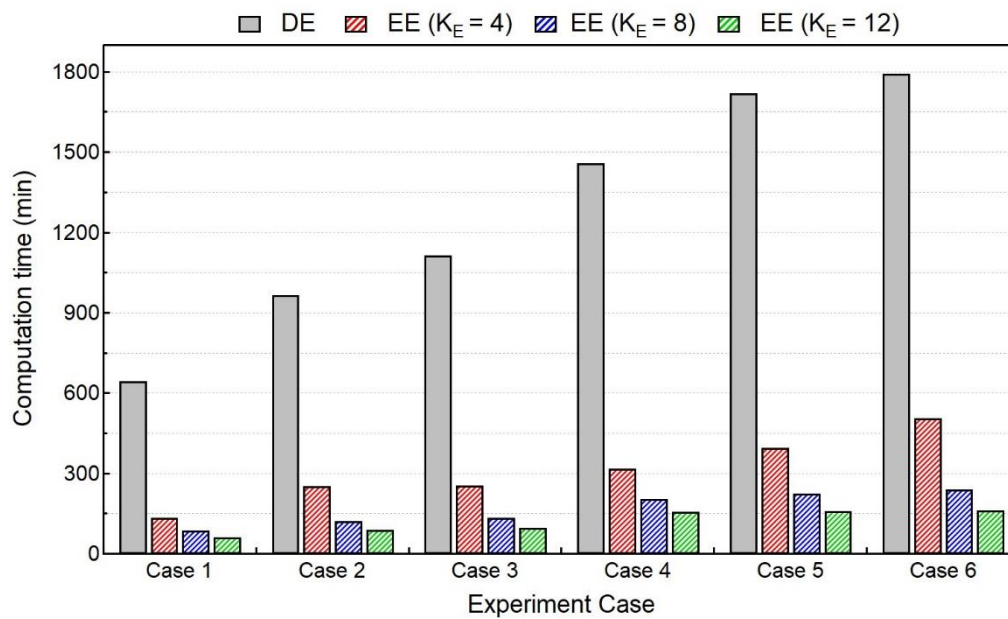


Figure 4. 34: Comparison of computation time for mechanical analysis between DE and EE heat source with different elongated length

The numerical results for in-situ distortion obtained with elongated ellipsoid heat source shows acceptable levels of accuracy but with drastically reduction in computation time (**Fig. 4.34**). These results are also verified with post-process line distortion results as shown in **Fig. 4.35**. Here also, the numerical model with  $K_E = 4$  and 8 values, for all experiment cases, predicts the substrate line-deformation that is in good agreement with experiment results. Therefore, a thermo-mechanical model with calibrated elongated ellipsoid heat source can be helpful in predicting the part-scale workpiece deformation in a practical computation time with a factor of 5-10 with  $K_E = 4$  and 8 values respectively.

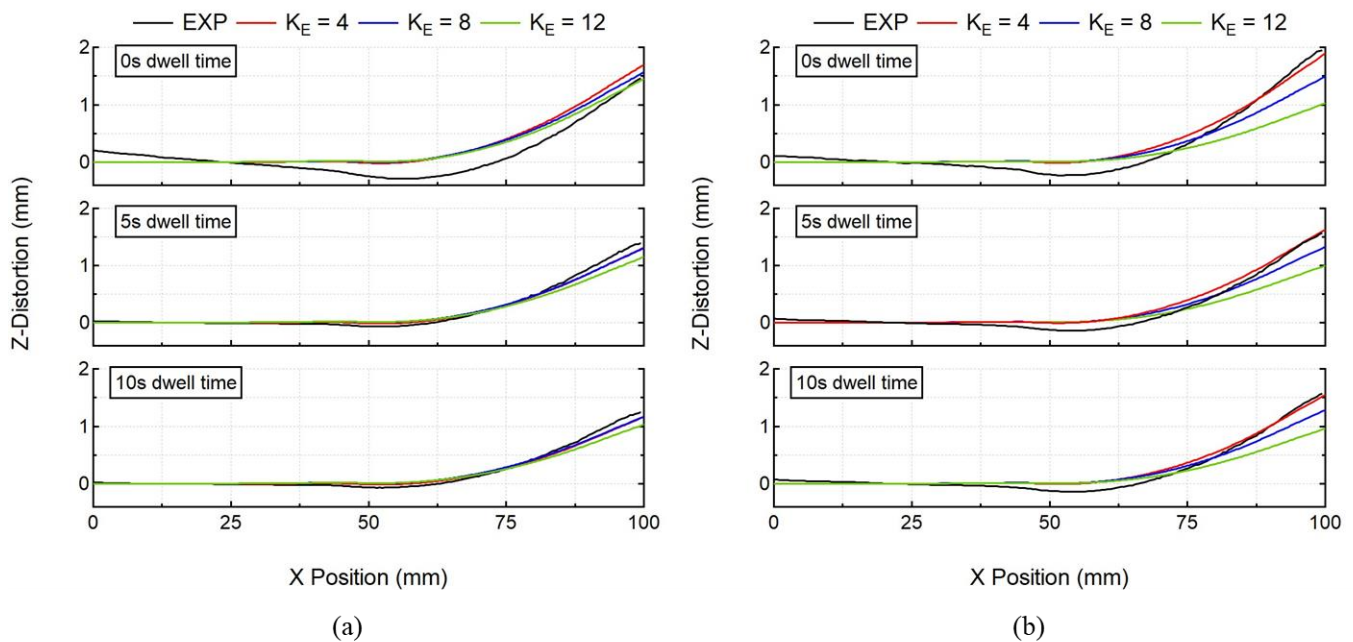


Figure 4. 35: Comparison of numerical results using Elongated Ellipsoid with experimental post-process line distortion results of Optical scanner for all cases. (a) 1-bead wall, (b) 2-bead wall

## 4.7 Conclusions

In this chapter, a 3D Thermo-Elasto-Plastic FE model with isotropic hardening is developed to analyse the in-situ and post-process distortion accumulated in LDED process. The effect of inter-layer dwell time and number of beads is studied. The thermo-mechanical model is validated for different inter-layer dwell times and number of beads. The main conclusions of this work are the following:

- The computed temperature history predicted by the thermal model is in good agreement. The maximum average deviation at thermocouple location is of 13.2°C in comparison with the experiment measurements (case 3).
- The mechanical model with stress relaxation is in good agreement with in-situ and post-process distortion measurements. The maximum average deviation of in-situ distortion at LDS location without stress relaxation model is 0.313 mm, while with the stress relaxation model it is 0.041 mm, in comparison with the experiment measurements (case 6), with computation average deviation reduced to a factor of 8. The model without SR over-predicted the distortion by over 35-85% and the model with SR yielded higher computation accuracy (maximum error of 9.4%)
- The computed distortion without stress relaxation is significantly over-estimated as it does not include the effects of liquefaction and process induced annealing behaviour in DED. However, by using stress relaxation model, the computed distortion is in good agreement with experiment results.
- For cantilever tooling with SS316L material, with an increase of inter-layer dwell time, distortion decreases and with an increase in number of beads, distortion increases. The numerical model demonstrated its versatility by capturing these trends with good accuracy.

- The computation time can be reduced drastically by a factor of 10 using EE heat source model. Without considering the exception (case 4 with  $K_E = 8$ ), EE model with  $K_E = 4$  and 8 values result in the maximum average deviation of 0.25mm. The EE model with  $K_E = 4$  and 8 values yield computation errors less than 20% (exception Case 4). The local accuracy of the model (temperature, distortion) may be affected but the global values of temperature and distortion are in agreement with the experiment measurements.
- Large-part simulation can be done with reasonable computation time employing EE heat source model.

*In next Chapter i.e., Chapter 5, the developed Thermo-Mechanical model is further tested with double bead walls of much larger dimensions and of much higher layers (100) to demonstrate the feasibility of EE model to correctly capture material response for large-part fabricated in LDED process.*

# Chapter 5: Efficient thermo-mechanical model for large parts by LDED<sup>3</sup>

|  |     |
|--|-----|
| Chapter 5: Efficient thermo-mechanical model for large parts by LDED ..... | 122 |
| 5.1 Introduction.....  | 123 |
| 5.2 Modeling approach.....   | 123 |
| 5.2.1 Thermal analysis .....   | 123 |
| 5.2.2 Mechanical Analysis.....   | 124 |
| 5.3 Experiment Set-Up of a SS 316L large wall build by LDED process.....   | 125 |
| 5.4 Numerical implementation.....  | 127 |
| 5.4.1 FEA solver.....  | 127 |
| 5.4.2 FEM mesh .....   | 127 |
| 5.4.3 Material deposition modeling.....                                    | 127 |
| 5.4.4 Model calibration and boundary conditions.....                       | 128 |
| 5.5 Results and discussion .....   | 128 |
| 5.5.1 Comparison of temperature evolution .....                            | 128 |
| 5.5.2 Comparison of in-situ distortion evolution .....                     | 130 |
| 5.5.3 Comparison of post-process line distortion results .....             | 133 |
| 5.6 Conclusions.....   | 134 |

<sup>3</sup> The work presented in this particular chapter is the subject of the proceeding: Vaibhav Nain, Thierry Engel, Muriel Carin, and Didier Boisselier. 2022. "Numerical modeling for large-scale parts fabricated by Directed Energy Deposition." SPIE Photonics Europe 2022, 3-7 April 2022, Strasbourg, France, paper 12135-8. <https://doi.org/10.1117/12.2624947>

## 5.1 Introduction

The objective of the present chapter is to demonstrate the effectiveness of a thermo-mechanical model that employs the EE heat source model by simulating large parts fabricated by LDED within practical computation times.

In the last Chapter i.e., Chapter 4, it has been demonstrated that an EP model (Voce Non-Linear Isotropic Hardening Law) that employs DE heat source with and without stress relaxation (SR) correctly and over-predicts the mechanical response of the workpiece respectively. Also, the same EP model with EE heat source significantly reduces the computation time and yields acceptable levels of computation accuracy. However, both the DE and EE model were validated with relatively smaller layers' deposition length (50 mm) and height (number of deposited layers: 42). Therefore, in this chapter, the main objective is to validate the EE model with a relatively larger layer's deposition length (120 mm) and height (number of deposited layers: 50 and 100). In particular, it is interesting to find out if the recommended values of the dimensionless time increment size  $K_E$ , proposed in the previous chapters, are still relevant for larger walls and if a correction factor in the heat source is required. In the last two chapters i.e., Chapters 3 and 4, the effect of process parameters like dwell time, laser power, and the number of beads was analysed. Therefore, in this chapter, to demonstrate the EE model's capabilities i.e., reduction in computation time with desired accuracy levels for large-part LDED process simulation, the effect of the number of layers (deposited volume) is analysed. A thermo-mechanical model with EE heat source is validated with in-situ temperature and distortion experiment data obtained during the fabrication of two different double-beads with 50- and 100-layer high wall structures fabricated at Irepa Laser. The model is also validated with post-process distortion results.

## 5.2 Modeling approach

The simplification of the geometry, sequential coupled thermo-mechanical analysis is done in the same way as presented in Section 2 "Modeling Approach" of Chapter 4.

### 5.2.1 Thermal analysis

The thermal model being identical to that presented in Chapters 2, 3 & 4, will not be detailed here. This model is based on the resolution of Equations 2.1 and 2.2. An elongated ellipsoid source (Eq 4.11, 4.12, and 4.13) is applied with different elongated ellipsoid (EE) lengths presented in Table 5.1.

Table 5. 1: Elongated Ellipsoid (EE) heat source model parameters used in this chapter

| $K_E$ | Computation time step FEM ( $\Delta t$ )<br>(s) | EE length ( $\hat{a}$ )<br>(mm) | No. of sub-tracks per layer<br>(Wall Length/ $\hat{a}$ ) |
|-------|---|---------------------------------|--|
| 4     | 0.528   | 9.15                            | 28   |
| 8     | 1.056   | 18.3                            | 14   |
| 12    | 1.584   | 27.46                           | 10   |

The initial boundary conditions, convective and radiative heat losses are also identical to the formulation explained in Chapters 2, 3, and 4 and is based on Equations 2.4, 2.5, and 2.7. The natural and forced convective coefficient values are kept the same along with emissivity values as well. Also, specific heat capacity is

modified using the same method (Eq 2.8) mentioned in Chapter 2. Finally, an enhanced thermal conductivity factor of 2.5 is kept for thermal conductivity beyond melting temperature (Eq. 2.9) given in Chapter 2.

## 5.2.2 Mechanical Analysis

The mechanical model being identical to that present in Chapter 4, will not be detailed here. This model is based on the resolution of Equations 4.1, 4.2, and 4.3. Computation of elastic, thermal, and plastic strain is done in the same way as Chapter 4 (Eq. 4.4, 4.6, 4.7 and, 4.8). The same EP model with Non-Linear isotropic hardening law, which is explained in detail in Chapter 4 is also employed in this chapter, so it will not be detailed here. However, SS 316L powder is deposited on the structural steel (S235) substrate. The temperature-dependent material properties for SS 316L are presented in Chapter 4. For structural steel (S235), temperature-dependent thermo-mechanical properties are presented in Fig 5.1 (Prajadhiana et al., 2020) with a constant density value of 7800 kg/m<sup>3</sup>. As in chapter 3, linear interpolation is used to calculate the values between the given temperature dataset, and properties are kept constant beyond the fusion temperature.

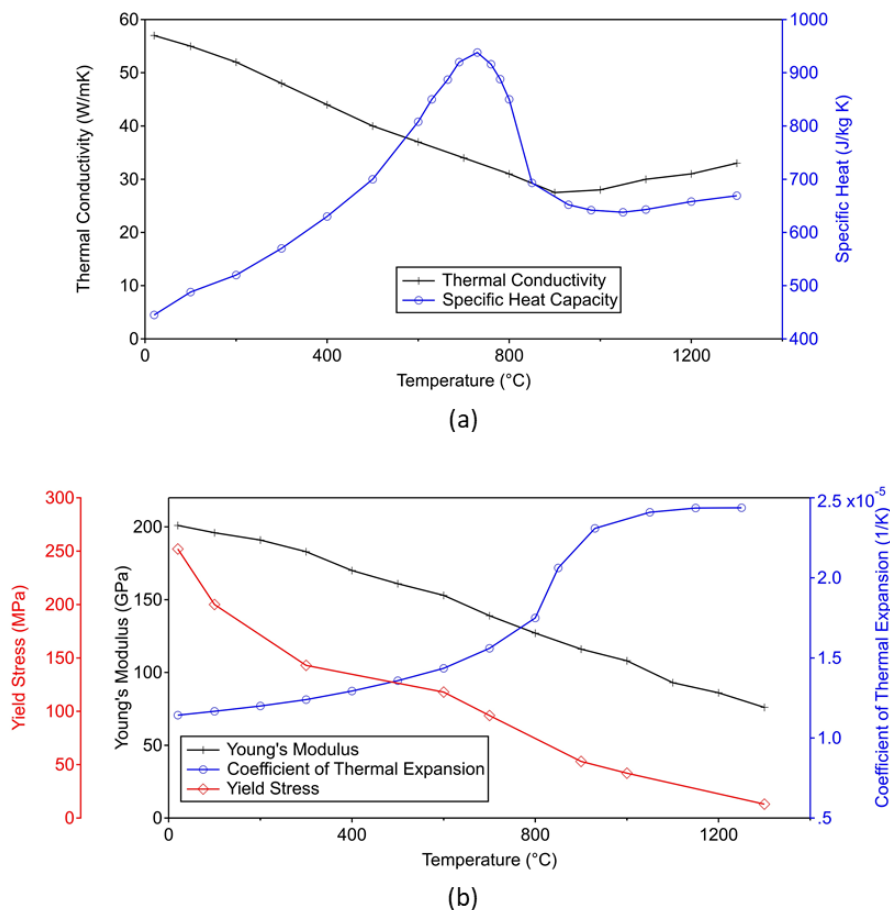


Figure 5. 1: Temperature-dependent material properties of S235 (Prajadhiana et al. 2020) used for the substrate  
(a) Thermal (b) Mechanical

For S235, the values of two parameters ( $\sigma_{sat}$  and  $\beta$ ) required for Voce Hardening Law are extracted by reverse-fitting the results from stress-strain data presented in the literature work (Prajadhiana et al., 2020) in comparison to results yielded by Voce Hardening law for different temperature as shown in Fig 5.2.

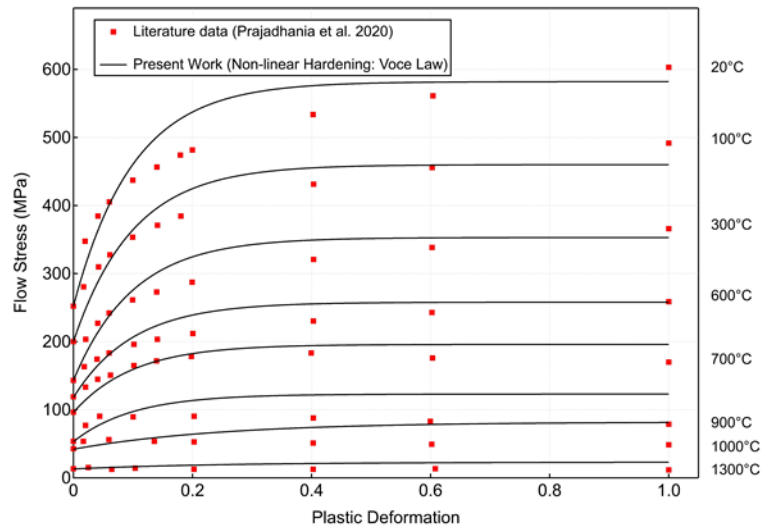


Figure 5. 2: Comparison of temperature-dependent flow curves for S235 material from the literature to the flow curves yielded by Voce hardening law by reverse fitting the data with different  $\sigma_{sat}$  and  $\beta$  values

To obtain the reverse data-fitting of the plastic deformation for S235 presented in Fig 5.2, extracted values of  $\sigma_{sat}$  and  $\beta$  are given in Table 5.2:

Table 5. 2: Temperature-dependent values of the parameters employed in Voce Non-Linear Hardening Law for S235

| Temperature | $\sigma_{sat}$ (MPa) | $\beta$ |
|-------------|----------------------|---------|
| 20          | 330                  | 10      |
| 100         | 260                  | 10      |
| 300         | 210                  | 10      |
| 600         | 140                  | 10      |
| 700         | 100                  | 10      |
| 900         | 70                   | 10      |
| 1000        | 40                   | 4       |
| 1300        | 10                   | 4       |

For SS 316L, extracted values of  $\sigma_{sat}$  and  $\beta$  are already presented in Chapter 4, so it is not presented here. Annealing induced stress relaxation (SR) modeling is implemented the same way as explained in Chapter 4. To have the consistency for numerical model throughout the work carried out in the thesis, same  $T_{relax} = 1000^{\circ}\text{C}$  is chosen for instantaneous stress relaxation temperature, as same material SS 316L is deposited in the experiments carried out under the scope of this chapter.

### 5.3 Experiment Set-Up of a SS 316L large wall build by LDED process

The numerical modeling approach explained in the previous Section 2 is applied to simulate the thermo-mechanical responses during the deposition of SS 316L on S235 substrate. Laser and machine details are not presented as it is already explained in Chapters 3 and 4.

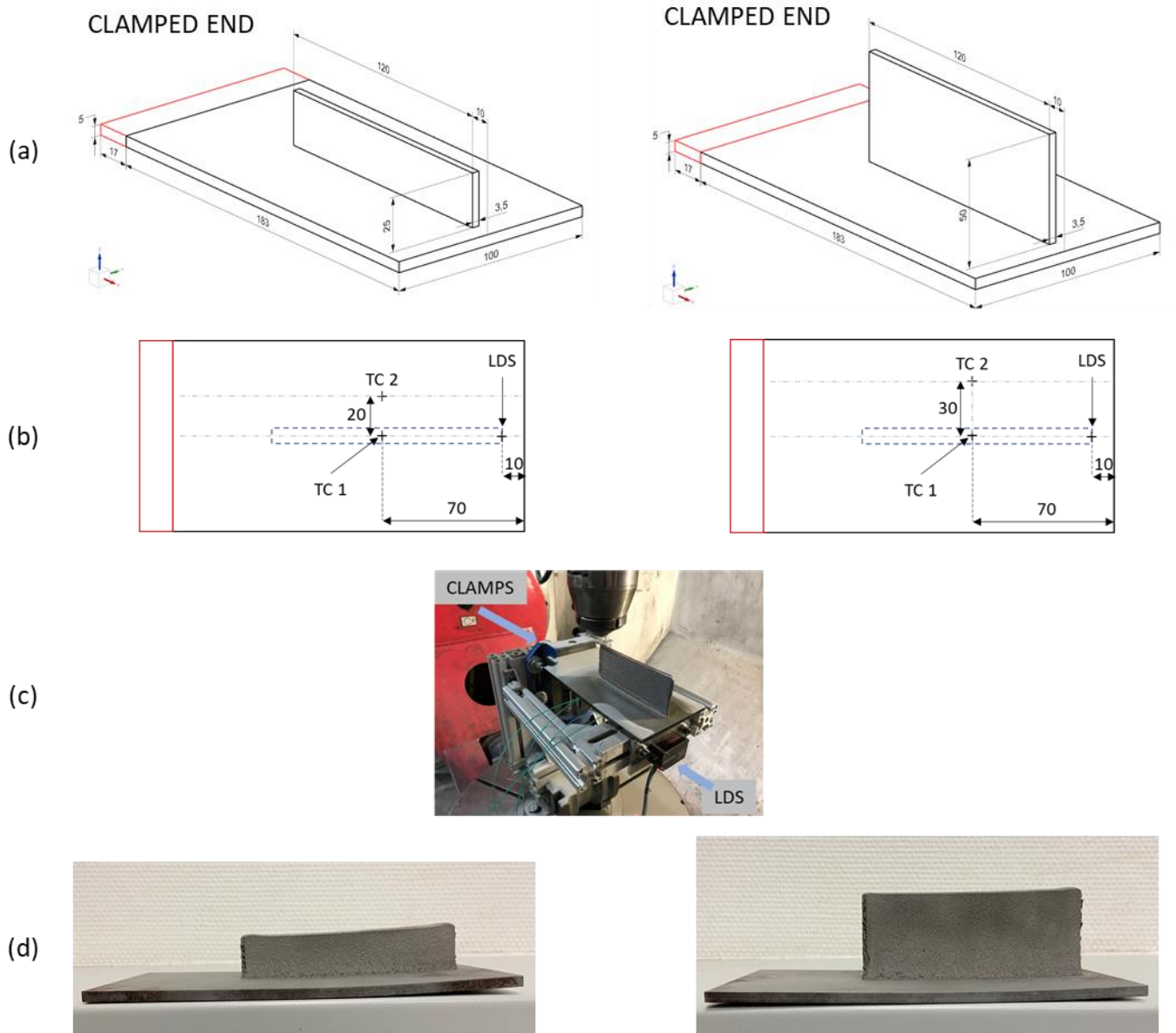


Figure 5. 3: (a) Substrate and deposited wall dimensions (in mm); (LEFT: 50 layers wall; RIGHT: 100 layers wall)  
 (b) Measurement locations at bottom of substrate  
 (c) Experimental set-up of tooling with clamped fixtures, in-situ measurement devices and deposited wall of 100 layers  
 (d) Post-process deposited part

Employing LDED technology, double adjacent beads thin wall structures of SS 316L were deposited on a structural steel (S235) substrate measuring 200 mm long, 100 mm wide, and 5 mm thick. All the experiments were performed with a scanning speed of 1 m/min with a zig-zag deposition strategy. Powder deposition rate of 13 g/min for SS 316L powder feedstock (Oerlikon, grain size 45-106  $\mu\text{m}$ ) was chosen. The diameter of the laser beam spot size was 2.2 mm in diameter at the top-surface of the substrate. Effect of number of layers is analysed by keeping laser power 800 W, laser scan speed 1m/min and dwell time of 0 s (waiting period between successive layers). In the first experiment, 50 layers were deposited, and then for second experiment, 100 layers were deposited. In both experiments of 50- and 100-layers deposition, the wall height was measured to be 25 mm and 50 mm respectively. However, the obtained values of wall length and width was same 120 mm and 3.5 mm respectively for 50- and 100-layers deposition. **Fig. 5.3(a)** shows the schematic of substrate's dimensions along with clamping conditions & planned wall build for both 50- and 100-layers wall. **Fig. 5.3(b)** shows the in-situ measurement locations for thermocouple and laser displacement sensor at the bottom face of the substrate both 50- and 100-layers wall. **Fig. 5.3(c)** shows the tooling with substrate

fixed to clamp and laser displacement sensor attached to the tooling for 100 layers wall, **Fig. 5.4(d)** shows the walls obtained for both 50- and 100-layers.

Two different thermocouples are employed to measure the *in-situ* temperature. Two different locations are chosen at the bottom face of the substrate to record the temperature evolution as shown in **Fig. 5.3(b)**, so that they do not fall under the deposition path of the laser on the top surface of the substrate and the effect of thermal diffusivity can also be analysed. Type of Thermocouples, data acquisition system (DAQ) and its acquisition frequency are kept same as explained in **Section 3.1 “Temperature measurement”** of **Chapter 3**. Similarly, the in-situ displacement of the bottom face of the substrate and the final deformed shape of walls are measured with the same way as explained in **Section 3.2 “In-situ distortion measurement”** and **Section 3.3 “Post-process line distortion measurement”** of **Chapter 4**.

## 5.4 Numerical implementation

### 5.4.1 FEA solver

As for the previous chapters, the computations are performed with the solver (PARDISO) and the adaptive time-stepping method. The computation time step of ( $\Delta t$ ), which depends upon the parameter  $K_E$  is taken during the material deposition period and ( $3 \times \Delta t$ ) during a period of cooling down once the deposition process is finished. All simulations are done on the same workstation (16 cores, 128 GB RAM, Intel Xeon W-2275 processor).

### 5.4.2 FEM mesh

Three-dimensional finite element meshes were generated in COMSOL Multiphysics as presented in **Fig. 5.4**. The same mesh is used for the thermal model as well as the mechanical model. The mesh for 50 layers wall contains 70,809 Hex-8 elements and the mesh for 100 layers wall contains 1,16,040 Hex-8 elements. The mesh elements for the wall builds are taken as 2 per laser radius in transversal (wall width), 1 per laser radius in longitudinal (deposition direction), and 1 per layer thickness. A coarse mesh is used for the substrate as the heat source moves away from the wall builds.

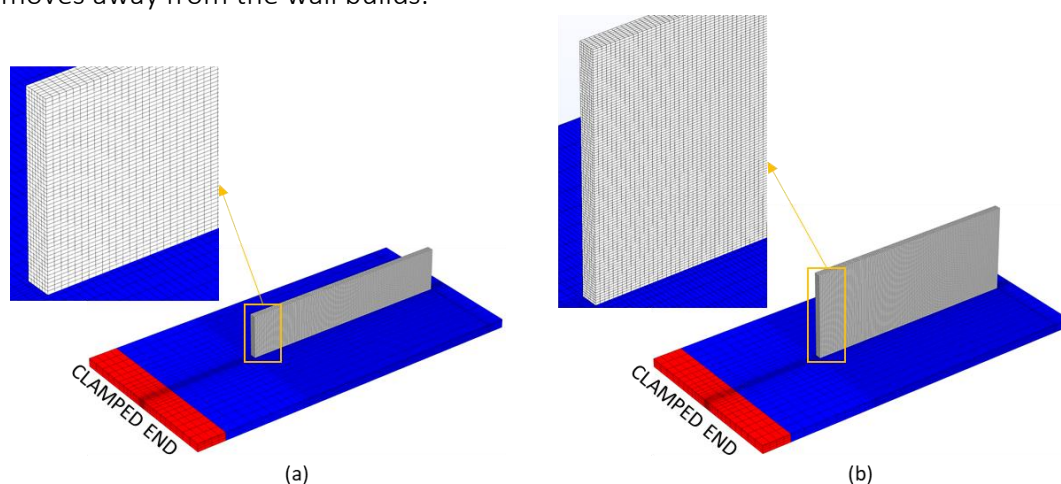


Figure 5. 4: FE meshes employed for numerical simulation of LDED process: (a) 50 layers wall; (b) 100 layers wall

### 5.4.3 Material deposition modeling

Material deposition modeling is done in the same way as explained in detail in **Section 4.3 “Quiet/Active Material Activation Method”** of **Chapter 4**, so it is not presented here in detail.

## 5.4.4 Model calibration and boundary conditions

As explained in **Chapters 2, 3, and 4**, layer geometry is simplified, parameterisation of numerical heat source (EE) and the effect of forced convection & heat loss due to conduction heat transfer from deposited part to the substrate is considered in the same way with same parameters values.

## 5.5 Results and discussion

### 5.5.1 Comparison of temperature evolution

The thermal model predicts the thermal response of the workpiece which is compared to the experimental measurements for both experiment cases. **Fig. 5.5** shows the experimental results, as measured by thermocouple 1 (TC1) in **Fig. 5.5(a)** and thermocouple 2 (TC2) in **Fig. 5.5(b)**, compared to numerical results at nodes corresponding to the thermocouple locations for 50-layer experiment case. As expected, TC1 records

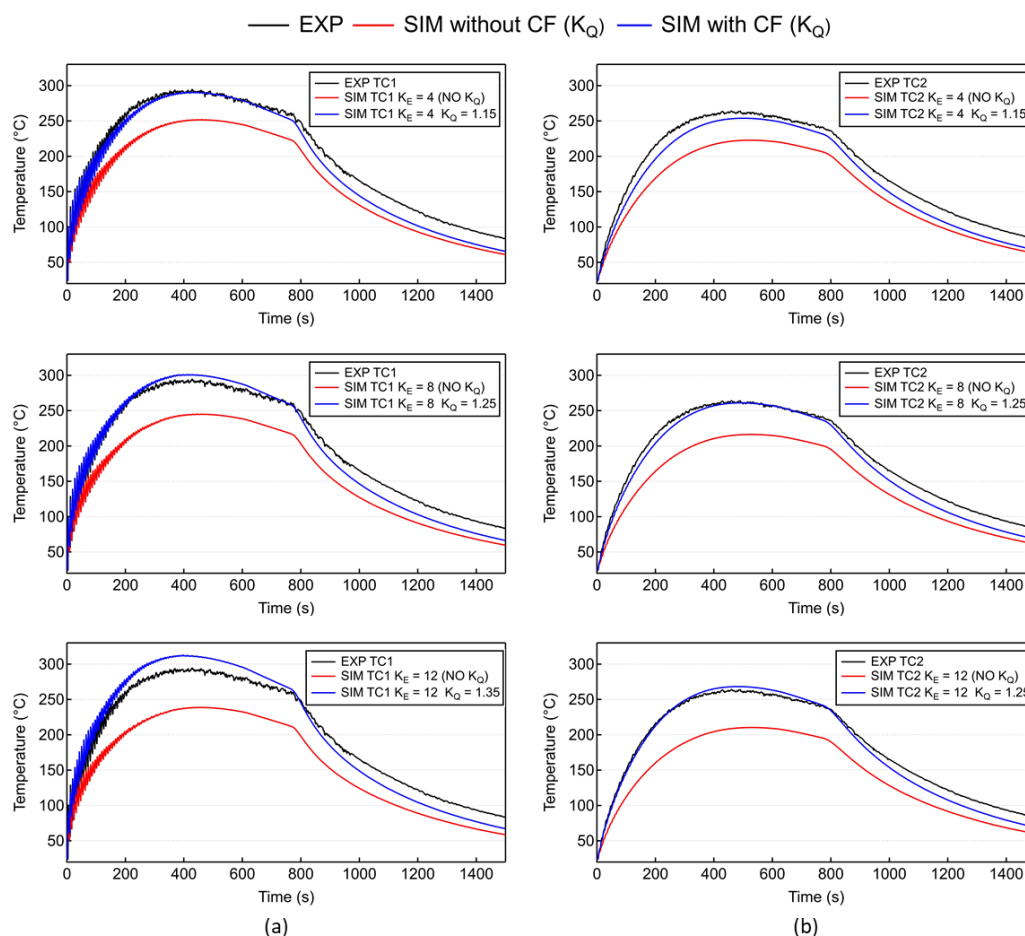


Figure 5. 5: Comparison of experiment (EXP) thermal results with numerical (SIM) thermal results for 50-layer wall using EE model with & without correction factor (CF denoted as  $K_Q$ ) with different  $K_E$  values  
(a) Thermocouple 1 (TC1) (b) Thermocouple 2 (TC2)

higher temperature evolution as it is located below the deposition path, as compared to TC2 that records lower temperature evolution because it is located 20 mm away from the deposition path in the transversal direction. The Elongated Ellipsoid (EE) model without correction factor (CF) successfully captures the temperature trends for all  $K_E = 4, 8,$  and  $12$  values. However, it yields computation errors due to the averaging of heat source, and the computation error increases with an increase of  $K_E$ . But, with the introduction of source CF i.e.,  $K_Q$  in heat source equation, computation errors reduce drastically. To yield correct results,  $K_Q$  value is increasing with an increase in  $K_E$  value and this trend has been established in **Chapter 3** and is also

published in the literature (Nain et al., 2021). With  $K_E = 4$ ,  $K_Q = 1.15$  yields correct thermal evolution at thermocouple location. But with an increase in  $K_E = 8$ , the value of CF should also be increased, therefore,  $K_Q = 1.25$  gives a correct fit with the experiment data. This trend is noticed when  $K_E = 12$ ,  $K_Q = 1.35$  seems to be computationally accurate. Therefore, source CF needs to be calibrated dependent upon the EE sub-track length.

The same comparison of temperature evolution at TC is done for 100-layers wall and is shown in **Fig. 5.6**. For the 100-layer wall experiment case, it was found that TC had a bad contact with the substrate with TC1 recording almost nothing from the start itself and TC2 had a lot of issues as well that resulted in incorrect data acquisition. However, TC2 recorded some data and this can be compared with the model. It can then be noticed in **Fig 5.6**, that the EE model with CF captures the TC2 temperature trend as compared to the EE model without CF. Therefore, for the numerical model for 100-layers, same conclusions can be made that

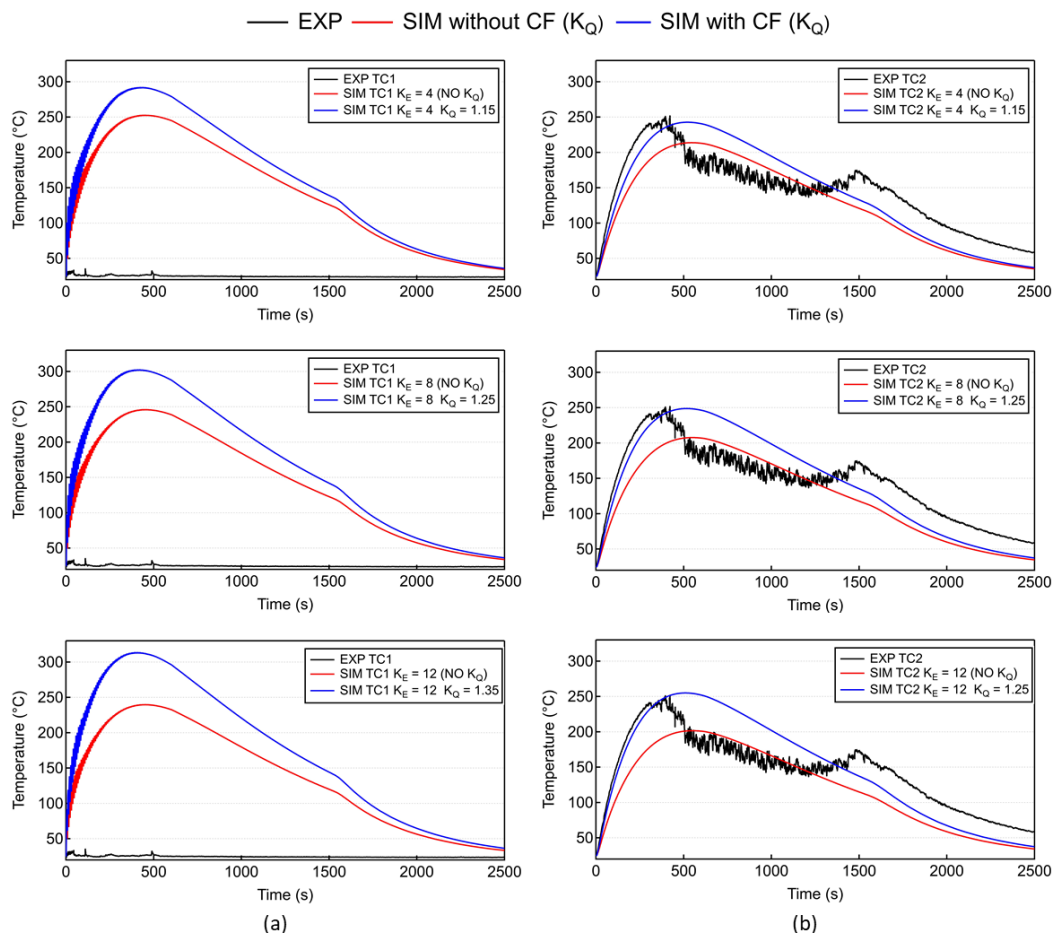


Figure 5. 6: Comparison of experiment (EXP) thermal results with numerical (SIM) thermal results for 100-layer wall using EE model with & without correction factor (CF denoted as  $K_Q$ ) with different  $K_E$  values  
(a) Thermocouple 1 (TC1) (b) Thermocouple 2 (TC2)

with an increase in  $K_E$ ,  $K_Q$  value needs to be increased to reduce the computation error. **Table 5.3** presents the results of computation time taken for thermal analysis with EE model with different  $K_E$  values. There are two important aspects that need attention and should be noted. With an increase in number of layers, computation time is increasing because of the large mesh size and higher computation time steps. Furthermore, with an increase in  $K_E$  value computation time is decreasing by a factor of 3 because of the reduced computation time steps in the analysis.

Table 5. 3: Comparison of computation time for thermal model using EE model with different  $K_E$  values

| $K_E$ | Computation time: Thermal model |                |
|-------|---------------------------------|----------------|
|       | 50-layer wall                   | 100-layer wall |
| 4     | 4 h 27 min                      | 14 h 15 min    |
| 8     | 3 h 03 min                      | 7 h 43 min     |
| 12    | 1 h 35 min                      | 5 h 04 min     |

Usually, in a conventional model that employs a Goldak's Double Ellipsoid, other Surface/Volumetric Gaussian, or Surface/Volumetric 3D Top-Hat heat source, to represent smooth continuous movement of laser heat source in the model, model should have a condition that  $K_E \leq 1$ . Nevertheless, it has been demonstrated in **Chapters 3 and 4** that  $K_E \leq 1$  usually takes more computation time up-to a factor of 10 as compared to EE model with different  $K_E$  values. But, in the present work, conventional model is not employed, therefore EE model is compared with different  $K_E$  values demonstrating that computation time is reduced up-to a factor of 3. However, compared to conventional model with  $K_E \leq 1$ , computation time is reduced up-to a factor 15-20, because conventional model with  $K_E \leq 1$  has to take almost 4-8 times more computation steps in the numerical analysis as compared to EE model with  $K_E = 4$ . For this chapter, only EE model is employed and it was decided that DE model will not be used keeping in mind the constraints of computation time and memory requirements.

## 5.5.2 Comparison of in-situ distortion evolution

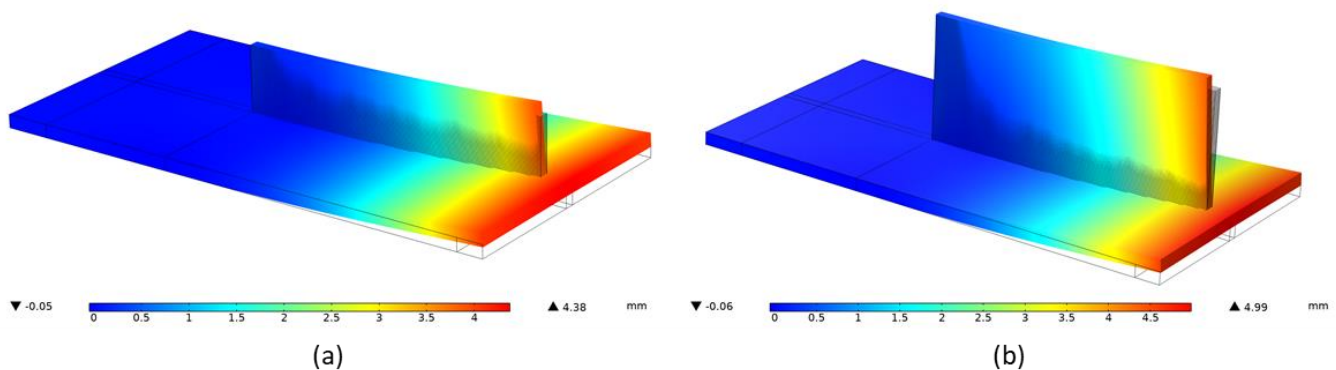


Figure 5. 7: Mechanical model showing final deformed shape (a) 50-layer wall (b) 100-layer wall

Workpiece is experiencing repeated thermal expansion and shrinkage behaviour due to the repeated thermal cycle of heating and cooling respectively during the complete LDED process. This repeated thermal cycle (heating & cooling) leads to the continuous accumulation of distortion throughout the LDED process. **Fig. 5.7** shows the final calculated deformed configuration (Z-displacement) for 50- and 100-layers wall experiment case ( $K_E = 4$  and NO CF).

Substrate deflection happens in the same way explained in **Chapter 4** with upwards and downward deflection during cooling thermal cycles respectively. As shown in **Fig 5.8**, these deflections are successfully recorded by LDS for 50-layer wall. It can be seen that distortion trend and accumulation are consistent throughout the deposition process that is coherent with the founding of **Chapter 4**. With each deposition of the layer, distortion magnitude keeps on increasing and this trend is consistent throughout the LDED process. Once the deposition process is finished, substrate is allowed to cool that results in upward movement of substrate resulting in increase of LDS values. Then substrate's temperature stabilises that results in a constant value in LDS recording.

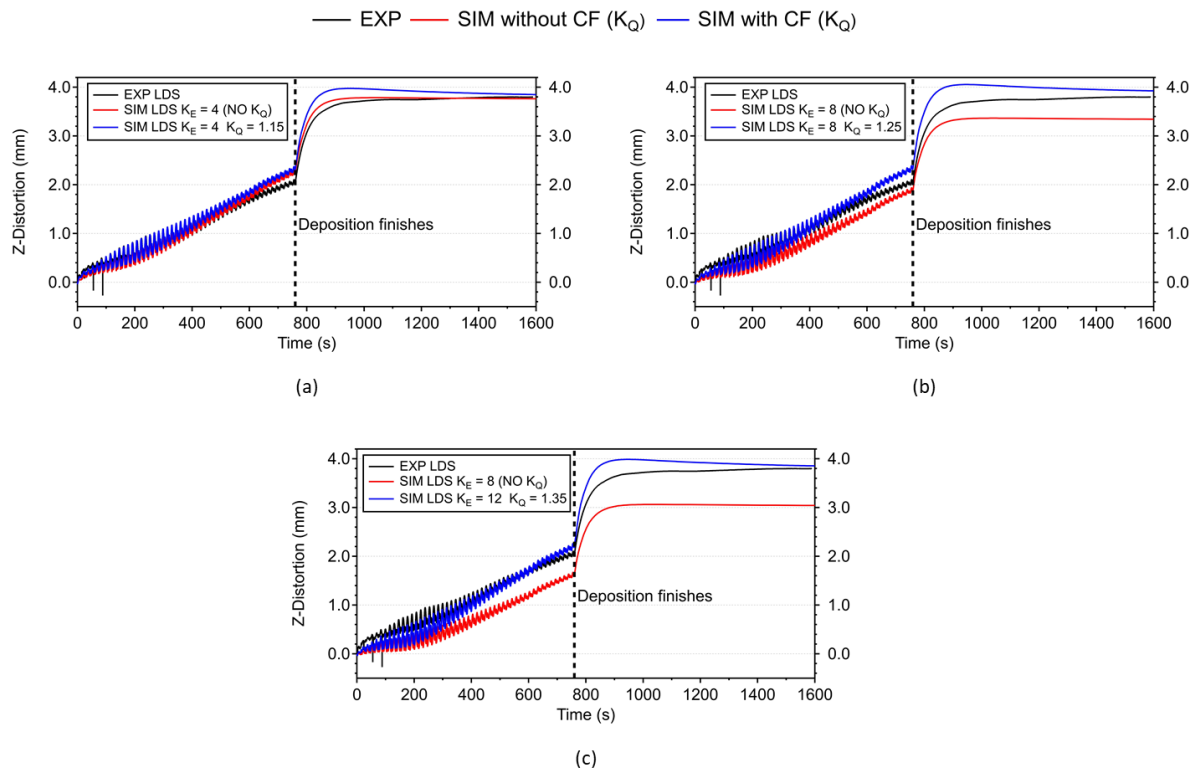


Figure 5. 8: Comparison of experiment (EXP) distortion results with numerical (SIM) distortion results at LDS location for 50-layer wall using EE model with & without correction factor (CF denoted as  $K_Q$ ) with different  $K_E$  values  
(a)  $K_E = 4$  (b)  $K_E = 8$  (c)  $K_E = 12$

The LDS data follows the same deflection pattern as was seen in Chapter 4 justifying the data acquisition consistency. As shown in **Fig 5.8**, all this complex phenomenon that results in upward and downward movement of the substrate is successfully modeled by EE model irrespective of  $K_E$  values. EE model with different  $K_E$  values correctly captures the distortion trend. However, EE model without correction factor (CF) yields computation errors and this error increases with an increase in  $K_E$  values from 4-12. Same conclusion was established in **Chapter 4** as well. But with the introduction of CF, EE model with CF correctly captures the distortion magnitude and reduces computation errors drastically. As discussed in the "Thermal results" section, source correction factor  $K_Q$  value needs to be optimised that depends upon  $K_E$  value. As observed in the "Thermal results" section, same trend can be seen here as well, that with an increase in  $K_E$  value from 4-12,  $K_Q$  value is also increasing from 1.15-1.35 resulting in minimum computation error.

**Fig. 5.9** shows the experimental results, as measured by Laser Displacement Sensor (LDS), compared to numerical results at nodes corresponding to the LDS location for 100-layer experiment case. For 100-layer wall experiment case, distortion trend and accumulation are consistent and keeps on increasing with an increase in the number of deposition layers. This trend is same as noticed in 50-layer wall. It can also be noticed that the final LDS recording for 50-layer wall is 3.8 mm (**Fig 5.8**), and for 100-layer wall, it is 4 mm (**Fig**

5.9). So, it can be said that with an increase in number of layers, distortion accumulation remains consistent, with a small increase in distortion magnitude as there is little difference between 50- and 100-layer walls final LDS recording. For the numerical model for 100-layers, same conclusions can be made that with an increase in  $K_E$ ,  $K_Q$  value needs to be increased to reduce the computation error.

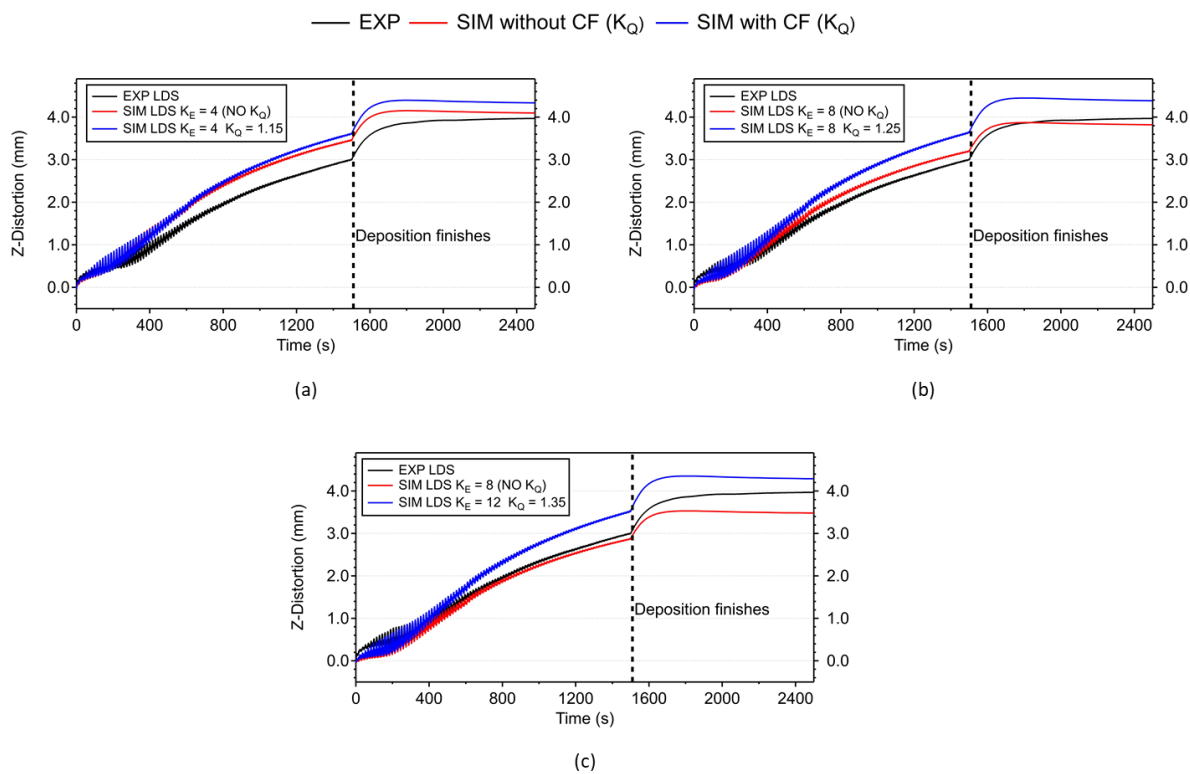


Figure 5. 9: Comparison of experiment (EXP) distortion results with numerical (SIM) distortion results at LDS location for 100-layer wall using EE model with & without correction factor (CF denoted as  $K_Q$ ) with different  $K_E$  values (a)  $K_E = 4$  (b)  $K_E = 8$  (c)  $K_E = 12$

**Table 5.4** presents the results of computation errors (final distortion value at LDS) and computation time taken for mechanical analysis with EE model with different  $K_E$  values. As concluded in the ‘‘Thermal results’’ section, with an increase in number of layers computation time is increasing because of the large mesh size and higher computation time steps. Moreover, with an increase in  $K_E$  value computation time is decreasing by a factor of 3 because of the reduced computation time steps in the analysis.

Table 5. 4: Comparison of computation time for mechanical model using EE model with different  $K_E$  values

| $K_E$ | Computation error: Mechanical model |         |                |         | Computation time: Mechanical model |                |
|-------|-------------------------------------|---------|----------------|---------|------------------------------------|----------------|
|       | 50-layer wall                       |         | 100-layer wall |         | 50-layer wall                      | 100-layer wall |
|       | NO CF                               | With CF | NO CF          | With CF |                                    |                |
| 4     | 1.055 %                             | 0.2 %   | 3%             | 8.96 %  | 10 h 29 min                        | 33 h 17 min    |
| 8     | 13.81 %                             | 2.1 %   | 4%             | 9.16 %  | 7 h 31 min                         | 15 h 50 min    |
| 12    | 20.05 %                             | 0.26 %  | 12.51%         | 7.64 %  | 5 h 3 min                          | 11 h 10 min    |

It was explained in the previous section and proven in Chapters 3 and 4, that conventional thermal model (DE) is computation expensive up-to a factor of 10 as compared to EE model. For the mechanical model also, this effect is same and EE model reduce the computation time up-to a factor 5-10 proven in **Chapter 4**. As shown

in **Table 5.4**, a comparison was done between the distortion value predicted by numerical model and experiment distortion measurement at LDS location. For 50-layer wall, EE model with CF successfully reduces the computation error and makes it possible to employ large CF value such as  $K_E = 12$ . However, for 100-layer wall, with the introduction of CF,  $K_E = 12$  works efficiently, but, with  $K_E = 4$  and 8 values, EE model with CF overpredicts the distortion values. Ideally, smaller values of  $K_E$  should be more accurate but this issue can be due to the fact that for larger number of layers, effect of annealing is more significant. In all simulations performed in Chapters 3 and 4,  $T_{relax} = 1000^\circ\text{C}$  is kept same. In the future, idea of  $T_{relax}$  that depends upon the number of deposition layers (deposited volume) or time dependent can be tested and explored. Nevertheless, even for 100-layers wall, EE model with CF results in computation error less than 10%.

It was found that for 50 and 100-layers wall, EE model without CF results in computation error exceeding 20% and 12% for 50-and 100-layers respectively, however EE model with CF significantly reduces the computation error falls under well accepted value of 10%. This highlights the fact that source correction factor (CF) needs to be considered when Elongated Ellipsoid (EE) model with different sub-track/elongated lengths is employed to model LDED process.

### 5.5.3 Comparison of post-process line distortion results

As explained in **Chapter 4**, part is 3D scanner with an optical scanner to get an idea of global part distortion. The part-scanning, data treatment and analysis are already presented in Chapter 4, so it will not be presented here. The post-process optical 3D scanning results for both 50- and 100-layer wall are presented in **Fig 5.10**.

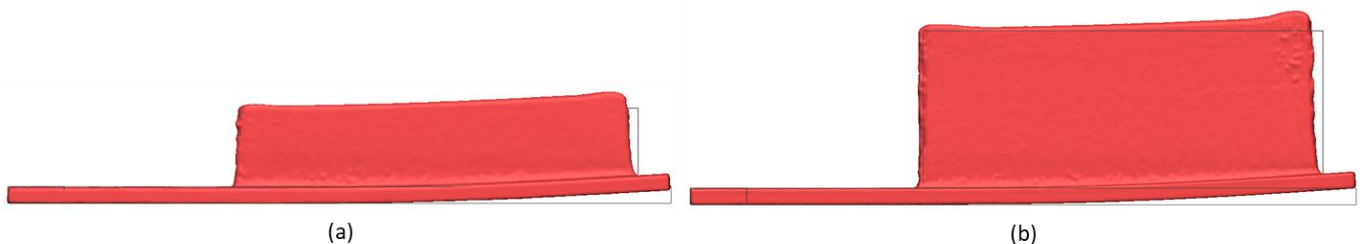


Figure 5. 10: Comparison of Post-Process 3D scan with reference CAD geometry for all experiment cases  
(a) 50-layer wall (b) 100-layer wall

The mechanical model's calculated distortions at part scale as shown in the previous section in **Fig. 5.7** show good agreement with experiment post-process distortions measured by Optical scanner for both experiment cases. The numerical model's post-process line distortion results compared with experiment data are presented in **Fig. 5.11**. For both 50- and 100-layer walls, it can be clearly seen that EE model without CF correctly captures the distortion trend however it underpredicts the distortion magnitude as compared to experimental results for both 50 and 100-layer wall. Same results were found in Chapter 4 as well. But, with the introduction of CF, EE model correctly captures the distortion trend as well as magnitude. This provides more justification that EE model with CF significantly reduces the computation time by keeping acceptable levels of computation accuracy.

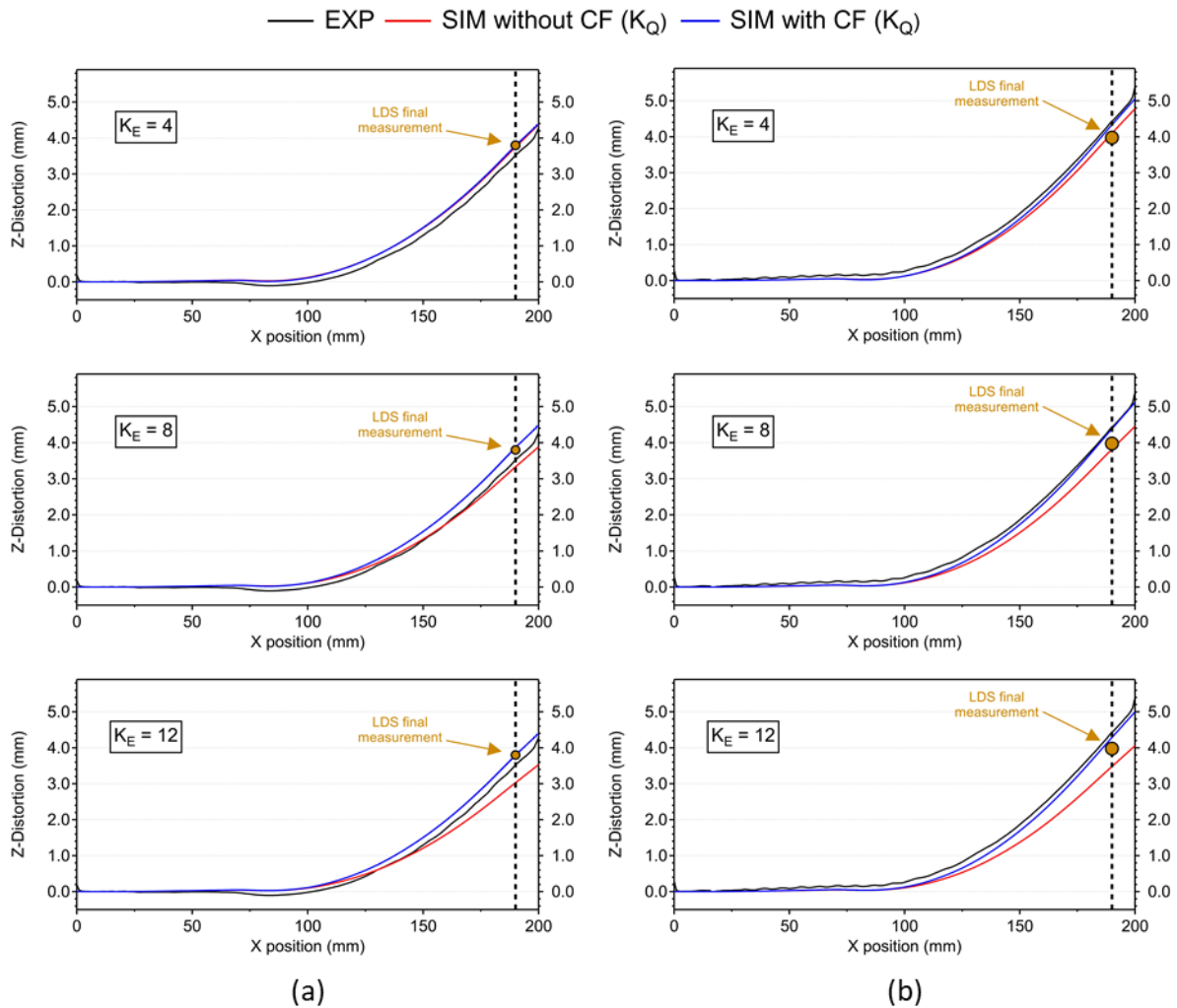


Figure 5. 11: Comparison of experimental post-process line distortion results of Optical scanner (EXP) with numerical results (SIM) using EE model with & without correction factor (CF denoted as  $K_Q$ ) with different  $K_E$  values (a) 50-layer wall (b) 100-layer wall

The final measurement recorded by LDS sensor before workpiece was unclamped is marked on the Fig. 5.11 also. This comparison highlights the fact that LDS sensor and Optical 3D scanner gives consistent values of distortion. It can be seen that for both experiment cases, global part-distortion trends and line-distortion remain the same that with an increase in number of layers leading to more distortion. It can be clearly seen in Fig 5.11, that free-end of substrate has a 4.2- and 5-mm deflection for 50- and 100-layer walls.

## 5.6 Conclusions

In this chapter, it has been demonstrated that the Elongated Ellipsoid (EE) heat source model that averages the heat source (laser energy) along its deposition path is able to perform the large-part process simulation for LDED. The emphasis is done on the choice of sub-track lengths and its impact on computation time to simulate large-parts. It should be noted that the calibrated relaxation temperature of 1000°C used for the previous chapters gives satisfactory results for larger parts also. The numerical study was successfully correlated with experiment data acquired by thermocouples, laser displacement sensor and 3D optical scanner. The main conclusions of this chapter are following:

- EE model with different  $K_E$  values was able to correctly capture the evolution of temperature and distortion trends obtained in the workpiece during LDED process.

- EE model successfully captured the effect of number of deposited and demonstrated its versatility when number of layers are changed from 50 to 100.
- A source correction factor (CF)  $K_Q$  for EE model is implemented that reduces the computation error drastically.
- EE model with CF yields an acceptable level of computation accuracy while reducing computation time significantly up-to a factor of 3 when  $K_E$  values are increased from 4 to 12.
- Computation time reduction is more significant (up-to a factor of 20) when EE model is compared with other conventional models such as Goldak Double Ellipsoid, Gaussian, Top-Hat etc.
- EE model demonstrated its capability of simulating large-part simulation as it was able to simulate 12 and 24 meters of metal deposition for 50- and 100-layer wall with-in practical computation times.

*In the next chapter i.e., Chapter 6, Multi-Scale approach and Inherent Strain method are developed, implemented and tested for process simulation of LDED process, to go further in the reduction of computation times for large-part simulation.*

# Chapter 6: Multi-scale model for LDED<sup>4</sup>

|  |     |
|--|-----|
| Chapter 6: Multi-scale model for LDED.....             | 136 |
| 6.1 Introduction.....                                  | 137 |
| 6.2 Experiment results.....                            | 137 |
| 6.3 Multi-scale method (Layer-by-Layer approach) ..... | 138 |
| 6.3.1 Modeling approach.....                           | 139 |
| 6.3.2 Numerical implementation .....                   | 141 |
| 6.3.3 Results and discussion .....                     | 142 |
| 6.3.4 Conclusions.....                                 | 151 |
| 6.4 Work in progress .....                             | 152 |
| 6.4.1 Inherent Strain-based Multi-scale model .....    | 152 |
| 6.4.2 Distortion compensation model .....              | 158 |
| 6.4.3 Technological transfer to SIEMENS.....           | 159 |

---

<sup>4</sup> It is planned that the work presented in this particular chapter will be the subject of the proceeding pending reviews in a peer-reviewed journal.

## 6.1 Introduction

The objective of the present chapter is to correctly implement, develop and identify the pros and cons of part-scale simulation models such as Multi-scaling models for real-part process simulation for LDED.

In the last few chapters i.e., Chapters 4 and 5, it has been demonstrated that a conventional meso-scale thermo-mechanical model that employs DE heat source works accurately for small-size parts (less than 50 layers) in LDED, however high computation time and large memory requirements start to become an issue. Therefore, it has been demonstrated that the same meso-scale thermo-mechanical model with the proposed EE heat source and source correction factor works efficiently for a real-size part (more than 50-100 layers) by reducing the computation time and lowering the computation resources significantly. But there are other modeling techniques (Multi-scale and IS-based methods) for real-size part process simulation that have been developed and used in the literature (Chen et al., 2021; Liang et al., 2021; Tran et al., 2020b), especially for other AM technologies such as LPBF/SLM.

However, there is a big difference in the scale of fabricated parts obtained with PBF and LDED technologies. Therefore, some research has already been done in the literature to investigate the feasibility of the same part-scale process simulation techniques (initially developed for L-PBF) for LDED technology (Lu et al., 2019b). Lu et al. found out that the same assumptions and modeling techniques that yielded correct results for PBF are not consistent with LDED and therefore exhibit high computation error. But still, these types of feasibility tests of employing these part-scale models for LDED are done in lesser numbers. Therefore, in this chapter, the first objective is to successfully implement and develop these modeling techniques in COMSOL Multiphysics. Then, the second objective of this chapter is to investigate the suitability/effectiveness of these part-scale models for real-size parts in LDED.

## 6.2 Experiment results

Experiments performed and explained in Chapters 4 and 5 are taken as a reference for the comparison with the Numerical model. As a reminder, these experiments deposited single and double bead SS 316L walls ranging from 42 to 100 layers with laser power 800 W, and a scanning speed of 1m/min. To summarize, the design of experiments (DOE) with process parameters is presented in **Table 6.1**.

Table 6. 1: Design of Experiments (DOE) with process parameters of already finished experiments

| EXPERIMENT        | Dwell time $t_{DW}$ (s) | No. of beads $N_B$ | No. of layers $N_L$ | Deposited Length | EXPERIMENT ID |
|-------------------|-------------------------|--------------------|---------------------|------------------|---------------|
| 1-bead small wall | 0                       | 1                  | 42                  | 50               | 1             |
| 1-bead small wall | 5                       | 1                  | 42                  | 50               | 2             |
| 1-bead small wall | 10                      | 1                  | 42                  | 50               | 3             |
| 2-bead small wall | 0                       | 2                  | 42                  | 50               | 4             |
| 2-bead small wall | 5                       | 2                  | 42                  | 50               | 5             |
| 2-bead small wall | 10                      | 2                  | 42                  | 50               | 6             |
| 2-bead large wall | 0                       | 2                  | 50                  | 120              | 7             |
| 2-bead large wall | 0                       | 2                  | 100                 | 120              | 8             |

Therefore, in this chapter, for the sake of simplicity, Experiment ID is used to refer to a particular experiment. Then for each Experiment ID representing the actual experiment, its experiment results are compared with the numerical results obtained with part-scale models developed in this chapter.

### 6.3 Multi-scale method (Layer-by-Layer approach)

As explained in previous chapters, to correctly model the LDED process, laser input energy along with its movement need to be modeled. Furthermore, when the part-size increases, computation time and memory requirements become unfeasible. Therefore, the idea is to apply uniform heat input (up to melting temperature) for the entire layer at once, rather than modeling the laser energy with its deposition pattern. The heat input must be corrected concerning a conventional DE and EE model. The main aim is that heat input should be high enough to represent actual melting so that sufficient temperatures are reached in the layer when uniform heat input is applied. But for large parts comprising thousands of layers, this can still require high computation time. Therefore, this method is adjusted by combining/lumping actual physical layers into a representative “macro” layer as shown in Fig. 6.1.

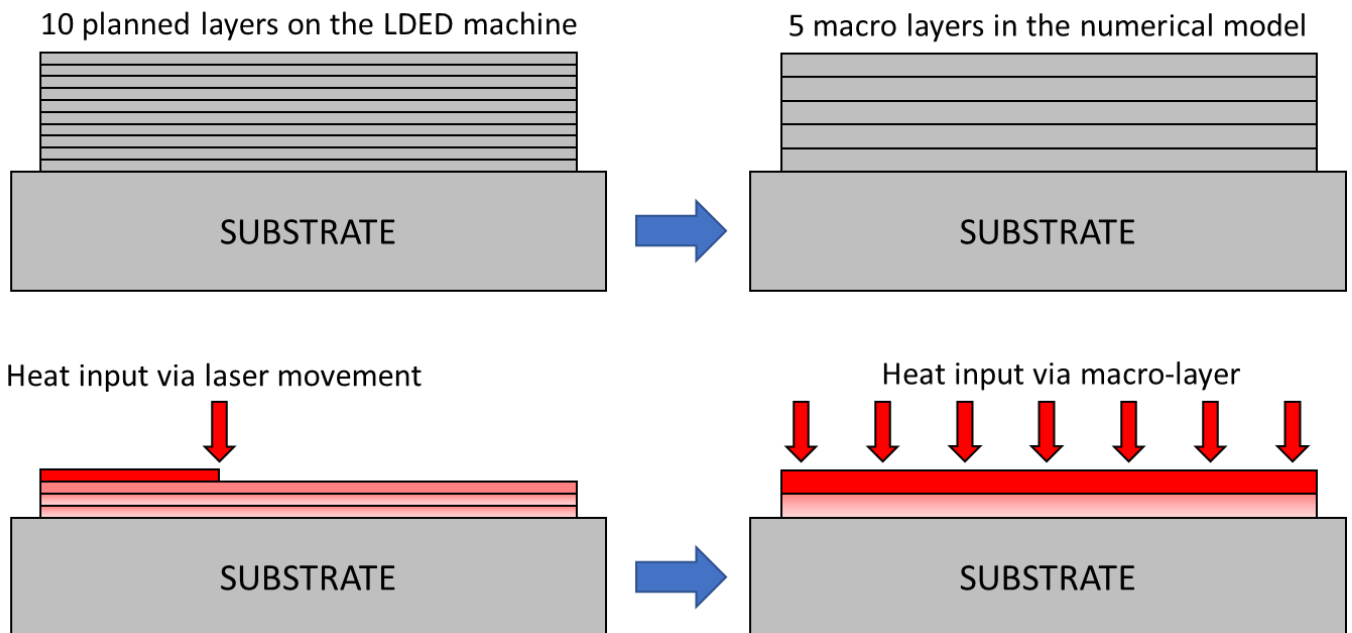


Figure 6. 1: Schematic of Multi-scale (Layer-by-Layer approach) part-scale model

Uniform heat input is applied on the macro layer at once, therefore heat input needs to be corrected again depending upon macro-layer thickness (number of layers combined/lumped). The material deposition is also done in the same way (Heat input) as well by numerically adding the macro layer at once i.e., in one computation time step. Therefore, this type of approach does not take into account scanning strategies. Material activation is done by employing the Quiet/Active material activation method as was done in the previous chapters.

The heat input is applied for the actual deposition time (exposure/flash time:  $t_f$ ) for a single layer i.e., if the time taken to deposit for a single layer is 3 seconds and then a dwell time of 5 seconds, in the Multi-scale model, the uniform heat input is applied for the same 3 seconds that will lead to the heating phase. Then, for a dwell period of 5 seconds, no heat input is applied and the newly deposited layer is allowed to cool as was the case in the actual experiment. Hence, the heat input function is a time-dependent step function that returns the value of one during the deposition of the respective layer and returns zero value during the dwell

period. Then the second layer is activated, heated, and cooled, in the same way, employing the step function and this process is repeated until the complete part is numerically deposited.

The Multi-scale (Layer-by-Layer) approach, where layer lumping/combining results in macro-layer is extensively employed for PBF technology in the literature (Ganeriwala et al., 2019; Gouge et al., 2019; Hodge et al., 2016) and has demonstrated its effectiveness by significantly reducing the computational resources requirement. However, this type of methodology indeed leads to computation inaccuracy as compared to a traditional meso-scale thermo-mechanical model that models laser movement for each layer, but this method provides an insight into the global response of the material much faster and practical computation time.

Therefore, in the present work, a Multi-scale approach is developed to investigate its effectiveness for LDED technology.

## 6.3.1 Modeling approach

The simplification of the geometry, sequential coupled thermo-mechanical analysis is done in the same way as presented in **Section 2 “Modeling Approach”** of Chapter 4.

### 6.3.1.1 Thermal Model

The initial boundary conditions, convective and radiative heat losses, are identical to the formulation explained in Chapters 2, 3, and 4 and are based on **Equations 2.4, 2.5, and 2.7**. The natural and forced convective coefficient values are kept the same as emissivity values. Also, specific heat capacity is modified using the same method (**Eq 2.8**) mentioned in **Chapter 2**. Finally, an enhanced thermal conductivity factor of 2.5 is kept for thermal conductivity beyond melting temperature (**Eq. 2.9**) given in **Chapter 2**.

#### 6.3.1.1.1 Heat source model

Instead of solving the laser movement along with laser-material interaction at the meso-scale, an equivalent uniform volumetric heat source is applied to the newly activated macro layer for a given deposition time (same deposition time from experiments) i.e., exposure/flash time ( $t_f$ ), see **Fig 6.2**.

$$Q_{macro} = \frac{AP}{L.W.T} \quad (6.1)$$

Where A is the absorption efficiency, P is the laser power, L, W, and T are the macro layer’s length, width, and thickness/height respectively. The exposure/flash time ( $t_f$ ) is the total amount of time taken to deposit the macro layer. It is worth reminding that in Chapters 3 and 4, for DE heat source model that captures laser movement, the value of A was 0.4, and it was sufficient to achieve peak melt-pool temperatures beyond the fusion temperature of the material that is coherent with the actual LDED process. Furthermore, the DE model was validated with thermocouple and LDS (distortion) data. Also, in Chapter 5, for the efficient EE model captures the laser travel, a correction factor (CF) was introduced with an A = 0.4 value so that sufficient peak melt-pool temperatures are achieved that represent actual physical phenomena. With this, the EE model was also validated with thermocouple and LDS data. In the Multi-scale model, the deposition sequence is not taken into account, and a uniform heat source is applied to the whole layer at once. With this approach, we cannot expect to have correct temperature gradients at the deposited layers, and the effect of moving heat source (zig-zag) on the temperature prediction at the thermocouple’s location on the substrate. The exact local thermal results cannot be reproduced with a global source applied over the entire length of the layer, so the

question arises whether this simplified approach can lead to an adequate global mechanical response. In other words, how to calibrate this global heat source to obtain satisfactory distortions. Here, we have chosen to calibrate the value of  $A$  by two approaches that are as following:

1. Thermal model should predict the correct temperature at the thermocouple location irrespective of the temperature predicted at the fabricated part.
2. Thermal model should predict the physical temperature at the fabricated part i.e., the material is activated in a layer-by-layer fashion. Heat input should be high enough so that the newly deposited layer experiences temperature around fusion temperature that corresponds to the actual phenomenon irrespective of the temperature predicted at the thermocouple location.

Therefore, different values of  $A$  are taken to perform a sensitivity analysis for all experiment cases. Finally, an optimized value for the  $A$  parameter was identified. The calibrations and choice of the value are elaborated in Section 6.3.3 (Results and discussion).

### 6.3.1.1.2 Macro-layer thickness

In the present work, the macro-layer thickness is taken as 1 actual physical layer thickness, as the number of layers deposited in the experiments is less than 100, so computation time and resources requirement will not be an issue. Therefore, the values of  $L$ ,  $W$ ,  $T$ , and  $t_f$  are the actual physical values and can be easily extracted from the obtained results from the previous chapters and are presented in **Table 6.2**. In the case of a double bead wall, the width of the macro layer is the width of the two beads and the exposure/flash/deposition time ( $t_f$ ) corresponds to the time required to deposit the two beads per layer. Note that no dwell time is applied during the deposition of the two beads for a given layer.

Table 6. 2: Uniform Heat Source parameters extracted values for different experiments (with  $t_{DW}$ : dwell time,  $N_B$ : number of beads,  $N_L$ : number of layers)

| EXPERIMENT ID                               | L (mm) | W (mm) | T (mm) | $t_f$ (s) |
|---|--------|--------|--------|-----------|
| 1 ( $t_{DW}$ : 0 s, $N_B$ : 1, $N_L$ : 42)  | 50     | 2.1    | 0.428  | 3         |
| 2 ( $t_{DW}$ : 5 s, $N_B$ : 1, $N_L$ : 42)  | 50     | 2.1    | 0.43   | 3         |
| 3 ( $t_{DW}$ : 10 s, $N_B$ : 1, $N_L$ : 42) | 50     | 2.1    | 0.433  | 3         |
| 4 ( $t_{DW}$ : 0 s, $N_B$ : 2, $N_L$ : 42)  | 50     | 3.4    | 0.552  | 6         |
| 5 ( $t_{DW}$ : 5 s, $N_B$ : 2, $N_L$ : 42)  | 50     | 3.4    | 0.559  | 6         |
| 6 ( $t_{DW}$ : 10 s, $N_B$ : 2, $N_L$ : 42) | 50     | 3.4    | 0.561  | 6         |
| 7 ( $t_{DW}$ : 0 s, $N_B$ : 2, $N_L$ : 50)  | 120    | 3.5    | 0.5    | 14.4      |
| 8 ( $t_{DW}$ : 0 s, $N_B$ : 2, $N_L$ : 100) | 120    | 3.5    | 0.5    | 14.4      |

Though not investigated/developed here, in the future, if the deposited layers are greater than 100, the macro-layer thickness could easily be increased.

### 6.3.1.2 Mechanical Model

The mechanical model being identical to that present in **Chapter 4**, will not be detailed here. This model is based on the resolution of **Equations 4.1, 4.2, and 4.3**. Computation of elastic, thermal, and plastic strain is

done in the same way as in **Chapter 4 (Eq. 4.4, 4.6, 4.7, and, 4.8)**. The same EP model with Non-Linear isotropic hardening law, which is explained in detail in **Chapter 4** is also employed in this chapter, so it will not be detailed here.

## 6.3.2 Numerical implementation

### 6.3.2.1 FEA solver

COMSOL Multiphysics-based solver (PARDISO) is employed to perform the FEM analysis. The adaptive time-stepping method is used rather than a strict formulation to reduce the computation time. As the material is deposited layer-by-layer, during the deposition period, the computation time step of ( $t_f$ ) is taken representing the layer is numerically deposited in one computation time step. For example, in Experiment ID 1 (single bead wall with 0s dwell time), actual deposition time ( $t_f$ ) for 1 layer is 3s, hence heat input is applied at the first layer for a duration of exposure/flash time i.e., ( $t_f$ ) from 0-3s and layer 1 is activated from 0s itself. Then from 3-6s, heat input is applied at the second layer for a duration of exposure/flash time i.e., ( $t_f$ ) and layer 2 is activated from 3s itself. However, for Experiment ID 4 (double bead wall with 0s dwell time), the actual deposition time ( $t_f$ ) for 1 layer is 6s, hence heat input is applied at the first layer for a duration of exposure/flash time i.e., ( $t_f$ ) from 0-6s and layer 1 is activated from 0s itself. Therefore, each layer experiences heat input for the exposure/flash/deposition time that depends upon the experimental conditions.

For the dwell period between layers, a computation step ( $t_{DW}$ ) is taken that represents the inter-layer cooling period is also solved in one computation time step. The computation time step of ( $3 \times t_f$ ) is taken during the period of cooling down once the deposition process is finished. All simulations are done on the same workstation (16 cores, 128 GB RAM, Intel Xeon W-2275 processor).

### 6.3.2.2 FEM mesh

For the sake of simplicity and comparison, identical meshes are employed in this chapter as taken for DE and EE heat source models in previous chapters. However, as the heat source does not move and uniform heat input is applied per layer, a coarse mesh could be used to reduce the computation time.

### 6.3.2.3 Material deposition model

Material deposition modeling is done in the same way as explained in detail in **Section 4.3 “Quiet/Active Material Activation Method”** of **Chapter 4**, so it is not presented here in detail.

However, as the layers are numerically deposited one by one (layer-by-layer), they are now activated concerning exposure/flash time ( $t_f$ ). Hence, the material is no more activated by following the moving laser and activating the material if the input source’s intensity is >5% heat source intensity. Here, to activate the material in a layer-by-layer fashion, an if condition is used in the following way to numerically activate the layer-by-layer approach.

$$if(dom == domain(t), 1,0) + solid.wasactive \quad (6.1)$$

As explained in Chapter 2 previously, an analytical function domain(t) is created that stores the COMSOL *Multiphysics*® 5.6 generated domain and surface number as a function of time, therefore taking into account the time. The variable *dom* is COMSOL *Multiphysics*® 5.6 generated identifier for different domains of the

CAD. The functioning of the domain(t) function is represented in Fig 6.2, which explains how this function activates the material in a layer-by-layer approach.

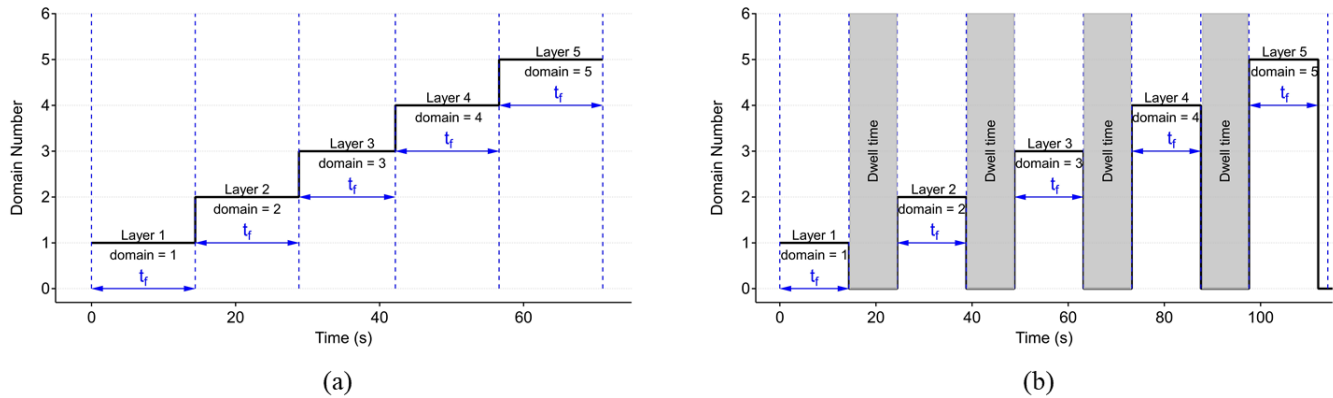


Figure 6. 2: Schematic of material activation strategy for Multi-scale method (layer-by-layer)  
(a) No dwell time (b) With dwell time (10s)

For the experiment cases (EXP ID 1,4 and 7-8) with no dwell time, as shown in Fig 6.2(a), during the exposure/flash time ( $t_f$ ) of the first layer, domain 1 i.e., layer 1 is activated, that is followed by the exposure/flash time of the second layer, for which domain 2 i.e., layer 2 is activated, and this trend is repeated until the numerical activation of the complete part. For the experiment cases (EXP ID 2-3 and 5-6) with dwell time, as shown in Fig 6.2(b), analysis with the dwell period, the domain(t) function returns zero value justifying no energy input to any layer during that period. The *solid.wasactive* command makes sure that once the material is activated, it can never be de-activated during the numerical analysis.

### 6.3.2.4 Model calibrations and boundary conditions

As explained in Chapters 2, 3, 4, and 5, layer geometry is simplified, the effect of forced convection and heat loss due to conduction heat transfer from the deposited part to the substrate is considered in the same way with the same parameter's values.

## 6.3.3 Results and discussion

In the first-time step, the first layer is activated and the uniform heat source is applied. Following this, the second layer is activated and the uniform heat source is applied, and this process is repeated until the complete wall is deposited and analyzed. As shown in Fig 6.3, successful implementation of a Multi-scale method was done that utilizes a Uniform Heat source with  $A = 0.4$  value, as this value was taken throughout the thesis work. It can be noticed (see color legend) that the newly activated layers experience a peak temperature of around 1000°C which is way lower than the fusion temperature of SS 316L i.e., 1450°C. However, it will be discussed in this section later, that with an  $A = 0.4$  value, the numerical model accurately predicts the temperature evolution at the TC location for most experiment cases.

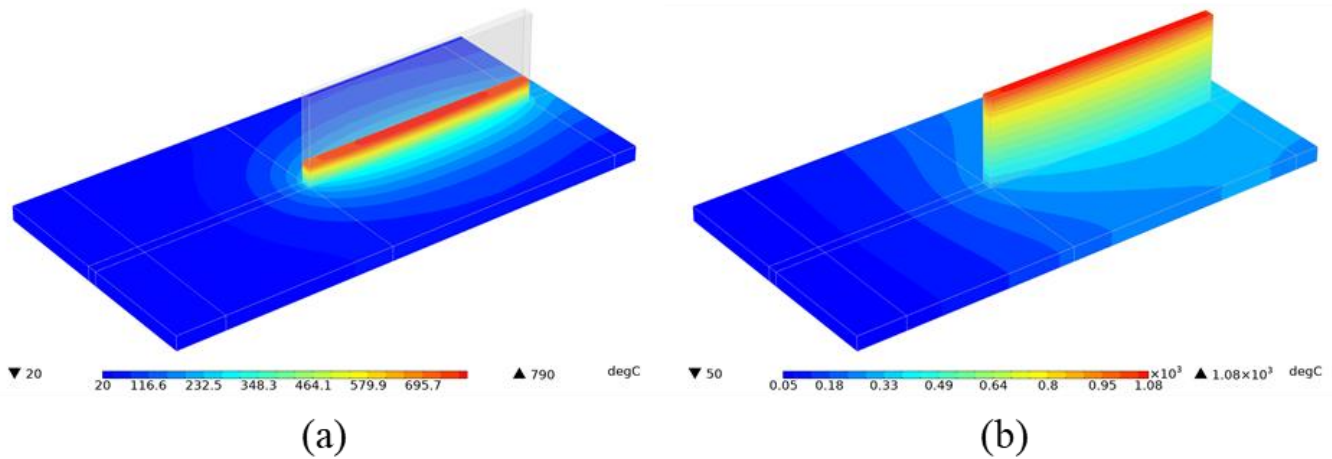


Figure 6. 3: Temperature field obtained with  $A = 0.4$  for Experiment ID 1  
(a) 10<sup>th</sup> (d) 42<sup>nd</sup> layer

Therefore, different values of  $A$  are taken e.g., 0.4, 0.5, 0.6, and 0.75 aiming to achieve peak temperature around fusion temperature. With  $A = 0.75$  value, the model yielded peak temperature around fusion temperature as shown in **Fig 6.4** (see color legend).

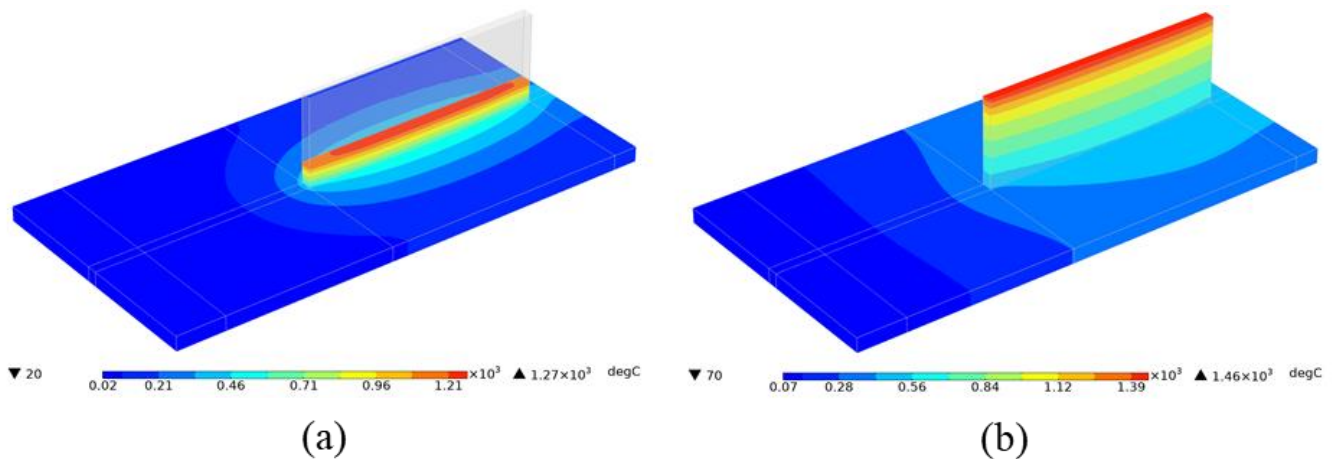


Figure 6. 4: Temperature field obtained with  $A = 0.75$  for Experiment ID 1  
(a) 10<sup>th</sup> (d) 42<sup>nd</sup> layer

However, it will be discussed in this section later, that with  $A = 0.75$  value, the numerical model significantly overpredicts the temperature evolution at the TC location for most experiment cases. Therefore, it is a choice if the model needs to be calibrated at the thermocouple ( $A = 0.4$ ) or fabricated part location ( $A = 0.75$ ). For all experiment cases, simulation was done with different  $A = 0.4, 0.5, 0.6,$  and  $0.75$  values and the numerical results are compared with experimental results to identify a correct  $A$  value.

Before proceeding to the results directly, there is one important point that needs to be considered. In the LDED process, each layer during its deposition experiences both a heating (current deposited material) and a cooling phase (already deposited material of the layer). Especially for 0 s dwell time, in the Multi-scale method as shown in **Fig 6.2(a)**, layers are deposited in a one-time step, and then in the next computation time step, the consequent layer is deposited. This does not allow the current deposited layer to experience a cooling phase. This is contrary to the actual experiment where the layer experiences both heating and subsequent cooling phase. Therefore, especially for experiments that have 0s dwell time, a modification in the model is

done in such a way that each layer experiences heating and cooling phenomena similar to the actual LDED process. For example, in Experiment ID 1 (single bead wall with 0s dwell time), the actual deposition time or exposure/flash time ( $t_f$ ) to deposit one layer is 3s and then the subsequent layer is deposited from 3-6s. As shown in **Fig 6.5**, applying the uniform heat source for the same exposure/flash time ( $t_f$ ) i.e., 3 s, the deposited layer experiences a heating phase, and subsequently, the next layer is deposited from 3-6s. and hence in this way, numerically deposited layers are not experiencing a cooling phase. It can be observed in **Fig 6.5(b)**, that the numerical model predicts thermo-mechanical response and is not able to capture the distortion trend (red curve). This is because, for 0 s dwell time, the model is not able to capture the cooling phenomenon that is happening in the actual process.

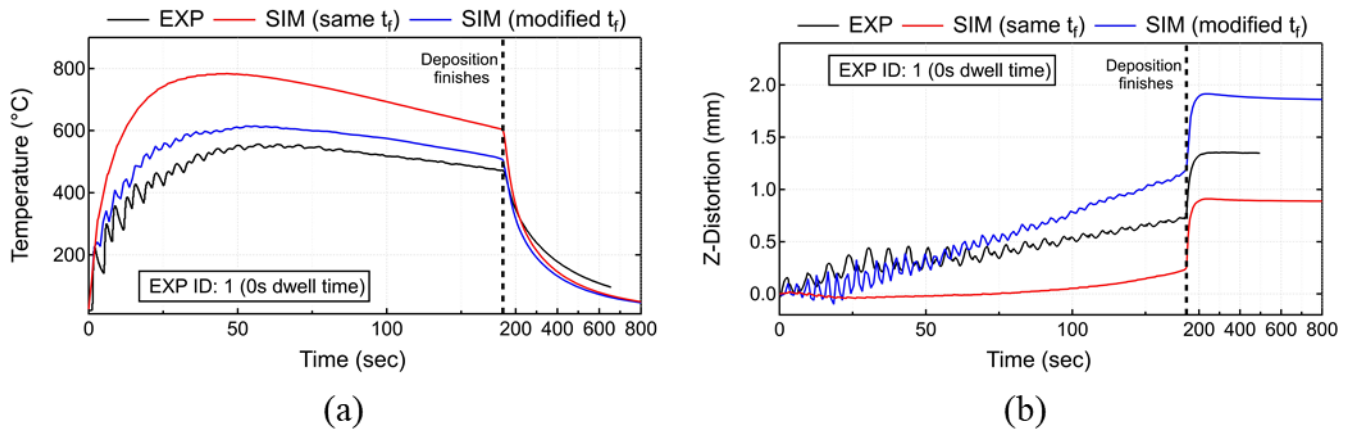


Figure 6. 5: Numerical results obtained with original  $t_f$  and modified  $t_f$  method for EXP ID 1 with  $A = 0.75$   
(a) Thermal (b) Mechanical results

Therefore, to account for the cooling phenomenon especially for 0 s dwell time experiments, the uniform heat source is applied for  $0.75 * t_f$ , and the remaining  $0.25 * t_f$ , is considered as a cooling phase. This implies that for  $0.75 * 3$  s duration, the uniform heat source is applied that leads to the heating phenomenon and the remaining  $0.25 * t_f$  phase will contribute to the cooling phenomenon as no heat input is prescribed. But it should be noted that each layer follows the actual deposition time planning i.e., layer 1 is numerically deposited in 3s and the second layer commences at 3s. This allows the model to follow the same layers deposition concerning time, but models both heating and cooling phases. The effect of modifying  $t_f$  that leads to the heating as well as cooling phase of the newly activated layer is shown in **Fig 6.5**. The value of  $0.75 * t_f$  and  $0.25 * t_f$  is chosen in such a way that the numerical model predicts peak temperature above fusion temperature (coherent to process) and after  $0.25 * t_f$  i.e., cooling phase, the temperature field is coherent with the results obtained with DE model. However, for 0s dwell time, different combinations of  $A$  value and heating/cooling phase can be chosen i.e.,  $0.6 * t_f$  and  $0.4 * t_f$  or something else, but the obtained temperatures must be coherent with the process physics.

It can be noticed in **Fig 6.5(a)** that with real  $t_f$  (red curve), the temperature rises continuously as the workpiece experiences a heating phase with the deposition of each new layer. There is no cooling phase as there is no dwell time, and this leads to an increase in temperature without a drop-down. This phenomenon is repeated until the newly activated layer is far high than the substrate leading to a decrease in temperature with further deposition of layers. However, with modified  $t_f$  (blue curve), with the deposition of a new layer in  $0.75 * t_f$  duration, newly layer experiences a cooling phase in  $0.25 * t_f$  resulting in a drop-down of temperature. This leads to better computational accuracy as compared to a model with real/same  $t_f$ . For the mechanical analysis, it can be seen in **Fig 6.5(b)** that model with the same/real  $t_f$  (red curve) predicts substrate moving downwards as the material is experiencing only temperature rise for the first  $t$  10-15 layers. This is contrary to the

experiment's trend as the substrate is moving upwards and downwards during the heating and cooling phases. But, with modified  $t_f$  (blue curve), the model captures the distortion trend accurately, however, fails to correctly capture the distortion magnitude. Therefore, for Experiment ID 1, 4, 7, and 8 that have 0s dwell time, modified  $t_f$  is used that signifies, for the newly activated layer, the uniform heat source is applied for  $0.75 \cdot t_f$  duration and let it cool for  $0.25 \cdot t_f$  duration. The heating phase of  $0.75 \cdot t_f$  duration and the cooling phase of  $0.25 \cdot t_f$  duration seems to be the acceptable choice as this duration allows the newly activated layer to achieve fusion temperatures but also allows the layer to drop down the temperature.

For 5 and 10s dwell time, the uniform heat source is applied to the actual deposition time i.e., exposure/flash time ( $t_f$ ) that leads to the heating phase. During specified actual dwell time layers are allowed to cool. So, there is no requirement of modifying the real value of  $t_f$  for experiment cases that have assigned dwell time (EXP ID 2, 3, 5, and 6).

### 6.3.3.1 Comparison of temperature evolution

The numerical results obtained with the Multi-scale method employing different A values for Experiment ID 1-6 are successfully compared with experimental results as shown in Fig 6.6.

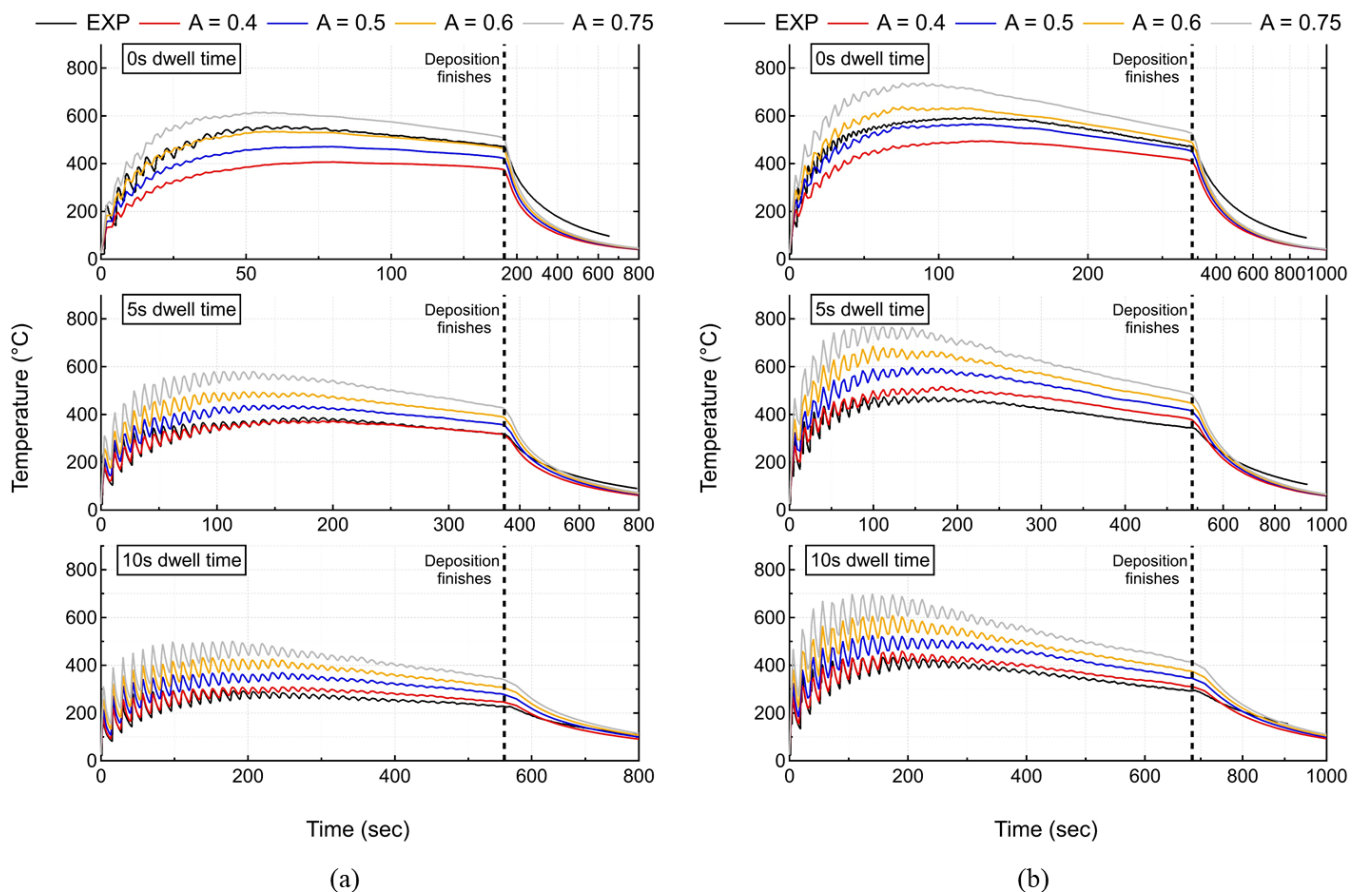


Figure 6. 6: Comparison of numerical results ( $A = 0.4, 0.5, 0.6,$  and  $0.7$ ) with recorded In-situ thermal history (EXP) of thermocouple 1 for Experiment ID 1-6.

(a) 1 bead wall (b) 2 bead wall

It can be seen that for experiment cases with dwell times of 5, and 10 s, a numerical model with  $A = 0.4$  seems to capture the temperature trend at the TC location correctly. However, for experiment cases with a dwell time of 0 s,  $A = 0.5$  gives correct results. A numerical model with an  $A = 0.75$  value significantly overpredicts the temperature evolution at the TC location. Therefore, some important information is extracted as follows:

- Thermal model with  $A = 0.4$ , and  $0.5$  value correctly captures the temperature evolution at TC location but underpredicts the peak temperature at fabricated part.
- Thermal model with  $A = 0.6$ , and  $0.75$  value significantly overpredicts the temperature evolution at TC location, but correctly predicts the peak temperature around fusion temperature at fabricated part.
- Thermal model correctly and consistently captures the temperature trends for all experiment cases irrespective of  $A$  value.
- Thermal model is not consistent as different  $A$  values are required to achieve computational accuracy depending upon the process parameters.

The computation thermal errors increase with an increase in the  $A$  value for most experiment cases as shown in **Table 6.3**. The errors further increase for the 2-bead wall when the deposited volume is increased. Hence suggests that with an increase in deposited volume, computation errors increase as the simplification is too loose.

Table 6. 3: Computation thermal error at thermocouple location for Multi-scale method employing different  $A$  values

| EXPERIMENT ID                              | Computation thermal error (%) |           |           |            |
|--|-------------------------------|-----------|-----------|------------|
|  | $A = 0.4$                     | $A = 0.5$ | $A = 0.6$ | $A = 0.75$ |
| 1 ( $t_{DW}: 0$ s, $N_B: 1$ , $N_L: 42$ )  | 35.2                          | 28.3      | 22.9      | 21.6       |
| 2 ( $t_{DW}: 5$ s, $N_B: 1$ , $N_L: 42$ )  | 12.2                          | 14.9      | 20        | 28.51      |
| 3 ( $t_{DW}: 10$ s, $N_B: 1$ , $N_L: 42$ ) | 9.4                           | 20.2      | 31.8      | 47         |
| 4 ( $t_{DW}: 0$ s, $N_B: 2$ , $N_L: 42$ )  | 28.2                          | 22.1      | 20.4      | 22.9       |
| 5 ( $t_{DW}: 5$ s, $N_B: 2$ , $N_L: 42$ )  | 13                            | 19.8      | 26.4      | 35         |
| 6 ( $t_{DW}: 10$ s, $N_B: 2$ , $N_L: 42$ ) | 6.6                           | 18.3      | 30.1      | 45.4       |
| 7 ( $t_{DW}: 0$ s, $N_B: 2$ , $N_L: 50$ )  | 24.6                          | 13.3      | 9         | 16.1       |
| 8 ( $t_{DW}: 0$ s, $N_B: 2$ , $N_L: 100$ ) | ---                           | ---       | ---       | ---        |

But this kind of analysis (layer-by-layer) takes relatively lesser computation time (1/2 times less than the EE model) as shown in **Table 6.4**, and can help understand the global response of the part.

Table 6. 4: Comparison of computation time for thermal analysis for different models

| EXPERIMENT ID                              | DE model    | EE model    |            |            | Multi-scale<br>(Layer-by-Layer) |
|--|-------------|-------------|------------|------------|---------------------------------|
|  |             | $K_E = 4$   | $K_E = 8$  | $K_E = 12$ |                                 |
| 1 ( $t_{DW}: 0$ s, $N_B: 1$ , $N_L: 42$ )  | 4 h 42 min  | 1 h 5 min   | 48 min     | 38 min     | 22 min                          |
| 2 ( $t_{DW}: 5$ s, $N_B: 1$ , $N_L: 42$ )  | 5 h 41 min  | 1 h 10 min  | 44 min     | 32 min     | 28 min                          |
| 3 ( $t_{DW}: 10$ s, $N_B: 1$ , $N_L: 42$ ) | 7 h 22 min  | 1 h 22 min  | 59 min     | 39 min     | 34 min                          |
| 4 ( $t_{DW}: 0$ s, $N_B: 2$ , $N_L: 42$ )  | 8 h 36 min  | 2 h 32 min  | 1 h 58 min | 1 h 34 min | 43 min                          |
| 5 ( $t_{DW}: 5$ s, $N_B: 2$ , $N_L: 42$ )  | 9 h 5 min   | 3 h 14 min  | 2 h 15 min | 1 h 55 min | 54 min                          |
| 6 ( $t_{DW}: 10$ s, $N_B: 2$ , $N_L: 42$ ) | 10 h 20 min | 3 h 42 min  | 3 h 10 min | 2 h 36 min | 59 min                          |
| 7 ( $t_{DW}: 0$ s, $N_B: 2$ , $N_L: 50$ )  | ----        | 4 h 27 min  | 3 h 03 min | 1 h 35 min | 45 min                          |
| 8 ( $t_{DW}: 0$ s, $N_B: 2$ , $N_L: 100$ ) | ----        | 14 h 15 min | 7 h 43 min | 5 h 04 min | 2 h 17 min                      |

For Experiment ID 7-8, much longer and higher walls are deposited as compared to Experiment ID 1-6. It can be seen in **Fig 6.7** (see color legend), that even with  $A = 0.75$  value, the peak temperatures predicted by the model are much below the fusion temperature. Therefore, to achieve peak temperature around fusion temperature, a much higher value of  $A$  needs to take. A model employing  $A = 0.4, 0.5,$  and  $0$  values predicts peak temperature around  $600-800^{\circ}\text{C}$  at the fabricated part.

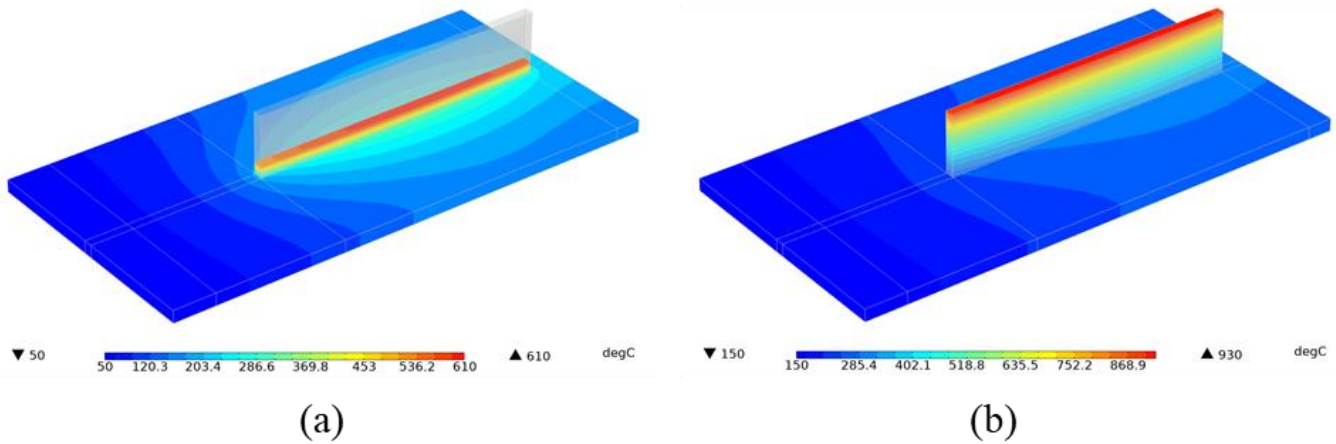


Figure 6. 7: Temperature field obtained with  $A = 0.75$  for Experiment ID 7  
(a) 10<sup>th</sup> (d) 50<sup>th</sup> layer

However, at the thermocouple location, the Multi-scale model with  $A = 0.6$  value correctly captures the temperature evolution as shown in **Fig. 6.8**. It is worth reminding again that for Experiment IDs 1 and 4, the model employing  $A = 0.5$  value gave accurate results at the thermocouple location. Hence again proves the point that the Multi-scale model captures the temperature trend correctly but it is not consistent in accurately capturing the temperature magnitude with a consistent  $A$  value. Hence, it can be concluded that the model calibration is done at the TC location yielded accurate results but with different  $A$  values. Hence the  $A$  value should be calibrated whenever there is a change of design or any other process parameter. On the contrary model calibration done at the fabricated part ( $A = 0.75$  and  $A > 0.75$ ) yields inaccurate results as compared to experiment results at TC. So, it depends upon the developer how does he/she want to calibrate the model. However, it can be said that the multi-scale model can be employed to understand the global thermal response of the fabricated part as it captures the trends correctly.

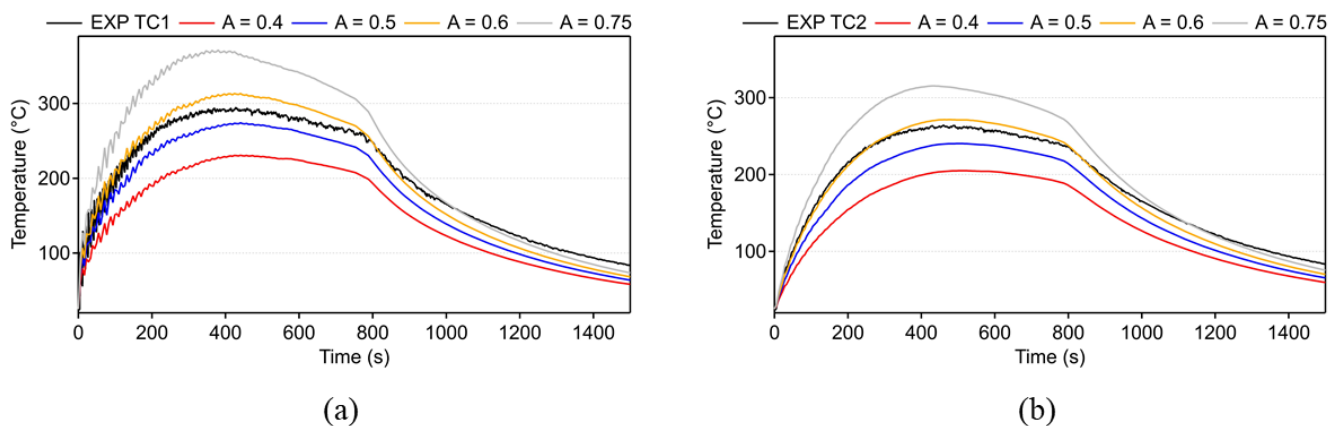


Figure 6. 8: Comparison of numerical results ( $A = 0.4, 0.5, 0.6,$  and  $0.7$ ) with recorded In-situ thermal history (EXP) of thermocouple 1 for Experiment ID 7.

(a) TC1 (b) TC2

It was previously explained in Chapter 5, that for Experiment ID 8 (100-layer wall), the thermocouple had some issues and it was not able to record the temperature recordings. Therefore, for Experiment ID 8, thermal results are not presented. However, the computation time for thermal analysis (1/2 times less than the EE model) is drastically reduced with this type of model and can be done in a few min/hours as shown in **Table 6.4**.

### 6.3.3.2 Comparison of in-situ distortion analysis

For the mechanical analysis, the numerical results obtained with the Multi-scale method for Experiment ID 1-6 are successfully compared with experimental results as shown in **Fig 6.9**.

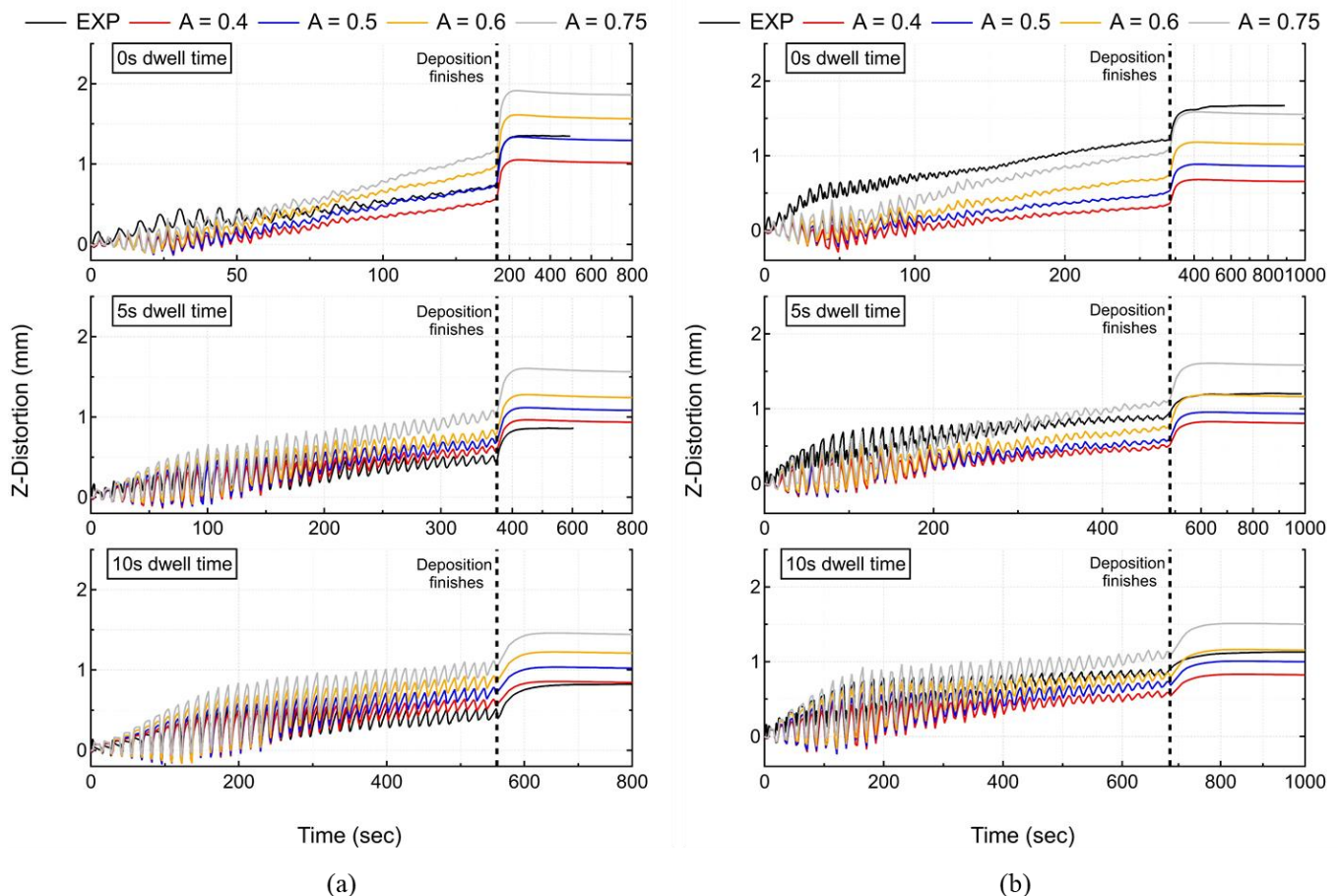


Figure 6. 9: Comparison of numerical results ( $A = 0.4, 0.5, 0.6,$  and  $0.7$ ) with recorded In-situ distortion history (EXP) of LDS for Experiment ID 1-6.

(a) 1 bead wall (b) 2 bead wall

Some of the observations made in the thermal model are coherent for the mechanical model also. For example:

- Model with  $A = 0.75$  value significantly overpredicts the distortion magnitudes for all experiment cases (except Experiment ID 4).
- For Experiment ID 1 (0 s dwell time), a model with  $A = 0.5$  value captures distortion accumulation correctly and yields accurate results.
- For Experiment ID 2 and 3, a model with  $A = 0.4$  seems to give accurate results.
- For Experiment ID 4, a model with  $A = 0.75$  fails to capture the distortion accumulation, however it gives an accurate final LDS distortion value.
- For Experiment ID 5 and 6, a model with  $A = 0.6$  seems to give accurate results.

The model for all experiment cases captures the distortion trends correctly, *however with different A values in different experiment cases*. Therefore, it again points to the fact that the model is inconsistent in terms of A value and its correct value needs to be identified first for each specific case, otherwise, the model yields higher computation errors. Instead of calculating and averaging errors at each computation time step, only the last value of LDS recording is considered to measure the mechanical errors that are shown in **Table 6.5**.

Table 6. 5: Computation mechanical error at LDS location for Multi-scale method employing different A values

| EXPERIMENT ID                               | Computation mechanical error (%) |         |         |          |
|---|----------------------------------|---------|---------|----------|
|   | A = 0.4                          | A = 0.5 | A = 0.6 | A = 0.75 |
| 1 ( $t_{DW}$ : 0 s, $N_B$ : 1, $N_L$ : 42)  | 25.01                            | 4.97    | 15.07   | 37.34    |
| 2 ( $t_{DW}$ : 5 s, $N_B$ : 1, $N_L$ : 42)  | 7.22                             | 23.54   | 42.19   | 79.48    |
| 3 ( $t_{DW}$ : 10 s, $N_B$ : 1, $N_L$ : 42) | 0.36                             | 21.17   | 44.43   | 72.58    |
| 4 ( $t_{DW}$ : 0 s, $N_B$ : 2, $N_L$ : 42)  | 61.07                            | 49.10   | 31.73   | 7.78     |
| 5 ( $t_{DW}$ : 5 s, $N_B$ : 2, $N_L$ : 42)  | 34.16                            | 23.33   | 4.16    | 30.83    |
| 6 ( $t_{DW}$ : 10 s, $N_B$ : 2, $N_L$ : 42) | 28.88                            | 12.88   | 0.44    | 31.55    |
| 7 ( $t_{DW}$ : 0 s, $N_B$ : 2, $N_L$ : 50)  | 52.60                            | 36.54   | 23.90   | 4.16     |
| 8 ( $t_{DW}$ : 0 s, $N_B$ : 2, $N_L$ : 100) | 47.93                            | 33.09   | 15.49   | 0.85     |

As can be noticed in **Table 6.5**, A values that result in computational mechanical error less than 10% (acceptable limit) are highlighted in green color. It can be noticed that the optimized value for each experiment is changing. Some noticeable trends are coherent with the thermal model, i.e., that the optimized value of A for the thermal model is generally consistent with the optimized value of A for the mechanical model also. As the build/deposited volume increases (from 1 bead (EXP ID 1-3) to 2 beads (EXP ID 4-6)), the required/optimized value of A is also increasing from 0.4 to 0.6 which leads to a minimum computation error. As was observed for the thermal model, this type of model can help understand the global thermo-mechanical response of the workpiece with a significantly reduced computation time as shown in **Table 6.6**.

Table 6. 6: Comparison of computation time for mechanical analysis for different models

| EXPERIMENT ID                               | DE model    | EE model    |             |             | Multi-scale<br>(Layer-by-Layer) |
|---|-------------|-------------|-------------|-------------|---------------------------------|
|   |             | $K_E = 4$   | $K_E = 8$   | $K_E = 12$  |                                 |
| 1 ( $t_{DW}$ : 0 s, $N_B$ : 1, $N_L$ : 42)  | 10 h 45 min | 2 h 16 min  | 1 h 28 min  | 1 h 2 min   | 40 min                          |
| 2 ( $t_{DW}$ : 5 s, $N_B$ : 1, $N_L$ : 42)  | 16 h 7 min  | 4 h 14 min  | 2 h 2 min   | 1 h 31 min  | 58 min                          |
| 3 ( $t_{DW}$ : 10 s, $N_B$ : 1, $N_L$ : 42) | 18 h 37 min | 4 h 16 min  | 2 h 15 min  | 1 h 38 min  | 1 h 27 min                      |
| 4 ( $t_{DW}$ : 0 s, $N_B$ : 2, $N_L$ : 42)  | 24 h 19 min | 5 h 20 min  | 3 h 26 min  | 2 h 38 min  | 1 h 6 min                       |
| 5 ( $t_{DW}$ : 5 s, $N_B$ : 2, $N_L$ : 42)  | 28 h 41 min | 6 h 37 min  | 3 h 47 min  | 2 h 40 min  | 1 h 14 min                      |
| 6 ( $t_{DW}$ : 10 s, $N_B$ : 2, $N_L$ : 42) | 29 h 55 min | 8 h 27 min  | 4 h 2 min   | 2 h 44 min  | 1 h 42 min                      |
| 7 ( $t_{DW}$ : 0 s, $N_B$ : 2, $N_L$ : 50)  | ----        | 10 h 29 min | 7 h 31 min  | 5 h 3 min   | 58 min                          |
| 8 ( $t_{DW}$ : 0 s, $N_B$ : 2, $N_L$ : 100) | ----        | 33 h 17 min | 15 h 50 min | 11 h 10 min | 2 h 40 min                      |

Again, for Experiment ID 7-8 (50 and 100-layer large wall), much longer and higher walls are deposited as compared to Experiment ID 1-6. It can be seen in **Fig 6.10**, that the multi-scale method fails to correctly capture the *distortion trends, however, the final distorted magnitude is correctly predicted (errors below 5% shown in Table 5.5)*. However, the same trend can be noticed, that with an increase in deposition volume (2 bead large walls of 50 and 100 layers), the required/optimized value of A is also increasing from 0.6 (2 bead small wall of 42 layers (EXP ID 5-6)) to 0.75 (Exp ID 7-8) that leads to minimum computation error.

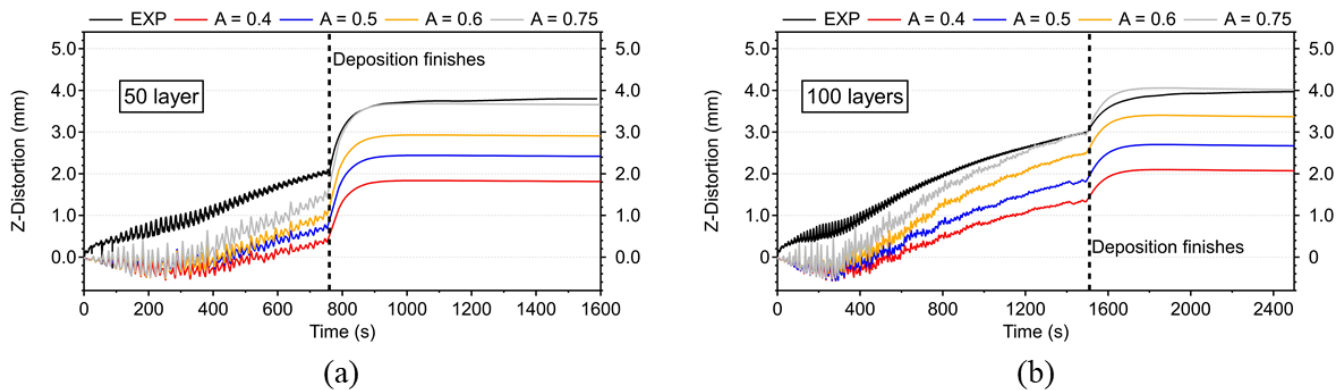


Figure 6. 10: Comparison of numerical results obtained from Multi-scale methods (SIM) with recorded In-situ distortion history (EXP) of LDS for Experiment ID 7-8.  
(a) EXP ID 7 (50-layer wall) (b) EXP ID 8 (100-layer wall)

Therefore, it can be concluded that the A value has to be calibrated for each experiment case, as it depends upon the deposited volume, otherwise, computational accuracy is compromised.

Also, the computation time for mechanical analysis is reduced significantly allowing to perform this type of simulation in a few hours as shown in **Table 6.6**.

As was observed in the thermal model, for the mechanical analysis also, employing a layer-by-layer approach using coarser mesh, computation time is further reduced up to a factor of 3 with the same computational accuracy justifying there was no adverse impact of mesh coarsening.

It is worth being reminded again, that all the analyses starting from meso-scale DE, and EE model in Chapters 4 and 5, and now for Multi-scale (layer-by-layer approach) part-scale is performed on fine resolution mesh. To fulfill the converge criteria, however, the same resolution of mesh size is not required for the EE model or Multi-scale model. This was recommended in Chapters 4, and 5, that the EE model will further reduce the computation time using the coarser mesh. To verify this point again, in this chapter, for Multi-scale analysis, the same analysis (layer-by-layer activation) was done with a coarser mesh, and it was observed that the computation time is further reduced up to a factor of 3 with the same computational accuracy justifying there was no adverse impact of mesh coarsening. Hence, it is recommended that for EE models or Multi-scale methods a coarse mesh should be utilized.

### 6.3.3.3 Comparison of post-process line distortion results

Finally, for Experiment ID 1-6, the numerical results are further compared with post-process line distortion results obtained by employing an Optical 3D scanner as shown in **Fig. 6.11 and 6.12**.

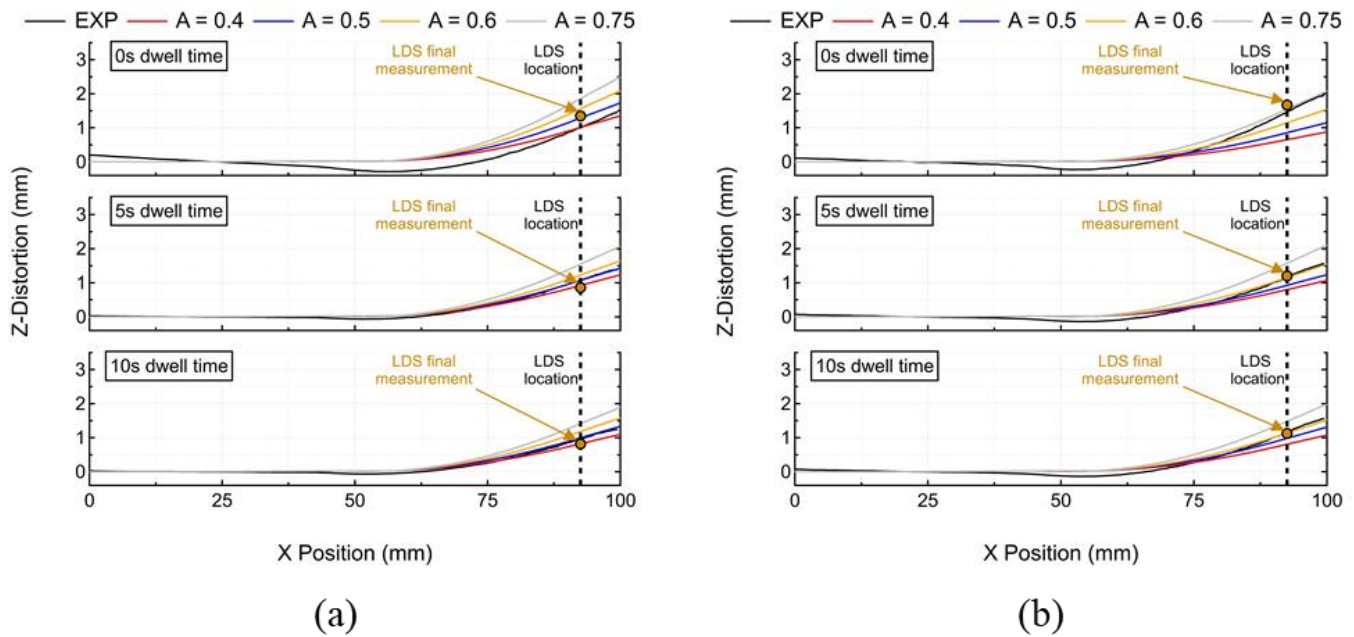


Figure 6. 11: Comparison of numerical results obtained from Multi-scale methods (SIM) experimental post-process line distortion results of Optical scanner (EXP) for different dwell times for Experiment ID 1-6.  
(a) 1-bead wall, (b) 2-bead wall

The numerical post-process line distortion results are coherent with the numerical in-situ distortion results. The results follow the same trend that the Multi-scale methods can be accurate but is not consistent as it requires optimizing the A value for each experiment case. However, irrespective of the A value, it provides an important insight into the global workpiece thermomechanical response. The numerical model's results for Experiment ID 7-8 are presented in Fig. 6.12.

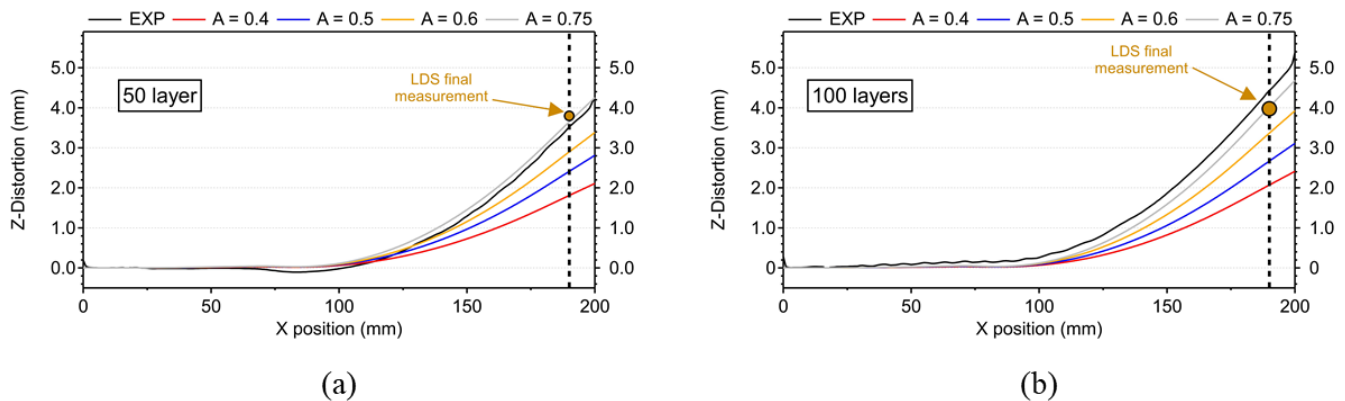


Figure 6. 12: Comparison of numerical results obtained from Multi-scale methods (SIM) experimental post-process line distortion results of Optical scanner (EXP) for different dwell times for Experiment ID 7-8.  
(a) EXP ID 7 (50-layer wall) (b) EXP ID 8 (100-layer wall)

The numerical model can capture the distortion trend of the substrate with an  $A = 0.75$  value and is coherent with the LDS results. The results follow the same conclusions derived from in-situ distortion results.

### 6.3.4 Conclusions

In this chapter, it has been demonstrated that the multi-scale model (layer-by-layer approach) that employs a uniform heat source and activates/deposits the material in a layer-by-layer fashion can perform large-part

process simulation for LDED, but with inconsistent accuracy. The emphasis is done on the peak temperature obtained in the newly activated layer should be coherent with process physics. The numerical model can capture the global response of the fabricated part but fails to capture the accumulation trends correctly. The main conclusions of this chapter are the following:

- For LDED, Multi-scale methods can be useful to understand the global trends in the thermo-mechanical response of the workpiece.
- Multi-scale method with proposed exposure/flash time ( $t_f$ ) strategy for a numerical heat source, especially for 0 s dwell time yields better computation accuracy.
- For LDED, for higher deposited volume (large-scale parts), Multi-scale methods require a higher A value that leads to error minimization.
- Multi-scale methods can simulate large parts but computation accuracy cannot be guaranteed as it requires manual optimization of the A value for each experiment case.

*In this chapter, the macro layer thickness is taken as the actual physical layer thickness. In future work, the effect of the macro-layer thickness (lumping/combining multiple layers) on computation accuracy and the time required for the analysis can be investigated.*

## 6.4 Work in progress

The DE, EE, and multi-scale models (layer-by-layer activation) were successfully developed, implemented, and experimentally validated in the first 2.5 years of the thesis work. In the last 6 months, emphasis was mainly on the thesis, journal, and conference paper writing. However, besides this, other numerical methods for the part-scale model are also being investigated by implementing and developing them on COMSOL Multiphysics® 5.6.

### 6.4.1 Inherent Strain-based Multi-scale model

#### 6.4.1.1 Background

Ideally, deformation and residual stress should be predicted by a transient thermomechanical simulation based on heat source models (DE and EE model). However, these models that capture laser movement are very time-consuming. Moreover, it is difficult to simulate complex large-scale parts in a detailed thermomechanical model as it is limited by computational power. Multi-scale model (layer-by-layer) can be one solution to overcome these pertaining issues and it can provide the final deformation of the complex large-scale part within a few hours.

The inherent Strain-based model is another solution to achieve a faster prediction, that was initially developed for welding technology (Ueda and Fukuda, 1989b; Yuan and Ueda, 1996). For detailed reviews of IS employed for PBF technology (Chen et al., 2021; Liang et al., 2021; Tran et al., 2020b) and Modified IS (MIS) dedicated for DED (Chen et al., 2019b; Liang et al., 2019, 2018b) can be found in the literature. Other than these, no publication for IS method dedicated to LDED was found in the literature.

A brief review of the Inherent strain (IS) theory is presented here. In welding mechanics, the total accumulated strain can be written as follows:

$$\varepsilon_{to} = \varepsilon_{el} + \varepsilon_{pl} + \varepsilon_{th} + \varepsilon_{tr} \quad (6.2)$$

Where  $\varepsilon_{to}$ ,  $\varepsilon_{el}$ ,  $\varepsilon_{pl}$ ,  $\varepsilon_{th}$ , and  $\varepsilon_{tr}$  is the total, elastic, plastic, thermal, and transformation strain respectively. Creep strain can also be added in the formulation, depending upon the model.

In the original IS theory, to extract/calculate the IS, only the final cooled state is considered. Therefore, thermal strain contribution is negated (Ueda and Fukuda, 1989b; Yuan and Ueda, 1996). Also, IS consists of only inelastic strains as they remain permanently in the welded domain. Elastic strain is relieved almost completely, therefore it is also negated. Finally, to simplify the model, phase transformation is also negated and thus the  $\varepsilon_{IS}$  equals the  $\varepsilon_{pl}$ .

$$\varepsilon_{IS} = \varepsilon_{pl} \quad (6.3)$$

Hence, based on **Eq. 6.3**, IS can be calculated easily from the detailed model. Then a fast Quasi-static elastic analysis (layer-by-layer) is performed that computes the distortion and stresses with the desired accuracy for the simple welding cases.

Therefore, irrespective of technology (PBF, LDED, or welding), any IS-based method employs the following procedures:

1. A detailed thermo-mechanical simulation is performed on a small representative model extracted from the original part model to compute/extract the IS.
2. The obtained IS values are then applied to the part-scale model to compute/predict mechanical response i.e., deformation and stresses.

But the original IS theory developed for welding technology is not compatible when it is applied to the AM technology, because the process physics of the AM processes are more complicated concerning welding. Indeed, a typical AM process involves the fabrication of new layers on the preceding layers during the multi-track/bead metal deposition process. The newly deposited layers also contribute to the mechanical response of the preceding layers as well. Therefore, extracting the correct IS for a part that employs multi-track and multi-layer metal deposition is still a complicated task even today. The IS are extracted from the mechanical response of the material that is highly dependent upon the boundary conditions, substrate dimensions, clamping constraints, especially for a large part of the LDED process, etc. Hence, IS needs to be calculated for each specific case as many factors including the process parameters such as input laser energy/power, and scanning speed influence the mechanical response of the part.

Therefore, Liang et al. developed a new or modified inherent strain (MIS) theory dedicated to LDED technology (Liang et al., 2018b). In the original IS theory, IS values are defined as the plastic strain values of the welded region at the cooled state. Instead of taking only plastic strain contribution, they considered the contribution of inelastic strains taking into account the contribution from plastic strain and thermal strain. However, they concluded that the MIS theory only works for single track/bead wall-like structures and it needs more development to validate the MIS theory for multi-track/bead DED parts.

Hence, in the thesis work, IS method is implemented and developed on COMSOL Multiphysics® 5.6 to investigate the pros and cons of this approach for LDED.

### 6.4.1.2 IS-based model idea and its implementation

To extract the IS, at first, a detailed thermomechanical simulation is performed on the representative model. In our work, we have considered the representative model as a 3-layer model as shown in **Fig. 6.13(a)** (EXP ID 1,  $t_{DW}$ : 0 s,  $N_B$ : 1,  $N_L$ : 42). The detailed model is the same as explained in Chapter 4 i.e., it employs a DE heat source model, an elastoplastic mechanical model with non-linear isotropic hardening that employs the stress relaxation model. The only difference is that in Chapter 4, the model was employed for 42 layers, but here in the IS-based model, it is employed for a 3-layer representative model.

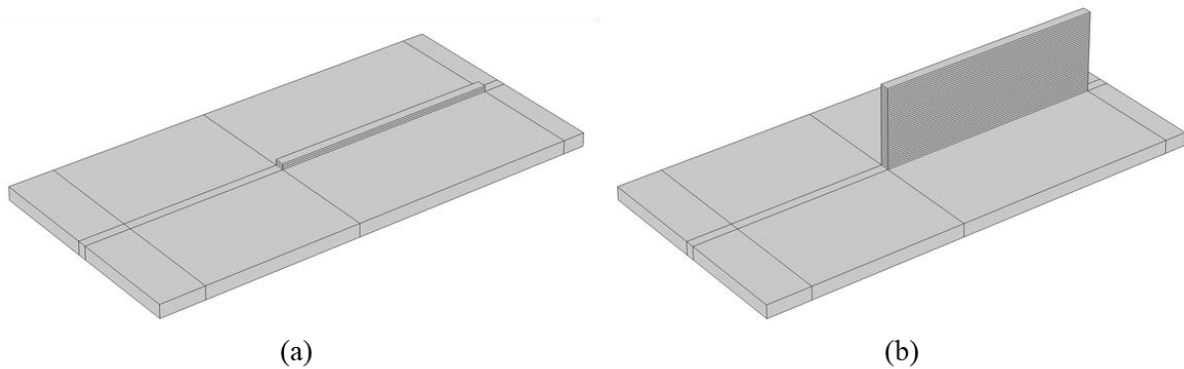


Figure 6. 13: Inherent Strain-based approach  
(a) Small representative 3-layer model (b) Original part-scale model

The 3-layer model considers the actual physical phenomenon of the LDED process. In the actual LDED process, every material point in the deposited part experiences a heating-cooling-heating-cooling phenomenon that represents melting-solidification-remelting/reheating-cooling respectively. Hence, a detailed 3-layer model can be a good representative model due to the following reasons:

- It considers the effect of deposition strategy as well as dwell time (cooling period).
- It also accounts for the effect of remelting the already deposited layer.
- It also considers the effect of an inter-layer (shrinkage) between two adjacent layers.
- Finally, it accounts for the reheating-cooling (3<sup>rd</sup> layer) that does not lead to melting but represents the temperature evolution of the remaining layers.
- Also, the part is allowed to cool down after the deposition of three layers as happens in the LDED process.

Therefore, the 1<sup>st</sup> layer can be taken as a representative layer from which IS values can be extracted after the part is cooled down, as it represents the IS behaviour of any layer in the original part. In our work, the IS values are calculated by considering only the inelastic strain contribution:

$$\varepsilon_{IS} = \varepsilon_{IN} \quad (6.4)$$

Where  $\varepsilon_{IN}$  is the inelastic strain that is calculated by averaging its values over the representative layer i.e., 1<sup>st</sup> layer after the part is allowed to cool at ambient temperature. In our work, we are not considering the elastic strain ( $\varepsilon_{el}$ ) contribution as they are fully recoverable, however, we are taking into account the plastic strain contribution (non-recoverable) and effects of stress/strain relaxation as well. It was demonstrated in Chapter 4 that it plays a significant role in the distortion accumulation in LDED. Therefore, in our work, IS values are computed with the following equation:

$$\varepsilon_{IN} = \varepsilon_{pl} + \varepsilon_{SR} \quad (6.5)$$

Where  $\varepsilon_{SR}$  accounts for the stress/strain relaxation due to the melting, annealing, and solid-state phase transformation. As was the case of welding, for LDED also, the IS values can be extracted by Eq. 6.3 as well that only considers the plastic strain.

### Calculation of Inherent Strain

At first, the detailed model as shown in Fig 6.13(a) is employed to perform thermo-mechanical analysis (elasto-plastic model). This model employs temperature-dependent material properties such as coefficient of thermal expansion (CTE), Young's modulus, and yield strength, along with thermal conductivity, specific heat, and density.

As discussed previously, the IS values are extracted from the 1<sup>st</sup> layer of the detailed model. To simplify the model, the material model is considered isotropic which leads to only six independent components in the strain tensor in a 3D problem. The strain matrix contains three normal strain components ( $\varepsilon_{XX}, \varepsilon_{YY}, \varepsilon_{ZZ}$ ) and three shear strain components ( $\varepsilon_{XY}, \varepsilon_{YZ}, \varepsilon_{XZ}$ ). It has been found in the literature that the shear strain components is of relatively much smaller magnitude as compared to normal strain components (Liang et al., 2019). Therefore, to further simplify the model, only normal strain components are considered in the IS values that can be rearranged into a vector form ( $\varepsilon_{XX}, \varepsilon_{YY}, \varepsilon_{ZZ}$ ). The average inherent strain vector ( $\varepsilon_{XX}^*, \varepsilon_{YY}^*, \varepsilon_{ZZ}^*$ ) is obtained by averaging the final IS values of the 1<sup>st</sup> layer after reaching the equilibrium state i.e., cooled state.

An assumption is made that the mechanical response of each layer is almost similar, and therefore the extracted IS represents the mechanical response of each layer. However, it largely depends upon the part design as a radical change in the design can also affect the IS value for the respective layers. Also, a few final layers of the part experience different thermal evolution, and this can contribute to different IS values for these layers. Ideally, different/varying IS values should be extracted from multiple detailed representative models concerning the build direction. However, it will require high computation cost to identify the trend of IS values concerning the height/location of the fabricated part/layers. In the present work, only one representative model (1<sup>st</sup> three layers) is employed to extract the IS values.

The idea remains the same, detailed representative model (3-layer model) is employed to simulate 3-layer deposition with a moving DE heat source model and subsequent cooling of the 3 layers. Then average values of inherent strains are extracted from the 1<sup>st</sup> layer i.e., the representative layer. This analysis is done for 3 different experiment cases i.e., EXP ID 1-3 to analyse the performance of IS model and to investigate if it is able to capture the effect of dwell time.

For EXP ID 1-3, after doing a detailed thermo-mechanical analysis on the 3-layer model, using Eq. 6.4, the average inherent strain vector ( $\varepsilon_{XX}^*, \varepsilon_{YY}^*, \varepsilon_{ZZ}^*$ ) are presented in Table 6.7.

Table 6. 7: Computed values of IS extracted from the 3-layer representative models for all experiment cases

| EXPERIMENT ID | $\varepsilon_{XX}^*$ | $\varepsilon_{YY}^*$ | $\varepsilon_{ZZ}^*$ |
|---------------|----------------------|----------------------|----------------------|
| 1             | -0.003               | -0.01035             | 0.013814             |
| 2             | -0.0027              | -0.01035             | 0.013584             |
| 3             | -0.00261             | -0.01035             | 0.013415             |

### Applying IS to the original part-scale model

The calculated IS values are applied sequentially to each newly deposited layer (layer-by-layer activation) on the original part-scale model as shown in **Fig. 6.13(b)**. To adapt to the layer-by-layer loading of the IS values, a quick static analysis (both Elastic and Elasto-Plastic) is performed to predict the deformation at the part-scale. However, it is a pre-requisite to find a solution to load the IS ( $\epsilon_{XX}^*$ ,  $\epsilon_{YY}^*$ ,  $\epsilon_{ZZ}^*$ ) into the part-scale model (quasi-static). This is because IS cannot be applied as an external load to a FEM model in COMSOL Multiphysics® 5.6. Therefore, a feasible approach is taken by applying the IS ( $\epsilon_{XX}^*$ ,  $\epsilon_{YY}^*$ ,  $\epsilon_{ZZ}^*$ ) as orthotropic CTE of the respective layer. A unit temperature difference ( $\Delta T$ ) is applied to the newly deposited/activated layer in a layer-by-layer manual as the load as shown in **Fig. 6.14(a)**.  $T_{ref}$  represents the reference temperature i.e., 20°C, and  $T_{up}$  is the prescribed temperature of the newly deposited layer i.e., 21°C.  $XX\_cte$ ,  $YY\_cte$ , and  $ZZ\_cte$  represents the values of IS vector  $\epsilon_{XX}^*$ ,  $\epsilon_{YY}^*$ , and  $\epsilon_{ZZ}^*$  i.e., (For EXP ID1: -0.003, -0.01035, 0.013814). The IS values are loaded sequentially to the newly activated layer and applied only to the fabricated part shown in **Fig. 6.14(b)**. This approach of applying IS values on a part-scale model is being employed extensively in the literature (Y.-X. Wang et al., 2008) as well as in commercial software.

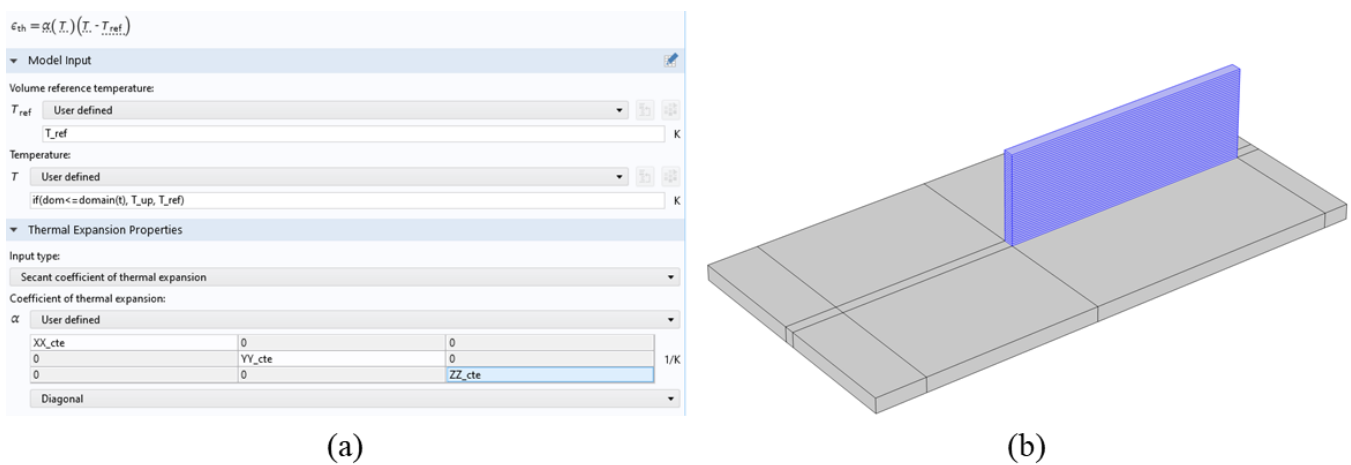


Figure 6. 14: (a) Loading IS vector via orthotropic CTE  
(b) Applying IS vector only to the deposited part

Then a quick pure elastic model with loaded IS values are employed to predict the deformation. Also, an elasto-plastic model (isotropic linear hardening) with loaded IS values are employed to make a comparison between the two material models. Here also, for the sake of continuity and comparison with the previous chapters, the same mesh (size and pattern) is employed that was detailed in Chapter 4, however, for this type of analysis, a coarser mesh can be used.

#### 6.4.1.3 Results and discussion

The pure elastic and elastoplastic analysis took around 4 and 20 minutes respectively for each experiment case irrespective of dwell time. This kind of analysis can be the fastest solution as long as it is accurate. It was observed the part-scale model is extremely sensitive to the IS values. So, it is paramount to accurately calculate/extract these values, otherwise, the slightest change in these values results in big changes in part-scale model results. The final deformation for EXP ID 1 predicted by both elastic and elasto-plastic analysis is shown in **Fig 6.15**.

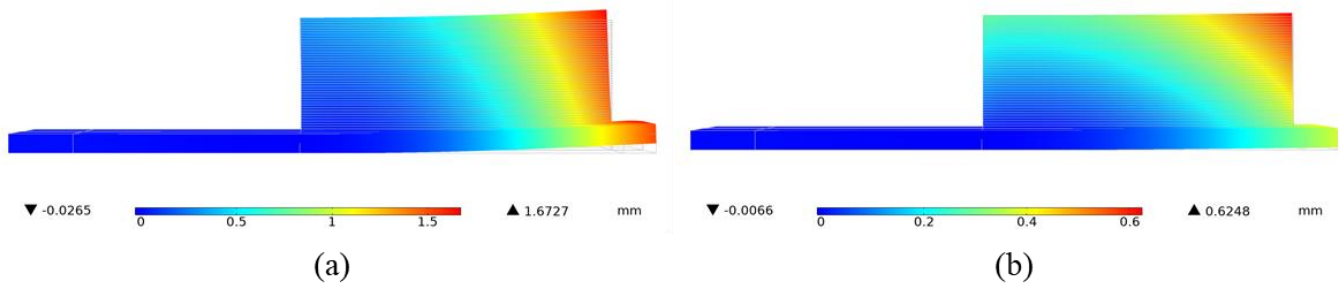


Figure 6. 15: Deformation prediction by IS-based model for EXP ID 1 (one bead wall, 42 layers)  
(a) Pure elastic analysis (b) Elasto-plastic analysis

As the part-scale model only employs a static mechanical analysis, it is of no use to compare the thermal response. Also, this kind of analysis does not capture the distortion accumulation (in-situ) correctly, on the contrary, it helps in predicting the final deformation of the part scale. Therefore, the line distortion results (EXP) obtained by the FARO 3D scanner are compared with IS model results for both elastic and elastoplastic analysis. For EXP ID 1-3, results obtained by IS model are compared with experimental data as shown in Fig. 6.16.

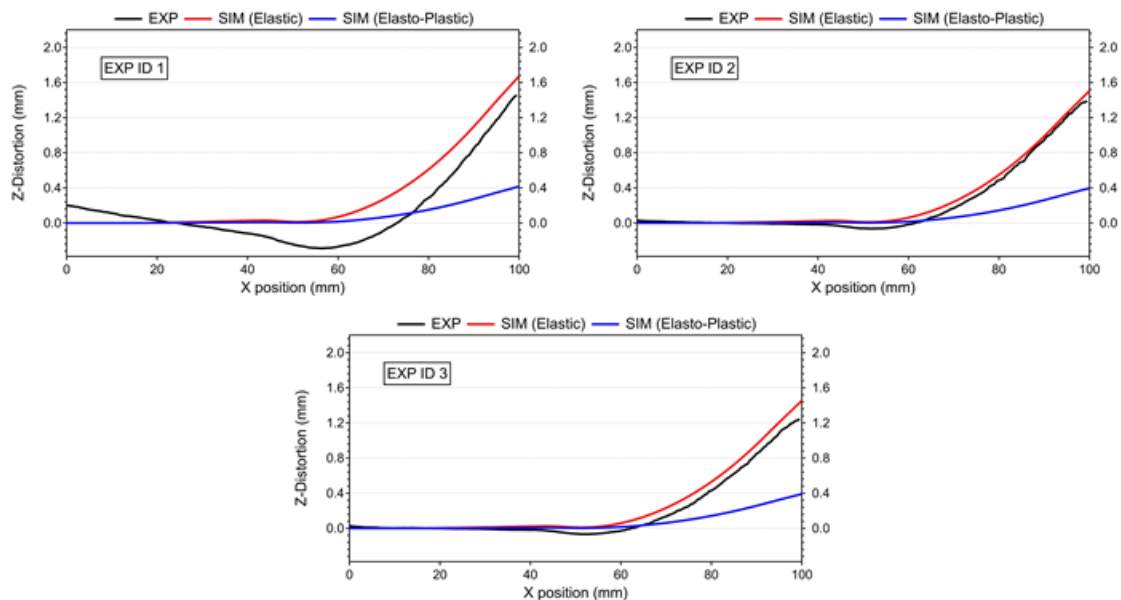


Figure 6. 16: Comparison of IS-based model results with experiment line distortion results for EXP ID 1-3

The elastic analysis results in much better computational accuracy as compared to elasto-plastic analysis. However, even with elastic analysis, the model is slightly over-predicting the final deformation magnitude. The first trials with IS-based model gives promising results. However, more testing needs to be done especially on the hypothesis of extracting/computing IS values before making a claim that IS-based model is validated for LDED part.

Currently, in the research work, the IS-based model is also employed to perform the analysis for EXP ID 4-8 as well. It can be observed that IS-based model is the fastest and can give simulation results within few minutes as compared to DE, EE, and Multi-scale approach (Layer-by-Layer) which still takes few hours.

#### 6.4.1.4 Conclusions

- First trials with IS-based model for LDED part yield promising results.
- IS-based model further needs to be improved and calibrated to improve the computational accuracy.

- IS-based model needs to be tested on different part design justifying its versatility.
- A new hypothesis needs to be developed to extract single and multiple IS from the 3-layer or more-layers representative model.

Therefore, the IS-based model should be refined, improved, and well-calibrated before this methodology can be used for large-scale LDED parts. It is being planned that the improved IS-based model will be combined with the EE model to calculate and extract multiple IS in the detailed model at different locations/heights much faster.

## 6.4.2 Distortion compensation model

Distortions can be predicted by the proposed LDED process simulation methods. Once the part-scale distortion field is obtained, a numerical model can be used to generate distortion-compensated geometry that can be a promising method to fabricate geometrically accurate parts in the first iteration.

Idea is to invert the calculated distortions (numerical model) to derive/generate the distortion compensated geometry. Then, numerical analysis is again performed on the compensated geometry that reduces the part distortion significantly.

This idea is implemented in COMSOL Multiphysics and the first trial was done on a simple 2D geometry as shown in Fig 6.17. Here, the idea is to demonstrate the effectiveness of distortion compensation model only, therefore focus was not to capture correct deformation (trends and magnitude) with thermomechanical model, as it can be seen in the Fig 6.17 that deformation trend is not accurate.

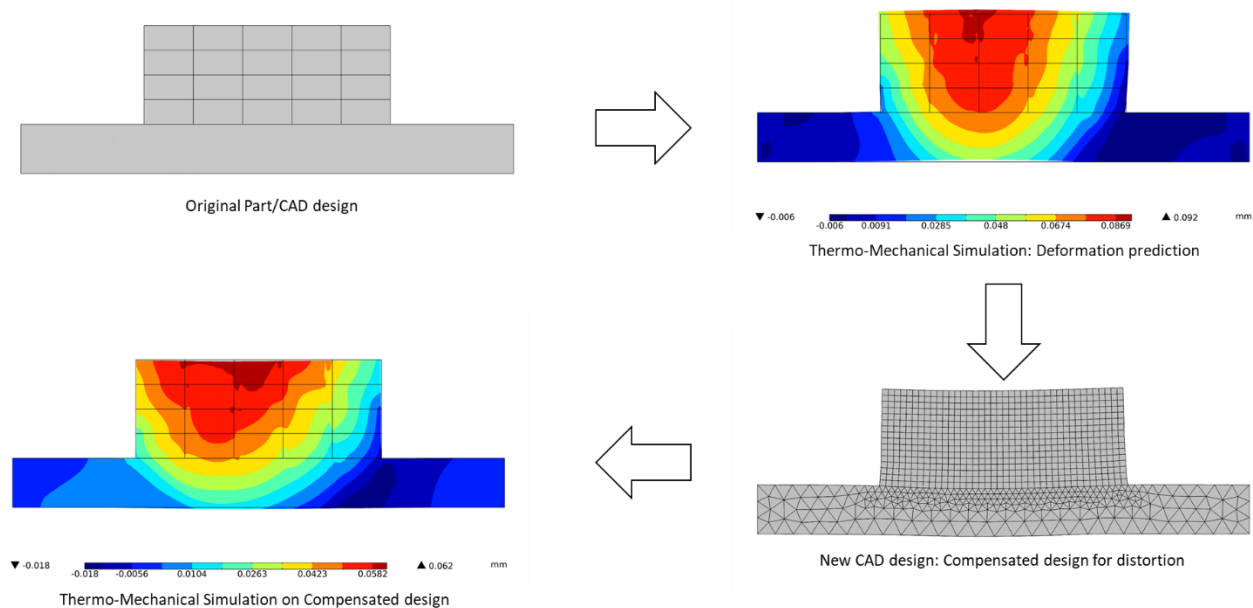


Figure 6. 17: Complete LDED process simulation digital chain starting

The case study is very simple and a proof that the idea is correctly implemented in the software. The LDED process simulation digital chain involves following steps:

- Start with original CAD design
- Thermomechanical analysis to predict deformation
- Compare and analyze deformation over the original CAD model (see color legend)
- Invert the deformation and generate distortion compensated geometry.

- Again, perform thermomechanical analysis over the distortion compensated CAD.
- Compare and analyze deformation over the original CAD (see color legend), with single iteration distortion magnitude is reduced by over 30%.

The calculated distortions on the compensated deformed geometry are reduced by over 30% after a single compensation iteration. The proposed LDED process simulation digital chain can be employed to fabricate part first time right.

*In the present work, this idea is tested on a 2D model only. But the idea seems coherent with the stated objective of fabricating geometrically accurate part at the first trial. Therefore, it is planned that the distortion compensated model will be implemented, developed and tested on a 3D CAD. After it's successful calibration, it will be integrated to the LDED process simulation digital chain.*

### 6.4.3 Technological transfer to SIEMENS

As indicated in the general introduction, one of the objectives of this thesis was to implement and transfer numerical developments in SIEMENS NX software within the framework of PhD project. Most of the PhD work (Chapter 4 and 5) is already been transferred and integrated in SIEMENS NX environment. Main idea of elongated heat source averaged over its deposition path that follows the deposition strategy has been already adopted and integrated. It has also been established in SIEMENS NX environment that employing elongated heat source leads to reduction of the computation time drastically however keeping the desired computation accuracy. The proposed work in the PhD concerning Non-linear isotropic hardening model with specified parameters "is in the process" of being developed and integrated in SIEMENS NX environment.

A new application "Multi-axis Additive" as shown in **Fig. 6.18** is being added to the global SIEMENS NX Simcenter DED digital chain.

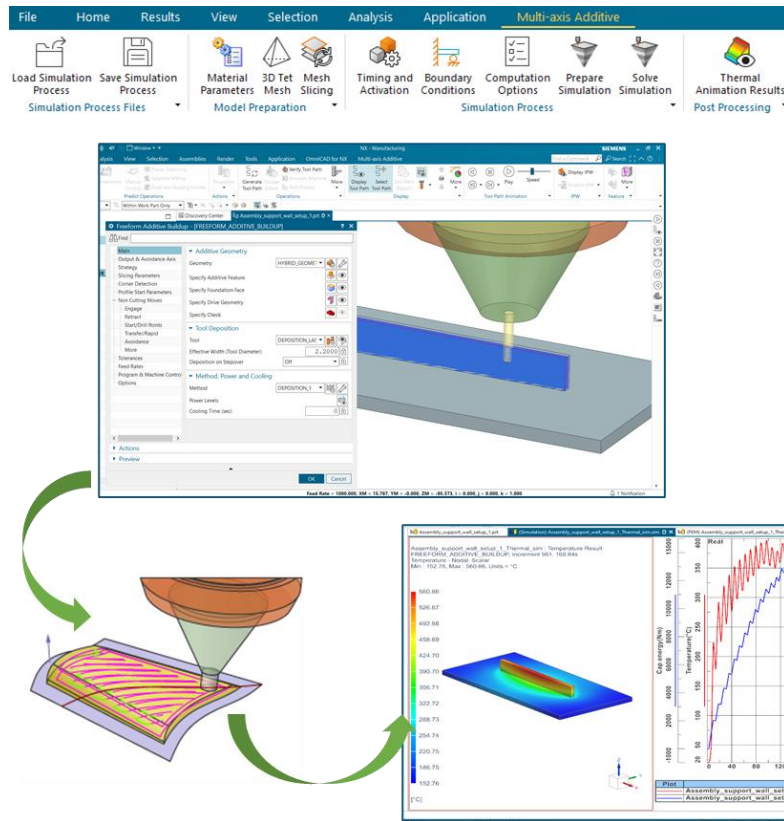


Figure 6. 18: SIEMENS new Multi-axis Additive module

The new Multi-axis Additive module has the following sequential modules:

- Seem-less connection between NX Multi-axis deposition and Simcenter 3D Multi-axis Additive
- Transfer toolpath information to Simcenter
- Automatically create meshes and boundary conditions using the toolpath information
- Start transient thermo-mechanical analysis with elongated uniform heat source model
- Review temperature and distortion results

In the present PhD research work, besides the work done on COMSOL, especially in the last few months, SIEMENS's new module testing is also being done as a part of the thesis. The first version of the new SIEMENS LDED process simulation software (Multi-axis Additive) will be released in 2022.

# General Conclusions and Future Work

## General conclusion

Thermo-mechanical models of the AM processes must be developed to avoid the costly trial and error approach that is widely being used in the industry to produce parts. Efficient FE models with the capability of simulating large DED parts must be developed. But, to have more confidence and faith in the FE models, their predictions must be validated with experimental data. Usually, the numerical model is validated with post-process experimental data, but it has been demonstrated that in-situ experimental data provide more insight into the process physics.

In this thesis, the primary focus is done on the development of a conventional and efficient thermomechanical model dedicated to DED processes. Several experiments were performed to extract in-situ and post-process experimental data that is used to validate the simulations. Some interesting conclusions can be derived from the thesis work which can be useful for researchers in this domain:

- Chapter 2 focused on developing and identifying a suitable metal deposition model and equivalent heat source dedicated to the LDED process. The primary finding was that the Double Ellipsoid (DE) volumetric heat source yields stable accurate results as compared to other equivalent heat sources. The Quiet/Active material activation method was found to be the most reliable, and easy to implement on COMSOL Multiphysics® 5.6 as compared to Hybrid and ALE methods.
- Chapter 3 applied the thermal model developed in Chapter 2 to model the in-situ temperature of the Stainless Steel 316L (SS 316L) LDED fabricated wall. In-situ experiments were designed and performed to record the thermal response during the manufacturing of a single bead wall. The primary finding was that the DE model resulted in a computational accuracy of 96%, but leads to high computation time. The efficient model that employs Elongated Ellipsoid (EE) heat source with different elongated lengths ( $K_E$ ) resulted in the reduction of computation time up to a factor of 10 while yielding computational accuracy of 75-95%. A new source correction factor ( $K_Q$ ) is developed that reduces the computation error within the range of 5%.
- Chapter 4 focused on developing the conventional and efficient thermo-mechanical model for the LDED process capable to simulate the thermo-mechanical responses of SS 316L LDED fabricated wall (42 layers). The primary finding was that the conventional thermo-mechanical model that employs the DE model with the standard material constitutive model accounting for elastic, plastic, and thermal strain was unable to capture the mechanical response of SS 316L. The model without stress relaxation (SR) over-predicted the distortion by over 35-85%. An instantaneous relaxation model was developed to account for the annealing, and solid-state phase transformation induced stress relaxation that yields close agreement with experimental results with a maximum error of 9%. Finally, the efficient model employing EE heat source exhibits computation error below 20% and achieves a reduction in computation time by a factor of 10.
- Chapter 5 applied the efficient model from Chapter 4 to model the thermo-mechanical responses for much larger and higher SS 316L fabricated walls (50 and 100 layers). The source correction factor ( $K_Q$ )

from Chapter 3 is also applied to compensate for the loss of intensity due to heat source averaging. The primary finding was that the efficient model without  $K_Q$  exhibited computation error exceeding 20%. However, the model with  $K_Q$  reduced the computation error below 10%. The efficient model demonstrated its effectiveness in simulating large parts with practical computation time and an acceptable level of computation accuracy.

- Chapter 6 investigated the feasibility of the Layer-by-Layer approach and Inherent Strain-based part-scale models for the LDED. The primary finding was that the layer-by-layer approach provides important insight into the global thermo-mechanical response of the LDED fabricated part within a few minutes/hours. However, it fails to provide an understanding of the process physics and leads to high computational inaccuracy.

## Future work

- Experimental validations

A new design of experiment with complex part fabrication needs to be done to further improve and validate the conventional and efficient models. A 3D Digital Image Correlation (DIC) system should be used to extract in-situ distortions at the fabricated part from multiple points/locations. This type of experimental data will help in improving the computational accuracy of the FE models. Experimental validations can also be supplemented by non-contact thermal measurements carried out at the fabricated part under construction. Measurements by multispectral pyrometry or multispectral thermal camera allow better precision on the temperature when the emissivity is not known. Melt-pool measurements (High speed camera) especially at the last layer could be useful to further improve the calibration of numerical heat source. Numerical models should also be validated with experimental stress results which is also an important issue in additive manufacturing (AM).

- Other material

In the thesis work, FE models are validated for only SS 316L material. However, Ti-6Al-4V, Inconel 625, Inconel 178, and Aluminium are very popular materials in the LDED industry and are used extensively. The FE models should also be validated for these and new materials.

- Improve Efficient model

In the thesis work, FE models employed the Quiet/Active material activation method. But it is well proven that Hybrid material activation reduces the computation burden drastically. Therefore, an efficient model should be developed with a Hybrid material activation method. To further reduce the computation time for the efficient model, an adaptive meshing algorithm that also contributes to the reduction of computation resources needs to be developed and incorporated into the model.

- Develop Inherent Strain (IS)-based methods

For very large parts, a moving source simulation (DE model) can be infeasible due to its requirement of strict spatial discretization and relatively smaller computational time steps. Instead, an IS-based method dedicated to LDED should be developed. In the IS-based methods,

the accumulation of plastic strain within layers should be understood and calculated by the moving DE source simulation. Then, this plastic strain/s can be applied to the layer-by-layer model which will drastically reduce the computation time.

- Combine Efficient model with IS-based method

Plastic strain calculation by moving DE source simulation requires computation time of hours/days, especially for large parts. Also, applying one plastic strain for a large complex shape large LDED part will result in computational accuracy. This is because the behaviour/response of the part changes depending upon the part location (layer number) and part design. Therefore, to develop an accurate IS-based model for LDED, multiple inherent plastic strains need to be calculated. A traditional moving DE source simulation will be infeasible as it will require impractical computation time. Therefore, it can be an interesting idea to employ an efficient EE model to extract multiple inherent plastic strains that can be done in a few hours or days. Then, these multiple plastic strains can be applied to the layer-by-layer model, thus making it possible to simulate very large parts in a feasible time.

- Develop compensation model and integrate with FE model

Parts distort during the deposition process in AM due to the repeated thermal cycles. Modifying/changing the original geometry/CAD in such a way that the accumulated distortion during AM process causes it to achieve the desired shape, is a technique commonly known as Distortion Compensation. This is an innovative and useful method to achieve geometrically accurate parts. Numerical simulation can be an important tool to predict the accumulated distortion during the AM process. Then, the FE model generates the compensated geometries and drastically reduces the time and money wastage arising due to the experimental trial and error approach.

# Résumé étendu de la thèse

Ce travail de thèse porte sur le procédé LDED (Laser Directed Energy Deposition). L'objectif est de développer un modèle par éléments finis capable de prédire les distorsions et contraintes résiduelles lors de la fabrication additive de pièces de grande structure (dépôt de matière de plusieurs mètres). Ces développements visent à fournir un outil numérique permettant de minimiser ces contraintes et déformations avec une meilleure maîtrise des paramètres opératoires.

## Chapitre 1

Le chapitre 1 présente un état de l'art des différents travaux de la littérature sur les procédés de fabrication additive. Ce chapitre vise à donner une meilleure vision des techniques numériques employées par les différents chercheurs dans le passé, ce qui permettra d'orienter les choix dans les développements numériques de ce travail de thèse.

Une brève introduction présente les principales caractéristiques de la technologie LDED, suivie d'un rapide état de l'art sur les modèles numériques développés dans le cadre des procédés de soudage, souvent à la base des travaux numériques appliqués aux procédés de fabrication additive, en raison des grandes similitudes au niveau des phénomènes physiques. Cet état de l'art montre que, pour la modélisation des procédés de fabrication additive, deux types d'approches sont rencontrés selon l'échelle d'espace considérée, à savoir l'échelle méso ou macroscopique. Tout d'abord, une revue de la littérature est donnée sur l'approche mésoscopique, s'intéressant principalement à décrire les phénomènes à l'échelle du bain. On distinguera les modèles purement conductifs de ceux intégrant les écoulements dans le bain fondu. L'accent est porté sur les modèles conductifs, vu les objectifs de la thèse. La méthodologie classique utilisée pour résoudre les équations d'un problème thermique adapté au procédé LDED est détaillée. Il s'en suit une introduction à l'analyse mécanique, en détaillant les différents travaux sur le sujet ainsi que les moyens expérimentaux permettant de valider ces modèles thermomécaniques. Une discussion est abordée sur l'utilité d'un couplage fort ou non entre les deux physiques (thermique et mécanique), qui conduira, pour la suite de ce travail à retenir un couplage faible thermomécanique. Ce chapitre présente également les différentes méthodes pour modéliser l'apport de matière, en insistant sur les avantages et inconvénients de ces méthodes. Le chapitre se poursuit en présentant les travaux de la littérature qui proposent des techniques pour minimiser les contraintes et déformations lors des procédés LDED. Des modèles à l'échelle de la pièce sont ensuite présentés dans le cas du procédé LDED. Deux approches sont principalement proposées dans la littérature, à savoir les méthodes de déformations inhérentes et les méthodes multi-échelles. Les méthodes de déformations inhérentes ont d'abord été développées dans le cadre des procédés de soudage et procédés PBF (Powder Bed Fusion, procédé de fusion sur lit de poudre), avant d'être étudiées pour le cas du procédé LDED. Le chapitre se termine en détaillant les objectifs de ce travail de thèse et en expliquant et justifiant la méthodologie retenue au vu de l'état de l'art et son originalité.

## Chapitre 2

Dans le chapitre 2, différentes techniques numériques pour modéliser l'apport de matière en LDED sont discutées, en particulier, les méthodes « Quiet element », « active element », hybride (couplant ces deux méthodes), et la méthode ALE (Arbitrary Lagrangian Eulerian) sont étudiées. Toutes ces méthodes sont mises en œuvre dans le logiciel COMSOL Multiphysics® 5.6. Ces modèles d'apport de matière sont couplés à un

modèle thermique prenant en compte l'apport de chaleur dû au faisceau laser, la fusion du matériau, les transferts de chaleur par conduction, ainsi que les pertes par convection et rayonnement au niveau de la surface de la pièce construite. Les résultats numériques sont comparés à des mesures par thermocouples issues de données de la littérature pour la fabrication LDED d'un mur en alliage de titane. Les comparaisons entre les différentes techniques pour modéliser l'apport de matière sont discutées en termes de temps de calcul, précision, adaptabilité et facilité de mise en œuvre. Il est ainsi conclu que le meilleur choix, pour un modèle thermomécanique appliqué à de grandes structures, porte sur une méthode hybride « Quiet/Active » couplée à un terme source de chaleur volumique utilisant une double ellipsoïde.

### Chapitre 3

Dans le chapitre 3, un modèle thermique 3D transitoire utilisant la méthode Quiet/Active element est développé pour simuler le procédé LDED. Pour modéliser finement l'apport de chaleur, une source Goldak double ellipsoïde est implémentée en prenant soin d'imposer des pas de temps tel que le laser parcourt une distance ne dépassant pas son rayon durant le pas de temps. Ce modèle est utilisé pour simuler la construction d'un mur de 20 couches d'acier 316L pour différents paramètres opératoires. Les résultats numériques montrent un bon accord avec des données expérimentales issues de thermocouples soudés sur la face envers du substrat également en acier 316L. En vue de réduire les temps de calcul, la source est ensuite modifiée à l'aide d'une ellipsoïde allongée, moyennant l'énergie du laser sur un intervalle de temps et d'espace. Il est ainsi montré qu'en choisissant avec soin cet intervalle, il est possible de représenter assez fidèlement l'apport d'énergie tout en réduisant considérablement les temps de calcul. Un premier choix proposé permet une réduction des temps de calcul d'un facteur 5 à 10 tout en gardant une erreur relative entre modèle et expérience inférieure à 10%. Il est également montré que l'introduction d'un facteur correctif pour la source allongée permet d'améliorer la précision du modèle. Enfin, une relation est proposée pour définir ce terme correctif en fonction du nombre de segments utilisés pour appliquer la source et des temps de calcul conduisant à la meilleure précision des calculs.

### Chapitre 4

Le chapitre 4 présente un modèle thermomécanique pour calculer le comportement mécanique d'une pièce fabriquée par le procédé LDED. Les distorsions et contraintes résiduelles générées par les cycles thermiques répétées en fabrication additive peuvent, en effet, conduire au rejet des pièces obtenues. La compréhension de la réponse thermomécanique résultant des phénomènes physiques induits lors des procédés de fabrication additive reste encore une tâche délicate fortement dépendante des matériaux utilisés et des paramètres opératoires. Dans ce travail, un modèle 3D thermo-élasto-plastique est implémenté dans le logiciel COMSOL Multiphysics®. La source de la chaleur est dans un premier temps de type Goldak double ellipsoïde. La construction de murs en acier 316L de 42 couches avec un ou deux cordons est simulée pour différents temps de pause inter cordons, ce temps influençant fortement la réponse thermique et par conséquent la réponse mécanique qui en résulte. Des temps de pause variant de 0 à 10 s sont choisis. L'ensemble de ces cas d'études est également reproduit expérimentalement. En se basant sur les travaux de la littérature, la prise en compte d'une restauration de l'écrouissage est introduite dans le modèle mécanique. Ce phénomène présent lors des cycles thermiques à hautes températures conduit à une réduction des contraintes. Pour le modéliser dans le cadre de ce travail, les contraintes sont annulées dès que les températures dépassent une certaine température, choisie de manière à obtenir le meilleur accord entre expérience et modèle. La comparaison porte sur les mesures de déplacement in situ obtenues à l'aide d'un capteur laser ainsi qu'une mesure de la déformée finale donnée par numérisation 3D du mur à l'aide d'un Faro® scanner laser. Il est ainsi montré

qu'une augmentation du temps de pause permet de réduire les déplacements du substrat et de la distorsion globale du mur. Un bon accord entre modèle et expérience est observé, à condition de bien prendre en compte le phénomène de relaxation. Enfin, il est également montré que l'utilisation de la source de chaleur allongée présentée au chapitre 3 permet une réduction des temps de calcul d'un facteur 10 pour un calcul complet thermomécanique, ce qui justifie pleinement son intérêt pour la simulation de grandes pièces.

## **Chapitre 5**

Le chapitre 5 est consacré à l'application du modèle thermomécanique utilisant la source ellipsoïdale allongée pour des murs de plus grandes dimensions. Trois longueurs de source sont testées pour analyser l'influence sur la réponse thermomécanique. Des dépôts d'acier 316L sont réalisés sur un substrat en acier S235. Des murs de 50 et 100 couches avec un ou deux cordons juxtaposés sont réalisés expérimentalement et numériquement. Les températures du substrat en face envers sont mesurées par thermocouple alors que les déplacements in situ du substrat sont mesurés à l'aide d'un capteur laser. Le modèle avec les différentes longueurs de source reproduit globalement bien la réponse thermomécanique observée expérimentalement, avec, cependant, une sous-estimation des valeurs calculées par le modèle. Il est montré qu'une augmentation de la longueur de la source de chaleur conduit à une réduction importante des temps de calcul, mais avec une augmentation des erreurs entre modèle et expérience. L'introduction d'un facteur correctif sur la source de chaleur permet néanmoins de réduire considérablement ces erreurs. Par comparaison avec des sources de chaleur classiques (Goldak double ellipsoïde, gaussienne, top-hat), la réduction des temps de calcul peut atteindre un facteur 20 grâce à l'utilisation de la source de chaleur ellipsoïdale allongée, qui permet l'utilisation de pas de temps plus grands. Ainsi, pour simuler un mur de 100 couches représentant un dépôt de 24 mètres de long, seulement 11h de calcul sont nécessaires en choisissant judicieusement la longueur de la source allongée et le facteur correctif, pour une erreur relative inférieure à 10%.

## **Chapitre 6**

Le dernier chapitre est consacré à l'étude de méthodes multi-échelles pour réduire les temps de calcul. Ces méthodes consistent à appliquer l'apport de chaleur sur des blocs pouvant représenter des couches entières, voire plusieurs couches ou cordons juxtaposés. L'avance de la source de chaleur n'est alors pas prise en compte, permettant ainsi l'emploi de plus grands pas de temps, mais aussi un maillage plus grossier, puisque les gradients thermiques sont réduits. La configuration du mur avec un simple ou double cordon est reprise ici pour des couches variant de 42 à 100 couches. Les blocs sont définis comme étant une couche entière comprenant les deux cordons juxtaposés dans le cas d'un double mur. La source de chaleur est uniforme dans tout le bloc, appliquée durant un temps  $t_f$ , suivi d'un temps de refroidissement pour tenir compte du temps de pause entre couche. Il est cependant montré qu'un temps de refroidissement est nécessaire même dans le cas où il n'y a pas de temps de pause, pour éviter un échauffement aberrant de la pièce. Bien que les temps de calcul soient extrêmement courts (seulement quelques heures), les comparaisons en termes de température et déplacement montrent néanmoins que les erreurs entre expérience et modèle sont relativement importants. Néanmoins, les tendances sont relativement bien reproduites, avec notamment une diminution des distorsions avec l'augmentation du temps de pause. Ce chapitre se termine en montrant l'intérêt de deux autres méthodes, à savoir la méthode des déformations inhérentes et la méthode de compensation. La première méthode permet de réduire de façon drastique les temps de calcul tout en prédisant des distorsions finales satisfaisantes notamment en présence de temps de pause inter couche. La deuxième méthode permet de proposer une solution pour minimiser les distorsions en modifiant la trajectoire du dépôt.

# Appendix

## Chapter 2

### 1. Mesh convergence criteria

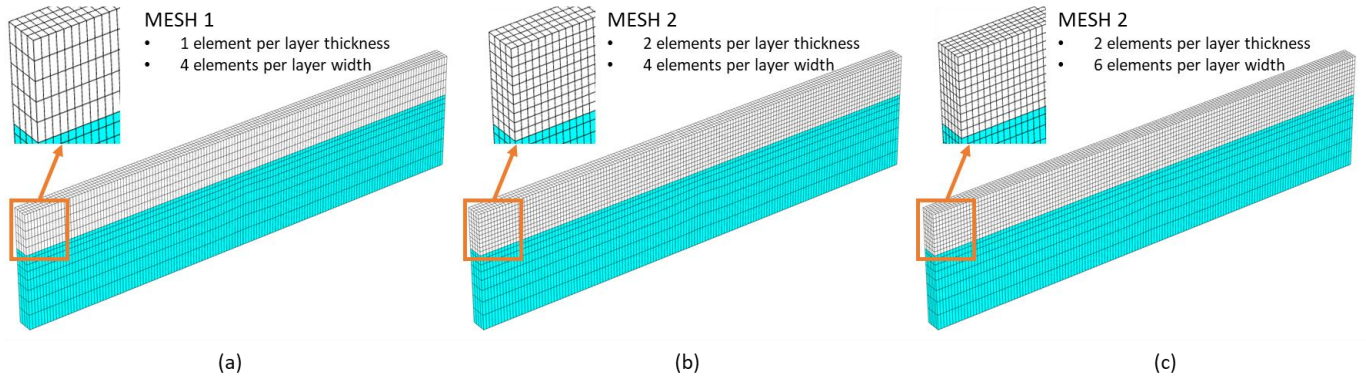


Figure A. 1: Illustrations of 3 different mesh employed for mesh convergence criteria

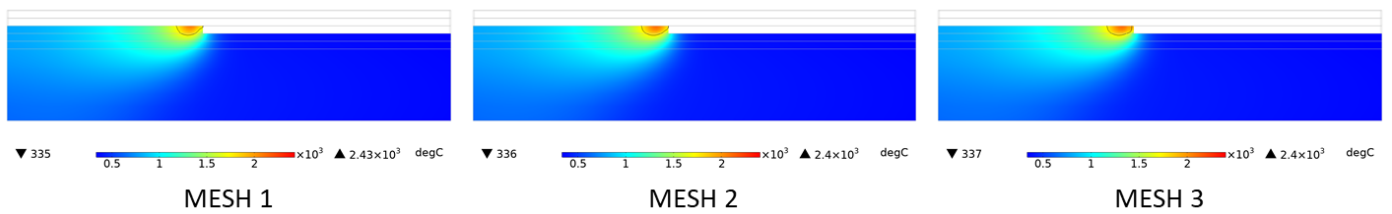


Figure A. 2: Melt-pool temperature and dimensions obtained with 3 different mesh

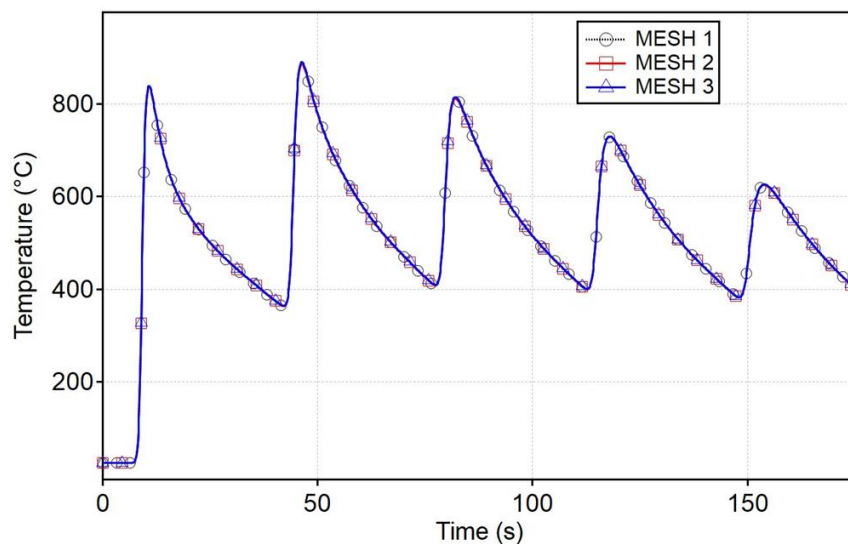


Figure A. 3: Temperature evolution at thermocouple location obtained with 3 different mesh

## Chapter 3

### 1. Experimental temperature data recorded by thermocouples 1 and 2

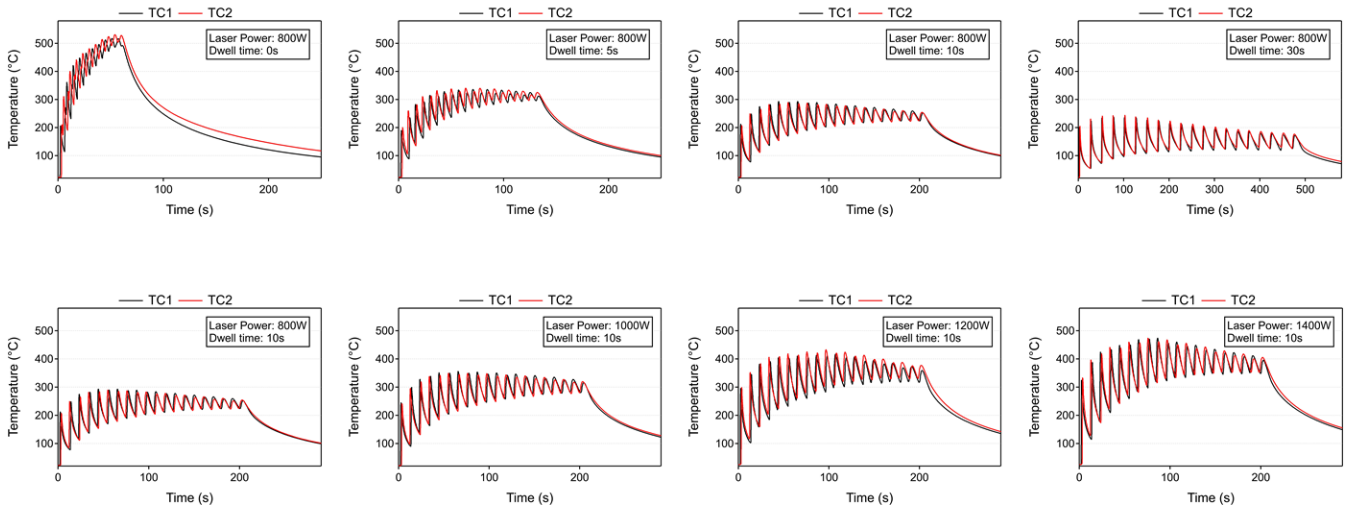


Figure A. 4: Experimental data recorded from thermocouples 1 and 2 for all experiment cases defined in Chapter 3

## Chapter 4

### 1. SS 316L material properties taken from the literature

(Adhitan and Raghavan, 2017; Biegler et al., 2018b; Deng and Kiyoshima, 2010; Jiang et al., 2012; Li et al., 2020; Mills, 2002b)

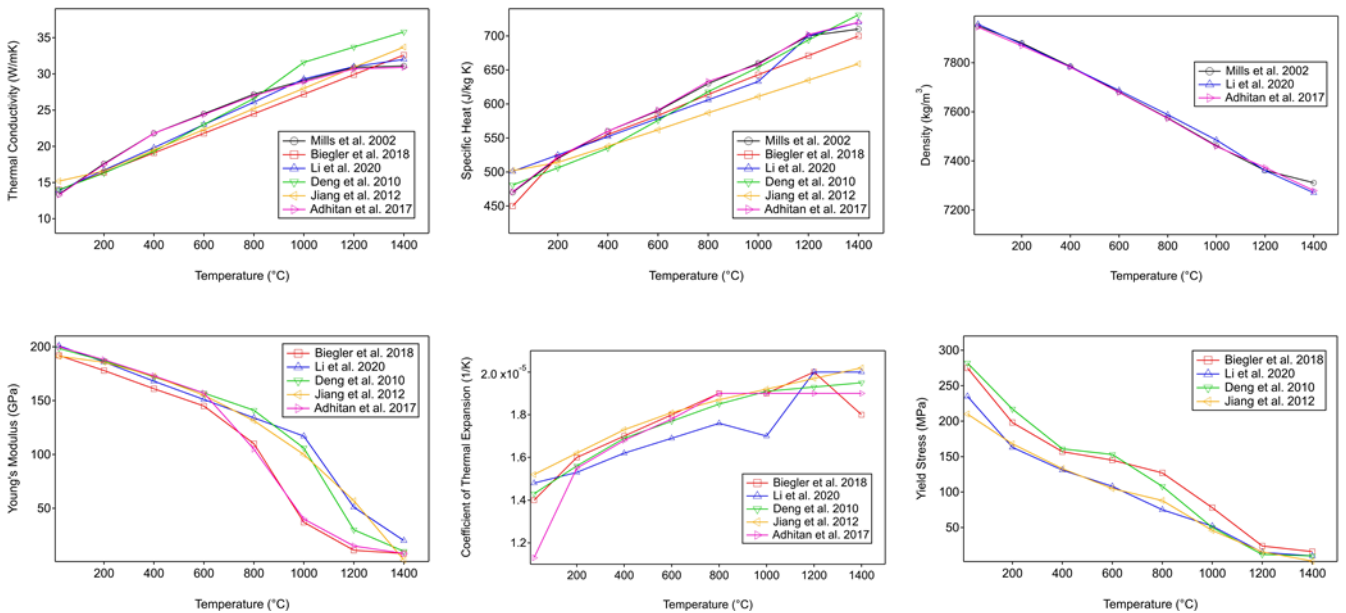


Figure A. 5: Comparison of temperature-dependent material properties for SS 316L obtained from literature

In the present work, for the thermo-mechanical model, we have employed material properties taken from the reference (Biegler et al., 2018b).

## 2. SATOH test (multiple cycles)

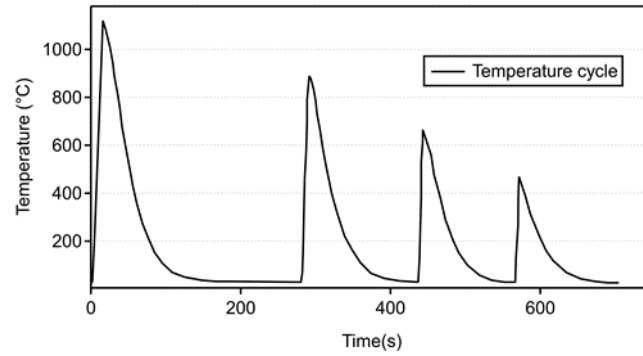


Figure A. 6: Thermal cycle for SATOH test

Multi-cycle thermal loading as shown in **Fig A.6** is tested for SATOH test. This type of thermal loading can be employed in SATOH test as LDED process results in same type of thermal cycle.

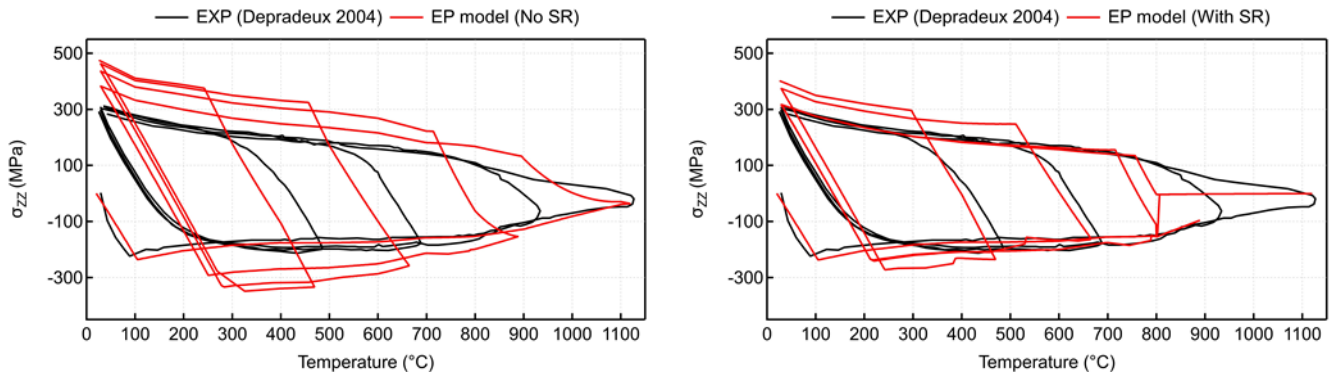


Figure A. 7: Comparison of experiment results (EXP) with elastoplastic (EP) model with and without stress relaxation (SR) with arbitrary relaxation temperature of 800 °C for SATOH test with multiple thermal cycles

## 3. Experimental temperature data recorded by thermocouples 1 and 2

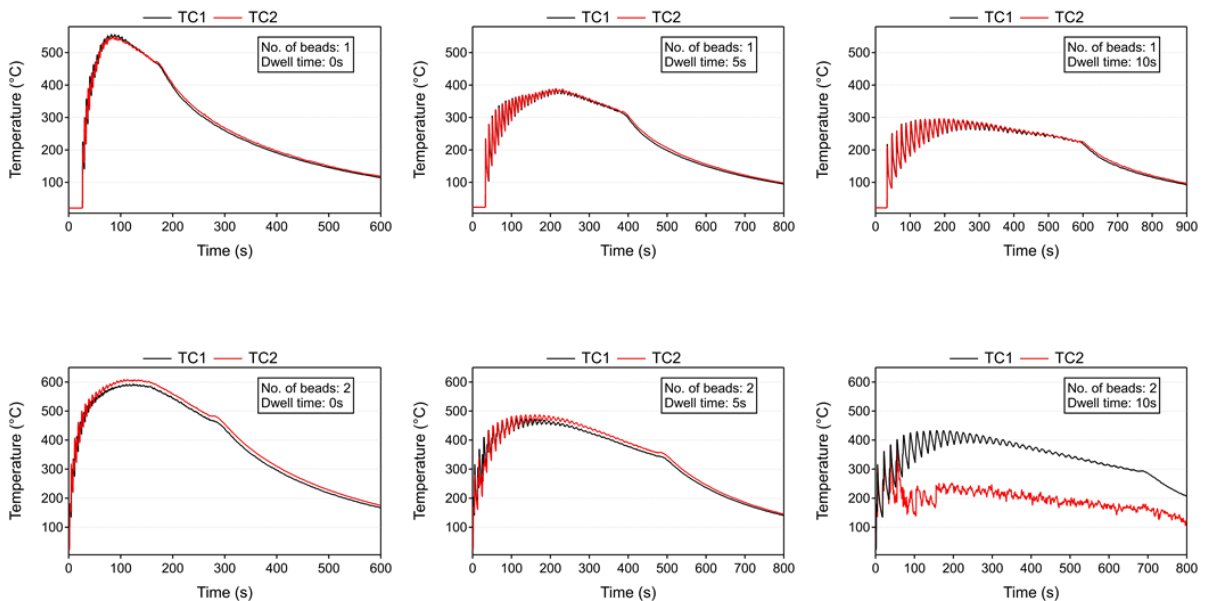


Figure A. 8: Experimental data recorded from thermocouples 1 and 2 for all experiment cases defined in Chapter 4

## References

- Acevedo, R., Sedlak, P., Kolman, R., Fredel, M., 2020. Residual stress analysis of additive manufacturing of metallic parts using ultrasonic waves: State of the art review. *J. Mater. Res. Technol.* 9, 9457–9477. <https://doi.org/10.1016/j.jmrt.2020.05.092>
- Adhitan, R.K., Raghavan, N., 2017. Transient Thermo-mechanical Modeling of stress Evolution and Re-melt Volume Fraction in Electron Beam Additive Manufacturing Process. *Procedia Manuf.*, 27th International Conference on Flexible Automation and Intelligent Manufacturing, FAIM2017, 27-30 June 2017, Modena, Italy 11, 571–583. <https://doi.org/10.1016/j.promfg.2017.07.151>
- Afazov, S., Semerdzhieva, E., Scrimieri, D., Serjouei, A., Kairoshev, B., Derguti, F., 2021. An improved distortion compensation approach for additive manufacturing using optically scanned data. *Virtual Phys. Prototyp.* 16, 1–13. <https://doi.org/10.1080/17452759.2021.1881702>
- Aggarangsi, P., Beuth, J.L., 2006. Localized Preheating Approaches for Reducing Residual Stress in Additive Manufacturing. <https://doi.org/10.26153/tsw/7174>
- Alimardani, M., Toyserkani, E., Huissoon, J.P., 2007a. A 3D dynamic numerical approach for temperature and thermal stress distributions in multilayer laser solid freeform fabrication process. *Opt. Lasers Eng.* 45, 1115–1130. <https://doi.org/10.1016/j.optlaseng.2007.06.010>
- Alimardani, M., Toyserkani, E., Huissoon, J.P., 2007b. Three-dimensional numerical approach for geometrical prediction of multilayer laser solid freeform fabrication process. *J. Laser Appl.* 19, 14–25. <https://doi.org/10.2351/1.2402518>
- Alvarez, P., Ecenarro, J., Setien, I., Sebastian, M.S., Echeverria, A., Eciolaza, L., n.d. Computationally efficient distortion prediction in Powder Bed Fusion Additive Manufacturing. *Int. J. Eng. Res.* 2, 8.
- Anca, A., Fachinotti, V.D., Escobar-Palafox, G., Cardona, A., 2011. Computational modelling of shaped metal deposition. *Int. J. Numer. Methods Eng.* 85, 84–106. <https://doi.org/10.1002/nme.2959>
- Andersson, B.A.B., 1978. Thermal Stresses in a Submerged-Arc Welded Joint Considering Phase Transformations. *J. Eng. Mater. Technol.* 100, 356–362. <https://doi.org/10.1115/1.3443504>
- Apsley, L.K., Bodell, C.I., Danton, J.C., Hayden, S.R., Kapila, S., Lessard, E., Uhl, R.B., 2015. Providing services related to item delivery via 3d manufacturing on demand. US20150052024A1.
- Argyris, J., Szimmat, J., Willam, K., 1982. Computational aspects of welding stress analysis. [https://doi.org/10.1016/0045-7825\(82\)90126-8](https://doi.org/10.1016/0045-7825(82)90126-8)
- Baiges, J., Chiumenti, M., Moreira, C.A., Cervera, M., Codina, R., 2021. An adaptive Finite Element strategy for the numerical simulation of additive manufacturing processes. *Addit. Manuf.* 37, 101650. <https://doi.org/10.1016/j.addma.2020.101650>
- Bayat, M., Dong, W., Thorborg, J., To, A.C., Hattel, J.H., 2021a. A review of multi-scale and multi-physics simulations of metal additive manufacturing processes with focus on modeling strategies. *Addit. Manuf.* 47, 102278. <https://doi.org/10.1016/j.addma.2021.102278>
- Bayat, M., Klingaa, C.G., Mohanty, S., De Baere, D., Thorborg, J., Tiedje, N.S., Hattel, J.H., 2020. Part-scale thermo-mechanical modelling of distortions in Laser Powder Bed Fusion – Analysis of the sequential flash heating method with experimental validation. *Addit. Manuf.* 36, 101508. <https://doi.org/10.1016/j.addma.2020.101508>
- Bayat, M., Nadimpalli, V.K., Biondani, F.G., Jafarzadeh, S., Thorborg, J., Tiedje, N.S., Bissacco, G., Pedersen, D.B., Hattel, J.H., 2021b. On the role of the powder stream on the heat and fluid flow conditions during Directed Energy Deposition of maraging steel—Multiphysics modeling and experimental validation. *Addit. Manuf.* 43, 102021. <https://doi.org/10.1016/j.addma.2021.102021>

- Benzley, S.E., Perry, E., Merkley, K., Clark, B., Sjaardema, G., 1995. A comparison of all hexagonal and all tetrahedral finite element meshes for elastic and elasto-plastic analysis, in: In Proceedings, 4th International Meshing Roundtable. pp. 179–191.
- Biegler, M., Elsner, B.A.M., Graf, B., Rethmeier, M., 2020. Geometric distortion-compensation via transient numerical simulation for directed energy deposition additive manufacturing. *Sci. Technol. Weld. Join.* 25, 468–475. <https://doi.org/10.1080/13621718.2020.1743927>
- Biegler, M., Graf, B., Rethmeier, M., 2018a. In-situ distortions in LMD additive manufacturing walls can be measured with digital image correlation and predicted using numerical simulations. *Addit. Manuf.* 20, 101–110. <https://doi.org/10.1016/j.addma.2017.12.007>
- Biegler, M., Marko, A., Graf, B., Rethmeier, M., 2018b. Finite element analysis of in-situ distortion and bulging for an arbitrarily curved additive manufacturing directed energy deposition geometry. *Addit. Manuf.* 24, 264–272. <https://doi.org/10.1016/j.addma.2018.10.006>
- Brickstad, B., Josefson, B.L., 1998. A parametric study of residual stresses in multi-pass butt-welded stainless steel pipes. *Int. J. Press. Vessels Pip.* 75, 11–25. [https://doi.org/10.1016/S0308-0161\(97\)00117-8](https://doi.org/10.1016/S0308-0161(97)00117-8)
- Cadiou, S., 2019. Modélisation magnéto-thermohydraulique de procédés de fabrication additive arc-fil (WAAM) (phdthesis). Université de Bretagne Sud.
- Cambon, C., 2021. Étude thermomécanique du procédé de fabrication métallique arc-fil : approche numérique et expérimentale (phdthesis). Université Montpellier.
- Chen, Q., Liang, X., Hayduke, D., Liu, J., Cheng, L., Oskin, J., Whitmore, R., To, A.C., 2019a. An inherent strain based multiscale modeling framework for simulating part-scale residual deformation for direct metal laser sintering. *Addit. Manuf.* 28, 406–418. <https://doi.org/10.1016/j.addma.2019.05.021>
- Chen, Q., Liang, X., Hayduke, D., Liu, J., Cheng, L., Oskin, J., Whitmore, R., To, A.C., 2019b. An inherent strain based multiscale modeling framework for simulating part-scale residual deformation for direct metal laser sintering. *Addit. Manuf.* 28, 406–418. <https://doi.org/10.1016/j.addma.2019.05.021>
- Chen, Q., Taylor, H., Takezawa, A., Liang, X., Jimenez, X., Wicker, R., To, A.C., 2021. Island scanning pattern optimization for residual deformation mitigation in laser powder bed fusion via sequential inherent strain method and sensitivity analysis. *Addit. Manuf.* 46, 102116. <https://doi.org/10.1016/j.addma.2021.102116>
- Cheng, L., Liang, X., Bai, J., Chen, Q., Lemon, J., To, A., 2019. On utilizing topology optimization to design support structure to prevent residual stress induced build failure in laser powder bed metal additive manufacturing. *Addit. Manuf.* 27, 290–304. <https://doi.org/10.1016/j.addma.2019.03.001>
- Chew, Y., Pang, J.H.L., Bi, G., Song, B., 2015. Thermo-mechanical model for simulating laser cladding induced residual stresses with single and multiple clad beads. *J. Mater. Process. Technol.* 224, 89–101. <https://doi.org/10.1016/j.jmatprotec.2015.04.031>
- Chiumenti, M., Cervera, M., Salmi, A., Agelet de Saracibar, C., Dialami, N., Matsui, K., 2010. Finite element modeling of multi-pass welding and shaped metal deposition processes. *Comput. Methods Appl. Mech. Eng.* 199, 2343–2359. <https://doi.org/10.1016/j.cma.2010.02.018>
- Chiumenti, M., Neiva, E., Salsi, E., Cervera, M., Badia, S., Moya, J., Chen, Z., Lee, C., Davies, C., 2017. Numerical modelling and experimental validation in Selective Laser Melting. *Addit. Manuf.* 18, 171–185. <https://doi.org/10.1016/j.addma.2017.09.002>
- Courtois, M., 2014. Modélisation thermohydraulique tri-dimensionnelle du soudage laser de flans rabotés et validation expérimentale (These de doctorat). Lorient.
- Dai, H., Francis, J.A., Stone, H.J., Bhadeshia, H.K.D.H., Withers, P.J., 2008. Characterizing Phase Transformations and Their Effects on Ferritic Weld Residual Stresses with X-Rays and Neutrons. *Metall. Mater. Trans. A* 39, 3070–3078. <https://doi.org/10.1007/s11661-008-9616-0>

- Dai, K., Shaw, L., 2002. Distortion minimization of laser-processed components through control of laser scanning patterns. *Rapid Prototyp. J.* 8, 270–276. <https://doi.org/10.1108/13552540210451732>
- Dass, A., Moridi, A., 2019. State of the Art in Directed Energy Deposition: From Additive Manufacturing to Materials Design. *Coatings* 9, 418. <https://doi.org/10.3390/coatings9070418>
- Deng, D., Kiyoshima, S., 2010. Numerical simulation of residual stresses induced by laser beam welding in a SUS316 stainless steel pipe with considering initial residual stress influences. *Nucl. Eng. Des.* 240, 688–696. <https://doi.org/10.1016/j.nucengdes.2009.11.049>
- Deng, D., Murakawa, H., 2006. Numerical simulation of temperature field and residual stress in multi-pass welds in stainless steel pipe and comparison with experimental measurements. *Comput. Mater. Sci.* 37, 269–277. <https://doi.org/10.1016/j.commatsci.2005.07.007>
- Denlinger, E.R., 2015. thermo-mechanical model development and experimental validation for metallic parts in additive manufacturing.
- Denlinger, Erik R, Heigel, J.C., Michaleris, P., 2015. Residual stress and distortion modeling of electron beam direct manufacturing Ti-6Al-4V. *Proc. Inst. Mech. Eng. Part B J. Eng. Manuf.* 229, 1803–1813. <https://doi.org/10.1177/0954405414539494>
- Denlinger, Erik R., Heigel, J.C., Michaleris, P., Palmer, T.A., 2015. Effect of inter-layer dwell time on distortion and residual stress in additive manufacturing of titanium and nickel alloys. *J. Mater. Process. Technol.* 215, 123–131. <https://doi.org/10.1016/j.jmatprotec.2014.07.030>
- Denlinger, E.R., Irwin, J., Michaleris, P., 2014. Thermomechanical Modeling of Additive Manufacturing Large Parts. *J. Manuf. Sci. Eng.* 136. <https://doi.org/10.1115/1.4028669>
- Denlinger, E.R., Michaleris, P., 2016. Effect of stress relaxation on distortion in additive manufacturing process modeling. *Addit. Manuf.* 12, 51–59. <https://doi.org/10.1016/j.addma.2016.06.011>
- Deo, M.V., Michaleris, P., 2003. Mitigation of welding induced buckling distortion using transient thermal tensioning. *Sci. Technol. Weld. Join.* 8, 49–54. <https://doi.org/10.1179/136217103225008919>
- Depradeux, L., 2004. Simulation numérique du soudage - Acier 316L : validation sur cas tests de complexité croissante (These de doctorat). Lyon, INSA.
- Ding, J., Colegrove, P., Mehnen, J., Ganguly, S., Sequeira Almeida, P.M., Wang, F., Williams, S., 2011. Thermo-mechanical analysis of Wire and Arc Additive Layer Manufacturing process on large multi-layer parts. *Comput. Mater. Sci.* 50, 3315–3322. <https://doi.org/10.1016/j.commatsci.2011.06.023>
- Dunbar, A.J., Denlinger, E.R., Heigel, J., Michaleris, P., Guerrier, P., Martukanitz, R., Simpson, T.W., 2016. Development of experimental method for in situ distortion and temperature measurements during the laser powder bed fusion additive manufacturing process. *Addit. Manuf.* 12, 25–30. <https://doi.org/10.1016/j.addma.2016.04.007>
- Fallah, V., Alimardani, M., Corbin, S.F., Khajepour, A., 2011. Temporal development of melt-pool morphology and clad geometry in laser powder deposition. *Comput. Mater. Sci.* 50, 2124–2134. <https://doi.org/10.1016/j.commatsci.2011.02.018>
- Farahmand, P., Kovacevic, R., 2014. An experimental–numerical investigation of heat distribution and stress field in single- and multi-track laser cladding by a high-power direct diode laser. *Opt. Laser Technol.* 63, 154–168. <https://doi.org/10.1016/j.optlastec.2014.04.016>
- Fessler, J.R., Merz, R., Nickel, A.H., Prinz, F.B., Weiss, L.E., 1996. Laser Deposition of Metals for Shape Deposition Manufacturing. <https://doi.org/10.15781/T29Z90X7D>
- Foroozmehr, E., Kovacevic, R., 2010. Effect of path planning on the laser powder deposition process: thermal and structural evaluation. *Int. J. Adv. Manuf. Technol.* 51, 659–669. <https://doi.org/10.1007/s00170-010-2659-6>

- Francis, J.A., Bhadeshia, H.K.D.H., Withers, P.J., 2007. Welding residual stresses in ferritic power plant steels. *Mater. Sci. Technol.* 23, 1009–1020. <https://doi.org/10.1179/174328407X213116>
- Francis, J.A., Stone, H.J., Kundu, S., Rogge, R.B., Bhadeshia, H.K.D.H., Withers, P.J., Karlsson, L., 2009a. Transformation Temperatures and Welding Residual Stresses in Ferritic Steels. Presented at the ASME 2007 Pressure Vessels and Piping Conference, American Society of Mechanical Engineers Digital Collection, pp. 949–956. <https://doi.org/10.1115/PVP2007-26544>
- Francis, J.A., Turski, M., Withers, P.J., 2009b. Measured residual stress distributions for low and high heat input single weld beads deposited on to SA508 steel. *Mater. Sci. Technol.* 25, 325–334. <https://doi.org/10.1179/174328408X372074>
- Free, J.A., Porter Goff, R.F.D., 1989. Predicting residual stresses in multi-pass weldments with the finite element method. *Comput. Struct.* 32, 365–378. [https://doi.org/10.1016/0045-7949\(89\)90048-5](https://doi.org/10.1016/0045-7949(89)90048-5)
- Friedman, E., 1975. Thermomechanical Analysis of the Welding Process Using the Finite Element Method. *J. Press. Vessel Technol.* 97, 206–213. <https://doi.org/10.1115/1.3454296>
- Gan, Z., Liu, H., Li, S., He, X., Yu, G., 2017a. Modeling of thermal behavior and mass transport in multi-layer laser additive manufacturing of Ni-based alloy on cast iron. *Int. J. Heat Mass Transf.* 111, 709–722. <https://doi.org/10.1016/j.ijheatmasstransfer.2017.04.055>
- Gan, Z., Yu, G., He, X., Li, S., 2017b. Numerical simulation of thermal behavior and multicomponent mass transfer in direct laser deposition of Co-base alloy on steel. *Int. J. Heat Mass Transf.* 104, 28–38. <https://doi.org/10.1016/j.ijheatmasstransfer.2016.08.049>
- Ganeriwala, R.K., Strantza, M., King, W.E., Clausen, B., Phan, T.Q., Levine, L.E., Brown, D.W., Hodge, N.E., 2019. Evaluation of a thermomechanical model for prediction of residual stress during laser powder bed fusion of Ti-6Al-4V. *Addit. Manuf.* 27, 489–502. <https://doi.org/10.1016/j.addma.2019.03.034>
- Ghosh, S., Choi, J., 2005. Three-dimensional transient finite element analysis for residual stresses in the laser aided direct metal/material deposition process. *J. Laser Appl.* 17, 144–158. <https://doi.org/10.2351/1.1961688>
- Glicksman, M.E., 2010. *Principles of Solidification: An Introduction to Modern Casting and Crystal Growth Concepts*. Springer Science & Business Media.
- Gockel, J., Beuth, J., Taminger, K., 2014. Integrated control of solidification microstructure and melt pool dimensions in electron beam wire feed additive manufacturing of Ti-6Al-4V. *Addit. Manuf.*, Inaugural Issue 1–4, 119–126. <https://doi.org/10.1016/j.addma.2014.09.004>
- Gockel, J., Fox, J., Beuth, J., Hafley, R., 2015. Integrated melt pool and microstructure control for Ti-6Al-4V thin wall additive manufacturing. *Mater. Sci. Technol.* 31, 912–916. <https://doi.org/10.1179/1743284714Y.0000000704>
- Goldak, J., Chakravarti, A., Bibby, M., 1984. A new finite element model for welding heat sources. *Metall. Trans. B* 15, 299–305. <https://doi.org/10.1007/BF02667333>
- Gouge, M., Denlinger, E., Irwin, J., Li, C., Michaleris, P., 2019. Experimental validation of thermo-mechanical part-scale modeling for laser powder bed fusion processes. *Addit. Manuf.* 29, 100771. <https://doi.org/10.1016/j.addma.2019.06.022>
- Gouge, M., Michaleris, P., Denlinger, E., Irwin, J., 2018. Chapter 2 - The Finite Element Method for the Thermo-Mechanical Modeling of Additive Manufacturing Processes, in: Gouge, M., Michaleris, P. (Eds.), *Thermo-Mechanical Modeling of Additive Manufacturing*. Butterworth-Heinemann, pp. 19–38. <https://doi.org/10.1016/B978-0-12-811820-7.00003-3>
- Gouge, M.F., Heigel, J.C., Michaleris, P., Palmer, T.A., 2015. Modeling forced convection in the thermal simulation of laser cladding processes. *Int. J. Adv. Manuf. Technol.* 79, 307–320. <https://doi.org/10.1007/s00170-015-6831-x>

- Griffith, M., Schlienger, M.E., Harwell, L.D., Oliver, M.S., Baldwin, M.D., Ensz, M.T., Smugeresky, J.E., Essien, M., Brooks, J., Robino, C.V., Hofmeister, W.H., Wert, M.J., Nelson, D.V., 1998. Thermal Behavior in the Lens Process. <https://doi.org/10.26153/tsw/584>
- Grum, J., Žnidaršič, M., 2004. Microstructure, Microhardness, and Residual Stress Analysis of Laser Surface Cladding of Low-Carbon Steel. *Mater. Manuf. Process.* 19, 243–258. <https://doi.org/10.1081/AMP-120029854>
- Gu, M., Goldak, J.A., 1994. Steady-State Formulation for Stress and Distortion of Welds. *J. Eng. Ind.* 116, 467–474. <https://doi.org/10.1115/1.2902130>
- Hajjalizadeh, F., Ince, A., 2019. Finite element–based numerical modeling framework for additive manufacturing process. *Mater. Des. Process. Commun.* 1, e28. <https://doi.org/10.1002/mdp2.28>
- He, X., Fuerschbach, P.W., DebRoy, T., 2003. Heat transfer and fluid flow during laser spot welding of 304 stainless steel. *J. Phys. D: Appl. Phys.* 36, 1388–1398. <https://doi.org/10.1088/0022-3727/36/12/306>
- He, X., Mazumder, J., 2007. Transport phenomena during direct metal deposition. *J. Appl. Phys.* 101, 053113. <https://doi.org/10.1063/1.2710780>
- Heigel, J.C., Michaleris, P., Palmer, T.A., 2016. Measurement of forced surface convection in directed energy deposition additive manufacturing. *Proc. Inst. Mech. Eng. Part B J. Eng. Manuf.* 230, 1295–1308. <https://doi.org/10.1177/0954405415599928>
- Heigel, J.C., Michaleris, P., Reutzel, E.W., 2015. Thermo-mechanical model development and validation of directed energy deposition additive manufacturing of Ti–6Al–4V. *Addit. Manuf.* 5, 9–19. <https://doi.org/10.1016/j.addma.2014.10.003>
- Hibbitt, H.D., Marcal, P.V., 1973. A numerical, thermo-mechanical model for the welding and subsequent loading of a fabricated structure. *Comput. Struct.* 3, 1145–1174. [https://doi.org/10.1016/0045-7949\(73\)90043-6](https://doi.org/10.1016/0045-7949(73)90043-6)
- Hodge, N.E., Ferencz, R.M., Vignes, R.M., 2016. Experimental comparison of residual stresses for a thermomechanical model for the simulation of selective laser melting. *Addit. Manuf., Special Issue on Modeling & Simulation for Additive Manufacturing* 12, 159–168. <https://doi.org/10.1016/j.addma.2016.05.011>
- Huang, Y., Ansari, M., Asgari, H., Farshidianfar, M.H., Sarker, D., Khamesee, M.B., Toyserkani, E., 2019. Rapid prediction of real-time thermal characteristics, solidification parameters and microstructure in laser directed energy deposition (powder-fed additive manufacturing). *J. Mater. Process. Technol.* 274, 116286. <https://doi.org/10.1016/j.jmatprotec.2019.116286>
- Irwin, J., Michaleris, P., 2016. A Line Heat Input Model for Additive Manufacturing. *J. Manuf. Sci. Eng.* 138. <https://doi.org/10.1115/1.4033662>
- Jendrzewski, R., Śliwiński, G., 2007. Investigation of temperature and stress fields in laser clad coatings. *Appl. Surf. Sci., Laser synthesis and processing of advanced materials* 254, 921–925. <https://doi.org/10.1016/j.apsusc.2007.08.014>
- Jendrzewski, R., Śliwiński, G., Krawczuk, M., Ostachowicz, W., 2004. Temperature and stress fields induced during laser cladding. *Comput. Struct.* 82, 653–658. <https://doi.org/10.1016/j.compstruc.2003.11.005>
- Jiang, W., Zhang, Y., Woo, W., 2012. Using heat sink technology to decrease residual stress in 316L stainless steel welding joint: Finite element simulation. *Int. J. Press. Vessels Pip.* 92, 56–62. <https://doi.org/10.1016/j.ijpvp.2012.01.002>
- Jiang, Y., Cheng, Y., Zhang, X., Yang, J., Yang, X., Cheng, Z., 2020. Simulation and experimental investigations on the effect of Marangoni convection on thermal field during laser cladding process. *Optik* 203, 164044. <https://doi.org/10.1016/j.ijleo.2019.164044>

- Johnson, K.L., Rodgers, T.M., Underwood, O.D., Madison, J.D., Ford, K.R., Whetten, S.R., Dagel, D.J., Bishop, J.E., 2018. Simulation and experimental comparison of the thermo-mechanical history and 3D microstructure evolution of 304L stainless steel tubes manufactured using LENS. *Comput. Mech.* 61, 559–574. <https://doi.org/10.1007/s00466-017-1516-y>
- Kim, T., Ha, K., Cho, Y.-R., Jeon, J.B., Lee, W., 2019. Analysis of residual stress evolution during powder bed fusion process of AISI 316L stainless steel with experiment and numerical modeling. *Int. J. Adv. Manuf. Technol.* 105, 309–323. <https://doi.org/10.1007/s00170-019-04204-0>
- Kiran, A., Hodek, J., Vavřík, J., Urbánek, M., Džugan, J., 2020. Numerical Simulation Development and Computational Optimization for Directed Energy Deposition Additive Manufacturing Process. *Materials* 13, 2666. <https://doi.org/10.3390/ma13112666>
- Labudovic, M., Hu, D., Kovacevic, R., 2003. A three dimensional model for direct laser metal powder deposition and rapid prototyping. *J. Mater. Sci.* 38, 35–49. <https://doi.org/10.1023/A:1021153513925>
- Lampa, C., Kaplan, A.F.H., Powell, J., Magnusson, C., 1997. An analytical thermodynamic model of laser welding. *J. Phys. Appl. Phys.* 30, 1293–1299. <https://doi.org/10.1088/0022-3727/30/9/004>
- Lee, C.-H., Chang, K.-H., Lee, C.-Y., 2008. Comparative study of welding residual stresses in carbon and stainless steel butt welds. *Proc. Inst. Mech. Eng. Part B J. Eng. Manuf.* 222, 1685–1694. <https://doi.org/10.1243/09544054JEM1244>
- Li, Chao, Guo, Y., Fang, X., Fang, F., 2018. A scalable predictive model and validation for residual stress and distortion in selective laser melting. *CIRP Ann.* 67, 249–252. <https://doi.org/10.1016/j.cirp.2018.04.105>
- Li, C., Liu, J.F., Fang, X.Y., Guo, Y.B., 2017. Efficient predictive model of part distortion and residual stress in selective laser melting. *Addit. Manuf.* 17, 157–168. <https://doi.org/10.1016/j.addma.2017.08.014>
- Li, C., Liu, J.F., Guo, Y.B., 2016. Prediction of Residual Stress and Part Distortion in Selective Laser Melting. *Procedia CIRP*, 3rd CIRP Conference on Surface Integrity 45, 171–174. <https://doi.org/10.1016/j.procir.2016.02.058>
- Li, C., Liu, Z.Y., Fang, X.Y., Guo, Y.B., 2018. Residual Stress in Metal Additive Manufacturing. *Procedia CIRP*, 4th CIRP Conference on Surface Integrity (CSI 2018) 71, 348–353. <https://doi.org/10.1016/j.procir.2018.05.039>
- Li, L., Anand, S., 2020. Hatch pattern based inherent strain prediction using neural networks for powder bed fusion additive manufacturing. *J. Manuf. Process.* 56, 1344–1352. <https://doi.org/10.1016/j.jmapro.2020.04.030>
- Li, L., Zhang, X., Cui, W., Liou, F., Deng, W., Li, W., 2020. Temperature and residual stress distribution of FGM parts by DED process: modeling and experimental validation. *Int. J. Adv. Manuf. Technol.* 109, 451–462. <https://doi.org/10.1007/s00170-020-05673-4>
- Li, Y., Yang, H., Lin, X., Huang, W., Li, J., Zhou, Y., 2003. The influences of processing parameters on forming characterizations during laser rapid forming. *Mater. Sci. Eng. A* 360, 18–25. [https://doi.org/10.1016/S0921-5093\(03\)00435-0](https://doi.org/10.1016/S0921-5093(03)00435-0)
- Liang, X., Chen, Q., Cheng, L., Hayduke, D., To, A.C., 2019. Modified inherent strain method for efficient prediction of residual deformation in direct metal laser sintered components. *Comput. Mech.* 64, 1719–1733. <https://doi.org/10.1007/s00466-019-01748-6>
- Liang, X., Cheng, L., Chen, Q., Yang, Q., To, A.C., 2018a. A modified method for estimating inherent strains from detailed process simulation for fast residual distortion prediction of single-walled structures fabricated by directed energy deposition. *Addit. Manuf.* 23, 471–486. <https://doi.org/10.1016/j.addma.2018.08.029>

- Liang, X., Cheng, L., Chen, Q., Yang, Q., To, A.C., 2018b. A modified method for estimating inherent strains from detailed process simulation for fast residual distortion prediction of single-walled structures fabricated by directed energy deposition. *Addit. Manuf.* 23, 471–486. <https://doi.org/10.1016/j.addma.2018.08.029>
- Liang, X., Dong, W., Chen, Q., To, A.C., 2021. On incorporating scanning strategy effects into the modified inherent strain modeling framework for laser powder bed fusion. *Addit. Manuf.* 37, 101648. <https://doi.org/10.1016/j.addma.2020.101648>
- Lindgren, L., Häggblad, H.-Å., McDill, J., Oddy, A., 1997. Automatic remeshing for three-dimensional finite element simulation of welding. [https://doi.org/10.1016/S0045-7825\(97\)00025-X](https://doi.org/10.1016/S0045-7825(97)00025-X)
- Lindgren, L.-E., 2001. Finite Element Modeling and Simulation of Welding Part 1: Increased Complexity. *J. Therm. Stress.* 24, 141–192. <https://doi.org/10.1080/01495730150500442>
- Lindgren, L.-E., Runnemalm, H., Näsström, M.O., 1999. Simulation of multipass welding of a thick plate. *Int. J. Numer. Methods Eng.* 44, 1301–1316. [https://doi.org/10.1002/\(SICI\)1097-0207\(19990330\)44:9<1301::AID-NME479>3.0.CO;2-K](https://doi.org/10.1002/(SICI)1097-0207(19990330)44:9<1301::AID-NME479>3.0.CO;2-K)
- Longuet, A., Robert, Y., Aeby-Gautier, E., Appolaire, B., Mariage, J.F., Colin, C., Cailletaud, G., 2009. A multiphase mechanical model for Ti–6Al–4V: Application to the modeling of laser assisted processing. *Comput. Mater. Sci., Proceedings of the 18th International Workshop on Computational Mechanics of Materials* 46, 761–766. <https://doi.org/10.1016/j.commatsci.2009.05.012>
- Lu, X., Lin, X., Chiumenti, M., Cervera, M., Hu, Y., Ji, X., Ma, L., Yang, H., Huang, W., 2019a. Residual stress and distortion of rectangular and S-shaped Ti-6Al-4V parts by Directed Energy Deposition: Modelling and experimental calibration. *Addit. Manuf.* 26, 166–179. <https://doi.org/10.1016/j.addma.2019.02.001>
- Lu, X., Lin, X., Chiumenti, M., Cervera, M., Hu, Y., Ji, X., Ma, L., Yang, H., Huang, W., 2019b. Residual stress and distortion of rectangular and S-shaped Ti-6Al-4V parts by Directed Energy Deposition: Modelling and experimental calibration. *Addit. Manuf.* 26, 166–179. <https://doi.org/10.1016/j.addma.2019.02.001>
- Lu, X., Lin, X., Chiumenti, M., Cervera, M., Li, J., Ma, L., Wei, L., Hu, Y., Huang, W., 2018a. Finite element analysis and experimental validation of the thermomechanical behavior in laser solid forming of Ti-6Al-4V. *Addit. Manuf.* 21, 30–40. <https://doi.org/10.1016/j.addma.2018.02.003>
- Lu, X., Lin, X., Chiumenti, M., Cervera, M., Li, J., Ma, L., Wei, L., Hu, Y., Huang, W., 2018b. Finite element analysis and experimental validation of the thermomechanical behavior in laser solid forming of Ti-6Al-4V. *Addit. Manuf.* 21, 30–40. <https://doi.org/10.1016/j.addma.2018.02.003>
- Lundbäck, A., Lindgren, L.-E., 2011. Modelling of metal deposition. *Finite Elem. Anal. Des.* 47, 1169–1177. <https://doi.org/10.1016/j.finel.2011.05.005>
- Madireddy, G., Li, C., Liu, J., Sealy, M.P., 2019. Modeling thermal and mechanical cancellation of residual stress from hybrid additive manufacturing by laser peening. *Nanotechnol. Precis. Eng.* 2, 49–60. <https://doi.org/10.1016/j.npe.2019.07.001>
- Manvatkar, V., De, A., DebRoy, T., 2014. Heat transfer and material flow during laser assisted multi-layer additive manufacturing. *J. Appl. Phys.* 116, 124905. <https://doi.org/10.1063/1.4896751>
- Manvatkar, V.D., Gokhale, A.A., Jagan Reddy, G., Venkataramana, A., De, A., 2011. Estimation of Melt Pool Dimensions, Thermal Cycle, and Hardness Distribution in the Laser-Engineered Net Shaping Process of Austenitic Stainless Steel. *Metall. Mater. Trans. A* 42, 4080–4087. <https://doi.org/10.1007/s11661-011-0787-8>
- Marimuthu, S., Clark, D., Allen, J., Kamara, A., Mativenga, P., Li, L., Scudamore, R., 2013. Finite element modelling of substrate thermal distortion in direct laser additive manufacture of an aero-engine component. *Proc. Inst. Mech. Eng. Part C J. Mech. Eng. Sci.* 227, 1987–1999. <https://doi.org/10.1177/0954406212470363>

- Marion, G., 2016. Modélisation de procédés de fabrication additive de pièces aéronautiques et spatiales en Ti-6Al-4V par dépôt et fusion sélective d'un lit de poudre par laser : Approche thermique, métallurgique et mécanique (phdthesis). Université Paris sciences et lettres.
- Masubuchi, K., 2013. Analysis of Welded Structures: Residual Stresses, Distortion, and Their Consequences. Elsevier.
- Michaleris, P., 2014. Modeling metal deposition in heat transfer analyses of additive manufacturing processes. Finite Elem. Anal. Des. 86, 51–60. <https://doi.org/10.1016/j.finel.2014.04.003>
- Michaleris, P. (Ed.), 2011. Front matter, in: Minimization of Welding Distortion and Buckling, Woodhead Publishing Series in Welding and Other Joining Technologies. Woodhead Publishing, pp. i–iii. <https://doi.org/10.1533/9780857092908.frontmatter>
- Michaleris, P., Tortorelli, D.A., Vidal, C.A., 1995. Analysis and optimization of weakly coupled thermoelastoplastic systems with applications to weldment design. Int. J. Numer. Methods Eng. 38, 1259–1285. <https://doi.org/10.1002/nme.1620380803>
- Miedzinski, M., 2017. Materials for Additive Manufacturing by Direct Energy Deposition. undefined.
- Milewski, J.O., 2017. Additive Manufacturing of Metals: From Fundamental Technology to Rocket Nozzles, Medical Implants, and Custom Jewelry, Springer Series in Materials Science. Springer International Publishing. <https://doi.org/10.1007/978-3-319-58205-4>
- Mills, K.C., 2002a. Ti: Ti-6 Al-4 V (IMI 318), in: Mills, K.C. (Ed.), Recommended Values of Thermophysical Properties for Selected Commercial Alloys, Woodhead Publishing Series in Metals and Surface Engineering. Woodhead Publishing, pp. 211–217. <https://doi.org/10.1533/9781845690144.211>
- Mills, K.C., 2002b. Fe - 316 Stainless Steel, in: Mills, K.C. (Ed.), Recommended Values of Thermophysical Properties for Selected Commercial Alloys, Woodhead Publishing Series in Metals and Surface Engineering. Woodhead Publishing, pp. 135–142. <https://doi.org/10.1533/9781845690144.135>
- Mishra, A.K., Aggarwal, A., Kumar, A., Sinha, N., 2018. Identification of a suitable volumetric heat source for modelling of selective laser melting of Ti6Al4V powder using numerical and experimental validation approach. Int. J. Adv. Manuf. Technol. 99, 2257–2270. <https://doi.org/10.1007/s00170-018-2631-4>
- Mochizuki, M., Hayashi, M., Hattori, T., 1999. Numerical Analysis of Welding Residual Stress and Its Verification Using Neutron Diffraction Measurement. J. Eng. Mater. Technol. 122, 98–103. <https://doi.org/10.1115/1.482772>
- Morville, S., 2012a. Modélisation multiphysique du procédé de Fabrication Rapide par Projection Laser en vue d'améliorer l'état de surface final (phdthesis). Université de Bretagne Sud.
- Morville, S., 2012b. Modélisation multiphysique du procédé de Fabrication Directe par Projection Laser en vue d'améliorer l'état de surface final (These de doctorat). Lorient.
- Morville, S., Carin, M., Carron, D., Le Masson, P., Gharbi, M., Peyre, P., Fabbro, R., 2012a. Numerical modelling of powder flow during coaxial laser direct metal deposition - comparaison between Ti-6Al-4V alloy and stainless steel 316L.
- Morville, S., Carin, M., Peyre, P., Gharbi, M., Carron, D., Le Masson, P., Fabbro, R., 2012b. 2D longitudinal modeling of heat transfer and fluid flow during multilayered direct laser metal deposition process. J. Laser Appl. 24, 032008. <https://doi.org/10.2351/1.4726445>
- Mukherjee, T., Zhang, W., DebRoy, T., 2017. An improved prediction of residual stresses and distortion in additive manufacturing. Comput. Mater. Sci. 126, 360–372. <https://doi.org/10.1016/j.commatsci.2016.10.003>
- Nain, V., Engel, T., Carin, M., Boisselier, D., Seguy, L., 2021. Development of an Elongated Ellipsoid Heat Source Model to Reduce Computation Time for Directed Energy Deposition Process. Front. Mater. 8, 512. <https://doi.org/10.3389/fmats.2021.747389>

- Neela, V., De, A., 2009. Three-dimensional heat transfer analysis of LENSTM process using finite element method. *Int. J. Adv. Manuf. Technol.* 45, 935. <https://doi.org/10.1007/s00170-009-2024-9>
- Nickel, A.H., Barnett, D.M., Prinz, F.B., 2001. Thermal stresses and deposition patterns in layered manufacturing. *Mater. Sci. Eng. A* 317, 59–64. [https://doi.org/10.1016/S0921-5093\(01\)01179-0](https://doi.org/10.1016/S0921-5093(01)01179-0)
- Nie, P., Ojo, O.A., Li, Z., 2014. Numerical modeling of microstructure evolution during laser additive manufacturing of a nickel-based superalloy. *Acta Mater.* 77, 85–95. <https://doi.org/10.1016/j.actamat.2014.05.039>
- Ocelík, V., Bosgra, J., de Hosson, J.Th.M., 2009. In-situ strain observation in high power laser cladding. *Surf. Coat. Technol.* 203, 3189–3196. <https://doi.org/10.1016/j.surfcoat.2009.03.050>
- Peyre, P., Aubry, P., Fabbro, R., Neveu, R., Longuet, A., 2008. Analytical and numerical modelling of the direct metal deposition laser process. *J. Phys. Appl. Phys.* 41, 025403. <https://doi.org/10.1088/0022-3727/41/2/025403>
- Peyre, P., Dal, M., POUZET, S. ebastien, Castelnau, O., 2017. Simplified numerical model for the laser metal deposition additive manufacturing process. *J. Laser Appl.* 29, Article number 022304. <https://doi.org/10.2351/1.4983251>
- Pinkerton, A.J., Li, L., 2004. Modelling the geometry of a moving laser melt pool and deposition track via energy and mass balances. *J. Phys. Appl. Phys.* 37, 1885–1895. <https://doi.org/10.1088/0022-3727/37/14/003>
- Piscopo, G., Atzeni, E., Salmi, A., 2019. A Hybrid Modeling of the Physics-Driven Evolution of Material Addition and Track Generation in Laser Powder Directed Energy Deposition. *Materials* 12, 2819. <https://doi.org/10.3390/ma12172819>
- Plati, A., Tan, J.C., Golosnoy, I.O., Persoons, R., van Acker, K., Clyne, T.W., 2006. Residual Stress Generation during Laser Cladding of Steel with a Particulate Metal Matrix Composite. *Adv. Eng. Mater.* 8, 619–624. <https://doi.org/10.1002/adem.200600063>
- Prajadhiana, K.P., Manurung, Y.H., Sulaiman, M.S., Adenan, M.S., 2020. Investigation on Welded T-Joint Distortion Using Virtual Manufacturing Tools with Simplified Procedure. *J. Korean Soc. Precis. Eng.* 37, 91–97. <https://doi.org/10.7736/JKSPE.019.090>
- Pratt, P., Felicelli, S.D., Wang, L., Hubbard, C.R., 2008. Residual Stress Measurement of Laser-Engineered Net Shaping AISI 410 Thin Plates Using Neutron Diffraction. *Metall. Mater. Trans. A* 39, 3155–3163. <https://doi.org/10.1007/s11661-008-9660-9>
- Qiao, D., Feng, Z., Zhang, W., Wang, Y., Crooker, P., 2014. Modeling of Weld Residual Plastic Strain and Stress in Dissimilar Metal Butt Weld in Nuclear Reactors. Presented at the ASME 2013 Pressure Vessels and Piping Conference, American Society of Mechanical Engineers Digital Collection. <https://doi.org/10.1115/PVP2013-98081>
- Ramard, C., 2018. Étude expérimentale et numérique du soudage multipasse : application à un acier de construction navale (phdthesis). Université de Bretagne Sud.
- Rangaswamy, P., Holden, T.M., Rogge, R.B., Griffith, M.L., 2003. Residual stresses in components formed by the laserengineered net shaping (LENS®) process. *J. Strain Anal. Eng. Des.* 38, 519–527. <https://doi.org/10.1243/030932403770735881>
- Ren, K., Chew, Y., Fuh, J.Y.H., Zhang, Y.F., Bi, G.J., 2019. Thermo-mechanical analyses for optimized path planning in laser aided additive manufacturing processes. *Mater. Des.* 162, 80–93. <https://doi.org/10.1016/j.matdes.2018.11.014>
- Runnemalm, H., Hyun, S., 2000. Three-dimensional welding analysis using an adaptive mesh scheme. *Comput. Methods Appl. Mech. Eng.* 189, 515–523. [https://doi.org/10.1016/S0045-7825\(99\)00304-7](https://doi.org/10.1016/S0045-7825(99)00304-7)

- Sankaré, S., 2007. Développement d'un procédé de fabrication rapide de composants mécaniques en alliages de titane par micro-rechargement laser (These de doctorat). Strasbourg 1.
- Satoh, K., Ohnishi, T., 1969. Transient Thermal Stresses of Weld Heat-Affected Zone by Both-Ends-Fixed Bar Analogy. *J. Jpn. Weld. Soc.* 38, 359–371. <https://doi.org/10.2207/qjws1943.38.359>
- Schlienger, M.E., Harwell, L.D., Oliver, M.S., Baldwin, M.D., Ensz, M.T., Smugeresky, E., Essien, M., Robino, C.V., n.d. THERMAL BEHAVIOR IN THE LENS PROCESS 8.
- Shan, X., Davies, C.M., Wangsdan, T., O'Dowd, N.P., Nikbin, K.M., 2009. Thermo-mechanical modelling of a single-bead-on-plate weld using the finite element method. *Int. J. Press. Vessels Pip., The NeT Residual Stress Measurement and Modelling Round Robin on a Single Weld Bead-on-Plate Specimen* 86, 110–121. <https://doi.org/10.1016/j.ijpvp.2008.11.005>
- Shiomi, M., Osakada, K., Nakamura, K., Yamashita, T., Abe, F., 2004. Residual Stress within Metallic Model Made by Selective Laser Melting Process. *CIRP Ann.* 53, 195–198. [https://doi.org/10.1016/S0007-8506\(07\)60677-5](https://doi.org/10.1016/S0007-8506(07)60677-5)
- Tekriwal, P., Mazumder, J., n.d. Finite Element Analysis of Three-Dimensional Transient Heat Transfer in GMA Welding 7.
- Thompson, S.M., Bian, L., Shamsaei, N., Yadollahi, A., 2015. An overview of Direct Laser Deposition for additive manufacturing; Part I: Transport phenomena, modeling and diagnostics. *Addit. Manuf.* 8, 36–62. <https://doi.org/10.1016/j.addma.2015.07.001>
- Tran, H.T., Liang, X., To, A.C., 2020a. Efficient prediction of cracking at solid-lattice support interface during laser powder bed fusion via global-local J-integral analysis based on modified inherent strain method and lattice support homogenization. *Addit. Manuf.* 36, 101590. <https://doi.org/10.1016/j.addma.2020.101590>
- Tran, H.T., Liang, X., To, A.C., 2020b. Efficient prediction of cracking at solid-lattice support interface during laser powder bed fusion via global-local J-integral analysis based on modified inherent strain method and lattice support homogenization. *Addit. Manuf.* 36, 101590. <https://doi.org/10.1016/j.addma.2020.101590>
- Tran Van, G., 2018. Détermination d'un critère de fissuration à chaud par liquation en fonction de la teneur en bore et de sa localisation pour l'acier inoxydable austénitique 316L. (Theses). Université de Bretagne Sud.
- Ueda, Y., Fukuda, K., 1989a. New Measuring Method of Three-Dimensional Residual Stresses in Long Welded Joints Using Inherent Strains as Parameters—Lz Method. *J. Eng. Mater. Technol.* 111, 1–8. <https://doi.org/10.1115/1.3226427>
- Ueda, Y., Fukuda, K., 1989b. New Measuring Method of Three-Dimensional Residual Stresses in Long Welded Joints Using Inherent Strains as Parameters—Lz Method. *J. Eng. Mater. Technol.* 111, 1–8. <https://doi.org/10.1115/1.3226427>
- Ueda, Y., Fukuda, K., Nakacho, K., Endo, S., 1975. A New Measuring Method of Residual Stresses with the Aid of Finite Element Method and Reliability of Estimated Values. [https://doi.org/10.2534/JJASNAOE1968.1975.138\\_499](https://doi.org/10.2534/JJASNAOE1968.1975.138_499)
- Ueda, Y., Yamakawa, T., 1973. Analysis of Thermal Elastic-Plastic Behavior of Metals during Welding by Finite Element Method. *J. Jpn. Weld. Soc.* 42, 567–577. <https://doi.org/10.2207/qjws1943.42.567>
- Vasinonta, A., Beuth, J., Griffith, M., 2000. Process Maps for Controlling Residual Stress and Melt Pool Size in Laser-Based SFF Processes 200. <https://doi.org/10.26153/tsw/3038>
- Wang, L., Felicelli, S., 2006. Analysis of thermal phenomena in LENS<sup>TM</sup> deposition. *Mater. Sci. Eng. A* 435–436, 625–631. <https://doi.org/10.1016/j.msea.2006.07.087>

- Wang, L., Felicelli, S., Gooroochurn, Y., Wang, P.T., Horstemeyer, M.F., 2008. Optimization of the LENS® process for steady molten pool size. *Mater. Sci. Eng. A* 474, 148–156. <https://doi.org/10.1016/j.msea.2007.04.119>
- Wang, Liang, Felicelli, S.D., Pratt, P., 2008. Residual stresses in LENS-deposited AISI 410 stainless steel plates. *Mater. Sci. Eng. A* 496, 234–241. <https://doi.org/10.1016/j.msea.2008.05.044>
- Wang, Y.-X., Zhang, P., Hou, Z.-G., Li, C.-Z., 2008. Inherent Strain Method and Thermal Elastic-Plastic Analysis of Welding Deformation of a Thin-Wall Beam. *J. Mech.* 24, 301–309. <https://doi.org/10.1017/S1727719100002434>
- Wang, Z., Denlinger, E., Michaleris, P., Stoica, A.D., Ma, D., Beese, A.M., 2017a. Residual stress mapping in Inconel 625 fabricated through additive manufacturing: Method for neutron diffraction measurements to validate thermomechanical model predictions. *Mater. Des.* 113, 169–177. <https://doi.org/10.1016/j.matdes.2016.10.003>
- Wang, Z., Stoica, A.D., Ma, D., Beese, A.M., 2018. Stress relaxation in a nickel-base superalloy at elevated temperatures with in situ neutron diffraction characterization: Application to additive manufacturing. *Mater. Sci. Eng. A* 714, 75–83. <https://doi.org/10.1016/j.msea.2017.12.058>
- Wang, Z., Stoica, A.D., Ma, D., Beese, A.M., 2017b. Stress relaxation behavior and mechanisms in Ti-6Al-4V determined via in situ neutron diffraction: Application to additive manufacturing. *Mater. Sci. Eng. A* 707, 585–592. <https://doi.org/10.1016/j.msea.2017.09.071>
- Wei, H.L., Mazumder, J., DebRoy, T., 2015. Evolution of solidification texture during additive manufacturing. *Sci. Rep.* 5, 16446. <https://doi.org/10.1038/srep16446>
- Wen, S., Shin, Y.C., 2011. Modeling of transport phenomena in direct laser deposition of metal matrix composite. *Int. J. Heat Mass Transf.* 54, 5319–5326. <https://doi.org/10.1016/j.ijheatmasstransfer.2011.08.011>
- Wen, S.W., Farrugia, D.C.J., 2001. Finite Element Modelling of Residual Stress in Pipe Welds. *Strain* 37, 15–18. <https://doi.org/10.1111/j.1475-1305.2001.tb01215.x>
- Withers, P.J., Bhadeshia, H.K.D.H., 2001. Residual stress. Part 1 – Measurement techniques. *Mater. Sci. Technol.* 17, 355–365. <https://doi.org/10.1179/026708301101509980>
- Wu, J., Ren, S., Zhang, Y., Cao, Y., Zhang, D., Yin, C., 2021. Influence of spatial laser beam profiles on thermal-fluid transport during laser-based directed energy deposition. *Virtual Phys. Prototyp.* 16, 444–459. <https://doi.org/10.1080/17452759.2021.1960734>
- Xie, R., Chen, G., Zhao, Y., Zhang, S., Yan, W., Lin, X., Shi, Q., 2019. In-situ observation and numerical simulation on the transient strain and distortion prediction during additive manufacturing. *J. Manuf. Process.* 38, 494–501. <https://doi.org/10.1016/j.jmapro.2019.01.049>
- Xie, R., Shi, Q., Chen, G., 2020a. Improved distortion prediction in additive manufacturing using an experimental-based stress relaxation model. *J. Mater. Sci. Technol.* 59, 83–91. <https://doi.org/10.1016/j.jmst.2020.04.056>
- Xie, R., Shi, Q., Chen, G., 2020b. Improved distortion prediction in additive manufacturing using an experimental-based stress relaxation model. *J. Mater. Sci. Technol.* 59, 83–91. <https://doi.org/10.1016/j.jmst.2020.04.056>
- Xiong, Y., Smugeresky, J.E., Lavernia, E.J., Schoenung, J.M., 2008. Processing and Microstructure of WC-CO Cermets by Laser Engineering Net Shaping. <https://doi.org/10.26153/tsw/7256>
- Yadollahi, A., Shamsaei, N., Thompson, S.M., Seely, D.W., 2015. Effects of process time interval and heat treatment on the mechanical and microstructural properties of direct laser deposited 316L stainless steel. *Mater. Sci. Eng. A* 644, 171–183. <https://doi.org/10.1016/j.msea.2015.07.056>

- Yan, G., Crivoi, A., Sun, Y., Maharjan, N., Song, X., Li, F., Tan, M.J., 2018. An Arrhenius equation-based model to predict the residual stress relief of post weld heat treatment of Ti-6Al-4V plate. *J. Manuf. Process.* 32, 763–772. <https://doi.org/10.1016/j.jmapro.2018.04.004>
- Yan, L., Li, W., Chen, X., Zhang, Y., Newkirk, J., Liou, F., Dietrich, D., 2017. Simulation of Cooling Rate Effects on Ti-48Al-2Cr-2Nb Crack Formation in Direct Laser Deposition. *JOM* 69, 586–591. <https://doi.org/10.1007/s11837-016-2211-8>
- Yang, Q., Zhang, P., Cheng, L., Min, Z., Chyu, M., To, A.C., 2016. Finite element modeling and validation of thermomechanical behavior of Ti-6Al-4V in directed energy deposition additive manufacturing. *Addit. Manuf., Special Issue on Modeling & Simulation for Additive Manufacturing* 12, 169–177. <https://doi.org/10.1016/j.addma.2016.06.012>
- Ye, R., Smugeresky, J.E., Zheng, B., Zhou, Y., Lavernia, E.J., 2006. Numerical modeling of the thermal behavior during the LENS® process. *Mater. Sci. Eng. A* 428, 47–53. <https://doi.org/10.1016/j.msea.2006.04.079>
- Yin, H., Felicelli, S., Wang, L., 2008. Fluid flow, heat and mass transfer in the molten pool of the LENS process. *TMS Annu. Meet.* 261–270.
- Yuan, M.G., Ueda, Y., 1996. Prediction of Residual Stresses in Welded T- and I-Joints Using Inherent Strains. *J. Eng. Mater. Technol.* 118, 229–234. <https://doi.org/10.1115/1.2804892>
- Zhang, L., Michaleris, P., 2004. Investigation of Lagrangian and Eulerian finite element methods for modeling the laser forming process. *Finite Elem. Anal. Des.* 40, 383–405. [https://doi.org/10.1016/S0168-874X\(03\)00069-6](https://doi.org/10.1016/S0168-874X(03)00069-6)
- Zhang, L., Reutzel, E.W., Michaleris, P., 2004a. Finite element modeling discretization requirements for the laser forming process. *Int. J. Mech. Sci.* 46, 623–637. <https://doi.org/10.1016/j.ijmecsci.2004.04.001>
- Zhang, L., Reutzel, E.W., Michaleris, P., 2004b. Finite element modeling discretization requirements for the laser forming process. *Int. J. Mech. Sci.* 46, 623–637. <https://doi.org/10.1016/j.ijmecsci.2004.04.001>

**Titre :** Modélisation thermomécanique performante de grandes pièces fabriquées par procédés de fabrication additive laser par dépôt de poudre

**Mots clés :** Fabrication additive laser par dépôt de poudre, Modèle thermomécanique, Loi de comportement élastoplastique, Restauration de l'écrouissage, Distorsions, Acier inoxydable 316L

**Résumé :** Les procédés de fabrication additive laser par dépôt de poudre offrent une opportunité unique pour la fabrication de grandes pièces à géométrie complexe. Cependant, les déformations mécaniques induites par ces procédés entraînent des défauts pouvant conduire à des pièces rebutées. Au cours de cette thèse, différents modèles ont donc été développés pour mieux comprendre l'apparition de ces déformations en fonction des paramètres opératoires. Un premier modèle thermomécanique prédit le comportement élastoplastique lors de la construction d'un mur en acier inoxydable 316L. L'apport de chaleur est modélisé par une source double ellipsoïdale mobile et la construction des couches se fait à l'aide d'une méthode hybride « Quiet/Active element ».

Un écrouissage isotrope non linéaire est considéré, avec prise en compte de la restauration d'écrouissage à hautes températures. Afin de réduire drastiquement les temps de calcul, une nouvelle source de chaleur est proposée utilisant une source ellipsoïdale allongée qui moyenne l'énergie sur un intervalle d'espace et de temps. Cependant, un intervalle d'espace trop grand diminue la précision du modèle. De nouveaux paramètres sont alors introduits afin d'identifier le meilleur compromis entre temps de calcul et précision. L'ensemble des modèles proposés est confronté avec succès avec des données expérimentales en termes de température et déplacement et ce pour différents paramètres opératoires. Enfin, des modèles multi-échelles basés l'activation par couche ou les méthodes de déformations inhérentes sont étudiés en vue de réduire les temps de calcul.

**Title :** Efficient thermomechanical modeling of large parts fabricated by Directed Energy Deposition Additive Manufacturing processes

**Keywords :** Directed Energy Deposition Additive Manufacturing, Thermomechanical model, Elastoplastic behavior, Stress relaxation model, Distortions, Stainless Steel 316L

**Abstract :** Directed Energy Deposition (DED) Additive Manufacturing technology offers a unique possibility of fabricating large-scale complex-shape parts. However, process-induced deformation in the fabricated part is still a big obstacle in successfully fabricating large-scale parts. Therefore, multiple numerical models have been developed to understand the accumulation of induced deformation in the fabricated part. The first model predicts the thermo-elastoplastic behavior that captures the laser movement. The laser-material interaction and metal deposition are modeled by employing a double ellipsoid heat source and the Quiet/Active material activation method respectively. A nonlinear isotropic hardening is considered, taking into account the stress relaxation at high temperatures.

Using this model as a reference case, an efficient model is developed with an objective to reduce the computation time and make it feasible to simulate large-part. The model employs an Elongated Ellipsoid heat source that averages the heat source over the laser path which reduces the computational burden drastically. However, averaging over large laser path results in inaccurate results. Therefore, new parameters are developed that identify the best compromise between computation time reduction and accuracy. Both models are validated with experimental data obtained from several experiments with different process parameters. Finally, other Multi-scale methods such as the Layer-by-layer method and Inherent Strain-based methods are implemented and explored.